Research Square

Preprints are preliminary reports that have not undergone peer review.
They should not be considered conclusive, used to inform clinical practice,
or referenced by the media as validated information.

Physical Discovery and Design from Incomplete Records

Sabitoj Singh Virk

sabitoj@umich.edu

Rensselaer Polytechnic Institute https://orcid.org/0000-0002-5801-5630

Akashdeep Singh Virk

Rensselaer Polytechnic Institute https://orcid.org/0000-0002-9157-4637

Research Article

Keywords: physical discovery; incomplete records; design; observation geometry; rheology; viscoelasticity; biomechanics; electrochemical impedance spectroscopy; superconductivity; compatible-answer principle

Posted Date: November 19th, 2026

DOI: https://doi.org/10.21203/rs.3.rs-11771654/v1

License: This work is licensed under a Creative Commons Attribution 4.0 International License.
Read Full License

Additional Declarations: The authors declare no competing interests.

Physical Discovery and Design from Incomplete Records

Sabitoj Singh Virk[1†*] and Akashdeep Singh Virk[1†]

[1] Rensselaer Polytechnic Institute, 110 8th St, Troy, NY 12180, United States of America

[†] Both authors contributed equally to this work.

[*] Correspondence: sabitoj@umich.edu

Incomplete experimental records, whether through lost metadata and specimen links[1–5] or inseparable material and apparatus responses[6–12], can yield consequential physical discoveries and actionable design rules for medicine, energy storage and materials processing. We formulate and test the compatible-answer principle: a record settles a question when every description compatible with the record and observation model supports the same conclusion; otherwise, answer-changing differences specify the relation required of the next observation or processing path. In pre-cirrhotic liver records lacking specimen correspondence, interventions associated with fewer transformed foci reduce cyclic dissipation by 27–40% at equal applied stress yet increase it at equal recorded strain.[13] Exact bounds across all 14,400 admissible reconstructions per design preserve this reversal and constrain equal-work loading changes. Independent tissue records confirm recurrence, including opposite work orderings in 59 of 60 human-brain participants.[14–16] Disease-model and clinical interventions translate these orderings into loading requirements. MMP9-associated softening in LIS1-mutant cortical organoids increases the five-second stress-step work coefficient 3.82-fold, requiring 48.8% lower stress for equal work,[17] while post-shunt brain mechanics from a 20-patient cohort define frequency-specific equal-work stress reductions of 2.8–7.3%.[18] Matching nonzero external branch impedances in parallel battery networks creates a shared fractional-linear map that recovers individual-cell spectra without branch-current measurements. Network acquisitions built from measured spectra preserve frozen capacity computations across four institutions and a seven-cell replication.[19–24] In pressure-quenched $Bi_{0.5}Sb_{1.5}Te_3$, pressure release reverses precursor rankings: the lower-transition source yields the higher ambient-pressure superconducting component, with a 7.4-K release-response contrast; a source-normalized 77-K trajectory advantage of at least 4.3 K remains identifiable despite a missing source transition.[25] Original surfactant measurements and measured microwave transfers test both branches through energetic orderings and fixed-readout preservation.[26,27] Together, these results connect physical discovery, clinical and mechanical loading, observation geometry and nonequilibrium state selection through a unifying information principle.

The energetic meaning of a material change depends on how it is loaded. The same remodelling can lower dissipation under a prescribed stress and raise it under a prescribed strain. When specimen identities are lost or measured responses remain entangled with an apparatus, the underlying system may no longer be uniquely reconstructable. Yet the physical ordering or operating requirement relevant to an experiment or intervention can remain fixed.

Experimental science repeatedly creates this separation between system reconstruction and question-specific decision. Physical measurements rarely isolate a specimen from handles, contacts, supports or acquisition hardware, while published datasets can retain values but lose the annotations needed to connect them.[1–5,28] Molecular handles and optical traps shape single-molecule trajectories, contact resistance changes apparent electronic transport, and instrument compliance alters recorded rheology.[6,8–11,29] Acquisition-specific artifacts can also become predictive shortcuts that fail when hardware changes.[7] Physical-inference studies recover molecular free energies and detect nonequilibrium dynamics,[30,31] while identifiability theory examines which parameters and predictions are fixed by partial observations.[32–34] Consequential scientific, engineering and clinical

decisions, however, often ask whether the remaining ambiguity can change a particular physical answer, such as an energetic ordering, a required loading adjustment, the input to an established computation or the ranking of recovered material states.

The compatible-answer principle formalizes this distinction. For a specified record and physical observation model, we map the complete family of compatible system descriptions to the target question. The record settles the question when the resulting answers coincide or remain within one decision class. If they cross a decision boundary, the distinctions among the underlying descriptions identify the physical relation that a new measurement or processing path must establish. Missing information therefore has two roles: answer-invariant uncertainty can remain unresolved, whereas answer-changing uncertainty becomes a design requirement. The aim is not to choose a preferred reconstruction, but to determine the set of physical answers permitted by the record.

We test this logic in three complementary roles. Tissue mechanics asks which energetic orderings and loading requirements survive missing specimen links.[13–18] Parallel battery networks ask how observation geometry can create a shared relation that recovers cell-resolved spectra and preserves an existing computation.[19–24] Pressure-quenched superconductivity asks whether incomplete release trajectories suffice to evaluate a precursor coordinate and rank recovered states.[25] Original surfactant measurements and measured microwave transfers provide direct tests of loading-specific ordering and fixed-readout preservation.[26,27] Taken together, these applications show how incomplete records can certify discoveries, determine loading requirements, enable cell-resolved signal recovery and rank processing trajectories, despite the systems' distinct underlying physics. What unifies them is not a shared constitutive model, but the information required to settle each physical question.

Work without a unique stiffness

In a material–support pair, the energy lost over a cycle can be better determined than the material's stiffness. Their series extensions add, so their compliances, or displacements per unit force, also add. Writing the material response as $C_m^* = C'_m - iC''_m$, a purely elastic support compliance C_e gives

$$C_o^* = C_m^* + C_e, C''_o = C''_m. \quad (1)$$

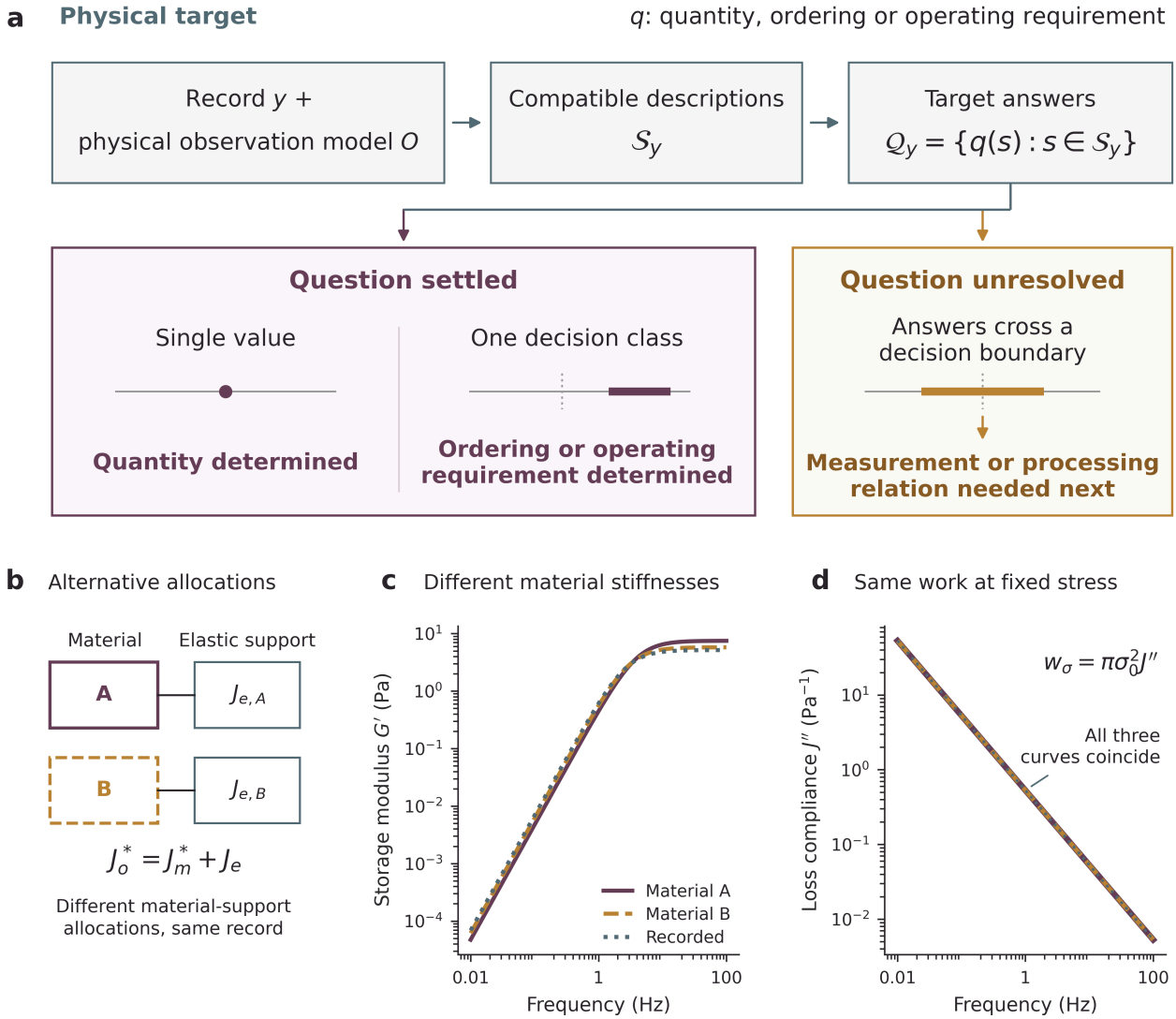
The support changes the in-phase motion and returns its stored energy. Loss compliance remains unchanged and determines the dissipated work at force amplitude F_0:

$$W_F = \pi F_0^2 C''. \quad (2)$$

For calibrated stress and strain, the corresponding work per volume is $w_\sigma = \pi \sigma_0^2 J''$, where $J^* = 1/G^*$ and $G^* = G' + iG''$. These established linear-response identities apply at the specified frequency and small amplitude.[8,9] Every admissible allocation of real series compliance therefore yields the same equal-force or equal-stress work, even while intrinsic stiffness remains unresolved.

The answer-set criterion asks whether the answers permitted by the record settle the target (Fig. 1a). Two passive single-Maxwell descriptions illustrate the procedure: reallocating elastic compliance changes the intrinsic spectrum while preserving the complete recorded response and loss compliance (Fig. 1b–d). This ambiguity extends to positive finite-Maxwell families (Supplementary Information S1). An inverse benchmark confirms that near-perfect response agreement can coexist with substantial material-reconstruction error (Extended Data Fig. 1).

Figure 1 | Physical discovery and design from compatible answer sets



Stiffness remains ambiguous; dissipated work is fixed.

Constructed passive responses with a purely elastic series contribution.

a, A record and physical observation model define the compatible descriptions S_y, which a target q maps to the answer set Q_y. If Q_y is a single value or lies entirely within one decision class, the record settles a quantity, ordering or operating requirement without selecting a preferred reconstruction. If Q_y crosses a decision boundary, the descriptions on opposite sides identify the measurement or processing relation needed next. **b,** Material and elastic support compliances add, $J_o^* = J_m^* + J_e$. Alternative allocations of real compliance give the same complete recorded response. **c,** Two passive single-Maxwell materials have different intrinsic storage moduli. Material A has viscosity $\eta = 0.3$ Pa s, relaxation time $\tau = 0.04$ s and support compliance $J_e = 0.06$ Pa^{-1}. Moving 0.04 Pa^{-1} of real compliance to the material gives material B a relaxation time of 0.052 s and support compliance 0.02 Pa^{-1}. Their respective supports produce the same recorded modulus. **d,** Both material loss compliances coincide with the recorded loss compliance, giving identical work density $w_\sigma = \pi \sigma_0^2 J''$ at a specified peak stress and frequency. All curves are exact constructed linear-response results with purely elastic support; material A is plum and solid, material B ochre and dashed, and the recorded response slate and dotted. Supplementary Information S1–S2 gives the derivation.

Let S_y contain the nonempty set of descriptions compatible with a record, its physical observation model and the admitted uncertainty. For a target q, the possible answers are

$$Q_y = \{q(s) : s \in S_y\}. \quad (3)$$

A single value identifies the target; a range confined to one side of a decision boundary settles an ordering or operating requirement. If the answer set crosses that boundary, the descriptions on opposite sides identify what a resolving observation must distinguish. Measurement uncertainty enters through the compatibility conditions. The decision is made from Q_y, not from a preferred element of S_y.

The answer set distinguishes a determined value, a settled ordering and an unresolved comparison. A resolving observation need distinguish only descriptions that imply different target answers. Elastic series compliance, unknown specimen matching and shared fractional-linear readout generate different compatible families; exact invariants, extremal bounds and reference calibration determine what each family preserves or what additional relation it requires.

Loading is part of that question. Measured loss stiffness determines work at fixed recorded displacement; at fixed recorded strain, $w_\gamma = \pi \gamma_0^2 G''$. Intrinsic material displacement is a distinct control. Force- and displacement-based expressions agree along the same actual trajectory, whereas fixing different amplitudes across states compares different trajectories. The invariant uses linear harmonic response and a purely elastic series contribution (Methods).

Energetic reversals survive data loss

The incomplete liver records reveal a reversal in energetic ordering that the missing specimen links could not erase. In the mutant-β-catenin experiments of Fan and colleagues, interventions associated with fewer transformed foci implied less cyclic work at equal applied stress, yet more at equal recorded strain (Fig. 2a, b). Fixing stress allows the tissues to deform differently; fixing deformation allows the stress to differ. The same tissue change therefore has opposite energetic consequences under these two loading conditions.[13]

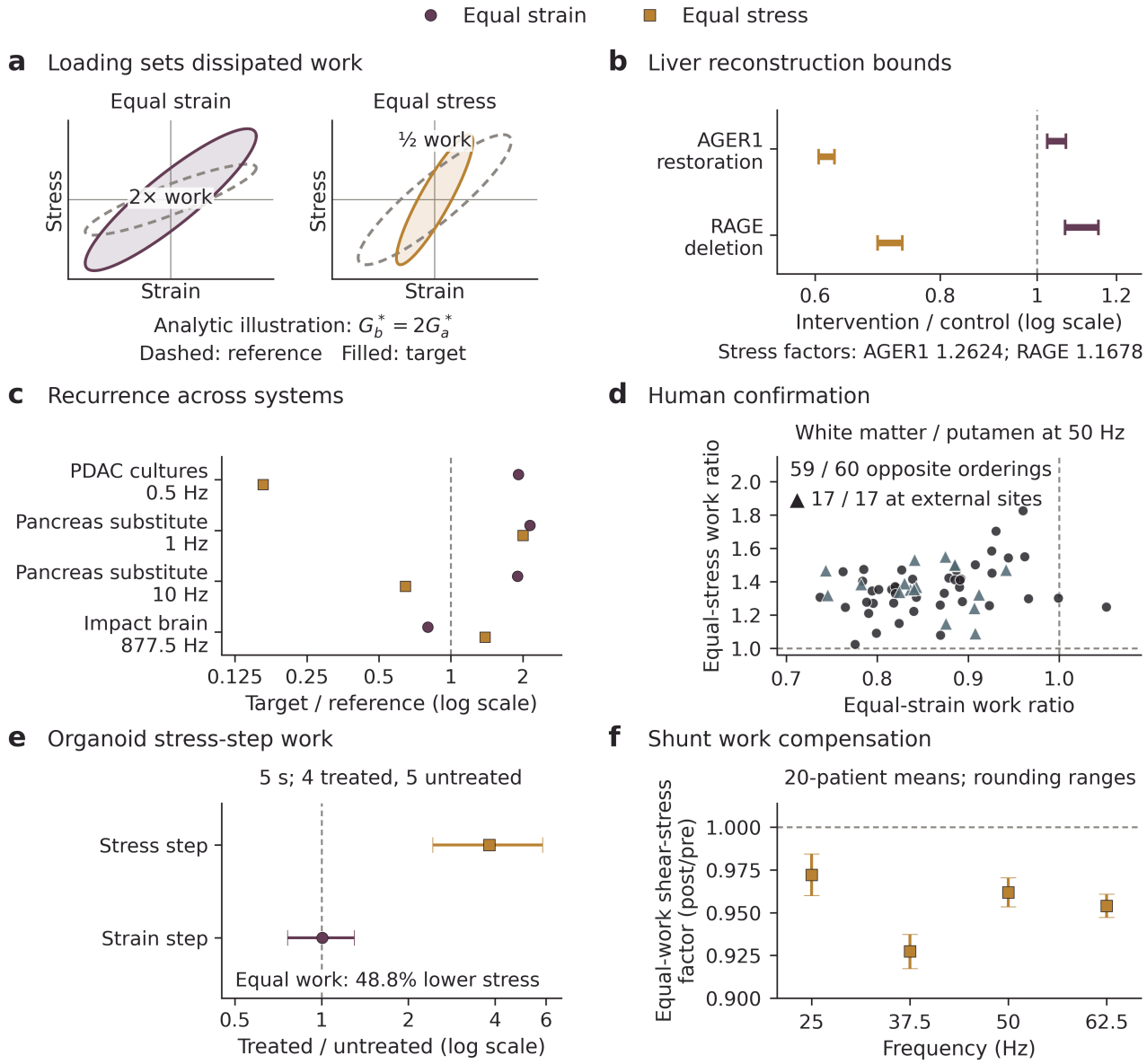
For two linked harmonic responses at the same frequency, the equal-stress work ratio is the equal-strain ratio divided by the ratio of squared complex-modulus magnitudes. A material can therefore dissipate more at fixed deformation while its increased response magnitude suppresses deformation enough to dissipate less at fixed stress. The record-specific calculations below retain the original pairing or all admissible pairings before applying the nonlinear transformations.

Each arm retained five storage moduli and five loss tangents, assumed to describe the same five mice, without their specimen correspondence. For storage modulus $g = G'$ and loss tangent $t = G''/G'$, the quantities that determine these two losses are

$$J'' = \frac{t}{g(1+t^2)}, G'' = gt. \quad (4)$$

Every admissible reconstruction preserved the reversal. Five mice per arm give 120 within-arm matchings and 14,400 cross-arm reconstructions for each intervention; rearrangement gives the exact extrema.[35] AGER1 restoration lowered inferred mean equal-stress work by 37–40%, and hepatocyte RAGE deletion lowered it by 27–31%, while both raised equal-recorded-strain work. Every intervention order statistic was also lower than its corresponding control order statistic for loss compliance, across every complete matching. Recovering the specimen identities could refine these magnitudes without changing the complete-record ordering. The lower mean equal-stress work also survived conservative independent omission from the unlinked lists (Supplementary Information S4).

Figure 2 | Loading determines work ordering and intervention compensation



a, Analytic harmonic loops: doubling complex modulus doubles equal-strain work and halves equal-stress work. Dashed loops denote reference; filled loops denote target. **b,** Exact liver work-ratio bounds over all 14,400 cross-arm reconstructions per design (five mice per arm). Labelled downward-rounded stress factors ensure no increase in calculated cohort-mean work across every admitted matching.[13] **c,** Paired PDAC cultures (0.5 Hz; three plates per condition), pancreas substitute/native means (1 and 10 Hz), and immediate/pre-injury brain means (877.5 Hz; five animals; 0.5-mm impact). The pancreas stiffness-match and loss-reversal comparisons use different frequencies.[14,16,36,37] **d,** White-matter/putamen ratios in 60 confirmation participants at 50 Hz, including 17 external-institution participants (slate triangles).[15] **e,** Five-second maintained-step coefficients for four MMP9-treated versus five untreated LIS1-mutant organoids, transformed before geometric-mean comparison.[17] The stress-step ratio is 3.821 (95% bootstrap interval, 2.429–5.843), requiring 48.8% lower stress for equal work; the strain-step ratio is 1.005. Whiskers show 95% within-group organoid bootstrap intervals. Work ends before unloading. **f,** Equal-work stress factors derived from 20-patient cohort-mean brain responses before and after shunting, at 25–62.5 Hz.[18] Whiskers show deterministic ranges from independent ±0.005-kPa component rounding. Statistical and frequency-specific details are in Supplementary Information S7.2 and S7.4.

Linked pancreatic-culture records reproduced the contrast: at day 21, three plates per condition gave a treated/untreated work-coefficient ratio of 1.912 at equal strain and 0.164 at equal stress.[14] Tissue-substitute comparisons made its design consequence explicit. Native and engineered pancreas nearly matched in reported mean storage modulus at 1 Hz (71 versus 73 kPa), yet their loss moduli differed 2.14-fold. At 10 Hz, the

primary-table mean responses instead gave 1.90-fold higher equal-strain loss and 35% lower reciprocal-response equal-stress loss for the engineered substitute (Fig. 2c). These frequency-specific comparisons show why stiffness matching alone does not specify energetic fidelity. Dental and chromosome records extend the loading-based comparison across material classes and scales (Extended Data Fig. 4; Supplementary Information S5 and S6).[36–40]

A regional contrast selected in human-brain study E was then tested unchanged in studies A–D reserved for confirmation. White matter showed lower calculated loss than putamen at equal strain but higher loss at equal stress in 59 of 60 eligible participants, including all 17 participants from two external acquisition institutions (Fig. 2d). The geometric-mean ratios were 0.855 (95% confidence interval, 0.838–0.872) and 1.355 (1.318–1.393), respectively. This contrast met the complete confirmation criterion, including practical effect thresholds and correction across the five discovery-selected pairs. Alternative regional summaries and stricter coverage retained its direction. Acute post-impact brain group means showed an analogous reversal (Fig. 2c; Supplementary Information S7.1 and S7.3).[15,16]

Interventions change equal-work loading

Changes in tissue mechanics determine the loading adjustment needed to maintain equal dissipation. For a specified linear-response waveform, duration and geometry, dissipated work W is the product of squared loading amplitude A and a positive material-work coefficient K. Equal work between reference a and target b therefore requires

$$W = A^2 K, \frac{A_b}{A_a} = \sqrt{\frac{K_a}{K_b}}.$$

The load–remodelling compensation relation converts the recovered work coefficient into an experimental setting. Harmonic stress uses loss compliance, harmonic strain uses loss modulus, and a maintained step uses the integrated dissipative response over its stated duration. The incomplete liver records bound the equal-work stress-amplitude factors of 1.262–1.286 after AGER1 restoration and 1.168–1.201 after RAGE deletion. Using downward-rounded factors of 1.2624 and 1.1678, respectively, cannot increase calculated cohort-mean work under any admitted matching. A compliant source supplies a second control: varying added elastic compliance switches the work ordering (Extended Data Fig. 5). Every complete reconstruction has exactly one positive crossover, bounded by 0.191–0.484 kPa^{-1} for AGER1 and 0.415–0.813 kPa^{-1} for RAGE. Thus, missing correspondence leaves both a robust loading decision and a sharply located experimental transition accessible.

The same correspondence bounds also determine the best uniform approximation to equal work: one stress factor keeps calculated cohort-mean work within 1.84% or 2.84% of control across every admitted reconstruction for AGER1 restoration or RAGE deletion, respectively (Supplementary Information S2).

MMP9-associated softening in LIS1-mutant cortical organoids increased stress-controlled dissipation and changed the loading required for equal work. MMP9 treatment approximately halved fitted instantaneous and equilibrium stiffness, yet increased the calculated five-second stress-step work coefficient 3.82-fold (Fig. 2e).[17] Equalizing the geometric-mean work of four treated and five untreated mutants therefore requires 48.8% lower stress amplitude. The strain-step coefficient ratio had a near-unity point estimate, giving a direct stress-versus-strain effect ratio of 3.80 (Supplementary Tables 18–19). Independent curve refitting recovered a 3.74-fold stress-controlled increase, and direct integration of viscous-branch power verified the work calculation. Treatment-associated softening therefore changes the loading required for equal work, with different consequences under stress and strain control.

Clinical shunting produced a frequency-specific unloading requirement in a 20-patient hydrocephalus cohort. Loss compliance reconstructed from cohort-mean moduli increased after shunting across all four measured frequencies from 25 to 62.5 Hz.[18] At unchanged shear-stress amplitude, calculated dissipation therefore increases by 5.81–16.29%; equal work requires 2.78–7.27% lower post-shunt stress amplitude (Fig. 2f). Every

frequency-specific factor remains below unity throughout the printed-input rounding ranges. At 62.5 Hz, a single positive source-compliance crossover at 0.272 kPa^{-1} also reverses the work ordering (Supplementary Information S7.4). The intervention thus defines an unloading requirement whose energetic interpretation depends on the source coupling.

Separate clinical reports establish that intracranial pulsatility is associated with shunt response and falls after intervention. At 12 months, 34 of 37 patients with elevated overnight pulse amplitude responded, compared with one of eight with low amplitude.[41] A separate 13-patient study found reduced pulse amplitude after shunting, with next-day normalization in nine; valve adjustments also changed pulsatility in the two patients examined.[42] These observations establish the clinical relevance of pulsatile loading and its modification by intervention.

Together, the biological analyses identify a loading-dependent energetic phenotype, confirm it in individuals and quantify how applied stress must change after disease-model and clinical interventions. The specimen-level descriptions remain unresolved, yet every admitted description supports the same ordering or a bounded loading decision. The battery problem asks the complementary design question: what observation relation must be created when the installed measurement does not preserve the required answer?

Designing cell-resolved observation

When the installed observation does not preserve the cell-specific coordinate required by a frozen computation, answer-changing ambiguity becomes a circuit-design specification. Connecting cells in parallel changes each local voltage response because current redistributes through the network. A capacity predictor trained on standalone spectra therefore encounters different input coordinates. We seek an interconnection condition that recovers those coordinates while leaving the predictor unchanged. Multi-cell impedance measurements and controlled interconnection resistance provide the relevant experimental setting.[43–45]

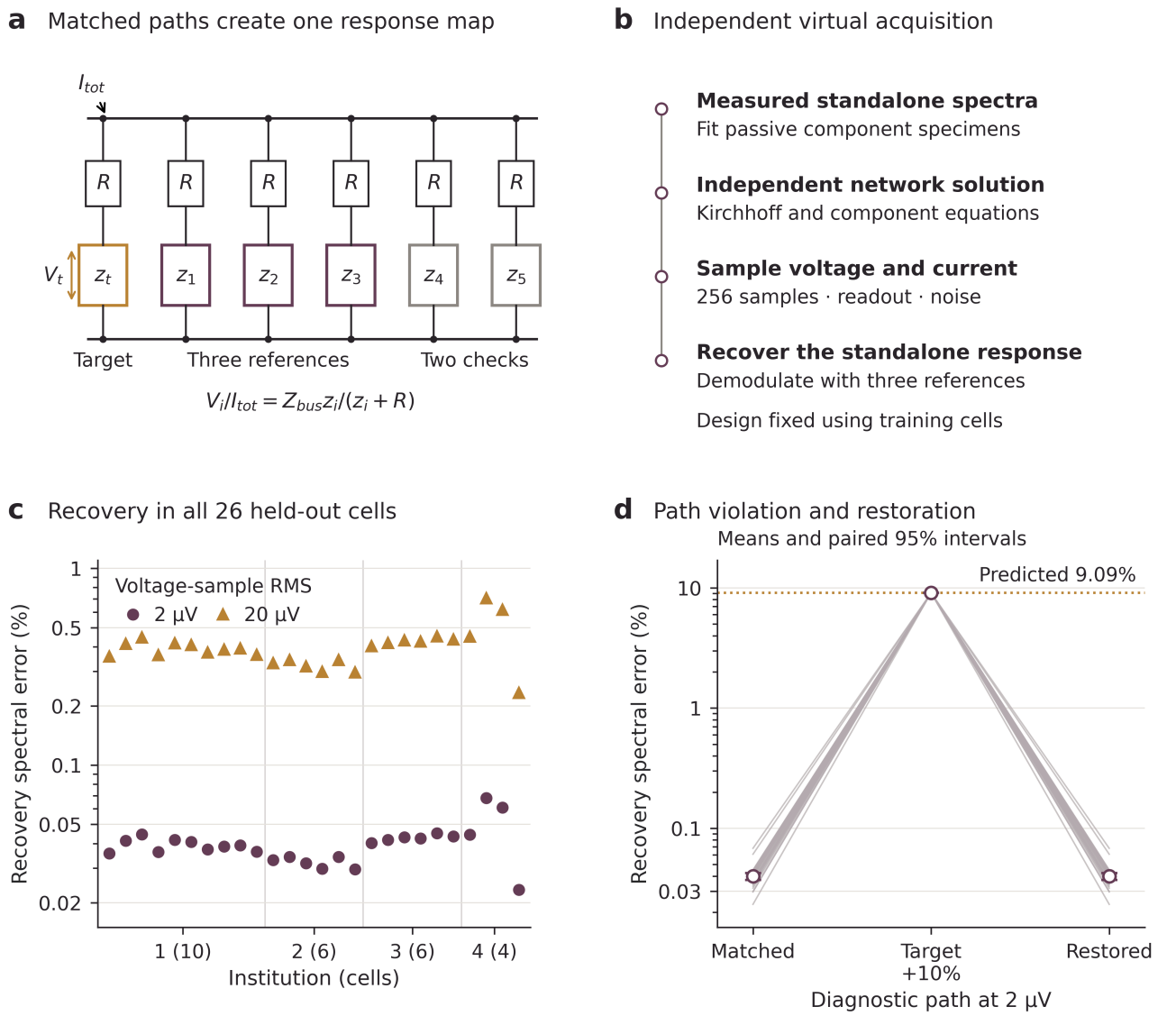
Consider a linear small-signal parallel network observed through its injected total current and a voltage tap across each cell. Branch currents remain unmeasured. Cell i has impedance z_i and total external branch impedance r_i. If Z_{bus} denotes bus voltage divided by total current, the cell-only voltage divided by that same current is

$$y_i = Z_{bus}\frac{z_i}{z_i + r_i}. \quad (5)$$

Matching the external totals, $r_i = R \neq 0$, creates a common fractional-linear relation $M(z) = Z_{bus}\, z/(z+R)$ (Fig. 3a). Other cells alter Z_{bus}, which remains shared by targets and references at each frequency and network state. The relation is nonsingular for finite nonzero Z_{bus} and R. The taps span only the cells: at $R = 0$, they collapse to the common bus response. Matching includes contacts and every external branch contribution while allowing cell spectra to differ. Independently known current standards establish the standalone frame without measuring every branch current.

Matching the complete external totals is sufficient to create this shared relation; as-manufactured welds, busbars and contacts need not be identical. During low-current diagnostic acquisition, native paths can be characterized and compensated using branch-specific trim or controlled impedance. Independently calibrated unequal branch and bus impedances instead admit a direct circuit inverse (Methods; Extended Data Fig. 7; Supplementary Information S10).

Figure 3 | Observation geometry creates recoverable cell responses



a, Equal nonzero total external branch impedances and finite nonzero bus impedance create a shared fractional-linear relation between cell impedance and cell-only voltage divided by injected total current. Three reference states calibrate the relation; two additional states are unused checks. **b,** Independent component equations generate voltage/current records from passive representations of measured spectra, followed by sampling, demodulation and decoding. Acquisition choices are fixed using training cells. **c,** Mean spectral recovery error for 26 held-out LiBforSecUse cells, comprising 4,297 records across four institutions, at 2 and 20 µV voltage-sample RMS noise.[22,23] Error is RMS fractional spectral deviation from the fitted standalone response. **d,** The same cells under matched paths, a target-only +10% path change and restored matching at 2 µV. Thin lines are cell means; symbols and whiskers give equal-cell means and paired 95% whole-cell bootstrap intervals, stratified within institution. The dotted line is the exact noiseless prediction, $100(1-1/1.1) = 9.09\%$. Restoration reproduces the matched result under paired noise. Summaries average records and five fixed noise realizations within each cell. Spectra and capacities are measured; network installation, readout changes and noise are simulated.

This shared relation makes a classical calibration available. For a target z and three distinct reference values a, b, c, a nonsingular fractional-linear map preserves

$$\chi = \frac{(z-b)(a-c)}{(z-c)(a-b)}. \quad (6)$$

Current target and reference observations determine χ. Inversion using the independently known present reference responses recovers the target in their frame. Conventional three-point calibration gives the same answer from the same information.[46–48] The constructive result is the circuit condition that supplies the common observation relation. Independently known branch and bus impedances in a calibrated frame also permit direct inversion (Methods; Extended Data Fig. 7).

For a constructed pair of networks with identical terminal and cell-tap spectra at every frequency, any deterministic decoder restricted to those observations has relative RMS error of at least 11/37 (29.73%) in one of the two target-cell spectra. This bound is tight for that pair and the defined metric, quantifying the obstruction that a resolving observation must remove (Supplementary Information S10.8).

Controlled recombinations of measured spectra from 248 cells test whether branch equality supplies the required relation across 7,440 held-out target panels.[19,20] Unequal contacts give 5.34% median relative RMS target error; matched external totals recover every target to numerical precision. Comparisons at equal impedance scales and exactly matched means isolate branch equality. Additional references and imposed-noise sweeps separately quantify calibration and inverse conditioning (Extended Data Figs. 7 and 8; Supplementary Information S10).

To test the design beyond this algebraic construction, we generated acquisitions from independently assembled component equations (Fig. 3b). Passive realizations of measured cell spectra were connected through external paths. Kirchhoff constraints and component equations generated voltage and current signals, followed by sampling, perturbation and demodulation. The component-level forward solver generated these signals independently of the decoder relation in equation (5). Decoding used current observations and standalone reference values, with target impedance excluded from its inputs. Separate transient integrations verified selected harmonic acquisitions.

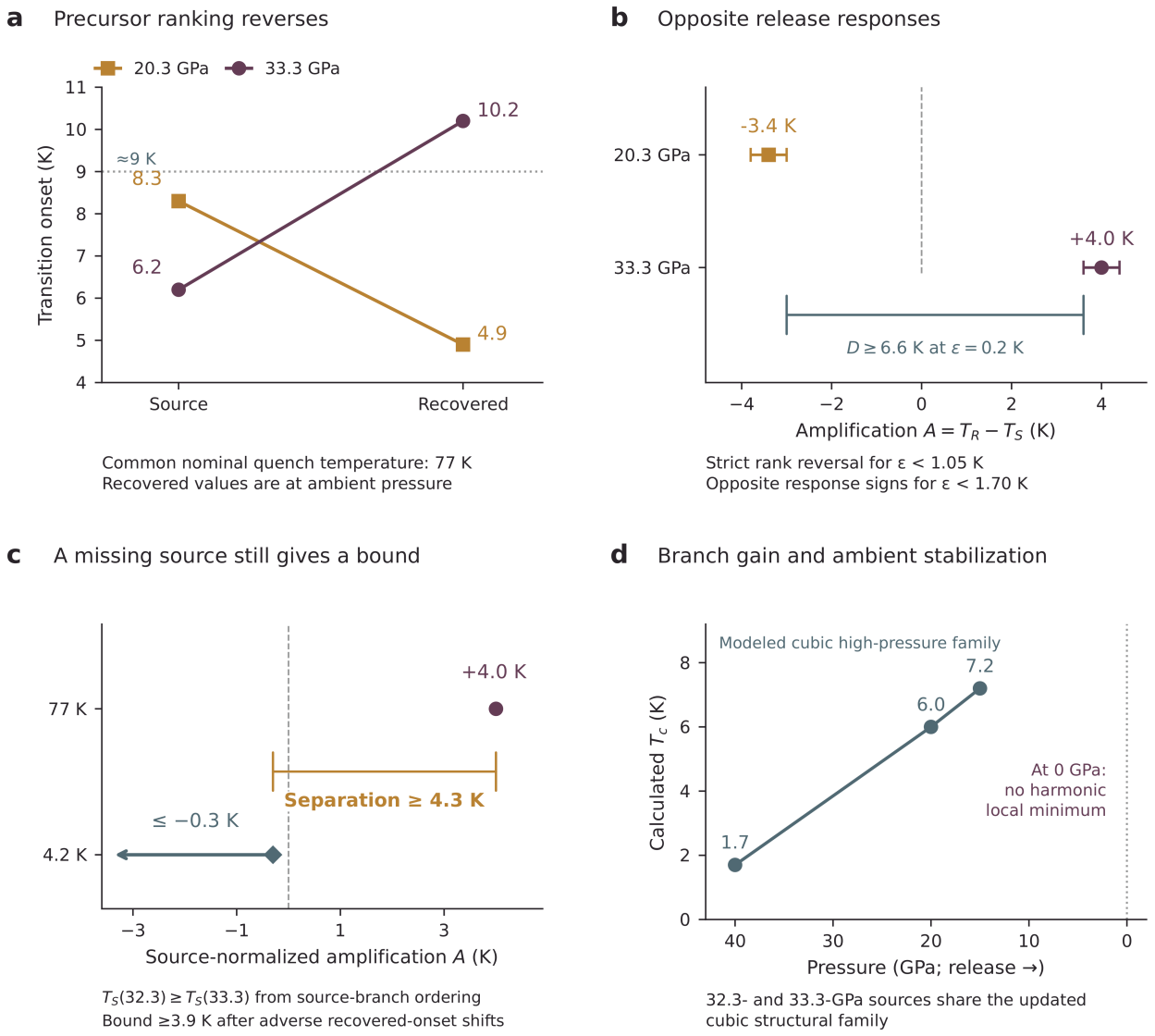
In LiBforSecUse, each of 26 physical cells was held out in turn. Only the other cells within its institution determined the frozen predictor, frequency mask, references, common resistance and excitation.[22,23,49] Across 4,297 records and five noise realizations, 2 μV RMS voltage-sample noise yielded 0.0399% cell-balanced spectral recovery error relative to the virtual standalone responses (95% whole-cell bootstrap interval, 0.0370–0.0424%; Fig. 3c). The largest cell mean was 0.0681%. Increasing the sample noise to 20 μV raised the aggregate error to 0.4002% (Extended Data Fig. 9).

A paired path-perturbation test deliberately violates the designed condition. Increasing only the target's external path by 10% produces the predicted $\hat{z} = z / 1.1$ response and 9.09% noiseless error; restoring the matched path restores the original result under identical noise realizations (Fig. 3d). Relative, absolute and heterogeneous-path sensitivities are retained in Supplementary Fig. 10g and Supplementary Information S10 and S12. The independently solved NREL–DENSO replication recovers seven prespecified held-out cells with 0.1779% cell-balanced spectral error at 2 μV (Extended Data Fig. 10).[24,50] Across the held-out cohorts, the recovered spectra closely preserve the frozen capacity predictions obtained from the corresponding virtual standalone responses.

Release reverses precursor ranking

Pressure-release records test whether a precursor property remains sufficient for ranking recovered states. In $Bi_{0.5}Sb_{1.5}Te_3$ (BST), pressure release reverses precursor ranking: two releases at the same nominal quench temperature of 77 K give opposite source-to-recovered orderings. The 20.3-GPa source falls from an onset transition of 8.3 K to 4.9 K after release, whereas the 33.3-GPa source rises from 6.2 K to a 10.2-K ambient-pressure transition component in the recovered mixed sample (Fig. 4a).[25] Increasing current from 10 to 100 mA shifts the high onset to 9.8 K, supporting its superconducting origin. The source with the lower transition therefore yields the recovered component 5.3 K higher.

Figure 4 | Pressure release reverses precursor ranking



a, Onset transitions for BST quenched at a common nominal temperature of 77 K from 20.3 GPa (ochre squares) and 33.3 GPa (plum circles) to ambient pressure.[25] The 10.2-K onset identifies the higher transition component in the recovered mixed sample. The dotted line marks the approximately 9-K measured compression maximum. **b,** Source-normalized changes, $A = T_R - T_S$. Whiskers span exact deterministic intervals under independent ±0.2-K perturbations of each source and recovered onset; the bracket gives the guaranteed response contrast, $D \geq 6.6$ K. The stated perturbation radii preserve strict rank reversal and opposite response signs. **c,** The 77-K trajectory from 33.3 GPa gives $A_{77} = +4.0$ K. Source-branch ordering constrains the 4.2-K trajectory from 32.3 GPa to $A_{4.2} \leq -0.3$ K, represented by the leftward half-line.[25] Their separation is at least 4.3 K, or 3.9 K after adverse ±0.2-K shifts of the recovered onsets with source ordering retained. **d,** Calculated transition temperatures along the modeled cubic high-pressure family; lines connect tabulated values.[25] No transition temperature is assigned to its unstable harmonic endpoint at 0 GPa. Updated diffraction places the two near-matched source pressures in the same cubic structural family.[51]

For trajectory j, define source-normalized amplification $A_j = T_{R,j} - T_{S,j}$. The two 77-K records give $A_{20.3} = -3.4$ K and $A_{33.3} = +4.0$ K, a 7.4-K release-response contrast (Fig. 4b). Independent symmetric perturbation of every endpoint by ϵ leaves the precursor rank reversal strict for $\epsilon < 1.05$ K and the opposite loss/amplification signs strict for $\epsilon < 1.70$ K. At the displayed-value stress $\epsilon = 0.2$ K, the release-response contrast remains at least 6.6 K. These inequalities exclude a common additive release shift, a common nonnegative retention factor and every nondecreasing source-transition-only release law. Source onset alone is therefore not an order-preserving precursor-selection coordinate.

A missing source value leaves a second trajectory result exact. Release from 32.3 GPa at 4.2 K yields 5.9 K. The reported decreasing source branch gives $T_S(32.3) \geq T_S(33.3)$, so

$$A_{77} - A_{4.2} = (10.2 - 5.9) + \left[T_S(32.3) - T_S(33.3)\right] \geq 4.3\,K. \quad (7)$$

The bound remains 3.9 K under adverse 0.2-K shifts of the recovered onsets (Fig. 4c). Updated diffraction places both near-matched sources in the same cubic high-pressure family while retaining nuclear order-disorder as a possible hidden coordinate.[51]

The 10.2-K component also lies 1.2 K above the approximately 9-K measured compression maximum, remaining 0.8 K above it under the same stress. Source calculations show that the modeled high-pressure basin can gain T_c on release but is not a harmonic local minimum at ambient pressure (Fig. 4d).[25] Beyond passive harmonic continuation of the modeled structures, the recovered component requires stabilization or transformation. Pressure release acts as a state-selection operation: precursor state and release history must be optimized jointly for the recovered superconducting outcome.

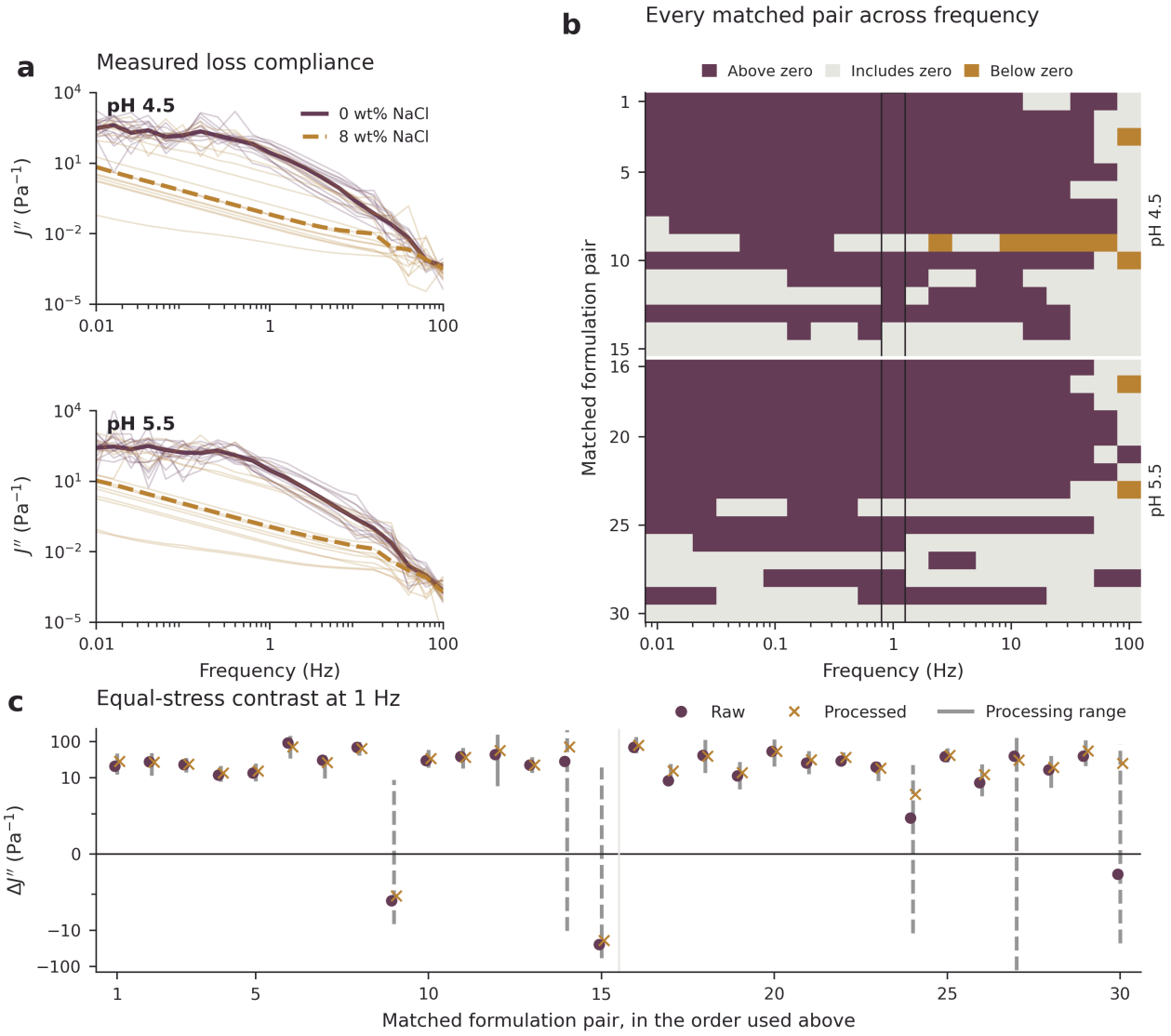
Original measurements determine energetic orderings

Original measurements then test both directions directly: surfactant rheology tests whether energetic orderings survive admitted response ambiguity (Fig. 5), while measured instrument transfers test whether a fixed physical readout is preserved after a change of observation frame (Fig. 6d).

Original surfactant measurements provide an experimental test of loading-specific inference across sixty formulations. Cocamidopropyl betaine and sodium lauryl ether sulfate (CAPB–SLES) mixtures combine two pH values, three nominal total active surfactant concentrations and five mixture fractions, matched between 0 and 8 wt% added NaCl. Frequency-sweep rheology yields 1,260 paired mean storage–loss responses from three runs per formulation at 21 frequencies from 0.01 to 100 Hz (Fig. 5a). The measured mean moduli determine loss compliance and the calculated cyclic work at a common small stress, without requiring a unique relaxation spectrum.

At 1 Hz, 24 of the thirty lower-salt-minus-higher-salt loss-compliance ranges are entirely positive, while six contain zero (Fig. 5c). Each is the exact deterministic envelope under the specified component-processing construction. Across all 630 pair–frequency comparisons, 420 envelopes lie above zero, ten below and 200 intersect zero (Fig. 5b). Within the elastic-series model, these orderings are independent of how real compliance is allocated between specimen and support. They directly establish whether adding salt raises or lowers work at the same imposed stress. Loss modulus answers the corresponding equal-strain question. The envelopes assess sensitivity to processing, with frequencies remaining nested within formulations.

Figure 5 | Energetic comparisons across sixty measured surfactant formulations



Lower salt minus higher salt: 24 of 30 processing ranges are positive at 1 Hz. Ranges describe processing sensitivity.

a, Loss compliance for sixty CAPB–SLES formulations at 21 frequencies (0.01–100 Hz), calculated from arithmetic-mean storage and loss moduli over three runs per formulation. Thin lines show individual formulations; thick lines are pointwise medians of fifteen formulations per pH/salt group. Plum and ochre denote 0 and 8 wt% added NaCl. **b,** Thirty salt pairs matched by pH and active composition at all 21 frequencies. Each cell classifies the lower-salt-minus-higher-salt loss-compliance difference over component rectangles centred on the processed responses. Plum and ochre indicate ranges entirely above or below zero; pale grey indicates ranges containing zero. The outlined column is 1 Hz. Pairs 1–15 have pH 4.5 and 16–30 have pH 5.5. **c,** All thirty 1-Hz comparisons in the same order. Circles and crosses denote raw and processed differences; segments give exact deterministic processing ranges. Solid segments identify twenty-four positive ranges; dashed segments identify six containing zero. The ordinate is $\Delta w / \left(\pi \sigma_0^2\right)$ for the equal-stress linear-response comparison. The symmetric-log axis is linear between −1 and 1 Pa^{-1}. These envelopes quantify processing sensitivity, with frequencies nested within formulations, the experimental units. Work is calculated from measured moduli; Supplementary Information S14 defines the processing ranges.

Preserving physical readouts across observation changes

A specified physical target can also be the output of an existing computation. Restoring its required observation coordinates allows that readout to be preserved across a changed acquisition. We tested this consequence with capacity as an independently measured outcome, keeping predictor parameters and auxiliary inputs fixed. Three input stages separate the effects: the original measured spectrum, its passive standalone realization and the response recovered after virtual installation. Prediction displacement compares recovered and virtual-standalone outputs. Capacity accuracy compares each output with the measured outcome.

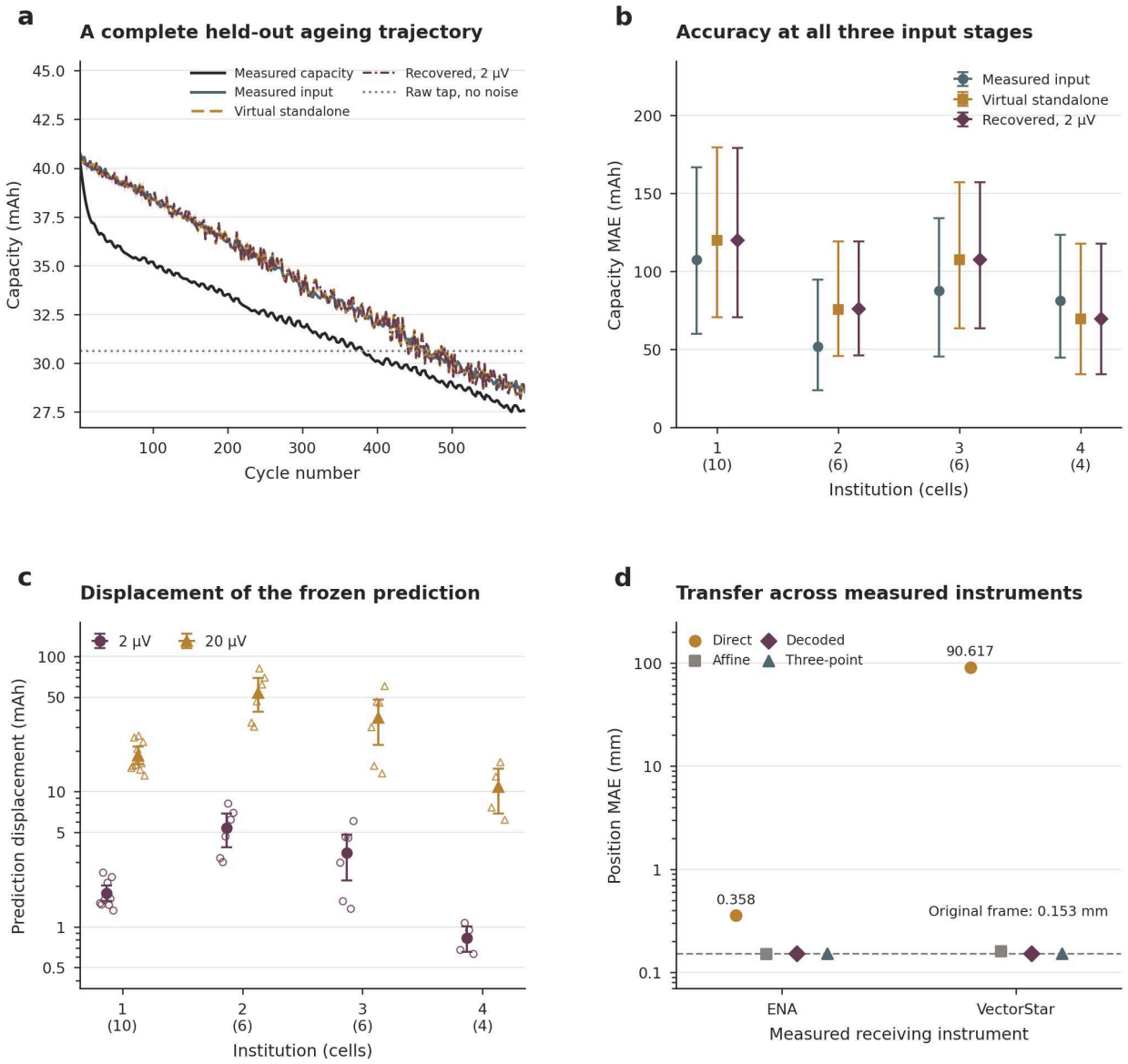
A Gaussian-process capacity predictor trained on 1,358 records from six cells was frozen before evaluation on 299 records from a seventh cell in the Zhang dataset.[21,52] Independently solved acquisition preserved the changing capacity trajectory in the frozen standalone calculation (Fig. 6a). At 2 μV RMS voltage-sample noise, spectral recovery error averaged 0.131% across five seed-specific record medians, and mean absolute prediction displacement was 0.0861 mAh. Capacity MAE was 2.234 mAh after recovery, 2.239 mAh with virtual standalone inputs and 2.201 mAh with original measured inputs. The full trajectory is summarized in Supplementary Information S12.

Whole-cell tests in LiBforSecUse extend this result across four institutions. Each of the 26 held-out cells had a predictor and acquisition design frozen using other cells from the same institution. At 2 μV, cell-balanced capacity MAE was 86.06 mAh for measured inputs, 99.11 mAh for virtual standalone inputs and 99.21 mAh after recovery (Fig. 6b). The paired increase due to recovery was 0.093 mAh (95% whole-cell bootstrap interval, 0.030–0.159 mAh). Cell-balanced mean absolute prediction displacement was 2.86 mAh (2.38–3.34 mAh; Fig. 6c). These comparisons show preservation of the specified standalone computation across whole-cell holdouts. Every cell appears in Extended Data Fig. 9, and Supplementary Information S12 retains both equal-cell and equal-institution aggregation.

The NREL–DENSO replication preserved the frozen standalone computation after acquisition: capacity MAE was 9.140 percentage points after recovery compared with 9.142 for virtual standalone inputs, with 0.203-point prediction displacement (Extended Data Fig. 10). The measured-input MAE of 2.235 points locates the larger change at the initial spectrum-to-circuit representation.[24,50] An exploratory follow-up added passive parallel RL elements to capture the high-frequency rise in real impedance. Standalone and recovered MAEs became 2.391 and 2.408 points, respectively, at 0.1772% recovery error, with acquisition settings and predictor still fixed (Supplementary Information S16 and Table 49). Representation governs fidelity to the measured spectrum; the designed observation relation governs recovery of that representation. Earlier exact frozen-function and nested-capacity comparisons are detailed in Extended Data Fig. 3 and Supplementary Information S15.

Measured instrument changes supply a complementary experimental test. In published sliding-transmission-line measurements, three reference settings define a fixed position readout in the original instrument’s frame.[26,27] Across seven held-out nominal positions, decoding reduces mean absolute position error from 0.358 to 0.153 mm on one other instrument and from 90.617 to 0.152 mm on the third, close to the 0.153-mm original-frame result (Fig. 6d). Same-reference affine alignment also performs well, and conventional three-point calibration agrees with decoding. Supplementary Information S18 evaluates the recovered scalar readout separately from complete spectral-coordinate discrepancies. Across the constructed battery acquisitions and measured microwave transfers, retained reference relations recover the coordinates required by the chosen computation.

Figure 6 | Reference recovery preserves a frozen computation



a, Frozen capacity predictions for all 299 records of held-out cell 35C02, using original spectra, fitted standalone responses, raw cell taps divided by total current, or decoded responses.[21] Raw taps precede added readout changes and noise. The recovered curve averages five fixed 2-µV noise realizations; shading spans their range. Black denotes measured capacity. **b,** LiBforSecUse capacity MAE for original measured, fitted standalone and recovered inputs across 26 whole-cell holdouts, comprising 4,297 records from four institutions.[22,23] Symbols and whiskers give equal-cell means and paired 95% whole-cell bootstrap intervals. **c,** Absolute prediction displacement from the fitted standalone baseline at 2 and 20 µV. Small points denote cell means; large symbols and whiskers summarize institutions. **d,** Fixed position readout across measured responses from three microwave instruments.[26,27] ENA and VectorStar each contribute seven held-out nominal positions, using the same three reference settings. The dashed line marks original ZNA-frame MAE. Battery spectra and capacities are measured, with simulated network/readout changes; microwave instrument changes are measured. Intervals in b,c condition on frozen models and five noise realizations.

Information for discovery and design

Across the three principal applications, the same criterion takes complementary physical forms. Tissue records preserve energetic orderings and loading requirements despite unresolved specimen responses. In parallel batteries, matching nonzero complete external branch impedances creates the shared observation relation required for cell-specific recovery and preservation of a frozen computation. In pressure-quenched $Bi_{0.5}Sb_{1.5}Te_3$, source transition temperature fails as an order-preserving selection coordinate, while exact bounds still identify a superior release trajectory despite incomplete source information. Together, these results connect discovery from incomplete records, observation geometry that creates a required relation and processing decisions that remain fixed under incomplete trajectories.

Across the biological systems, loading gives material changes their energetic meaning. Liver interventions preserve opposite work orderings across every admissible reconstruction; reserved human-brain data confirm a selected ordering in individuals; and organoid treatment and clinical shunting quantify equal-work loading changes. Separate clinical reports connect pulsatility with shunt response and its reduction after intervention.[41,42] The compensation relation supplies a common physical language for these disease-model and clinical interventions.

Published perturbation studies connect this loading dependence to cellular responses. In two-dimensional neural-stem-cell cultures with approximately matched initial modulus, relaxation favoured astrocytes; myosin-II or focal-adhesion-kinase inhibition attenuated the response, and pulsed RhoA activation reproduced its astrogenic component.[53] Our reanalysis places the independently measured lineage shifts alongside loading-specific work coefficients (Supplementary Information S8). Relaxation instead favoured neurogenesis in a dimensionality-controlled three-dimensional platform involving spectrin and EGR1.[54] Piezo1-dependent and myosin-dependent responses further locate the transmission of material mechanics in loading history, geometry and mechanosensor state.[55,56]

For batteries, the perturbation and restoration identify the designed circuit condition responsible for recovery. Separating measured, represented and recovered inputs locates a prediction change and distinguishes recovery fidelity from capacity accuracy. Matching can be implemented as a diagnostic architecture through an end-of-line or service fixture, a switchable low-current network, branch-specific trim or active virtual impedance. Calibrated unequal branch and bus impedances provide the alternative direct inverse.

For superconductors, maximizing the source transition can select the wrong precursor. Rank and trajectory bounds retain the decision despite endpoint perturbations and an unreported source onset. The selection target is recovered performance under a specified release history, so precursor state and trajectory must be considered jointly. Surfactant measurements, measured microwave transfer and electronic-transport sweeps supply complementary tests of loading-specific inference and calibrated readout (Supplementary Fig. 15; Extended Data Fig. 6).

Applying the principle begins with three specifications: the physical target, the observation model and the uncertainty admitted by the record. Invariants and bounds determine which conclusions survive every compatible description. When the answer is fixed, the record already yields a discovery or operating requirement; when the permitted answers cross a decision boundary, the distinctions responsible specify what a resolving observation or processing path must establish. This two-way operation turns incomplete records into physical conclusions, design conditions and testable processing choices without selecting a preferred full reconstruction.

Methods

Study design and physical conventions

Analyses retain their source units, loading conditions and evidence classes: exact identities, exhaustive correspondence bounds, paired-record reanalyses, published group-response transformations, measured-

spectrum network constructions, independent virtual acquisitions and source-defined superconducting trajectories. Frequencies, permutations, noise draws and folds are operations on the original units. Linked responses are transformed before their stated aggregation; group-mean transformations retain that level. No pooled effect is computed across different loading protocols. The Supplementary Information records every population and comparison family.

We use $e^{i\omega t}$, $G^* = G' + iG''$ and $J^* = 1/G^* = J' - iJ''$. Modulus, compliance and viscosity have units Pa, Pa^{-1} and Pa s. For stiffness, $C^* = 1/K^*$; chromosome units are pN nm^{-1} and nm pN^{-1}. At fixed peak amplitude and frequency, linear harmonic work density is

$$W_\sigma = \pi \sigma_0^2 J'', W_\gamma = \pi \gamma_0^2 G'', J'' = \frac{G''}{(G')^2 + (G'')^2}.$$

Work density is in J m^{-3} for Pa-valued stress/modulus. Repeated identical cycles multiply the coefficient by their number; absolute work additionally requires specimen volume or generalized-coordinate geometry. For real series compliance c and prescribed total strain, the coefficient is $D_c = G''/\left|1 + c\,G^*\right|^2$. An elastic series shift preserves loss compliance and terminal viscosity; complex compliance differences additionally require common support (S1–S2). The harmonic ordering identity is $R_\sigma = R_\gamma / M$, where $M = \left|G_b^*\right|^2 / \left|G_a^*\right|^2$. Opposite orderings require $(R_\gamma - 1)(R_\sigma - 1) < 0$.

For specified waveform, duration, geometry and state, $W = A^2 K$ gives equal-work amplitude factor $\sqrt{K_a / K_b}$. If $K_b / K_a \in [L, U]$, the admissible factors span $\left[U^{-1/2}, L^{-1/2}\right]$; any factor at most $U^{-1/2}$ prevents increased calculated work throughout that set. Conservative amplitude factors are rounded downward. Force/stress equivalence requires fixed loaded area and stress distribution. Beyond linear response, work is evaluated directly as $\oint \sigma\, d\varepsilon$; reciprocal harmonic predictions retain their applicable response model.

The controlled inverse benchmark retains 240 generating systems: eighty development and 160 held out, across eight observation regimes and four information settings. Its observation operator includes phase, inertia and compliance; response error and intrinsic-material error are scored separately. Generators, optimization objectives, information-specific constraints and all held-out property-query definitions are preserved in S3. The exact series-support illustration uses viscosity 0.3 Pa s, relaxation time 0.04 s, support compliance 0.06 Pa^{-1} and shift 0.04 Pa^{-1} (S1–S2).

Surfactant preparation and measurement

Sixty formulations combine total active CAPB–SLES concentrations of 8, 10 and 12 wt%, active-mass ratios 1:0, 2:1, 1:1, 1:2 and 0:1, pH 4.5 or 5.5, and 0 or 8 wt% added NaCl. Concentrations refer to final formulation mass after salt addition; supplier-labelled active contents determine stock masses. Stocks were CAPB Mackam C-37 (Galaxy Surfactants, USA) and SLES-60 (Colonial Chemical, USA), with deionized water, HCl (Sigma-Aldrich, USA) and NaCl (VWR Chemicals, USA).

Homogeneous magnetically stirred solutions equilibrated for 24 h at 25 °C, underwent pH adjustment, and equilibrated for another 24 h. Salt addition followed, then a further 24 h equilibration; pH was rechecked. A Kinexus rheometer used CP2/50 geometry (50 mm, 2°, approximately 0.0669-mm gap), a solvent trap, Peltier control at 25 °C and 5-min acquisition equilibration. Viscosity used increasing logarithmic shear-rate sweeps with displacement/steady-state timing and a maximum sampling time. Descending logarithmic frequency sweeps used 0.5% strain; 1-Hz amplitude sweeps identified the plateau and its 5% G'-decrease boundary. Three runs per formulation were averaged, producing 941 viscosity values and 1,260 paired mean moduli at 21 frequencies over 0.01–100 Hz.

Thirty salt pairs match pH and final active composition. Paired mean moduli are transformed before comparison. Separate log10-component smoothing uses a nine-point, second-order Savitzky–Golay filter with endpoint interpolation. Residual scale is 1.4826 times median absolute deviation about the residual median.

Smoothed logarithmic values plus/minus the residual scale define the positive component rectangles after exponentiation. Exact loss-compliance extrema over each rectangle include an interior loss-coordinate extremum when present; opposing endpoints give each salt-difference range. These are deterministic processing ranges. All raw/processed contrasts and 630 pair–frequency comparisons are retained (S14).

Liver, gels and paired tissue records

Fan publisher workbooks supply five mouse-level storage moduli, loss tangents and foci summaries per arm; each foci summary aggregates twenty image areas. The two genetic designs retain their separate comparisons.[13,57] Native rheology used parallel plates, room temperature, 2% recorded strain, 1 rad s^{-1} and 600 s. Within each arm, unlinked lists describe the same five mice. We enumerate all $5! = 120$ correspondences and 14,400 cross-arm reconstructions, transforming each reconstructed response before averaging. Rearrangement inequalities independently recover mean bounds. Rank envelopes, complete independent-omission configurations, exact-rational positive-crossover certificates and independent root bracketing are retained. The AGER1 source is MOESM5, sheets Fig 2k/2l/2n, E2:E6 versus F2:F6; RAGE uses MOESM10, Ext Data Fig 2g/2h/2e, D2:D6 versus F2:F6. Each group attains its matching extrema independently. The crossover certificate counts positive comparison crossings, while numerical brackets locate their endpoints. Gel workbooks supply six experiments per group at 37 °C, 1% strain and 1 rad s^{-1}; all 720 within-group and 518,400 cross-group matchings are included. These AGE-treated and BSA-control collagen–alginate IPN gels use MOESM6 Fig 3l/m and are distinct from the source rBM–alginate cell-assay matrices (S4).

Kpeglo day-21 PDAC cultures supply three plates per condition, with/without TGF-β1, measured at 2% strain and 0.5 Hz for 600 s.[14,36] Plate-paired components are transformed before averaging. Nine independent omission combinations, four raw-window/repeat-record choices and all twenty three-versus-three label allocations accompany the primary contrast. Joshi pancreatic comparisons transform published mean responses at their stated frequencies; Erisken dental comparisons retain the approximate reported rectangle, 37 °C, 10% strain and original frequency label, 0.1–100 rps.[37,38] The PDAC raw-window checks use the last 100 or 300 rows and original/repeated untreated plate 2; the source audit checks all 96 paired plate summaries. The dental reference is approximately $G' = 100$ Pa and $G'' = 10$ Pa; the hydrogel envelope is $G' \in [10^3, 10^4]$ Pa and $G'' \in [300, 1000]$ Pa. Dental source material comes from one miniature-pig donor sampled at three native sites. The pancreatic 1-Hz stiffness comparison and 10-Hz energetic comparison remain separate frequency-specific targets. Precise inputs, source units and sensitivities are in S5 and Supplementary Table 23.

Human brain discovery and confirmation

MRE134 provides stiffness/damping maps for 134 healthy adults. Study E supplies discovery; A–D supply confirmation.[15] With $h = \sqrt{1 + 4\xi^2}$, voxelwise conversion is

$$G' = \frac{\mu(1+h)}{2h^2}, G'' = \frac{\mu\xi(1+h)}{h^2}, J'' = \frac{4\xi}{\mu(1+h)}.$$

Bilateral regions use the Harvard–Oxford subcortical atlas at 25% threshold on a 2-mm grid. Valid voxels have finite positive μ, ξ. Regional medians of transformed values require 80% paired coverage and 100 valid voxels per region. Separate regional medians are never recombined into a synthetic modulus.

Discovery evaluates all 21 planned pairs. Selection requires opposite coefficient directions, symmetric 1.1-fold thresholds, 75% individual prevalence and Benjamini–Hochberg-adjusted conjunction $P < 0.05$. Untestable pairs receive $P = 1$. Five selected pairs enter confirmation with frozen directions/thresholds and Holm adjustment. Conjunction P is the larger of two two-sided one-sample t-test values on participant log ratios. Log-scale t intervals describe geometric-mean ratios; exact binomial intervals describe prevalence. Means, boundary erosion and 95% coverage are sensitivities. Seventeen external participants are included within the sixty eligible confirmation participants (S7.1).

Organoid and clinical intervention calculations

The source workbook supplies eighteen day-18 organoids: four controls, five LIS1 mutants, five treated controls and four treated mutants. The intervention compares four MMP9-treated with five untreated mutants; duplicate records are counted once.[17] With $\Delta J = 1/k_\infty - 1/k_0$ and $\tau_r = \tau\, k_\infty / k_0$, maintained-step viscous-work coefficients are

$$K_\sigma(T) = \frac{\Delta J}{2}\left(1 - e^{-2T/\tau}\right), K_\gamma(T) = \frac{k_0 - k_\infty}{2}\left(1 - e^{-2T/\tau_r}\right).$$

The five-second window ends before unloading. Coefficients are calculated per organoid before geometric-mean comparison; source aspiration normalization is retained. The stress-step coefficient follows aspiration creep; the strain-step coefficient is the reciprocal-control calculation. Elastic energy remaining at the window endpoint and later recovery are excluded from these finite-step coefficients. Independent least-squares response refits and direct viscous-power integration check the calculations. Dimensionless group ratios retain the common aspiration normalization; source-model, rounded-parameter and independently refitted estimates remain distinct. Duration checks and all nine leave-one-organoid-out intervention estimates accompany the primary analysis. Primary intervals use 50,000 within-group bootstrap resamples (seed 84360540). Exact two-sided mean-log permutations enumerate 126 intervention allocations; Holm adjustment covers LIS1/control, treated-LIS1/untreated-LIS1 and treated-LIS1/control. The separate rounded-parameter protocol contrast retains both coefficients per organoid and exhaustively enumerates 800,000 ordered bootstrap pairs with linearly interpolated percentiles (S7.2).

Boulet injury analysis retains all reported 877.5-Hz severity/region/time rows.[16] Freimann shunt analysis transforms cohort-mean components from twenty patients (fourteen primary, six secondary hydrocephalus), measured before and 91 ± 16 days after intervention at 25, 37.5, 50 and 62.5 Hz.[18] The equal-work factor is $\sqrt{J''_{pre}/J''_{post}}$. Independent ±0.005-kPa component intervals propagate printed rounding; finite-source crossover equations use common real compliance. The shunt calculation transforms published cohort means rather than averaging unreported patient-level compliances. Each frequency remains a separate condition. Intracranial-pressure endpoints retain their own cohorts and are not substituted for MRE shear stress (S7.3–S7.4).[41,42]

Neural matrix context and other physical records

The L0/L2/L4 figure-read parameters from Qiao et al.[53] give $E(t) = E_\infty + (E_0 - E_\infty)e^{-t/\tau_r}$. The creep time is $\tau_c = \tau_r E_0 / E_\infty$. Maintained-step coefficients use a 300-s horizon and 40/60/900-s sensitivities. Independent-uniform reading ranges use 100,000 draws per condition/horizon (seed 2317711121). Lineage endpoints, including alternative 26%/28% rat L4 Tuj1 readings, remain separately measured, condition-level observations (S8).

Chromosome responses comprise 212 native estimates from sixteen chromosomes at 1 Hz. Reciprocal transformation precedes stage averaging; the negative native loss estimate is retained. Paired-chromosome intervals use 20,000 resamples (seed 270101; S6).[39,40] Transport compares twelve 66-point target curves and two 62-point controls from one device. Linear/quadratic families each fit three nuisance coefficients in $m = a + ku/(1+cu)$, $u = (T/T_{ref})^\beta$, under $a \ge 0, k > 0, c \ge 0$, using unweighted source-ohm residuals and five contiguous withheld blocks. Retained fits, free-exponent profiles and independently checked fold aggregation are in S19.[58]

Reference information and controlled observation design

Three distinct current correspondences identify the nondegenerate projective readout. For equation (6), $A = \chi(a - b)$ and $B = a - c$ give $z = (Ac - Bb)/(A - B)$. Homogeneous coordinates retain valid infinite values; $0:0$ is undefined. Reference states, complex signs, feature order and preprocessing are preserved. Conventional three-point calibration uses the same information.[59] For the restricted circuit $y = Bz/(z + R)$, two generic references

give $R=(y_2-y_1)/(p_1-p_2)$ and $B=y_1+Rp_1$, with $p_j=y_j/z_j$ and nonzero denominator; independently known branch/bus values give $z_i=r_i y_i/(B-y_i)$, including unequal paths (S9; S10).

Ank data supply 248 usable cell histories, three charge states and 61 frequencies.[19,20] Seed 20261026 generates ten six-cell panels per target/state: 7,440 panels. The primary band contains twenty frequencies over 0.1–10 Hz. Three of five candidate references maximize worst-frequency pair separation normalized solely by candidate magnitudes; two remain checks. Lognormal branch terms have mean 0.1 mΩ and coefficient of variation 0.25; paired controls use 100-fold scaling, fixed equal paths and realized means. Candidate-only and six-spectrum normalization select different reference triples in 32 panels; both comparisons are documented in the analysis records (S20). Current observed reference separation and unused-check residuals are evaluated separately from the selection score. Kirchhoff construction, 1,500-panel conventional-calibration/full-frequency checks and paired 0.01% complex-RMS tap-noise tests are specified in S10.

Independent battery cohorts and frozen predictors

Each measured spectrum defines a passive virtual specimen. Original measured, virtual standalone and acquisition-recovered spectra enter the same frozen capacity predictor; representation and recovery errors remain separate.

Zhang retains 1,358 training records from six cells and 299 records from held-out 35C02, at sixty native frequencies, 0.01999–20,004.453 Hz; capacity is mAh.[21,52] NREL–DENSO holds out cells 7, 10, 13, 17, 24, 30 and 31 together, leaving 359 training records from 24 cells and 108 test records. Its 69 native frequencies span 0.00501–31,622.78 Hz. Relative C/3 capacity errors are percentage points.[24,50] LiBforSecUse supplies 4,297 records from 26 cells in four institutions. Each whole-cell holdout trains only on other cells from its institution. Its source preparation uses natural cubic splines on log frequency and leaves out-of-range values missing. Training-finite masks retain 60, 59, 60 and 60 frequencies; capacities are mAh. Repeated charge-state spectra share 765 cell–cycle capacity-check keys.[22,23,49]

Features are real/negative-imaginary impedance components, with recorded temperature/charge state for NREL and charge state for LiBforSecUse. Covariates remain unchanged across acquisition conditions. Capacity, state of health, cycle count and cell/institution identities are excluded. Gaussian processes use training-only means/population scales and a constant-amplitude isotropic squared-exponential kernel plus white noise. Amplitude, length and noise bounds are $[10^{-4},10^{4}]$, $[0.05,10^{3}]$ and $[10^{-7},1]$; initial values are $1,\sqrt{d},0.01$ with feature count d and jitter 10^{-10}. L-BFGS-B uses no restarts: 150 iterations for Zhang, or 75 on up to 64 evenly spaced rows per training cell for multicell cohorts, followed by refitting all training rows with fixed hyperparameters. The Zhang predictor uses all 120 impedance features. Training transformations and the constant mean are identical across measured, virtual and recovered inputs. Held-out spectra construct specimens under the fixed basis but never select acquisition settings or update the predictor. All models, masks and acquisition choices are hashed/frozen before test scoring; all 26 LiB folds are frozen before any evaluation (S12.1–S12.3).

Component acquisition and paired controls

Virtual impedance is $Z(s)=R_0+sL+K_C/s+\sum_{k=1}^{41}R_k/(1+s\tau_k)$, with nonnegative coefficients and logarithmic τ_k over 10^{-6}–10^{3} s. Fractional-residual nonnegative least squares uses unit-norm real/imaginary columns; terms below 10^{-9} of fitted resistance are pruned. Capacity never enters specimen fitting.

The six-branch network contains one target, three references and two unused checks. Independent component equations and Kirchhoff balance generate cell-only voltage taps; the decoder receives only current reference correspondences and the target tap. Multicell reference selection considers up to five evenly spaced source-order states per training cell. Three states from distinct cells maximize the minimum pair separation over the retained

frequency mask, normalized by candidate median magnitude; two further states remain unused checks. Resistance is the median across training cells of their within-cell median fitted impedance magnitude; current is capped at 3 A and by a 5-mV training-candidate tap peak. The single-cell design uses its prespecified five training rows, 0.9231307 Ω and 5 mA. The NREL settings are 1.491106 mΩ and 1.538819 A; LiB fold settings span 18.8465–23.1163 mΩ and 0.340419–0.953605 A. Every target/control uses frozen settings (S12.4–S12.5).

Four cycles per frequency use 64 samples/cycle, common complex gain/feedthrough and finite demodulation. Voltage-sample Gaussian RMS is 0, 2 or 20 μV; noisy conditions include shared 1-μA current-sample noise. Five fixed seeds reuse standardized samples across geometries/scales. These are time-sample noise specifications. The primary setting is 2 μV. Controls include target-only +10%, heterogeneous factors $(0.6, 0.8, 1, 1.2, 1.4, 1)$, paired restoration, zero external paths and measured-reference substitution. Reference impedances describe the actual virtual standards in primary decoding. A target-only path error can leave the reference checks unchanged; target matching is a separate design condition. Current balance, component-port closure, unused checks and independently integrated periodic trajectories verify acquisition (S12.6–S12.12).

The separate post hoc NREL follow-up adds 41 passive parallel-RL terms on the same grid, refits all 467 spectra, and retains the original predictor, reference identities, settings and five seeds. All 108 test rows, geometries/restoration and seven transient probes are retained at 0/2 μV (S16).

Endpoints and uncertainty

Recovery error is frequency RMS of $\left|Z^{rec} - Z^{virt}\right| / \left|Z^{virt}\right|$; prediction displacement is $\left|g\left(Z^{rec}, u\right) - g\left(Z^{virt}, u\right)\right|$. Original/virtual/recovered MAEs use the same measured capacity. Whole-cell analyses average seeds, then records within cells, then cells equally. Endpoint-specific worst cells and 10,000 paired whole-cell bootstrap samples (seed 202610319) are retained; LiB resampling preserves institutional cell counts of 10, 6, 6 and 4. Models stay fixed. All 46 prescribed acquisition/control conditions are retained for each of 4,405 whole-cell records, giving 202,630 record-condition predictions. Single-cell summaries remain record-level; repeated noise draws and charge states do not create additional cells. NREL contains two exact training/test input signatures affecting fourteen test rows; two LiB records share one cross-cell signature. These rows remain in primary splits; the separately labelled NREL diagnostic evaluates 94 records without refitting (S12.8–S12.13).

Electrical descriptor tests retain 120 spectra from twelve cells and sixteen complete tissue acquisitions from two pigs, using native frequencies without interpolation. The earlier fixed-function, nested-capacity and historical-map cohorts contain 2,301/eighteen, 1,921/fifteen and 780/six record/cell combinations, respectively; their complete settings remain in S15 and S17. Fixed anchors come from PJ097–PJ099; nested evaluation holds out five other cells per outer fold and confines preprocessing/selection to training subsets. Historical outcomes belong to original development; coordinate transport retains all predictor parameters, auxiliary inputs and reference spectra while changing only the declared observation maps. Measured microwave transfer uses thirty files from three instruments and ten nominal positions; 0, 93 and 192 mm calibrate seven held-out settings. All routes retain the same readout, references and 111 matched native frequencies over 3–14 GHz; phase separation ≥0.2 retains 89 frequencies. The fixed readout maps original-frame S_{11} to $\exp\left(-4\pi i f x / c_0\right)$ and minimizes mean squared chordal error over 0–192 mm. Full decoded-spectrum discrepancies are evaluated separately from nominal-position readout error (S18).[26,27,60–63]

Superconducting trajectories

Four BST source-defined pressure/quench histories retain onset criterion and component identity; 10.2 K denotes the high transition component of the recovered mixed sample.[25] The 20.3- and 33.3-GPa protocols share nominal 77-K quenching; the 32.3-GPa protocol uses 4.2 K. Define amplification $A = T_R - T_S$, contrast $D = A_{33.3} - A_{20.3}$ and envelope excess $E = T_R - T_{comp,max}$. Independent ±0.2-K displayed-onset stresses yield $D \in [6.6, 8.2]$ K by exact arithmetic and all sixteen corners. They are deterministic stresses, with exact first-

failure radii calculated separately: 1.05 K for ranking, 1.70 K for opposite signs, 1.85 K for positive contrast, 2.15 K for warm/cold advantage and 0.60 K for envelope excess.

The cold-source ordering $T_S(32.3) \geq T_S(33.3)$ gives $A_{77} - A_{4.2} \geq 4.3$ K. Perturbing only recovered endpoints gives ≥3.9 K while retaining that inequality. No cold-source point is imputed. Harmonic models and updated diffraction assignments retain their respective source labels (S13).[51]

Reproducibility

Exact bounds, processing and rounding sensitivities, sampling intervals and held-out errors retain separate definitions. CPython 3.12.14, NumPy 2.3.5, SciPy 1.17.0, pandas 2.2.3 and scikit-learn 1.8.0 define the numerical reference runtime. Source identities, inputs, frozen states, complete comparison families and numerical tolerances were retained for verification. Supplementary Information S20 catalogs these records.

Data availability

Public source datasets and published tabulated values are available through the repositories and publications cited in the manuscript and Supplementary Information. Original CAPB–SLES measurements and derived numerical records supporting the figures, tables and reported results are stored in a private repository for editorial and peer review and will be made publicly available upon acceptance of the work.

Code availability

Custom analysis code, frozen model objects, figure-generation scripts and numerical verification routines are stored in a private repository for editorial and peer review and will be made publicly available upon acceptance of the work. Third-party software and source-code repositories are identified in the Methods and references.

Acknowledgements

We thank Prof. Samiul Amin for providing access to the rheometer and materials in the Soft Matter Product Design group at the University of Miami, where the CAPB–SLES rheological measurements were performed.

Funding

No funding was obtained for this work.

Author contributions

S.S.V. and A.S.V. contributed equally to conceptualization, data curation, formal analysis, investigation, methodology, project administration, resources, software, supervision, validation, visualization, writing the original draft, and reviewing and editing the manuscript.

ORCID

Sabitoj Singh Virk https://orcid.org/0000-0002-5801-5630

Akashdeep Singh Virk https://orcid.org/0000-0002-9157-4637

Competing interests

The authors declare that they have no competing interests.

Additional information

Extended Data and Supplementary Information accompany this manuscript. Correspondence and requests for materials should be addressed to Sabitoj Singh Virk (sabitoj@umich.edu).

References

1. Jacobsson, T. J. et al. An open-access database and analysis tool for perovskite solar cells based on the FAIR data principles. Nat. Energy 7, 107–115 (2022). doi:10.1038/s41560-021-00941-3

2. Vines, T. H. et al. The availability of research data declines rapidly with article age. Curr. Biol. 24, 94–97 (2014). doi:10.1016/j.cub.2013.11.014

3. Wilkinson, M. D. et al. The FAIR Guiding Principles for scientific data management and stewardship. Sci. Data 3, 160018 (2016). doi:10.1038/sdata.2016.18

4. Ioannidis, J. P. A. et al. Repeatability of published microarray gene expression analyses. Nat. Genet. 41, 149–155 (2009). doi:10.1038/ng.295

5. Claeys, T. et al. lesSDRF is more: maximizing the value of proteomics data through streamlined metadata annotation. Nat. Commun. 14, 6743 (2023). doi:10.1038/s41467-023-42543-5

6. Woodside, M. T. et al. Direct measurement of the full, sequence-dependent folding landscape of a nucleic acid. Science 314, 1001–1004 (2006). doi:10.1126/science.1133601

7. DeGrave, A. J., Janizek, J. D. & Lee, S.-I. AI for radiographic COVID-19 detection selects shortcuts over signal. Nat. Mach. Intell. 3, 610–619 (2021). doi:10.1038/s42256-021-00338-7

8. Gottlieb, M. & Macosko, C. W. The effect of instrument compliance on dynamic rheological measurements. Rheol. Acta 21, 90 –94 (1982). doi:10.1007/BF01520709

9. Liu, C.-Y., Yao, M., Garritano, R. G., Franck, A. J. & Bailly, C. Instrument compliance effects revisited: linear viscoelastic measurements. Rheol. Acta 50, 537–546 (2011). doi:10.1007/s00397-011-0560-3

10. Neupane, K., Manuel, A. P. & Woodside, M. T. Protein folding trajectories can be described quantitatively by one-dimensional diffusion over measured energy landscapes. Nat. Phys. 12, 700–703 (2016). doi:10.1038/nphys3677

11. Bittle, E. G., Basham, J. I., Jackson, T. N., Jurchescu, O. D. & Gundlach, D. J. Mobility overestimation due to gated contacts in organic field-effect transistors. Nat. Commun. 7, 10908 (2016). doi:10.1038/ncomms10908

12. Blume-Kohout, R. et al. Demonstration of qubit operations below a rigorous fault tolerance threshold with gate set tomography. Nat. Commun. 8, 14485 (2017). doi:10.1038/ncomms14485

13. Fan, W. et al. Matrix viscoelasticity promotes liver cancer progression in the pre-cirrhotic liver. Nature 626, 635–642 (2024). doi:10.1038/s41586-023-06991-9

14. Kpeglo, D. et al. Modeling the mechanical stiffness of pancreatic ductal adenocarcinoma. Matrix Biol. Plus 14, 100109 (2022). doi:10.1016/j.mbplus.2022.100109

15. Hiscox, L. V. et al. Standard-space atlas of the viscoelastic properties of the human brain. Human Brain Mapping 41, 5282–5300 (2020). doi:10.1002/hbm.25192

16. Boulet, T., Kelso, M. L. & Othman, S. F. Long-Term In Vivo Imaging of Viscoelastic Properties of the Mouse Brain after Controlled Cortical Impact. Journal of Neurotrauma 30, 1512–1520 (2013). doi:10.1089/neu.2012.2788

17. Karlinski Zur, M. et al. Altered extracellular matrix structure and elevated stiffness in a brain organoid model for disease. Nature Communications 16, 4094 (2025). doi:10.1038/s41467-025-59252-w

18. Freimann, F. B. et al. Alteration of brain viscoelasticity after shunt treatment in normal pressure hydrocephalus. Neuroradiology 54, 189–196 (2012). doi:10.1007/s00234-011-0871-1

19. Ank, M., Kröger, T., Schreiber, M. & Lienkamp, M. Experimental analysis of lithium-ion cell procurement: Quality differences, correlations, and importance of cell characterization. J. Energy Storage 66, 107430 (2023). doi:10.1016/j.est.2023.107430

20. Ank, M., Kröger, T., Schreiber, M. & Lienkamp, M. Characterization data of 250 cylindrical lithium-ion cells. Technical University of Munich (2023). doi:10.14459/2023mp1699705

21. Zhang, Y., Tang, Q., Zhang, Y., Wang, J., Stimming, U. & Lee, A. A. Identifying degradation patterns of lithium ion batteries from impedance spectroscopy using machine learning. Nat. Commun. 11, 1706 (2020). doi:10.1038/s41467-020-15235-7

22. Chan, H. S. et al. Comparison of methodologies to estimate state-of-health of commercial Li-ion cells from electrochemical frequency response data. J. Power Sources 542, 231814 (2022). doi:10.1016/j.jpowsour.2022.231814

23. Guignard, F. & Hoffmann, J. LiBforSecUse processed data for machine learning modelling and uncertainty propagation. Version v1. Zenodo (2025). doi:10.5281/zenodo.17792537

24. Gasper, P., Schiek, A., Smith, K., Shimonishi, Y. & Yoshida, S. Predicting battery capacity from impedance at varying temperature and state of charge using machine learning. Cell Rep. Phys. Sci. 3, 101184 (2022). doi:10.1016/j.xcrp.2022.101184

25. Deng, L. et al. Creation, stabilization, and investigation at ambient pressure of pressure-induced superconductivity in Bi0.5Sb1.5Te3. Proc. Natl Acad. Sci. USA 122, e2423102122 (2025). doi:10.1073/pnas.2423102122

26. Hatab, Z., Abdi, A., Steinbauer, G., Gadringer, M. E. & Bösch, W. Propagation constant measurement based on a single transmission line standard using a two-port VNA. Sensors 23, 4548 (2023). doi:10.3390/s23094548

27. Hatab, Z. Propagation Constant Measurement Based on a Single Transmission Line Standard Using a Two-port VNA: Dataset and Code. Graz University of Technology (2023). doi:10.3217/6bd26-5cp67

28. Youngblut, N. D. et al. scBaseCount: An AI agent-curated, standardized, auto-updated single-cell data repository. Cell 189, 5932–5944.e6 (2026). doi:10.1016/j.cell.2026.08.025

29. Hossain, M. T., Macosko, C. W., McKinley, G. H. & Ewoldt, R. H. Instrument stiffness artifacts: avoiding bad data with operational limit lines of Gmax and Emax. Rheol. Acta 64, 67–79 (2025). doi:10.1007/s00397-024-01481-9

30. Collin, D., Ritort, F., Jarzynski, C., Smith, S. B., Tinoco, I. Jr & Bustamante, C. Verification of the Crooks fluctuation theorem and recovery of RNA folding free energies. Nature 437, 231–234 (2005). doi:10.1038/nature04061

31. Battle, C., Broedersz, C. P., Fakhri, N., Geyer, V. F., Howard, J., Schmidt, C. F. & MacKintosh, F. C. Broken detailed balance at mesoscopic scales in active biological systems. Science 352, 604–607 (2016). doi:10.1126/science.aac8167

32. Raue, A. et al. Structural and practical identifiability analysis of partially observed dynamical models by exploiting the profile likelihood. Bioinformatics 25, 1923–1929 (2009). doi:10.1093/bioinformatics/btp358

33. Kreutz, C., Raue, A. & Timmer, J. Likelihood based observability analysis and confidence intervals for predictions of dynamic models. BMC Syst. Biol. 6, 120 (2012). doi:10.1186/1752-0509-6-120

34. Machta, B. B., Chachra, R., Transtrum, M. K. & Sethna, J. P. Parameter space compression underlies emergent theories and predictive models. Science 342, 604–607 (2013). doi:10.1126/science.1238723

35. Hardy, G. H., Littlewood, J. E. & Pólya, G. Inequalities, 2nd edn (Cambridge University Press, 1952).

36. Kpeglo, D. Modeling the Mechanical Stiffness of Pancreatic Ductal Adenocarcinoma: dataset. University of Leeds (2022). doi:10.5518/952

37. Joshi, K. et al. Quantifying the viscoelastic properties of pancreatic tissue: a comparative study of human, porcine and engineered hydrogel. Ann. Biomed. Eng. (2026). doi:10.1007/s10439-026-04235-1

38. Erisken, C., Kalyon, D. M., Zhou, J., Kim, S. G. & Mao, J. J. Viscoelastic properties of dental pulp tissue and ramifications on biomaterial development for pulp regeneration. J. Endod. 41, 1711–1717 (2015). doi:10.1016/j.joen.2015.07.005

39. Witt, H. et al. Ion-mediated condensation controls the mechanics of mitotic chromosomes. Nat. Mater. 23, 1556–1562 (2024). doi:10.1038/s41563-024-01975-0

40. Witt, H. Data for the manuscript Ion-mediated condensation controls the mechanics of mitotic chromosomes. Zenodo, version 1 (2023). doi:10.5281/zenodo.7801755

41. Eide, P. K. & Brean, A. Cerebrospinal fluid pulse pressure amplitude during lumbar infusion in idiopathic normal pressure hydrocephalus can predict response to shunting. Cerebrospinal Fluid Research 7, 5 (2010). doi:10.1186/1743-8454-7-5

42. Eide, P. K. & Sorteberg, W. Changes in intracranial pulse pressure amplitudes after shunt implantation and adjustment of shunt valve opening pressure in normal pressure hydrocephalus. Acta Neurochirurgica 150, 1141–1147 (2008). doi:10.1007/s00701-008-0138-8

43. Ank, M., Göhmann, J. & Lienkamp, M. Multi-cell testing topologies for defect detection using electrochemical impedance spectroscopy: a combinatorial experiment-based analysis. Batteries 9, 415 (2023). doi:10.3390/batteries9080415

44. Jocher, P., Steinhardt, M., Ludwig, S., Schindler, M., Martin, J. & Jossen, A. A novel measurement technique for parallel-connected lithium-ion cells with controllable interconnection resistance. J. Power Sources 503, 230030 (2021). doi:10.1016/j.jpowsour.2021.230030

45. Moradpour, A., Kasper, M. & Kienberger, F. Quantitative cell classification based on calibrated impedance spectroscopy and metrological uncertainty. Batteries Supercaps 6, e202200524 (2023). doi:10.1002/batt.202200524

46. Huckemann, S. F., Kim, P. T., Koo, J.-Y. & Munk, A. Möbius deconvolution on the hyperbolic plane with application to impedance density estimation. Ann. Stat. 38, 2465–2498 (2010). doi:10.1214/09-AOS783

47. Arsenovic, A., Weikle, R. M. & Hesler, J. L. Reflectometer calibration with a pair of partially known standards. In 2015 European Microwave Conference, 327–330 (2015). doi:10.1109/EuMC.2015.7345766

48. Lawrence, K. C., Nelson, S. O. & Kraszewski, A. W. Automatic system for dielectric properties measurements from 100 kHz to 1 GHz. Trans. ASAE 32, 304–308 (1989). doi:10.13031/2013.31001

49. Chan, H. S. et al. LiBforSecUse Data Release – Impedance spectra of life cycle tests of commercial 18650 cells. Version V2. Zenodo (2022). doi:10.5281/zenodo.6418665

50. Gasper, P. et al. battery_capacity_from_eis: author code and data. GitHub https://github.com/NatLabRockies/battery_capacity_from_eis (accessed 31 October 2026).

51. Halbert, C. et al. High-pressure structures of Bi0.5Sb1.5Te3 at room temperature and in its superconducting states. Phys. Rev. Mater. 10, 094804 (2026). doi:10.1103/ks5f-s1hm

52. Zhang, Y. et al. Identifying degradation patterns of lithium ion batteries from impedance spectroscopy using machine learning. Zenodo (2020). doi:10.5281/zenodo.3633835

53. Qiao, E., Fulmore, C. A., Schaffer, D. V. & Kumar, S. Substrate stress relaxation regulates neural stem cell fate commitment. Proceedings of the National Academy of Sciences 121, e2317711121 (2024). doi:10.1073/pnas.2317711121

54. Qiao, E. et al. Spectrin mediates 3D-specific matrix stress-relaxation response in neural stem cell lineage commitment. Science Advances 10, eadk8232 (2024). doi:10.1126/sciadv.adk8232

55. Oliva, M. A. G. et al. Piezo1 regulates the mechanotransduction of soft matrix viscoelasticity. Nature Communications 16, 9155 (2025). doi:10.1038/s41467-025-64185-5

56. Huerta-López, C. et al. Cell response to extracellular matrix viscous energy dissipation outweighs high-rigidity sensing. Science Advances 10, eadf9758 (2024). doi:10.1126/sciadv.adf9758

57. Fan, W. et al. Author Correction: Matrix viscoelasticity promotes liver cancer progression in the pre-cirrhotic liver. Nature 648, E9 (2025). doi:10.1038/s41586-025-09947-3

58. Xia, Y. et al. Bandwidth-tuned Mott transition and superconductivity in moiré WSe2. Nature 650, 585–591 (2026). doi:10.1038/s41586-025-10049-3

59. scikit-rf developers. OnePort one-port calibration documentation. Accessed 27 October 2026. https://scikit-rf.readthedocs.io/en/latest/api/calibration/generated/skrf.calibration.calibration.OnePort.html

60. Jones, P. K., Stimming, U. & Lee, A. A. Impedance-based forecasting of lithium-ion battery performance amid uneven usage. Nat. Commun. 13, 4806 (2022). doi:10.1038/s41467-022-32422-w

61. Falagario, C., De Momi, E. & Mattos, L. S. In vivo tissue bioimpedance dataset. Sci. Data (2026). doi:10.1038/s41597-026-07652-y

62. Jones, P. K., Stimming, U. & Lee, A. A. Impedance-based forecasting of battery performance amid uneven usage. Zenodo, version 2 (2021). doi:10.5281/zenodo.6645536

63. Falagario, C., Mattos, L. S. & De Momi, E. In-vivo tissue bioimpedance dataset. Zenodo, version 2 (2026). doi:10.5281/zenodo.20408128

Extended Data

Physical Discovery and Design from Incomplete Records

Sabitoj Singh Virk and Akashdeep Singh Virk

ORCID

Sabitoj Singh Virk https://orcid.org/0000-0002-5801-5630

Akashdeep Singh Virk https://orcid.org/0000-0002-9157-4637

Contents

ED Fig. 1 | Response agreement and material recovery

ED Fig. 2 | Preserved relations on measured responses

ED Fig. 3 | Complete frozen-function and measured-capacity comparisons

ED Fig. 4 | Chromosome work changes in opposite directions under different loading comparisons

ED Fig. 5 | Elastic coupling produces one certified energetic reversal for every liver reconstruction

ED Fig. 6 | Transport windows and observation classes

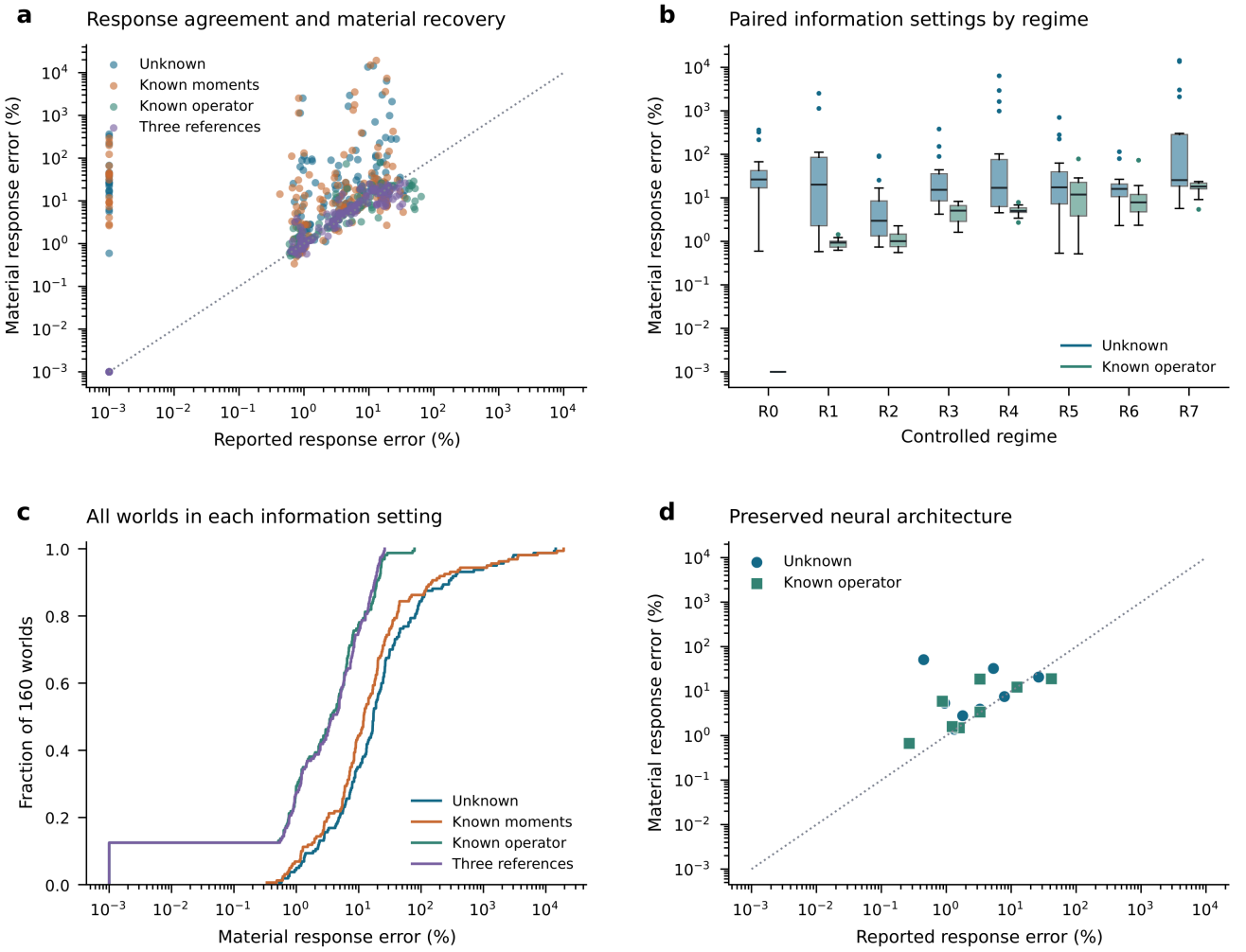
ED Fig. 7 | Reference information defines calibration and model checks

ED Fig. 8 | Acquisition verification and inverse conditioning

ED Fig. 9 | Whole-cell preservation across four institutions

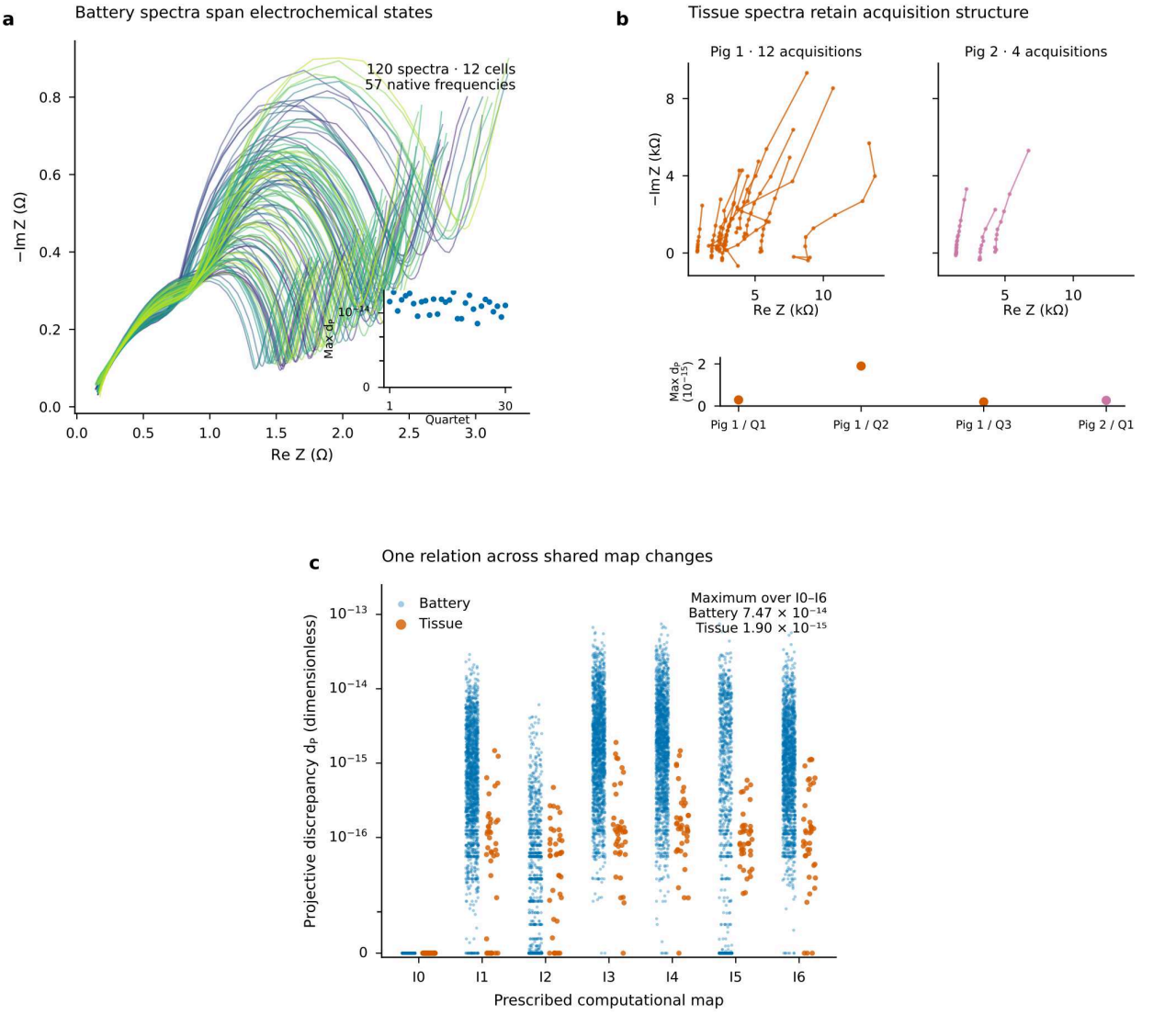
ED Fig. 10 | Prespecified NREL holdouts separate recovery from accuracy

Extended Data Figure 1 | Response agreement and material recovery



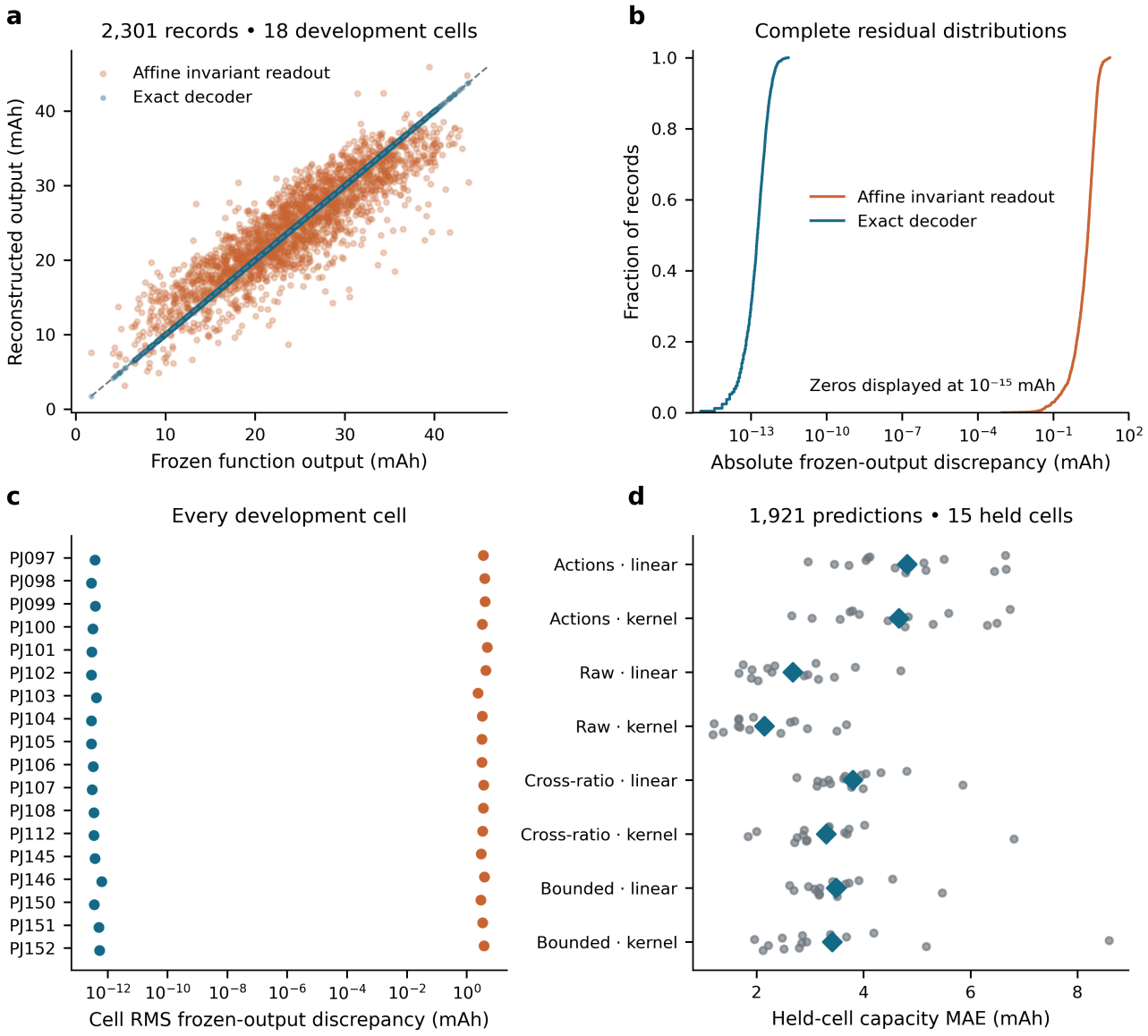
a, All 640 compact-model reconstructions from 160 held-out generating worlds under four information settings. Each error uses the world's three materials and stored frequencies. **b,** Intrinsic-modulus error for unknown and known operators, twenty worlds per regime and setting. Boxes show medians and interquartile ranges, whiskers extend to 1.5 interquartile ranges, and outliers are retained. R0, exact equivalence; R1, weak distortion; R2, strong distortion; R3, limited band; R4, spectrum mismatch; R5, operator mismatch; R6, correlation/outliers; R7, shifted generating family. **c,** Empirical cumulative distributions across all 160 worlds per information setting. **d,** Sixteen reconstructions using the preserved neural architecture on eight predefined worlds with paired unknown/known coefficients. Values below 0.001% are placed at that display floor without changing source values. Diagonals mark equal response and material errors. Supplementary Information S3 defines the generating regimes, information settings and scoring procedures.

Extended Data Figure 2 | Preserved relations on measured responses



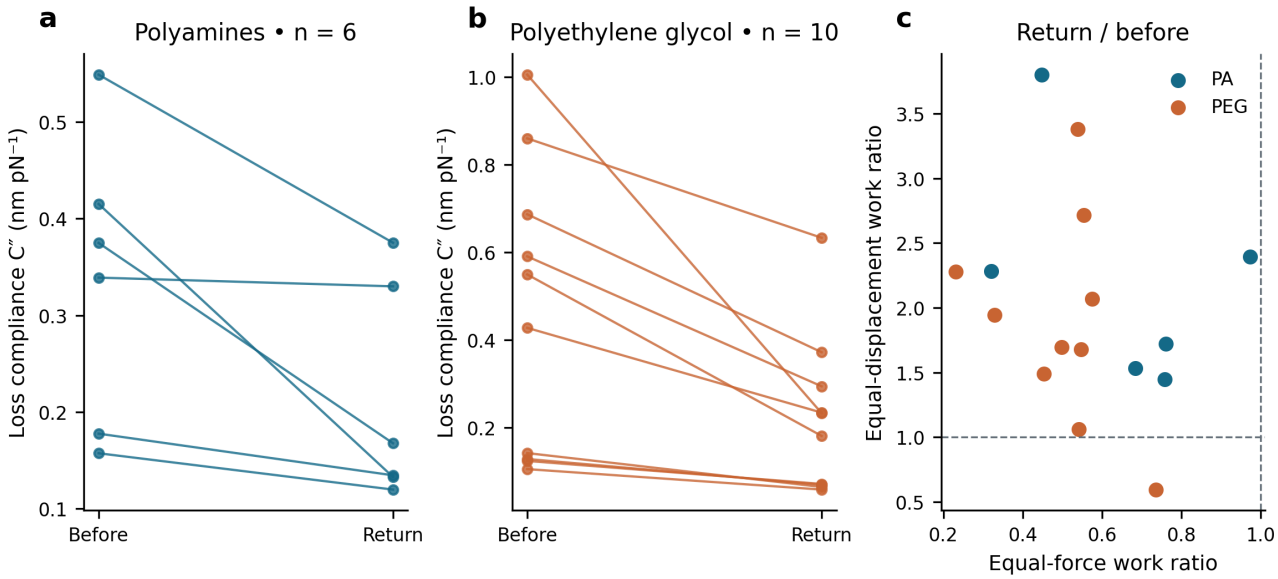
a, All 120 battery spectra from twelve cells at 57 native frequencies. The inset summarizes each quartet's maximum discrepancy under maps I0–I6. **b,** Sixteen complete tissue acquisitions, twelve from Pig 1 and four from Pig 2, at ten frequency means; the lower strip shows all four quartets. **c,** Quartet–frequency discrepancies under each admitted map, with 1,710 battery and forty tissue relations per map. Horizontal jitter separates overlapping points, and the symmetric-log ordinate preserves zero. Maximum discrepancies are 7.47×10^{-14} and 1.90×10^{-15}. The maps are computational transformations of the measured electrical responses. Target and reference states share the same coefficients at each frequency. Supplementary Information S17 defines the grouping and the nonshared and quadratic controls.

Extended Data Figure 3 | Complete frozen-function and measured-capacity comparisons



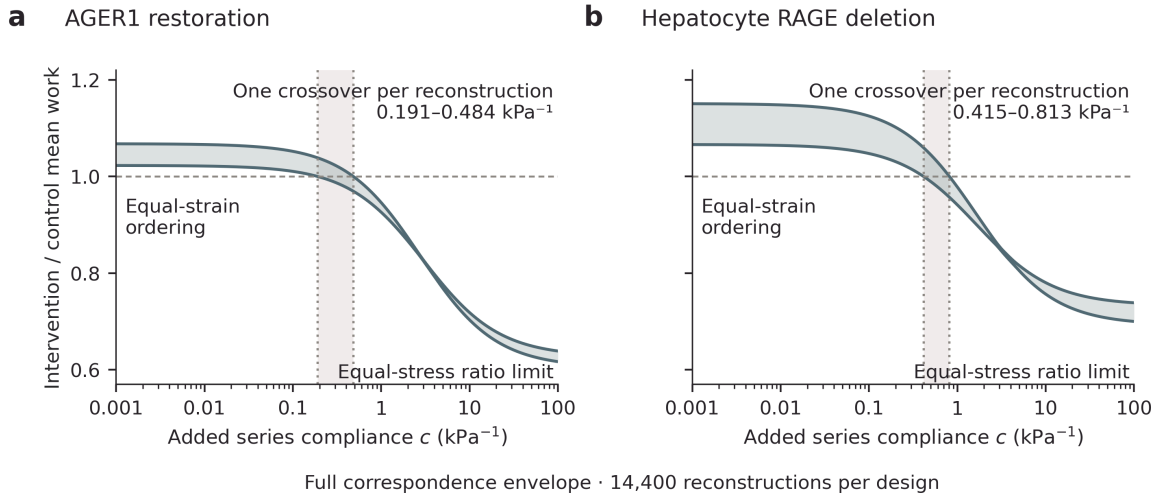
a, All 2,301 development records from eighteen cells, comparing the output of the original fixed linear function with the best affine readout of invariant coordinates (orange) and exact reference decoding (blue). The dashed line denotes equality. The target is the output of the same frozen function, with discrepancies expressed in mAh. **b,** Empirical cumulative distributions of all absolute output discrepancies. The affine projection has RMS discrepancy 3.620354 mAh; the maximum decoder discrepancy is 3.04823×10^{-12} mAh. Exact zeros are displayed at 10^{-15} mAh on the logarithmic axis. **c,** RMS output discrepancy within each of the eighteen development cells, using the same statistic for both constructions and the colours in **a**. **d,** The separate nested evaluation against measured capacity: grey circles show each of fifteen held-cell MAEs and blue diamonds show their equally weighted mean for each of eight representation/readout combinations. Every route predicts the same 1,921 outer records; the three reference-source cells remain available in the training partitions. Spectral representations also receive the same recorded action variables. The nested evaluation is conditional on those supplied variables (Supplementary Information, section S15).

Extended Data Figure 4 | Chromosome work changes in opposite directions under different loading comparisons



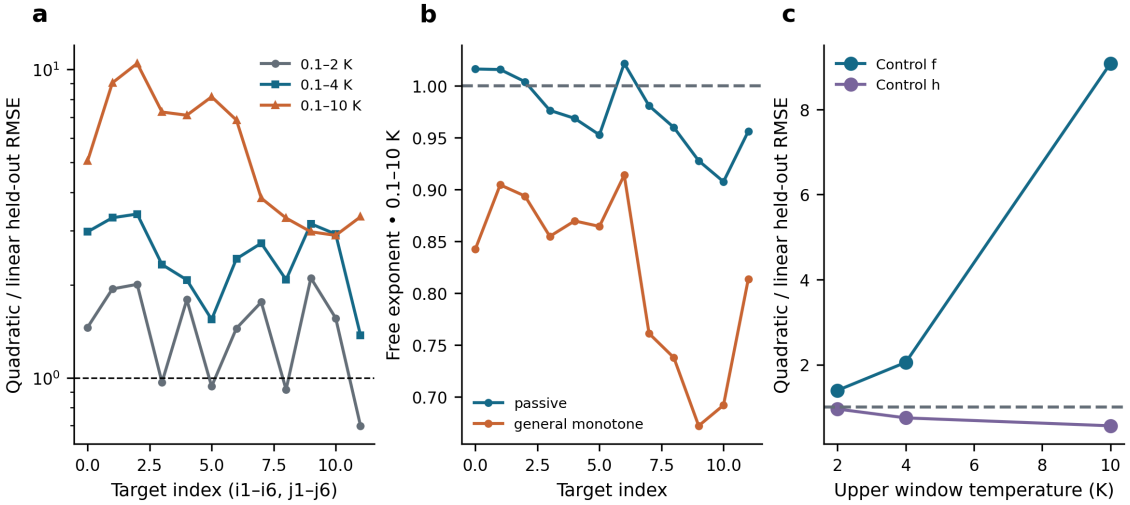
a,b, Native-derived stage-mean loss compliance before condensation and after return to the original buffer for all six polyamine and ten polyethylene-glycol chromosomes, respectively, at the verified 1 Hz frequency. Each line joins one chromosome. Native complex estimates are converted before stage averaging. All sixteen return values are lower; median paired ratios are 0.720287 and 0.539829. **c,** Return/before work ratios predicted for a common small oscillating force (horizontal, C'' ratio) and a common recorded displacement amplitude (vertical, K'' ratio). Each point is one chromosome. Dashed lines mark unity; sixteen equal-force ratios are below one and fifteen equal-displacement ratios exceed one. The two protocols differ; both expressions agree for the same actual trajectory. PA, polyamines; PEG, polyethylene glycol. The comparison concerns the recorded return window at the verified 1-Hz frequency. Equal-force and equal-recorded-displacement ratios use the measured loss compliance and loss stiffness, respectively. The force-controlled invariant applies to an additional purely elastic series compliance. Native measurements are from Witt et al.[39–40]. Supplementary Information S6 documents the stage and frequency audits and sensitivity checks; Supplementary Fig. 4 shows the native estimates and all three stages.

Extended Data Figure 5 | Elastic coupling produces one certified energetic reversal for every liver reconstruction



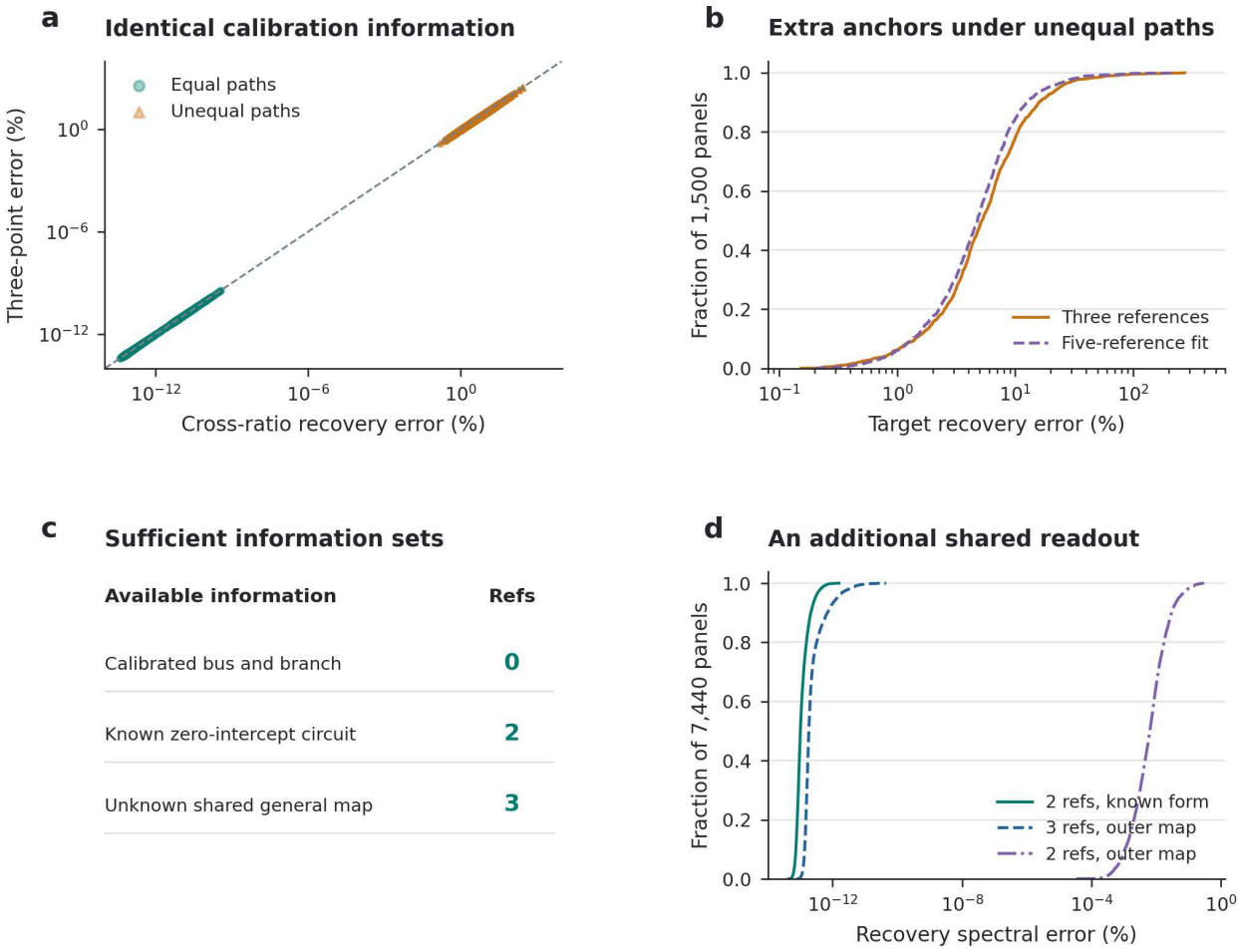
a,b, Sharp intervention/control mean-work envelopes for AGER1 restoration and hepatocyte RAGE deletion, respectively, at fixed remote strain amplitude after adding the same nonnegative, stationary, purely elastic series compliance c to every retained response. Shaded response bands include all 14,400 cross-arm reconstructions per design. Gray vertical bands span their unique positive crossover locations. The exact integer polynomial certificate gives one positive comparison crossing for every reconstruction; independent bisection reproduces the displayed endpoints. At c = 0 the comparison is the equal-recorded-strain work ratio. As c increases, the work ratio approaches its equal-stress loss-compliance ratio while both absolute works decrease to zero at fixed remote strain. The bands quantify missing correspondence at the reported input values and are not biological sampling intervals. Supplementary Information S4 gives the source inputs, endpoint witnesses and exact certificates.[13]

Extended Data Figure 6 | Transport windows and observation classes



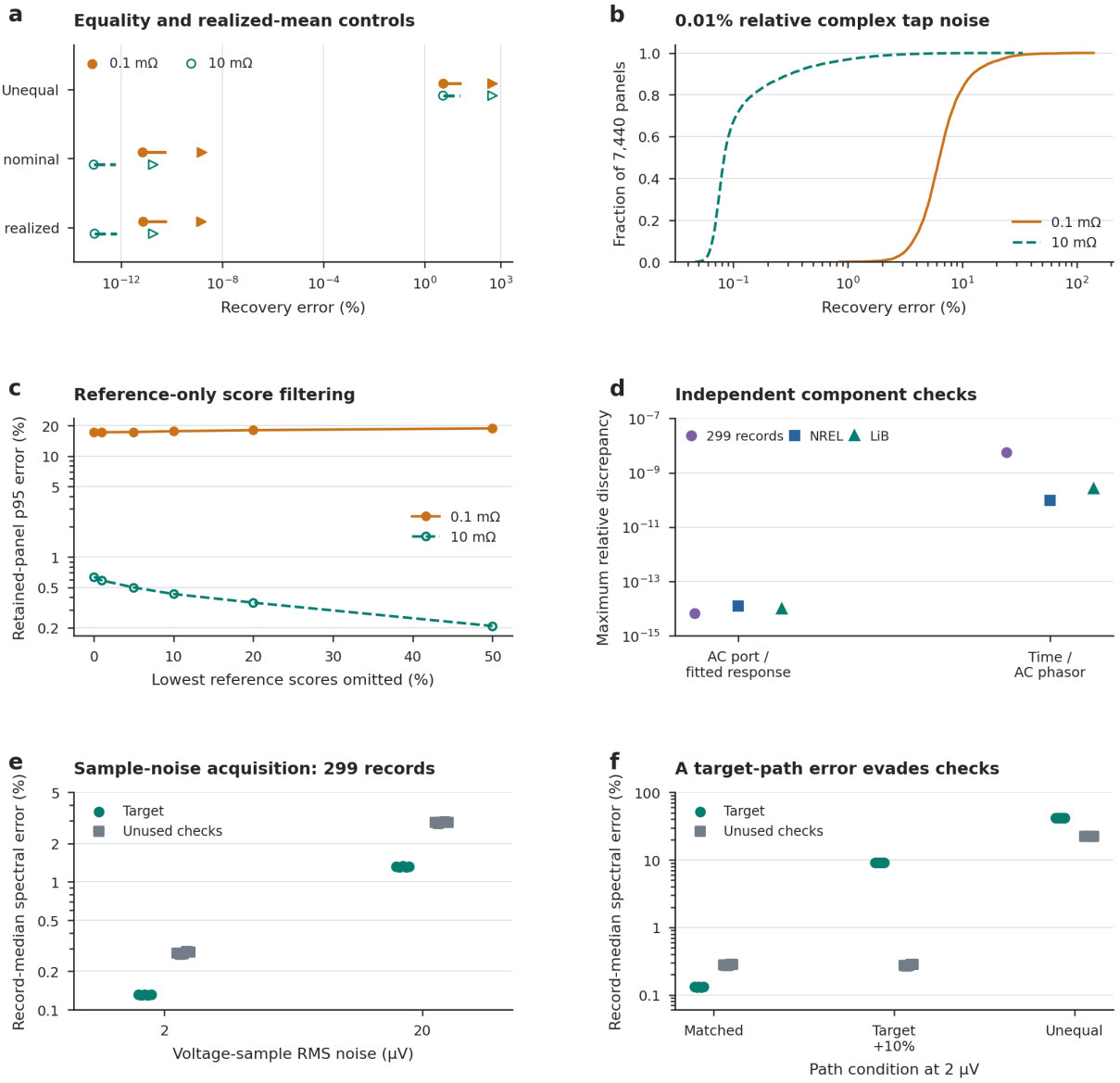
a, Ratios of quadratic to linear aggregate held-out RMSE for all twelve targets under the passive model in three temperature windows. All twelve favour linear over 0.1–4 and 0.1–10 K; eight do so over 0.1–2 K. **b,** Full-window free exponents for the passive and broader monotone observation classes. The latter permits a signed offset and negative reduced shunt coefficient while avoiding poles in the selected window. The free-exponent estimates show the dependence on the chosen observation class. **c,** Both zero-field controls across all windows under the passive model. Ratios below unity favour quadratic; the panel-h 0.1–4 K control gives 0.748935. All plotted results come from archived fits to native source-ohm responses using the same contiguous-block procedure. Lines connect saved conditions. All curves originate from one device; the contiguous blocks test temperature transfer within that device. Two broader-class control holdouts reach the negative-coefficient boundary. Supplementary Information S19 specifies the model classes, windows and holdout procedure. [58]

Extended Data Figure 7 | Reference information defines calibration and model checks



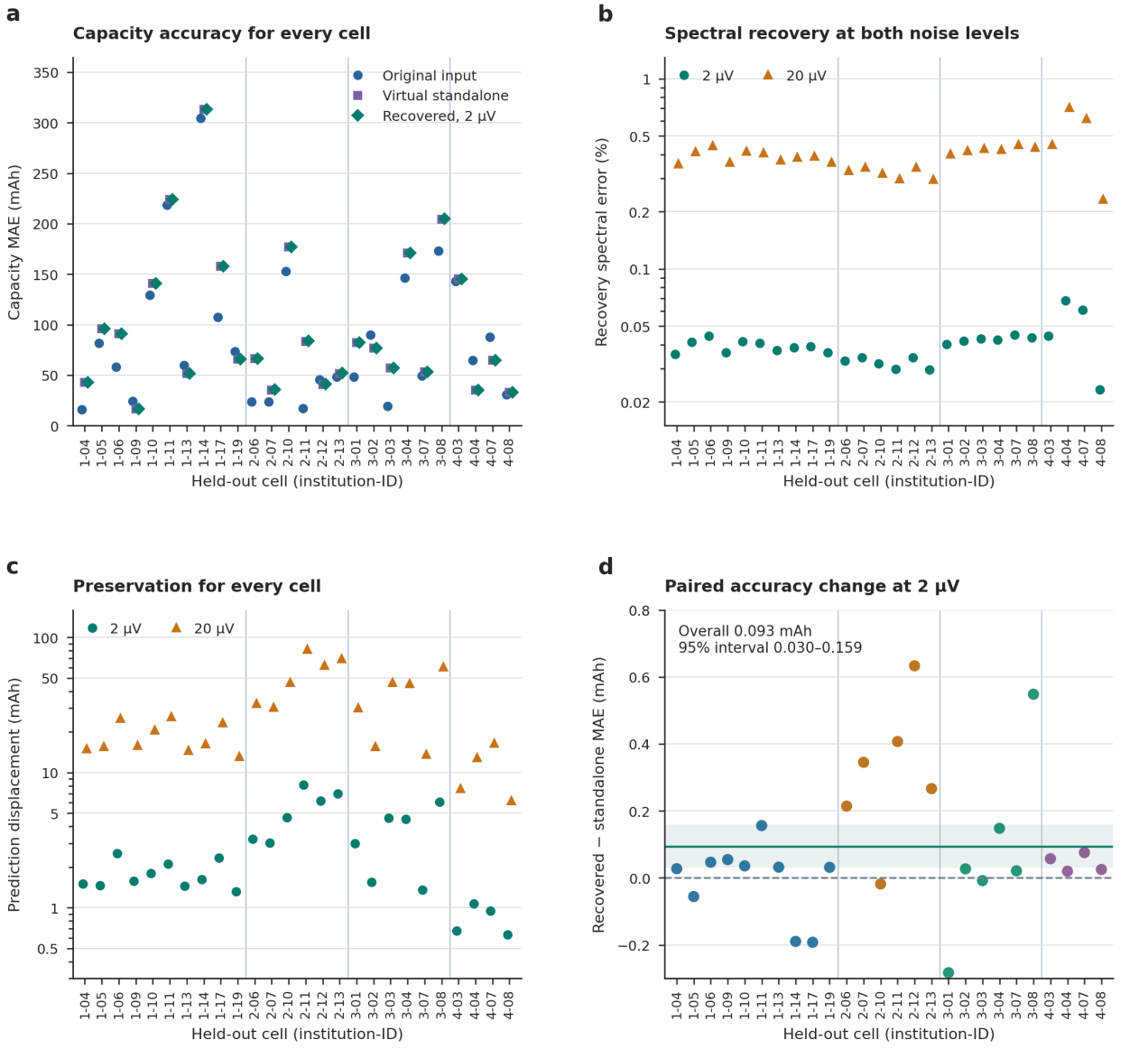
a, Cross-ratio and conventional normalized three-point calibration on identical information for 1,500 targets in each of four controlled equal/unequal branch conditions. The diagonal is equality. **b,** Three-reference and five-reference homogeneous fits on the same 1,500 unequal 0.1-mΩ panels. Additional anchors improve the approximate fit without establishing a common physical map. **c,** Three sufficient information sets: calibrated bus/branch values; the known restricted circuit form with two references; or a general shared map with three references. **d,** Two references recover the known zero-intercept circuit, and three recover an additional shared fractional-linear readout. Applying the restricted two-reference formula after that outer map is an observation-class mismatch. Each curve contains 7,440 targets. The panels use constructed networks of measured standalone spectra over twenty frequencies, 0.1–10 Hz, without added noise.[19–20] Matched-map residuals quantify numerical closure. No display floor is applied.

Extended Data Figure 8 | Acquisition verification and inverse conditioning



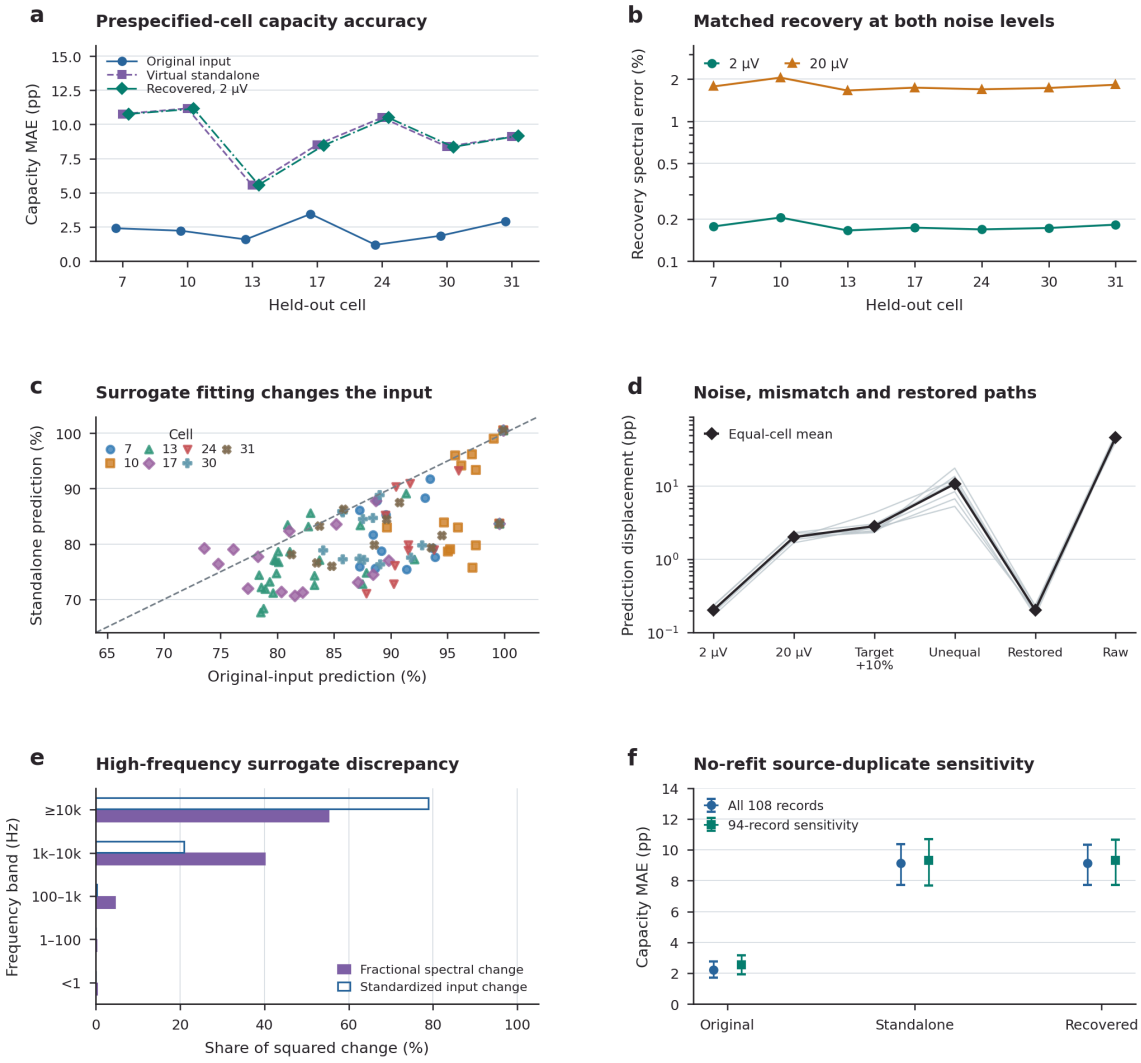
a, Saved noiseless scale controls, 7,440 targets per condition. Circles mark record medians, segments extend to p95 and triangles mark maxima. Equal paths use either the nominal resistance or each unequal panel's realized arithmetic mean. Identical unequal realizations are scaled from 0.1 to 10 mΩ. **b,** Equal-path recovery at the two scales under identical realizations of 0.01% circular complex relative tap noise. **c,** p95 after removing the lowest fractions of the candidate-only reference separation score. The score does not consistently rank stability across circuit scales. Panels a–c retain the earlier controlled recombination study and its perturbation model.[19–20] **d,** Maximum relative discrepancy between independently solved component ports and fitted standalone spectra, and between time-integrated and harmonic phasors. The single-cell, NREL and LiB studies retain 15, seven and 26 prespecified transient probes, respectively. These are numerical consistency checks. **e,f,** The separately sampled acquisition for all 299 records of one held-out cell.[21] Points are five fixed noise realizations; each reports a record-median spectral error. At matched paths, target and check errors grow with sample noise (e). A target-only path mismatch changes the target while leaving the unused reference checks matched (f). The 0.01% relative complex tap noise in b,c and the 2/20-μV voltage-sample RMS noise in e,f are different specified error models. Neither frequency points nor numerical noise realizations are additional physical cells.

Extended Data Figure 9 | Whole-cell preservation across four institutions



All 26 LiBforSecUse outer holdouts exclude every record from the indicated cell from that fold's training.[22–23] Vertical separators identify institutions 1–4 (ten, six, six and four cells). **a,** Cell-specific capacity MAE using original measured inputs, fitted standalone responses and responses recovered at 2 µV. **b,** Cell-mean RMS fractional spectral recovery error at 2 and 20 µV, relative to the fitted standalone spectrum. **c,** Cell-mean absolute change in the frozen capacity prediction from the fitted standalone baseline. **d,** Paired change in cell-specific MAE after matched recovery at 2 µV; the line and pale band mark the equal-cell mean and stratified 95% whole-cell bootstrap interval. Record-level errors are averaged over each cell and five fixed noise realizations before cell aggregation. Intervals condition on the frozen folds, acquisition settings and noise seeds. All 4,297 records are retained; Supplementary Information S12.11 and Table 40 give the complete cell-level results. Spectra and outcomes are measured; installation and readout changes are simulated.

Extended Data Figure 10 | Prespecified NREL holdouts separate recovery from accuracy



a,b, Seven prespecified NREL–DENSO test cells contribute 108 records.[24,50] Capacity MAE is evaluated for original measured, fitted standalone and recovered inputs (a); spectral recovery is relative to the fitted standalone response (b). Curves show cell means. **c,** Frozen predictions for each measured input and its fitted standalone counterpart before installation; the diagonal marks unchanged prediction. **d,** Cell-specific prediction displacement under matched 2/20-µV noise, target-only +10% mismatch, unequal paths, restored matching and raw installed input. Other decoded conditions use 2 µV; raw input has no added noise. Diamonds give equal-cell means. **e,** Exploratory frequency-band accounting of the frozen measured-to-standalone input change. Bars show each band's share of pooled squared fractional spectral change and squared standardized predictor-input change. **f,** No-refit source-overlap sensitivity comparing all 108 primary records with 94 records after excluding 14 test rows whose two exact input signatures also occur in training. The same seven cells and five noise realizations are retained. Error bars are paired 95% whole-cell bootstrap intervals conditional on the frozen model and noise seeds. Supplementary Information S12.9–S12.13 and S16 give complete results, diagnostics and the expanded-representation follow-up. Recovery preserves the virtual standalone computation; the preceding representation fit changes original-input accuracy. Network and readout changes are simulated.

References

13. Fan, W. et al. Matrix viscoelasticity promotes liver cancer progression in the pre-cirrhotic liver. Nature 626, 635–642 (2024). doi:10.1038/s41586-023-06991-9

19. Ank, M., Kröger, T., Schreiber, M. & Lienkamp, M. Experimental analysis of lithium-ion cell procurement: Quality differences, correlations, and importance of cell characterization. J. Energy Storage 66, 107430 (2023). doi:10.1016/j.est.2023.107430

20. Ank, M., Kröger, T., Schreiber, M. & Lienkamp, M. Characterization data of 250 cylindrical lithium-ion cells. Technical University of Munich (2023). doi:10.14459/2023mp1699705

21. Zhang, Y., Tang, Q., Zhang, Y., Wang, J., Stimming, U. & Lee, A. A. Identifying degradation patterns of lithium ion batteries from impedance spectroscopy using machine learning. Nat. Commun. 11, 1706 (2020). doi:10.1038/s41467-020-15235-7

22. Chan, H. S. et al. Comparison of methodologies to estimate state-of-health of commercial Li-ion cells from electrochemical frequency response data. J. Power Sources 542, 231814 (2022). doi:10.1016/j.jpowsour.2022.231814

23. Guignard, F. & Hoffmann, J. LiBforSecUse processed data for machine learning modelling and uncertainty propagation. Version v1. Zenodo (2025). doi:10.5281/zenodo.17792537

24. Gasper, P., Schiek, A., Smith, K., Shimonishi, Y. & Yoshida, S. Predicting battery capacity from impedance at varying temperature and state of charge using machine learning. Cell Rep. Phys. Sci. 3, 101184 (2022). doi:10.1016/j.xcrp.2022.101184

39. Witt, H. et al. Ion-mediated condensation controls the mechanics of mitotic chromosomes. Nat. Mater. 23, 1556–1562 (2024). doi:10.1038/s41563-024-01975-0

40. Witt, H. Data for the manuscript Ion-mediated condensation controls the mechanics of mitotic chromosomes. Zenodo, version 1 (2023). doi:10.5281/zenodo.7801755

50. Gasper, P. et al. battery_capacity_from_eis: author code and data. GitHub https://github.com/NatLabRockies/battery_capacity_from_eis (accessed 31 October 2026).

58. Xia, Y. et al. Bandwidth-tuned Mott transition and superconductivity in moiré WSe2. Nature 650, 585–591 (2026). doi:10.1038/s41586-025-10049-3

Supplementary Information

Physical Discovery and Design from Incomplete Records

Sabitoj Singh Virk and Akashdeep Singh Virk

ORCID

Sabitoj Singh Virk https://orcid.org/0000-0002-5801-5630

Akashdeep Singh Virk https://orcid.org/0000-0002-9157-4637

Sections S1–S3 develop the physical targets, exact work relations and reconstruction benchmark. Biological orderings and loading requirements follow in S4–S8; battery observation design and independent acquisition in S9–S12; superconducting trajectories in S13; surfactant measurements in S14; and preserved computations, measured transfers and transport in S15–S19. Data and analysis availability are stated in S20. This supplement contains 20 sections, 16 figures and 52 numbered tables.

Contents

S1 Physical targets and admissible material descriptions
S2 Work loading conditions and exact response bounds
S3 Controlled reconstruction and property queries
S4 Gel and liver bounds with unknown correspondence
S5 Evidence classes for loading-conditioned energetic fidelity
S6 Chromosome energetics and recovery
S7 Biological confirmation and compensation
S8 Molecular context for loading-dependent biological responses
S9 Reference reconstruction and preservation of a fixed computation
S10 Battery observation design and reference information
S11 Parallel-network recovery and masking
S12 Independently solved battery acquisition and preservation of frozen predictions
S13 Superconducting precursor selection and incomplete trajectory records
S14 Surfactant measurements and energetic comparisons
S15 Reference decoding and battery predictions
S16 Passive representation and acquisition follow-up
S17 Reference relations in measured electrical responses
S18 Retaining a physical readout across measured instrument changes
S19 Passive transport families and known temperature
S20 Data and analysis records

S1 Physical targets and admissible material descriptions

Let a description s specify the material, observation process and any unresolved correspondence between measurements. A record y and an observation model O define the nonempty compatible set $S(y)=\{s:O(s)=y\}$. For a physical question represented by $q(s)$, the available answers are $Q(y)=\{q(s):s\in S(y)\}$. The target is identifiable precisely when this image is a singleton. A non-singleton image can still determine an ordering or exclude a proposed value. With a justified measurement-error set E, compatibility instead requires $y-O(s)\in E$. The deterministic set and a probability interval have distinct definitions; a probability interpretation requires an associated error or sampling model.

The answer set distinguishes a determined value, a settled ordering and an unresolved comparison. If every admitted answer lies in one decision class, that conclusion is fixed even when the descriptions differ. If the answer set crosses a decision boundary, a resolving observation must distinguish descriptions that yield different decisions; the physical relation providing that distinction becomes an observation or processing requirement. An empty compatible set instead signals inconsistency between the record, the observation model and the admitted uncertainty.

Proposition 1. Elastic series ambiguity preserves a family of passive material descriptions. Suppose $J_o^*=J_m^*+J_e$, with a real nonnegative series compliance J_e. For every real shift a preserving the material and support admissibility conditions,

$$\tilde{J}_m^*=J_m^*+a,\tilde{J}_e=J_e-a,\tilde{G}_m^*=\frac{G_m^*}{1+aG_m^*}$$

produces exactly the same recorded response. For a positive finite-Maxwell material and $a\geq 0$, the transformed material has another positive finite-Maxwell representation. A sufficient simultaneous support condition is $0\leq a\leq \min_g J_{e,g}$ across the shifted configurations.

Proof. Adding the transformed material and support compliances cancels a identically, at every frequency. To establish physical admissibility beyond a single relaxation mode, combine repeated relaxation rates and write the complex-frequency response as

$$G(s)=\sum_{j=1}^{N}\frac{g_j s}{s+r_j},g_j>0,r_j>0.$$

On the real line away from its poles,

$$G'(s)=\sum_{j=1}^{N}\frac{g_j r_j}{(s+r_j)^2}>0.$$

For $a>0$, the transformed poles solve $G(s)=-1/a$. Monotonicity and the one-sided pole limits give one root between each adjacent pair of original negative poles and one between the pole nearest zero and zero. There is no further root to the left of the most negative pole. The original poles become removable singularities in $G/(1+aG)$. At each new pole $s_\star<0$, the residue equals $-1/\left[a^2G'(s_\star)\right]$, giving a Maxwell mass

$$\tilde{g}_\star=-\frac{1}{a^2 s_\star G'(s_\star)}>0,\tilde{r}_\star=-s_\star>0.$$

The transformed response vanishes at zero and has positive finite high-frequency limit $G_\infty/(1+aG_\infty)$. These properties determine its positive Maxwell partial-fraction representation. At $a=0$ the original material is recovered. Thus the indistinguishable alternatives can both represent stable passive relaxation, rather than only unconstrained algebraic curves.

For one Maxwell fluid, $G(s)=\eta s/(1+\tau s)$ gives $\tilde{\tau}=\tau+a\eta$ while retaining η. Figure 1 uses $\eta=0.3$ Pa s, $\tau=0.04$ s, $J_e=0.06$ $\mathrm{Pa^{-1}}$ and $a=0.04$ $\mathrm{Pa^{-1}}$. The alternative material relaxation time is 0.052 s and its support compliance is

0.02 Pa^{-1}. Both recorded responses have apparent relaxation time 0.058 s. The example changes the intrinsic high-frequency stiffness without changing the complete recorded response, loss compliance or terminal viscosity.

An observation transformation preserves a relation when the relation takes the same value for every admitted transformed tuple. Shared transformations impose a common structure across the compared states; that structure is specified separately for the energetic comparison and the reference decoder. Identifying a particular physical target does not require that every coordinate of the underlying material description be identifiable.

S2 Work loading conditions and exact response bounds

Proposition 2. A real series contribution leaves equal-force cyclic work identifiable. For linear harmonic response with $C^{*} = C' - iC''$ and imposed force $F(t) = F_0 \cos \omega t$,

$$x(t) = F_0 \left(C' \cos \omega t + C'' \sin \omega t \right), W_F = \oint F \, dx = \pi F_0^2 C''.$$

Proof. Substitution gives an integrand proportional to $-C' \sin \omega t \cos \omega t + C'' \cos^2 \omega t$. The mixed term integrates to zero over the period and the squared cosine contributes one half of the period. A real series compliance changes only C' and therefore contributes no net cyclic work. This conclusion holds separately in states with different real elastic series compliances. Replacing force and extension by stress and strain gives $w = \pi \tau_0^2 J''$ per unit volume and mean dissipated power $\omega \tau_0^2 J'' / 2$.

At a prescribed recorded displacement amplitude, $W_x = \pi x_0^2 K''$. Reciprocity gives $C'' = K'' / \left(K'^2 + K''^2 \right)$ and $x_0 = \left| C^{*} \right| F_0$ for the same actual trajectory, so the two work formulas agree on that trajectory. Across different states, equal force and equal displacement define different comparisons. For positive storage and loss stiffnesses, let $t_j = K''_j / K'_j$ and $r = K'_2 / K'_1$. Then

$$\frac{C''_2}{C''_1} = \frac{t_2}{t_1} \frac{1 + t_1^2}{1 + t_2^2} \frac{1}{r}.$$

An increased loss tangent can therefore accompany decreased equal-force dissipation if the stiffness increase exceeds the stated threshold. The chromosome analysis evaluates these normalized work ratios from each native complex estimate; its static prestress is not substituted for an oscillatory force amplitude.

Sharp distance between elastic explanations. At one frequency, independent arbitrary real offsets can remove the real part of a compliance difference but cannot remove its imaginary part. Consequently

$$\inf_{a \in \mathbb{R}} \left| \Delta C^{*} - a \right| = \left| \Delta C'' \right|.$$

If the two admissible real parts range independently over the nonempty closed intervals I_1 and I_2, the minimum is $\sqrt{\left(\Delta C'' \right)^2 + dist\left(I_1, I_2 \right)^2}$. The first result follows by setting the real residual to zero; the second follows by choosing the closest admissible real endpoints. Both bounds are attained in their stated classes.

Across a spectrum, one frequency-independent real offset leaves additional information. For complex differences v_j, positive weights w_j and weighted real mean $\bar{v}_R$, completing the square gives

$$\min_{a \in \mathbb{R}} \sum_j w_j \left| v_j - a \right|^2 = \sum_j w_j \left(\operatorname{Im} v_j \right)^2 + \sum_j w_j \left(\operatorname{Re} v_j - \bar{v}_R \right)^2, \bar{v}_R = \frac{\sum_j w_j \operatorname{Re} v_j}{\sum_j w_j}.$$

Restricting a to a closed interval I adds $\left(\sum_j w_j \right) dist\left(\bar{v}_R, I \right)^2$. Allowing an unrelated real offset at every frequency instead removes the second term. These results identify the spectral information preserved by the specified support model.

Exact reciprocal error geometry. If $|z-\hat{z}| \le \epsilon < |\hat{z}|$, the reciprocal image is exactly

$$\left| \frac{1}{z} - \frac{\bar{\hat{z}}}{|\hat{z}|^2 - \epsilon^2} \right| \le \frac{\epsilon}{|\hat{z}|^2 - \epsilon^2}.$$

To prove the result, substitute $z = 1/u$ into the original disk inequality, multiply by $|u|^2$ and complete the square. Relative to the nominal reciprocal, the reverse triangle inequality gives the convenient bound

$$\left| \frac{1}{z} - \frac{1}{\hat{z}} \right| \le \frac{\epsilon}{|\hat{z}|\left(|\hat{z}| - \epsilon\right)}.$$

The exact image-disk centre and its radius must be used together. For two compliance estimates with valid absolute error radii e_1, e_2, their loss difference lies within $e_1 + e_2$ of the estimated difference. A bounded change in dissipative background adds its own allowance; a purely real support contributes zero to this loss-direction allowance. The CAPB processing rectangles and the biological bootstrap intervals retain their separate definitions in the relevant application sections.

Compensation under specified linear response

Scaling a prescribed waveform by amplitude A scales its linear response by the same factor. Work is the integral of one conjugate variable against the increment of the other, so its dissipative part scales as A². Once the waveform, duration, geometry, source and material state are specified, write W = A²K with K > 0. The work ratio between target b and reference a and the equal-work target are

$$M = \left(\frac{A_b}{A_a} \right)^2 \frac{K_b}{K_a}, \quad M = 1 \Rightarrow \frac{A_b}{A_a} = \sqrt{\frac{K_a}{K_b}}.$$

This relation applies to the specified protocol. Changes in cycle count, duration, volume or loaded geometry belong inside K or require an explicit additional factor. For dissipated work density per harmonic cycle, the coefficients are πJ″ under prescribed peak stress and πG″ under prescribed peak strain. Organoid step coefficients are finite-time viscous-work integrals. They are not substitutes for single-frequency loss compliance or loss modulus.

Incomplete records and guaranteed bounds

Suppose all admissible reconstructions constrain the positive ratio R = K_b/K_a to [L,U]. Monotonic transformation gives the set of admissible equal-work amplitude factors $[1/\sqrt{U}, 1/\sqrt{L}]$. This interval contains the equal-work setting for each allowed reconstruction; it does not assert that one amplitude equalizes every reconstruction simultaneously. Choosing $A_b/A_a \le 1/\sqrt{U}$ guarantees $W_b/W_a \le 1$ throughout the retained set. The equal-work interval and the conservative no-increase setting answer different questions. For the liver cohort-mean comparison, downward-rounded stress factors of 1.2624 and 1.1678 give maximum work ratios of 0.9999194102 and 0.9999897020 across every matching, respectively. Downward rounding preserves the inequality; ordinarily rounded descriptive interval endpoints need not do so. The guarantee concerns the cohort mean under each reconstruction at the retained inputs, rather than an unknown correspondence of individual mice.

The liver calculations at 1 rad s⁻¹ condition on the storage-modulus and loss-tangent marginal lists describing the same five mice in each arm, at their fixed reported values. All 120 within-arm assignments and 14,400 cross-arm reconstructions per comparison are retained, without choosing a preferred specimen assignment. The resulting harmonic stress-amplitude factors are 1.262–1.286 for AGER1 restoration and 1.168–1.201 for RAGE deletion. The exact rational certificates for averages across reconstructed liver specimens belong to S4 and remain the required reconstruction-level proof. A crossover for two complex responses, derived below, does not replace those certificates.[13]

A single stress setting with minimum worst-case work error

A single loading setting can also minimize the largest departure from equal work across all admissible reconstructions. Let the positive work-coefficient ratio lie in the attained interval [L,U], and let a ≥ 0 be the target/reference stress-amplitude factor. The resulting work ratio is a²R. Its largest absolute deviation from unity occurs at an endpoint:

$$D(a) = max\ \{\ |a^2 L - 1|,\ |a^2 U - 1|\ \}\ .$$

Write t = a². For t below 2/(L+U), the endpoint error 1−tL exceeds the balanced value; for t above it, the endpoint error tU−1 exceeds that value. Equating these endpoint errors therefore gives the unique positive minimax setting when L < U:

$$a^* = \sqrt{\frac{2}{L+U}}, \qquad D^* = \frac{U-L}{U+L}.$$

For L = U, the same formula gives exact equal work and zero error. The result depends only on the attained endpoint bounds; it does not require a probability model for the unknown specimen matching.

For AGER1 restoration, L = 0.6047790245 and U = 0.6274383027 give a* = 1.274005615 and a worst relative work deviation of 1.838902741%. For hepatocyte RAGE deletion, L = 0.6928123889 and U = 0.7332609984 give a* = 1.184251818 and a worst deviation of 2.836362410%. The settings therefore keep calculated cohort-mean work within 1.84% and 2.84% of control, respectively, across all 14,400 admitted reconstruction pairs for each comparison (S4). These are deterministic correspondence guarantees at the retained inputs.

The minimax setting balances a possible work increase against a possible decrease. It answers a different operating question from the conservative no-increase factors above, which remain 1.2624 and 1.1678. No single setting is claimed to equalize every admitted reconstruction exactly.

Finite elastic source and crossover

For a lossless series compliance $c \geq 0$, let $e = \gamma + c\sigma$ and $\sigma = G^* \gamma$. Solving the coupled problem gives $\gamma = e/\left(1 + c\,G^*\right)$ and $W_c = \pi\, e_0^2 D_c$, with

$$D_c = \frac{G''}{\left(1 + cG'\right)^2 + \left(cG''\right)^2}, W_c = \pi\, e_0^2 D_c.$$

Write $G_a^* = x_a + i\,y_a$ and $G_b^* = x_b + i\,y_b$, with positive loss components. The denominators are positive. Multiplying their product into $D_c\left(G_b^*\right) - D_c\left(G_a^*\right)$ therefore preserves its sign. At a crossover, the resulting quadratic satisfies

$$A_2 c^2 + A_1 c + A_0 = 0,$$

$$A_0 = y_b - y_a,$$

$$A_1 = 2\left(y_b x_a - y_a x_b\right),$$

$$A_2 = y_b\left(x_a^2 + y_a^2\right) - y_a\left(x_b^2 + y_b^2\right).$$

Retain real nonnegative roots and check the sign on both sides. A root at zero is a boundary tie; a repeated root can be a tangency. If the quadratic coefficient vanishes, solve the remaining linear equation. Identically zero coefficients describe equal response functions rather than a unique crossover. The solver retains small nonzero coefficients and uses high-precision arithmetic for near-degenerate cases. Numerical precision does not reduce uncertainty in the measured components.

For proportional remodelling $G_b^* = a G_a^*$ with $a > 0$ and $a \neq 1$, the positive crossover simplifies to

$$c_* = \frac{1}{\sqrt{a}\left|G_a^*\right|}.$$

At c = 0, D_c = G″. At large c, D_c tends to zero for fixed remote amplitude, while $c^2 D_c$ tends to J″. The ratio of two finite-source coefficients consequently tends to the corresponding loss-compliance ratio. Keeping e_0/c fixed gives the prescribed-stress limit. When the source itself changes between states, the equal-work remote-amplitude factor is $\sqrt{D_{c_a}\left(G_a^*\right) / D_{c_b}\left(G_b^*\right)}$.

Component uncertainty and hydraulic modes

For f = log J″ and x = G′, y = G″, the gradient is

$$\nabla f = \left[-\frac{2x}{x^2 + y^2}, \frac{1}{y} - \frac{2y}{x^2 + y^2} \right].$$

For the log ratio L, assemble the joint gradient h as $(-\nabla f_a, \nabla f_b)$. The first-order variance is Var(L) ≈ $h^T \Sigma h$, using the full component covariance Σ. The log compensation factor is minus one half of the log coefficient ratio, so its variance is one quarter as large. Within-state component covariance and between-state linkage must be retained. Published marginal standard deviations do not supply that covariance. Positive-component rounding boxes instead define deterministic sensitivity sets; they are not sampling intervals.

Hydraulic coupling is a separate extension. For a validated pressure–volume mode $C_t^* = \Gamma / G^*$, the tissue-work ratio is $\left(\Gamma_b / \Gamma_a\right)\left(p_b / p_a\right)^2 \left(J''_b / J''_a\right)$. For prescribed source-volume amplitude, a storage-and-drainage model uses the effective complex source compliance $\left[C_h - i / \left(\omega R_{out}\right)\right] / \Gamma$. Those mode and geometry assumptions require independent validation. The four shunt material-response targets below require only the same-frequency source table; they do not use unmeasured pressure amplitudes or hydraulic geometry.

S3 Controlled reconstruction and property queries

The controlled benchmark has eight regimes, each containing thirty independent generating worlds. Indices 0–9 are development and 10–29 are held out, yielding 80 and 160 worlds. Three materials share an observation operator within each world. The seed is $842019 + 10007\,r + 107\,i$, with separate streams for material, operator and noise draws. Most worlds use 21 logarithmically spaced frequencies from 0.01 to 100 Hz; the limited-band regime uses six from 0.1 to 10 Hz. Dense scoring uses 301 frequencies from 0.001 to 1,000 Hz.

Supplementary Table 1 | Controlled regimes.

Code	Generating description	Fitted modes	Measured frequencies
R0	Exact elastic series equivalence; one mode	1	21
R1	Weak or absent observation distortion; two modes	2	21
R2	Strong matched distortion; two modes	2	21
R3	Limited bandwidth; two modes	2	6
R4	Seven-mode spectrum	2	21
R5	Observation operator mismatch	2	21
R6	Correlation and outliers	2	21
R7	Three-mode development; 24-mode shifted test family	2	21

The four information settings are unknown operator, supplied exact viscosity moments, known operator coefficients, and three Newtonian reference viscosities of 0.1, 1 and 10 Pa s. There are 960 inverse cases and

three starting fits per case. Generating truths are used for scoring after fitting, not as undeclared inputs. Standard component noise has scale $\rho\, max\left(\left|Y\right|, 0.003\, Pa\right) + 10^{-6}$ Pa, with $\rho = 0.02$ except declared regimes. Exact equivalence controls have no realized noise. R6 adds correlated and outlier perturbations, and R5 changes the generating observation operator without changing the fitted one. Known coefficients cannot repair a mismatched operator.

Masses and relaxation times are optimized logarithmically within 10^{-6}–10^{5} Pa and 10^{-5}–10^{3} s. Exact moments are enforced by the material parameterization. Three bounded least-squares starts use analytic residual Jacobians. The fitted discrepancy groups separate real and imaginary components for each material or reference. Nominal group limits use independent-Gaussian chi-square quantiles with a Bonferroni allocation across groups; coverage is not claimed under the deliberately misspecified regimes. Pole avoidance and parameter bounds are additional feasibility requirements.

The reported response and intrinsic material scores use $\left[N^{-1}\sum_{j}\left|a_j - b_j\right|^2 / \left(\left|b_j\right|^2 + 10^{-12}\, Pa^2\right)\right]^{1/2}$, displayed as percentages. They are distinct from standardized fit residuals. The headline exact-equivalence response error of 2.21×10^{-14}% coexists with 26.45% material error. References resolve that exact subset to numerical precision; the full held-out unknown and reference material errors are 17.28% and 3.89%. Extended Data Fig. 1 shows the variation across regimes and the comparison using the preserved neural architecture.

Property searches target storage and loss moduli at 0.1, 1 and 10 Hz, terminal viscosity and a smooth relaxation-band mass. For the latter, each modal mass is weighted by logistic shoulders at 0.01 and 1 s with width 0.25 in natural-log time. Constrained endpoint searches optimize log properties while refitting nuisance parameters. The audit uses a second, admissibly transformed starting state within the same nominal directional allowance. Feasible attained extrema are witnesses; finite optimization cannot certify global extrema. Empirical acceptance also requires successful optimization in both directions.

All screening scores assess a common explored point estimate. Development selects pooled thresholds maximizing accepted count with at least twenty queries from five worlds and at most 5% observed errors above 20%. The fixed thresholds are then applied to 5,120 held-out queries. The underlying property-query records report acceptance and error among accepted queries; these summaries are not per-property coverage guarantees. Rate intervals use 1,000 world-level bootstrap resamples retaining all dependent queries. The analytically zero gradient of an exactly supplied viscosity moment is used in the displayed Fisher control. Limited bootstrap and uncertain-reference comparisons remain separate, smaller protocols. The complete query-level results and analysis settings are retained in the analysis records (S20).

S4 Gel and liver bounds with unknown correspondence

The Fan workbook contains separate lists of storage modulus and loss tangent for each rheology group. The primary collagen/alginate comparison uses six entries per list in each of the BSA control and AGE groups. The protocol and shared caption support the premise that each pair of lists describes the same six experiments, but the workbook does not link entries specimen by specimen. The 2025 correction concerns a separate AFM display. [13,57]

Let $a_i = 1/G'_i$ and $b_j = t_j/\left(1+t_j^2\right)$. For a correspondence π, the group mean is $n^{-1}\sum_i a_i b_{\pi(i)}$. If $a_i \le a_j$ and $b_k \le b_l$, changing the crossed pairing to the ordered pairing changes the sum by $\left(a_j - a_i\right)\left(b_l - b_k\right) \ge 0$. Repeated swaps prove the minimum and maximum in the Methods section on liver and gel matching bounds. The transformed *b* values must be sorted because $t/\left(1+t^2\right)$ is not globally monotone in t.

The archived calculation explicitly enumerates 720 permutations per gel group and 518,400 cross-group ratios, independently checking the sorting formula. The exact reported-point ratio range is 1.320850825–1.345959562. Positive compliance converts it directly to the range of mean work per volume at equal small stress amplitude.

Measurements were at 1 rad s^{-1}, 37 °C and 1% strain; 1 rad s^{-1} is approximately 0.159 Hz and must not be relabelled 1 Hz.

The bound identifies the range of the finite reported cohort under the same-experiment premise, with the measured values held fixed. It describes correspondence uncertainty rather than sampling or measurement uncertainty. Supplementary Fig. 1 and the source tables give all seventeen within-domain contrasts across eleven groups, including their different directions. The collagen–alginate gel comparison is distinct from the rBM–alginate cell-assay matrices. Native genetic liver cohorts are analysed separately below.

S4.1 Complete gel correspondence enumeration

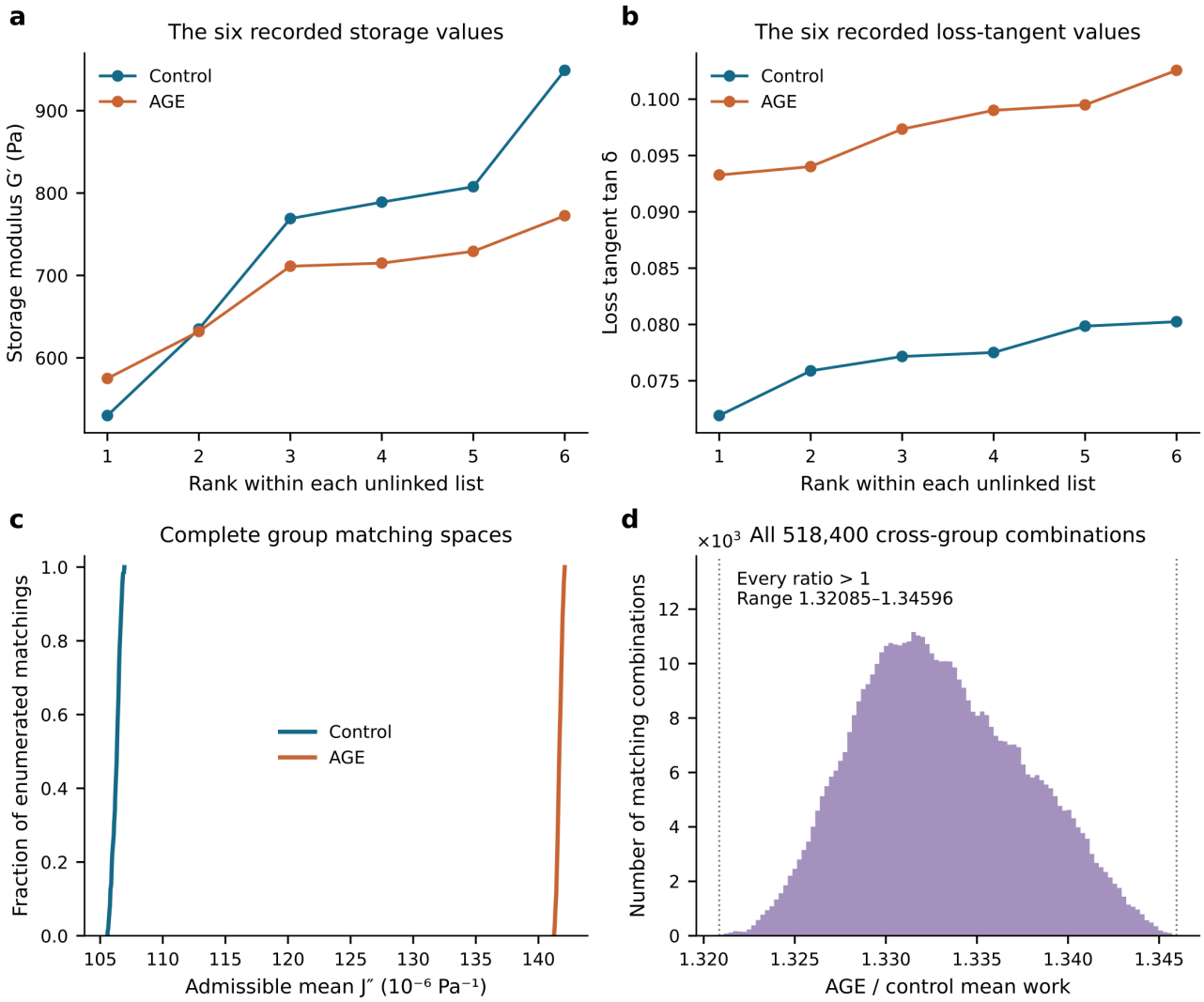
Supplementary Fig. 1c,d show all attainable gel means and the complete cross-group ratio distribution. For each group, every one of the $6! = 720$ bijections between storage modulus and loss tangent is evaluated, using each recorded value once. The 720 means recomputed directly from the original marginal lists reproduce the saved enumeration to numerical precision. Taking every AGE mean over every control mean then gives exactly 518,400 ratios, with extrema 1.3208508247 and 1.3459595624. The sorting construction and full enumeration therefore supply the same endpoint bounds. [13]

Supplementary Table 2 | Complete ranges of mean loss compliance.

Group	Values in each list	Admissible matchings	Minimum mean J″ (10^{-6} Pa^{-1})	Maximum mean J″ (10^{-6} Pa^{-1})
BSA control	6	720	105.576620	106.933803
AGE	6	720	141.243603	142.101862

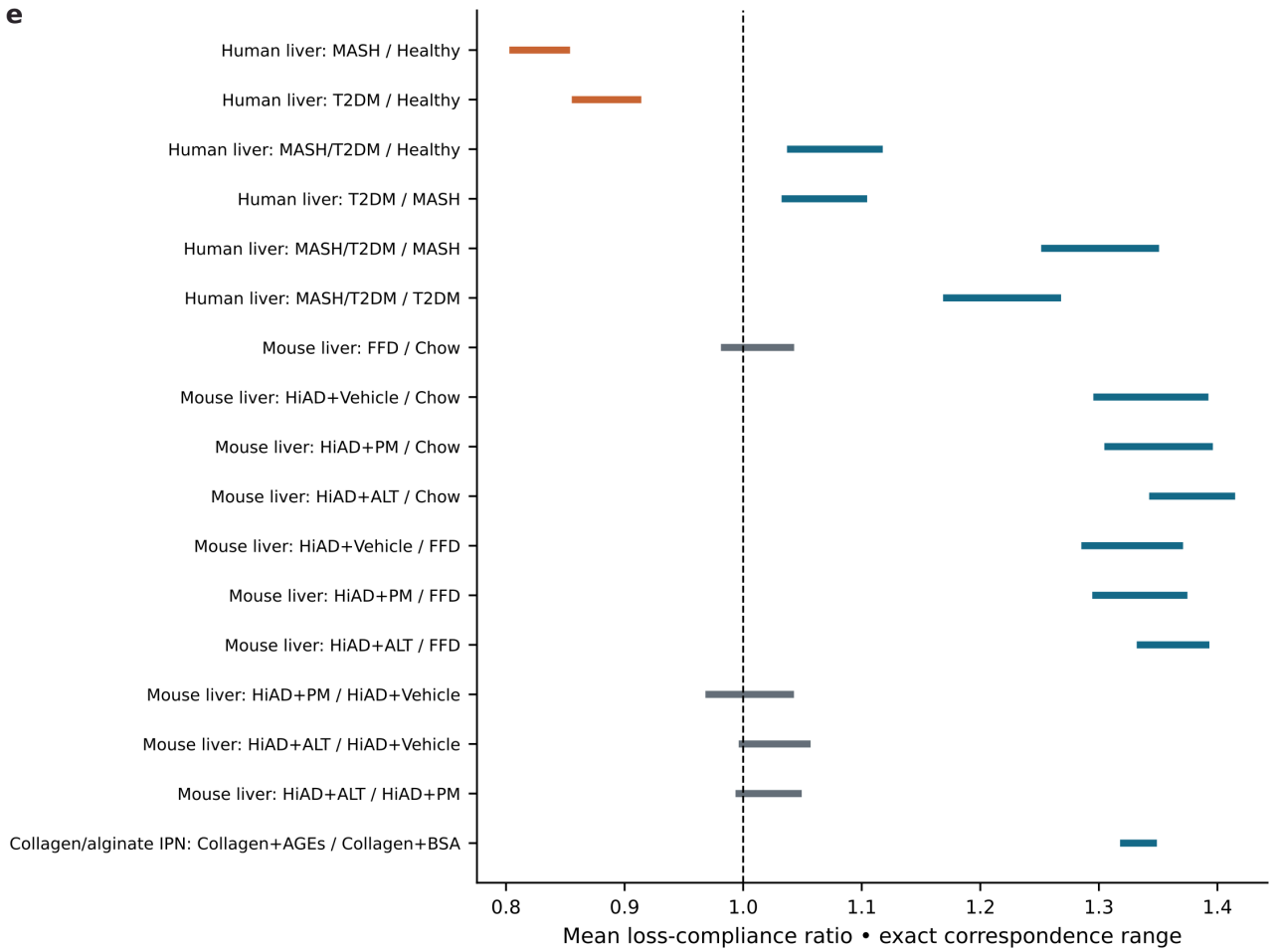
The two group intervals do not overlap. At common small stress amplitude σ_0, $\overline{w} = \pi \sigma_0^2 \overline{J''}$, so every admissible correspondence retains the greater mean work with AGEs. The histogram in Supplementary Fig. 1 counts all admissible assignments of the retained marginal lists. Recovering specimen links would select an admissible mean inside the stated interval.

Supplementary Figure 1 | Complete gel matching spaces and the full within-domain comparison family



a,b, The original six storage-modulus values (a) and six loss-tangent values (b) in each gel group, sorted within each list. Rank orders each marginal list; all 720 cross-list correspondences are enumerated explicitly. **c,** Cumulative fractions of all 720 admissible group means of $J''=t/\left[G'\left(1+t^2\right)\right]$, with $t=\tan\delta$. The control and AGE ranges are separated for every assignment. **d,** Histogram of all 518,400 ratios formed from the two complete sets of group means, using 100 equal-width bins. Dotted lines mark the exact minimum and maximum, 1.320850825 and 1.345959562. Every ratio exceeds one. The finite enumeration holds the measured lists fixed and assumes that each group's lists refer to the same six experiments; histogram counts enumerate admissible assignments. At common small stress and frequency, the ratios also give mean cyclic work per volume. [13]

Supplementary Figure 1 (continued) | Complete gel matching spaces and the full within-domain comparison family



e, Each segment shows the exact finite-list range of the numerator/denominator mean loss-compliance ratio over all admissible within-group correspondences. All seventeen within-domain contrasts from eleven source groups are retained. The dashed line marks unity; blue indicates the entire range above one, orange below one, and grey a range including one. Lists are assumed to describe the same experiments within each group. Segments are exact finite-record correspondence bounds for the retained source lists. Human and mouse tissue groups and collagen/alginate gels remain separate cohorts. FFD, fast-food diet; HiAD, high-AGE diet; PM, pyridoxamine; ALT, alagebrium, as defined by the source study. The direction is determined separately for each tissue or gel comparison. Supplementary Information S4 gives the rearrangement proof and source cells. [13]

S4.2 Native liver intervention records

The same correspondence construction applies to the native liver experiments of Fan et al. [13] We analysed two genetic designs separately: AAV8-mediated AGER1 reconstitution versus the GFP control, and hepatocyte-specific RAGE deletion versus the floxed control. Each design includes wild-type and mutant β-catenin arms. The source reports five mice per arm; transformed foci were summarized from 20 areas per mouse. The independent unit in the present comparison is the mouse, and the foci analysis uses the five published mouse-level summaries rather than the individual image fields.

AGER1 inputs come from workbook 41586_2023_6991_MOESM5_ESM.xlsx, sheets Fig 2k (storage modulus), Fig 2l (loss tangent) and Fig 2n (transformed foci), rows 2–6. Columns C, D, E and F represent GFP/wild-type β-catenin, AGER1/wild-type, GFP/mutant and AGER1/mutant, respectively. RAGE inputs come from workbook 41586_2023_6991_MOESM10_ESM.xlsx, sheets Ext Data Fig 2g, Ext Data Fig 2h and Ext

Data Fig 2e, respectively, rows 2–6. Their columns C, D, E and F represent floxed/wild-type, floxed/mutant, RAGE-deleted/wild-type and RAGE-deleted/mutant. Thus the principal mutant comparisons use E versus F for AGER1 and D versus F for RAGE. The analysis source table preserves these locations and native numbers (S20).

Liver oscillatory measurements were acquired by parallel-plate shear rheometry at room temperature, 2% strain and 1 rad s^{-1} for 600 s. [13] These native tissue records are distinct from the collagen–alginate gel measurements above and from the rBM–alginate matrices used for the source cell assays. Within each arm, the inference assumes that the separate modulus and loss-tangent lists refer to the same five experiments. All admissible correspondences are retained; row order is not treated as a specimen identifier.

For storage modulus $g_i > 0$, loss tangent $t_j > 0$ and bijection π, the reconstructed positive loss compliance and recorded-frame loss modulus are

$$J''_{i,\pi} = \frac{t_{\pi(i)}}{g_i\left[1+t^2_{\pi(i)}\right]}, G''_{i,\pi} = g_i t_{\pi(i)}. \quad \text{(S4a)}$$

At a common small stress amplitude, mean work per volume is $\pi\sigma_0^2\overline{J''}$; at a common recorded strain amplitude it is $\pi\gamma_0^2\overline{G''}$. These expressions distinguish the physical loading questions. Each arm has $5! = 120$ rheological reconstructions, and each two-arm comparison has $120^2 = 14,400$. The five mice per arm are the biological units; reconstruction enumerates their admissible response-component correspondences.

Supplementary Table 3 | Native genetic-cohort response bounds. Each row contains five mice and 120 admissible rheological correspondences. J″ values are in kPa^{-1}; G″ values are in Pa. The table retains all four arms of each design.

Design	β-catenin	Arm	Mean J″ minimum	Mean J″ maximum	Mean G″ minimum	Mean G″ maximum
AGER1	Wild-type	GFP	0.705830	0.729490	72.473842	74.928711
AGER1	Wild-type	AGER1	0.548294	0.557840	60.847011	61.956033
AGER1	Mutant	GFP	0.775369	0.791942	60.327724	61.930370
AGER1	Mutant	AGER1	0.478950	0.486496	63.347858	64.418263
RAGE	Wild-type	Floxed	0.951081	0.983049	54.699664	56.741058
RAGE	Wild-type	Deleted	0.847421	0.855344	47.254032	47.763293
RAGE	Mutant	Floxed	1.011558	1.017880	46.133519	46.449565
RAGE	Mutant	Deleted	0.705200	0.741736	49.526905	53.095112

S4.3 Loading-specific intervention comparisons

Write $m_{A,-}$ and $m_{A,+}$ for the minimum and maximum group mean of a positive response in arm A, with $A = 0$ denoting control and $A = 1$ intervention. Because the two arms' missing correspondences can vary independently, the sharp intervention/control ratio interval is

$$\left[\frac{m_{1,-}}{m_{0,+}}, \frac{m_{1,+}}{m_{0,-}}\right]. \quad \text{(S4b)}$$

For mutant β-catenin cohorts, every reconstruction gives lower mean J″ after AGER1 reconstitution or hepatocyte RAGE deletion (Fig. 2b). The corresponding energy reductions at common small stress are 37.26–39.52% and 26.67–30.72%, respectively. Conversely, the same records give higher mean G″: 2.29–6.78% and 6.63–15.09% greater energy at common recorded strain. The difference follows from the measured storage and

loss components in equation (S4a); it is not a change in the underlying records. Table 4 also gives the full conservative omission envelope defined in S4.5.

Supplementary Table 4 | Mutant-cohort energetic comparisons. Ratios are intervention/control. Each complete comparison has five mice per arm and includes all 14,400 rheological reconstruction pairs. Omission retains four values per list per arm and includes every permitted deletion and remaining correspondence. All intervals are finite-record correspondence bounds.

Intervention	Equal-stress work ratio	Equal-recorded-strain work ratio	Equal-stress ratio after conservative omission
AGER1 reconstitution	0.604779–0.627438	1.022888–1.067805	0.517525–0.715260
Hepatocyte RAGE deletion	0.692812–0.733261	1.066251–1.150901	0.596963–0.879094

S4.4 Ordering of complete empirical response distributions

The complete mutant-cohort records determine an ordering beyond the mean contrast. For arm A and correspondence π, let $J''_{A,(k),\pi}$ denote the kth smallest reconstructed response. We computed its extrema over all 120 correspondences. For both genetic designs,

$$\max_{\pi_1} J''_{1,(k),\pi_1} < \min_{\pi_0} J''_{0,(k),\pi_0}, k = 1,\ldots,5. \quad \text{(S4c)}$$

Thus every intervention order statistic is lower than the corresponding control order statistic under every admissible reconstruction (Supplementary Fig. 2c,d). This is an empirical first-order stochastic ordering: the intervention empirical cumulative distribution is everywhere at least as large as the control distribution. The comparison pairs corresponding sorted ranks under every admissible reconstruction. It permits overlap of the two empirical supports.

For any common nondecreasing function ϕ, equation (S4c) gives

$$\frac{1}{5}\sum_{k=1}^{5} \phi\left(J''_{1,(k),\pi_1}\right) \le \frac{1}{5}\sum_{k=1}^{5} \phi\left(J''_{0,(k),\pi_0}\right). \quad \text{(S4d)}$$

The inequality is strict for a strictly increasing ϕ. This follows by applying the same monotone function to each ordered-rank inequality and summing. It preserves the direction of the transformed mean comparison, while numerical effect sizes can change.

The enumeration was checked by a separate assignment calculation. For a threshold z, form the binary matrix $B_{ij}(z) = 1\{t_j / [g_i(1+t_j^2)] \le z\}$. The minimum and maximum numbers of responses below z are the minimum and maximum costs of a complete bipartite assignment. The minimum attainable kth order statistic is the first candidate threshold whose maximum assignment count reaches k; its maximum is the first threshold whose minimum count reaches k. Testing the 25 candidate responses reproduces every enumerated rank endpoint. The source files also retain explicit attaining permutations.

Supplementary Table 5 | Smallest control-minus-intervention gap at each ordered rank. Values are kPa^{-1}. Each entry minimizes over all 14,400 pairs of complete rheological reconstructions. All ten gaps are positive.

Design	Rank 1	Rank 2	Rank 3	Rank 4	Rank 5
AGER1	0.033412	0.173649	0.272889	0.244961	0.282104
RAGE	0.455798	0.113964	0.123775	0.098436	0.008632

S4.5 Conservative omission sensitivity

When specimen identity is unresolved, omitting a specified mouse does not identify which entries should be removed from the separate lists. We therefore independently omitted one storage-modulus value and one loss-

tangent value in each arm and enumerated every remaining correspondence. Each arm has $5^2 \times 4! = 600$ four-record rheological configurations, giving 360,000 two-arm comparisons. The mean equal-stress work reduction retains its direction in both mutant intervention experiments throughout this enlarged set (Table 4).

The rank-by-rank ordering in S4.4 is a statement about the complete five-record cohorts. Some conservative four-record deletion configurations permit overlap at a corresponding ordered rank. The surviving omission guarantee is the lower mean stress-controlled loss; the complete-record rank and coupling claims retain their stated populations.

S4.6 A certified reversal under prescribed elastic coupling

The opposite equal-stress and equal-recorded-strain comparisons can be connected by a specified mechanical construction. Append a common, stationary, purely elastic series compliance $c \geq 0$ to each retained response $G^* = g(1 + it)$. In the same stress–strain coordinates, the combined response is $G_c^* = 1/(1/G^* + c)$. Its positive loss modulus is

$$D(c; g, t) = \Im G_c^* = \frac{gt}{1 + 2cg + c^2 g^2 (1 + t^2)}. \quad \text{(S4e)}$$

At common total strain amplitude γ_0, work per cycle and volume is $\pi \gamma_0^2 D(c; g, t)$. The added element dissipates no energy. At $c = 0$, $D = G''$; as $c \to \infty$, $c^2 D \to J''$. Thus the ratio of intervention to control mean work tends to the equal-stress J″ ratio. At fixed total strain both absolute works tend to zero as c^{-2}, so the limit compares response ratios at the prescribed total strain.

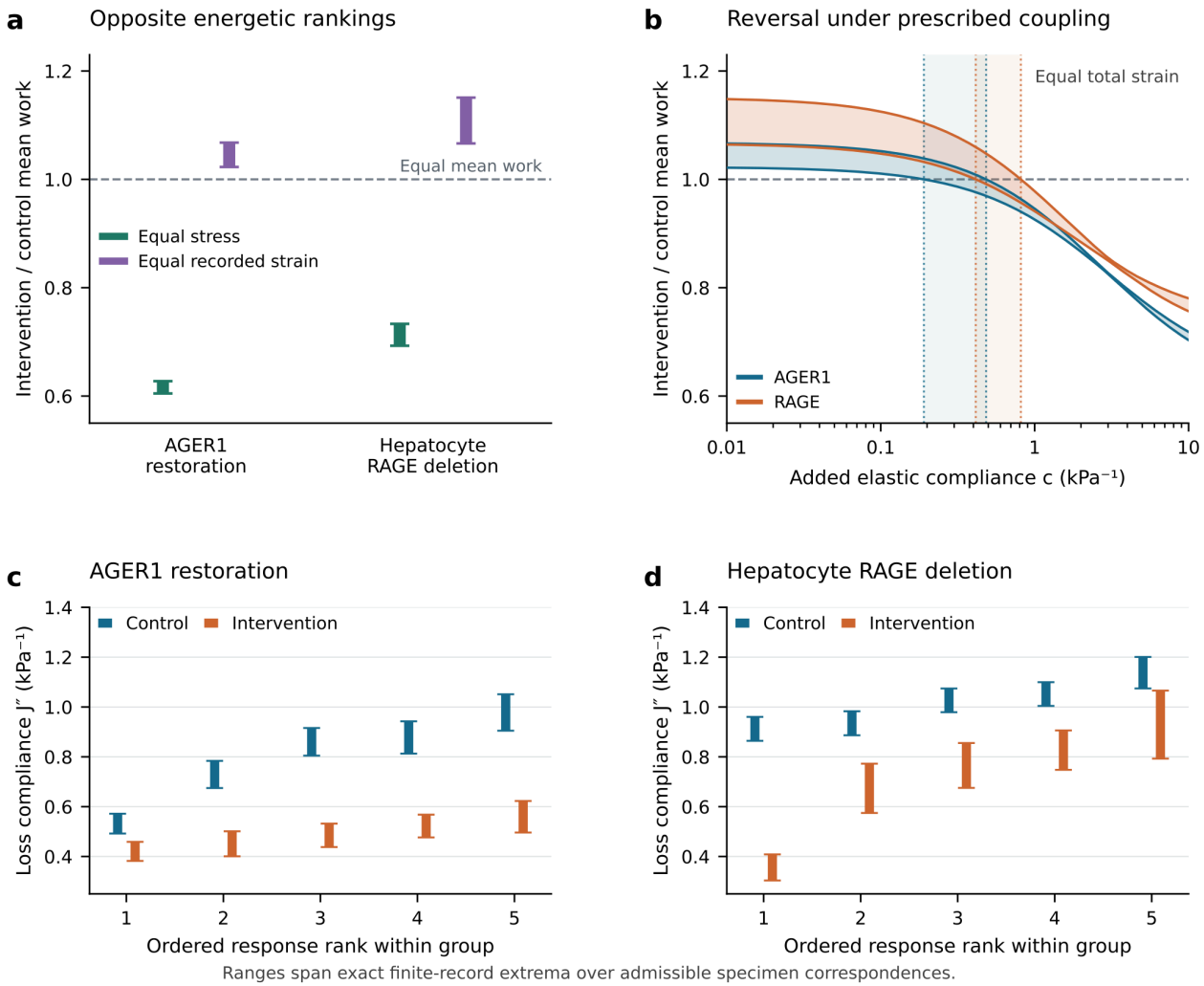
At every prescribed c, the sharp ratio envelope is obtained by applying equation (S4b) to the 120 means of $D(c)$ in each arm. The complete curves are shown in Extended Data Fig. 5. Every one of the 14,400 intervention/control reconstructions in each genetic experiment crosses unity exactly once for positive c. The possible crossing locations span 0.190853–0.483839 kPa^{-1} for AGER1 and 0.414604–0.813464 kPa^{-1} for RAGE. Below the lower endpoint, every comparison has greater intervention work; above the upper endpoint, every comparison has lower intervention work. Inside the interval, missing correspondence can affect the sign.

This global single-crossing statement was certified algebraically. For a fixed correspondence, the five positive denominators in equation (S4e) yield a group rational function with numerator degree eight and denominator degree ten. Subtracting the control from intervention group response and clearing positive denominators gives a degree-18 polynomial. Published decimal inputs were represented as exact rationals and a positive rescaling $x = 300c$ was used only for conditioning. In every one of the 14,400 polynomials per design, the constant coefficient is positive, the leading coefficient is negative and the nonzero coefficient sequence has exactly one sign variation. Descartes' rule therefore permits exactly one positive root, while the endpoint signs ensure it exists. This certificate establishes a unique reversal of the comparison; it does not require monotonicity of the ratio at every c.

Two independent calculations locate the interval endpoints: explicit bisection of all 14,400 reconstruction pairs and root-finding on the lower and upper envelopes. A separate exact-rational evaluation brackets the four extreme roots in [0.000190852683, 0.000190852684], [0.000483839083, 0.000483839084], [0.000414604064, 0.000414604065] and [0.000813464363, 0.000813464364] Pa^{-1}, respectively. These narrow brackets certify numerical localization with the retained decimal records held fixed.

The calculation defines a testable mechanical consequence of the reconstructed responses. Here c is a prescribed appended compliance in the reported response frame. Varying this compliance connects the equal-strain and equal-stress comparisons, with a unique certified crossover for every complete reconstruction.

Supplementary Figure 2 | Complete liver correspondence and ordered-rank envelopes



a, Intervention/control ratios of inferred mean cyclic work in the mutant-β-catenin mouse cohorts of Fan et al. [13]. AGER1 restoration and hepatocyte RAGE deletion give lower work at equal small stress but higher work at equal recorded strain. Each arm contains five storage moduli and five loss tangents, assumed to describe the same five mice; bars span all 120 within-arm matchings and 14,400 two-arm reconstructions. Measurements were acquired at 1 rad s^{-1}. **b,** Predicted work ratios at equal total strain when the same stationary, purely elastic series compliance c is appended to each recorded response. Coloured envelopes span every rheological correspondence; vertical bands mark the possible crossover locations: 0.191-0.484 kPa^{-1} for AGER1 and 0.415-0.813 kPa^{-1} for RAGE. Every complete reconstruction has exactly one positive crossover, certified from the retained decimal records. The appended compliance c is the controlled variable in the prospective crossover experiment. **c,d,** Complete-record loss-compliance ranges at each ordered rank for AGER1 (c) and RAGE (d). Every intervention rank remains below its control counterpart across all matchings; each rank refers to an ordered value within its reconstructed list. Bands span exact correspondence extrema for the retained records. Work is inferred in linear harmonic response under the stated loading condition. Complete-record rank dominance and mean-ordering robustness under independent omissions are reported as separate certificates.

The analysis records (S20) retain the cited source-file identifiers, eight genetic-cohort source tables, all comparison and rank endpoints, attaining assignments for ordering, every crossing location, and the exact polynomial and rational-sign verification code. The original public workbooks remain available through their cited source. Source precision is retained in the machine-readable files.

S5 Evidence classes for loading-conditioned energetic fidelity

Finite records and inference targets

The retained biological analyses (Fig. 2; Supplementary Figs. 2–3 and 5–8) ask which energetic comparisons follow from their response records. Fan supplies exact finite-record correspondence bounds; Kpeglo supplies paired plate-level responses; Joshi supplies published-mean calculations; and Erisken supplies an approximate literature-envelope calculation.[13,14,36,37,38] The tables below identify these evidence classes. Figure 2 and S7 connect the records to individual confirmation and loading compensation. Liver intervals span all admissible correspondences; paired culture responses, published means and approximate published ranges retain their distinct definitions.

For linear complex response $M^{*} = a + ib$, define positive loss compliance as $J'' = b/\left(a^2 + b^2\right)$. Work per cycle per volume at common strain amplitude is $w_\varepsilon = \pi \varepsilon_0^2 b$, whereas common stress amplitude gives $w_\sigma = \pi \sigma_0^2 J''$. For two individual responses A and B, the orientation $R_\varepsilon > 1$, $R_\sigma < 1$ occurs exactly when

$$1 < \frac{b_A}{b_B} < \frac{\left|M_A^{*}\right|^2}{\left|M_B^{*}\right|^2}.$$

These are established linear-response identities. The recovered orderings, admissible-record bounds and measurement-design implications are the results of the present application. For a paired complex response, reciprocal transformation determines loss compliance and thereby the equal-stress work coefficient.

Liver correspondence and coupling

For each five-record arm, $G'' = gt$ and $J'' = t/\left[g\left(1 + t^2\right)\right]$ are evaluated over all $5! = 120$ within-arm assignments, with 14,400 two-arm reconstructions for each intervention/control comparison. AGER1 ratios are 1.0228884279 –1.0678052932 at equal recorded strain and 0.6047790245–0.6274383027 at equal small stress. The corresponding RAGE ratios are 1.0662512260–1.1509009714 and 0.6928123889–0.7332609984. The source angular frequency is 1 rad s^{-1}. Matching envelopes are exact extrema over admissible correspondences with the reported values held fixed and each pair of lists assumed to concern the same five mice.

An added real series compliance c gives the effective loss coefficient

$$D_c = \frac{b}{(1 + ca)^2 + (cb)^2}.$$

At zero added compliance $D_0 = b$, while $c^2 D_c \to J''$ as $c \to \infty$. The work ratio approaches the equal-stress coefficient ratio; actual work at fixed total strain tends to zero. Exact polynomial certificates in the retained historical analysis establish a single positive crossing for each complete reconstruction. The global crossing intervals are 0.1908526836–0.4838390840 kPa^{-1} for AGER1 and 0.4146040646–0.8134643636 kPa^{-1} for RAGE. Independent numerical root-finding reproduces the interval endpoints. The appended compliance is the controlled variable in the prospective crossover experiment.

The complete-record sorted loss-compliance ranks all retain the intervention-below-control ordering. Independent omissions preserve the mean direction, while some omitted configurations permit overlap at a corresponding rank.

PDAC recurrence and plate-level sensitivity

Day-21 ratios of mean plate coefficients from paired summaries are $R_\gamma = 1.9120743535$ and $R_\sigma = 0.1639447123$. Omitting one plate from each arm gives strain ratios 1.1667087993–3.2714579297 and stress ratios 0.1049975444–0.4031133764. Four raw-window/repeat choices yield strain ratios 1.7388493185–2.2568289798 and stress ratios 0.1079765398–0.2081701571. Every retained sensitivity choice preserves the direction. The primary denominator is the untreated PDAC culture condition.

The retained full culture-day series is shown descriptively in Supplementary Fig. 3; culture-day records are separate samples. Each day-21 condition contains three plates. Exact two-sided label-permutation values are 0.30 for the loss-modulus contrast and 0.10 for loss compliance; corresponding one-sided values are 0.15 and 0.05. Omission analyses test dependence on plate composition; time-window and repeat-record choices test processing robustness.

Published summaries and nonlinear averaging

At 10 Hz, the primary-table pancreatic components give ratios of 1.901195789 for equal-strain work and 0.645348702 for reciprocal mean-response equal-stress work. Table 23 retains these inputs, their printed-value rounding sensitivity and the separately identified historical-precision calculation. The figure uses the primary-table comparison.

At 1 Hz the Joshi engineered/native ratios are 1.0281690141 for storage modulus and 2.1395348837 for loss modulus. At 10 Hz the reported mean responses produce a strain coefficient ratio of 1.9011957886 and a reciprocal mean-response stress coefficient ratio of 0.6453487019. The stress coefficient is calculated by reciprocating each published mean complex response. At 1 Hz both coefficients instead exceed unity: the reciprocal mean-response stress ratio is 1.9995705937. Frequency labels must remain attached to each comparison.

In general,

$$\frac{\bar{b}}{\bar{a}^2+\bar{b}^2} \neq \overline{\frac{b_i}{a_i^2+b_i^2}}.$$

The dental literature envelope gives a strain ratio of 30–100 and stress ratio of 0.0030272755–0.505 relative to the fixed approximate native reference. Its extrema quantify the stated rectangular construction from published ranges.

Supplementary Table 6 | Biological input records and evidence classes

The table identifies the source units, calculated targets and response conditions for each evidence class.

System	Retained units	Inference	Scope
Fan AGER1 and RAGE liver	Five mice per arm; two intervention/control designs	Bounds over all storage–loss-tangent assignments	Same-specimen premise; 1 rad s^{-1}; fixed reported values
Kpeglo day-21 PDAC cultures	Three paired plates per condition	Ratios of mean plate coefficients	Linear-response interpretation; 0.5 Hz
Joshi native and engineered pancreas	Published mean responses at 1 and 10 Hz	Mean-response coefficient ratios	Specimen-linked pairs unavailable; stress comparison is linearized
Erisken dental pulp and gels	Approximate source summaries; native sampling at three sites in one donor	Literature-envelope calculation	Fixed approximate native reference and rectangular hydrogel ranges

Sources: Fan et al.; Kpeglo et al. and the accompanying dataset; Joshi et al.; Erisken et al.[13,14,36,37,38]

Supplementary Table 7 | Liver work ratios and prescribed coupling crossovers

Ratios compare intervention with its own control in the mutant-β-catenin cohorts. Bounds admit all 120 assignments per arm and 14,400 cross-arm reconstructions per genetic design. The added real compliance is prescribed at equal total strain. All entries are exact finite-record extrema under the retained-value and same-specimen premises.

Intervention	Equal recorded strain ratio	Equal small stress ratio	Crossover compliance (kPa⁻¹)
AGER1 restoration	1.022888–1.067805	0.604779–0.627438	0.190853–0.483839
Hepatocyte RAGE deletion	1.066251–1.150901	0.692812–0.733261	0.414604–0.813464

Supplementary Table 8 | Primary PDAC comparison and analysis sensitivities

Ratios compare the day-21 TGF-β1 condition with untreated PDAC cultures. Primary calculations transform each paired plate summary before averaging across plates. Raw-window checks transform each paired raw row before within-window and then plate averaging. The nine omissions quantify plate-composition sensitivity, and the four raw-window/repeat choices quantify processing sensitivity.

Analysis choice	Plates per arm	Equal strain ratio	Equal stress ratio
Deposited plate summaries	3	1.912074	0.163945
One plate omitted per arm, all nine choices	2	1.166709–3.271458	0.104998–0.403113
Last 300 raw rows, original control plate 2	3	2.256829	0.112321
Last 300 raw rows, repeat control plate 2	3	1.808051	0.199563
Last 100 raw rows, original control plate 2	3	2.187778	0.107977
Last 100 raw rows, repeat control plate 2	3	1.738849	0.208170

Supplementary Table 9 | Dental comparison from approximate published ranges

The calculation treats approximate literature values as a fixed native reference and rectangular hydrogel envelope enclosing the agarose/alginate summaries. Derived extrema describe this prescribed literature-envelope construction. The source reports a linear-response range, 37 °C, 10% strain and a frequency span labelled 0.1–100 rps, retained without relabelling as Hz.

Quantity	Approximate native reference	Hydrogel envelope	Gel/native ratio
Storage modulus (Pa)	100	1,000–10,000	10–100
Loss modulus (Pa)	10	300–1,000	30–100
Loss compliance (Pa⁻¹)	0.000990099	0.00000299730–0.000500000	0.003027–0.505000

The maximum gel loss compliance is attained at $(G', G'') = (1000, 1000)$ Pa. The minimum occurs at $(10000, 300)$ Pa. The source's three native sampling sites come from one miniature-pig donor. Source: Erisken et al., DOI 10.1016/j.joen.2015.07.005.

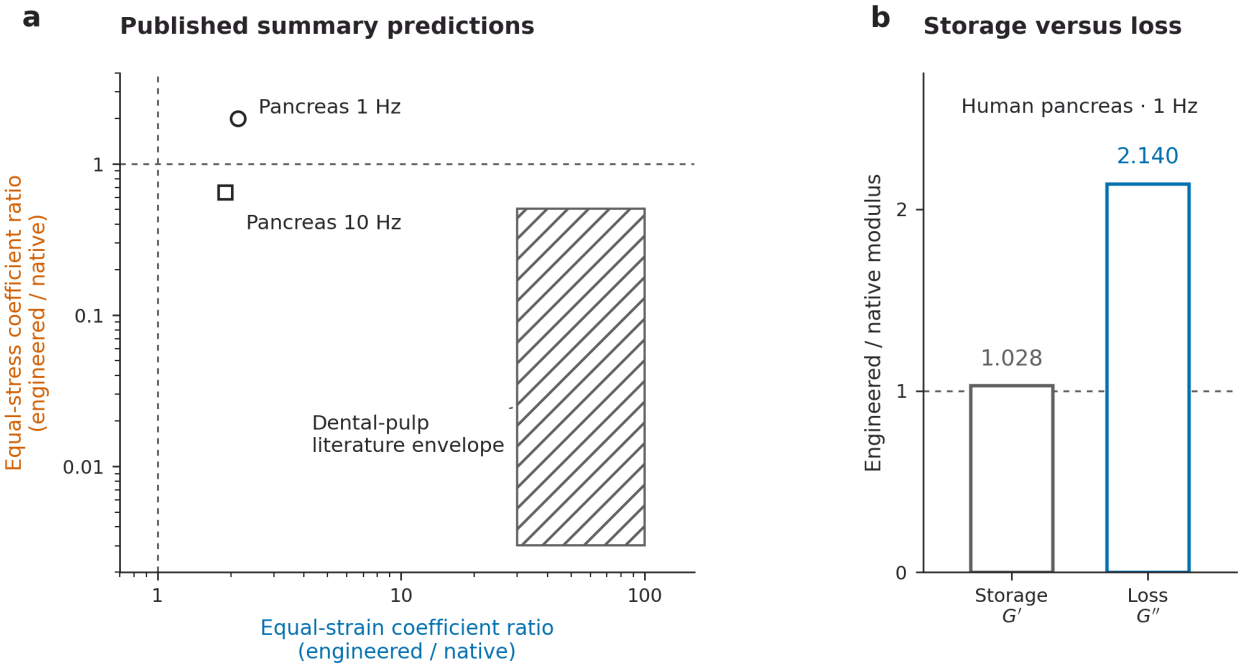
Extended biological evidence index

S7.1 and Tables 12–14 contain the complete human-brain discovery and confirmation families, participant coverage, exclusions and sensitivities. S7.2 and Tables 15–19 retain individual organoid curves, source-model parameters, independent refits, finite-duration work and protocol contrasts. S7.3 and Table 20 preserve both acute-injury severities, both regions and every visit. S7.4 and Tables 21–22 reconstruct all four shunt

frequencies, rounding boxes and crossover regimes. S7.5 and Table 23 retain the comparison directions, loading protocols, independent units and uncertainty classes.[15,16,17,18]

The compensation derivation in S2 supplies the amplitude rule and the two-response crossover equation. The reconstruction-level rational certificates in S4 establish the bounds for the liver averages. Complete selected regional comparisons and protocol sensitivities remain in the source-data families.

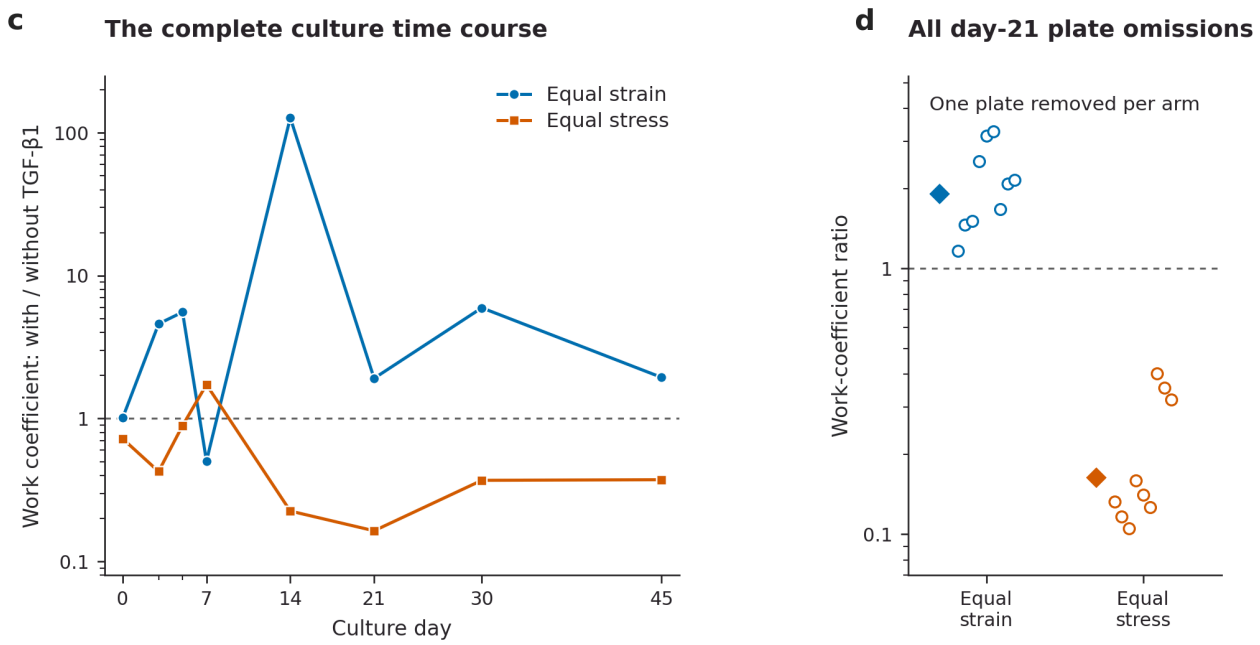
Supplementary Figure 3 | Native–engineered comparisons and the complete pancreatic culture time course



Open symbols and bars: published mean responses. Hatching: approximate literature envelope.
Dashed lines: equal ratios. Loss-modulus bars give the equal-strain work-coefficient ratio.

a, Open symbols show engineered/native pancreatic coefficient ratios calculated from the published mean complex responses at 1 Hz and primary supplied table values at 10 Hz.[37] The equal-strain and reciprocal mean-response equal-stress ratios are 2.140 and 2.000 at 1 Hz, and 1.901 and 0.645 at 10 Hz. The hatched rectangle retains the dental-pulp literature envelope: strain ratios 30–100 and stress ratios 0.003027–0.505, calculated from approximate reference and agarose/alginate ranges.[38] **b,** At 1 Hz, the pancreatic storage-modulus ratio is 1.028 while the loss-modulus ratio is 2.140; similar storage therefore does not ensure matching loss. Dashed unity lines mark equal ratios. Open points and bars are published-summary calculations; the hatched rectangle is a conditional literature envelope. Stress coefficients invert the published mean complex response. S5 and Supplementary Table 9 retain the underlying assumptions and sources.

Supplementary Figure 3 (continued) | Native–engineered comparisons and the complete pancreatic culture time course



c: Eight separate culture-day groups; lines connect summaries. d: Nine deterministic omission pairs. Open circles: omissions; filled diamonds: all three plates per arm. Both panels use 0.5-Hz measurements.

c, All eight recorded culture days compare pancreatic ductal adenocarcinoma cultures with and without TGF-β1, using three plates per condition and day.[14,36] Storage and loss measurements are paired within each plate, and loss compliance is calculated before averaging. Lines connect separate culture-day summaries under the stated linear-response interpretation at 0.5 Hz. **d,** Every day-21 combination obtained by removing one plate from each condition: nine omission pairs. Open circles show omission ratios and filled diamonds retain all three plates per arm. All omissions retain higher equal-strain and lower equal-stress coefficients with TGF-β1; ranges are 1.167–3.271 and 0.105–0.403, respectively. These are deterministic sensitivities of the same plate records. Dashed unity lines mark equal ratios. Supplementary Table 8 retains the omission and raw-window analyses.

S6 Chromosome energetics and recovery

Witt and colleagues' native complex stiffness estimates are the input, rather than values read from a published plot. The paired cohort comprises six polyamine and ten polyethylene-glycol chromosomes. Before, condensation and return membership is reconstructed by agreement with rounded source stiffness and loss-tangent summaries. Maximum relative discrepancy is approximately 4.3×10^{-5}. Frequency lookup against native workspaces identifies the analyzed records as 1 Hz, including the nested records requiring additional checks. The article's general 0.1 Hz description does not replace this record-specific audit. [39,40]

Every native complex estimate is reciprocated before within-chromosome stage averaging. Averaging stiffness and then taking its reciprocal would answer a different nonlinear summary and is not substituted. A negative native loss estimate is retained; all stage means used in the paired comparison are positive. Two condensed-stage estimates are omitted to match the supplied summaries and then restored in sensitivity analysis. Because neither belongs to the before or return stage, the return contrast is unchanged. Supplementary Fig. 4 displays the complete sequence and the native repeat structure.

Supplementary Table 10 | Paired return contrasts at 1 Hz.

Arm	Pairs	Median loss-compliance ratio	Mean change (nm pN⁻¹)	Descriptive 95% bootstrap interval	Median loss-stiffness ratio
Polyamines	6	0.720287	−0.125536	−0.206346 to −0.050781	2.001845
Polyethylene glycol	10	0.539829	−0.241011	−0.387739 to −0.126487	1.820723

All sixteen loss-compliance ratios are below one, whereas fifteen loss-stiffness ratios are above one. The reported percentages are one minus the median paired compliance ratio. Bootstrap resampling uses 20,000 draws of paired chromosomes with archived seed 270101. Initial-condensation intervals span zero in both arms (Supplementary Fig. 4).

The comparison concerns the recorded return window at the audited 1-Hz frequency, with the original calibrated complex response as input. Equal-force and equal-recorded-displacement ratios use loss compliance and loss stiffness, respectively. Under the purely elastic series model, the loss component is invariant to allocation of real compliance. The nominal 50-pN prestress is distinct from the oscillatory force amplitude. Extended Data Fig. 4 displays the normalized work ratios for the two specified small-amplitude loading protocols.

Native estimates and the specimen-level energetic comparison

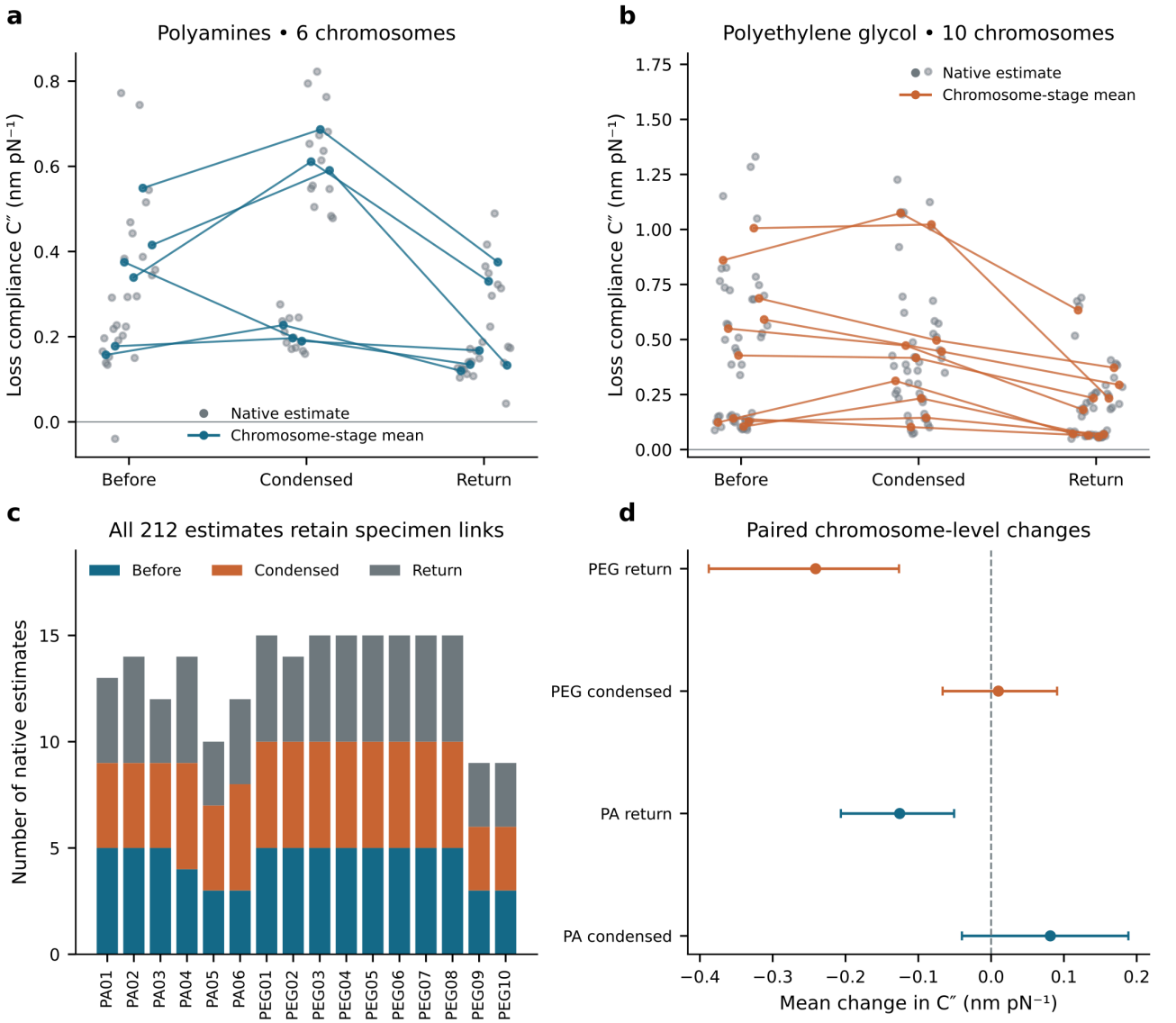
Supplementary Fig. 4 displays the 212 retained native estimates together with all 48 chromosome-stage means. Direct recomputation of each stage mean from the native loss-compliance values reproduces the supplied table to numerical precision (maximum absolute difference 1.2×10^{-16} nm pN⁻¹). The sixteen chromosomes, rather than their repeated estimates, define the paired comparison. The complete before–condensed–return sequence and repeat counts are retained below. At equal small force amplitude, work ratios follow C''; at equal displacement amplitude, they follow K''. All sixteen return/before force-controlled ratios are below one and fifteen displacement-controlled ratios are above one. [39,40]

Supplementary Table 11 | Native repeat counts, stage means and work ratios.

ID	Native counts (B/C/R)	Before C″ (nm pN⁻¹)	Condensed C″ (nm pN⁻¹)	Return C″ (nm pN⁻¹)	Return/before work: equal force	Return/before work: equal displacement
PA01	5/4/4	0.157340	0.227322	0.119759	0.761145	1.720658
PA02	5/4/5	0.177622	0.196598	0.134516	0.757315	1.448531
PA03	5/4/3	0.374885	0.189697	0.167670	0.447257	3.800470
PA04	4/5/5	0.339023	0.610883	0.329991	0.973357	2.392401
PA05	3/4/3	0.548964	0.686465	0.375085	0.683260	1.531578
PA06	3/5/4	0.415201	0.590455	0.132797	0.319837	2.283032
PEG01	5/5/5	0.123521	0.311987	0.070996	0.574771	2.070315
PEG02	5/5/4	0.860201	1.073933	0.633124	0.736019	0.595207
PEG03	5/5/5	0.549402	0.472376	0.180608	0.328737	1.945238
PEG04	5/5/5	0.141437	0.102163	0.064075	0.453030	1.489222
PEG05	5/5/5	0.427441	0.416302	0.233829	0.547044	1.677860
PEG06	5/5/5	0.104827	0.232747	0.058080	0.554053	2.717086
PEG07	5/5/5	0.127933	0.144596	0.068870	0.538332	3.380282
PEG08	5/5/5	1.005732	1.022363	0.232573	0.231247	2.278889
PEG09	3/3/3	0.686811	0.496351	0.371789	0.541326	1.059420
PEG10	3/3/3	0.590676	0.445441	0.293931	0.497619	1.696207

B, C and R denote before, condensed and return stages. Counts refer to the selected 1-Hz native records. PA and PEG denote polyamine and polyethylene-glycol protocols. Stage means use the native reciprocal-first calculation described above; the work ratios compare specified loading conditions at the same frequency.

Supplementary Figure 4 | Native chromosome measurements retain the complete paired stage structure



a,b, All 212 retained native loss-compliance estimates (grey points) and their 48 chromosome-stage means (coloured points and lines) for six polyamine-treated chromosomes (a) and ten polyethylene-glycol-treated chromosomes (b). Lines follow each chromosome from before condensation through the condensed state to buffer return. Horizontal offsets separate chromosomes for display. Each native complex stiffness estimate is reciprocated before stage averaging; all selected measurements are at 1 Hz. **c,** The number of native estimates in each chromosome and stage. These estimates are nested within the sixteen chromosomes. **d,** Mean paired changes in loss compliance from the initial state, with descriptive 95% percentile intervals from 20,000 bootstrap resamples of chromosomes within each arm. Both condensed and return contrasts are displayed. The force-controlled work comparison uses the loss-compliance component and retains a lower return-stage mean for every chromosome. The specimen-level repeat counts and force- and displacement-controlled ratios are supplied in Supplementary Information section S6. [39,40]

S7 Biological confirmation and compensation

This section gives the independent evidence units and uncertainty definitions behind the biological comparisons. The numbered tables summarize the principal values; the underlying machine-readable tables retain complete rows, source cells, contrast families and sensitivities. Supplementary Figs. 5–8 integrate participant confirmation, organoid responses, complete injury trajectories and clinical shunt calculations.

S7.1 Human brain confirmation

The source cohort contains 134 healthy participants. Study E supplies 66 discovery participants; 68 participants in studies A–D were reserved for confirmation, of whom 60 met the primary white-matter/putamen eligibility criteria. The 17 eligible participants at the two external acquisition institutions are included in those 60. Table 12 retains the participant eligibility and exclusion record.[15]

Supplementary Table 12 | Human participant flow

Study	Role	Source n	Eligible n	Excluded n	External
E	Discovery	66	66	0	No
A	Confirmation	12	11	1	Yes
B	Confirmation	19	12	7	No
C	Confirmation	6	6	0	Yes
D	Confirmation	31	31	0	No

The external participants are nested within confirmation. Complete participant coverage, demographic and exclusion records are retained in the analysis records (S20).

Voxelwise nonlinear transformation preceded regional summarization. For white matter divided by putamen at 50 Hz, confirmation gave an equal-strain ratio of 0.854913 and an equal-stress ratio of 1.354732, with opposite ordering in 59/60 participants. Table 13 reports geometric-mean ratios and 95% log-scale t intervals for the discovery, confirmation and nested external subsets; study-wise and participant-level results are displayed in Supplementary Fig. 5. The external subset is not added to the confirmation denominator.

Supplementary Table 13 | Human regional work coefficients

Subset	n	Opposite	Strain ratio [95% CI]	Stress ratio [95% CI]
Discovery E	66	58/66	0.849 [0.820, 0.880]	1.532 [1.477, 1.590]
Confirmation A-D	60	59/60	0.855 [0.838, 0.872]	1.355 [1.318, 1.393]
External sites A+C	17	17/17	0.850 [0.821, 0.880]	1.366 [1.299, 1.436]

White matter/putamen at 50 Hz. Ratios are geometric means of paired participant ratios.

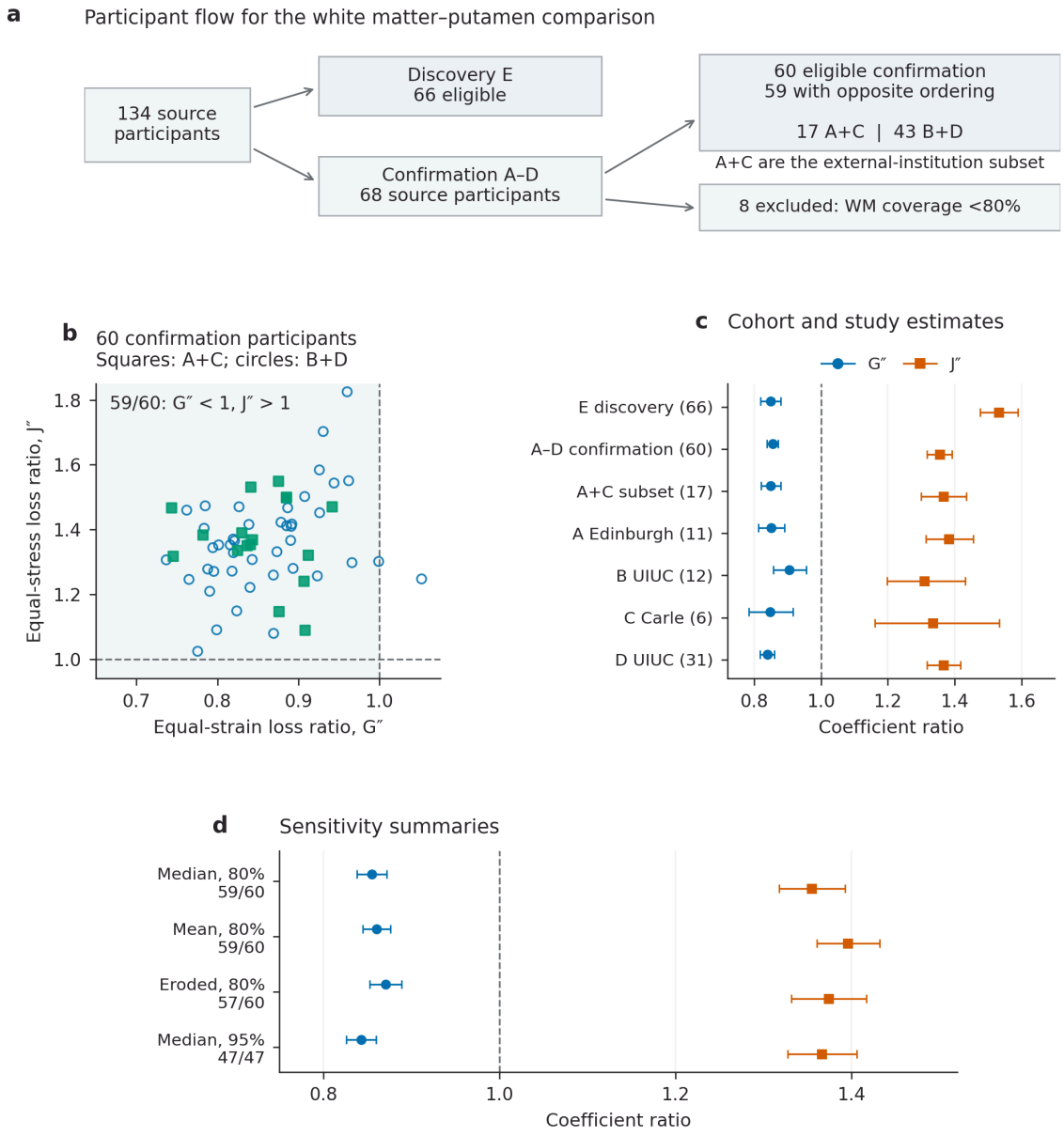
The complete discovery family contained 21 planned pairs. Five discovery-selected contrasts entered the declared confirmation family. White matter/putamen was the one pair satisfying all confirmation criteria; the remaining outcomes are retained in Table 14. Regional means preserved 59/60 opposite orderings, erosion retained 57/60, and stricter coverage retained 47/47. The full family is retained independently of which contrast appears in the main figure.

Supplementary Table 14 | Complete selected confirmation family

Regional pair	n	Strain ratio	Stress ratio	Holm P	Confirmed
White matter / Putamen	60	0.855	1.355	4.16e-22	Yes
White matter / Pallidum	60	0.918	1.439	1.47e-07	No
Thalamus / Putamen	68	0.767	1.055	0.066	No
Putamen / Hippocampus	68	1.592	1.043	0.368	No
Pallidum / Hippocampus	68	1.482	0.991	0.777	No

Confirmation requires the retained direction, both practical thresholds and adjusted statistical criterion. The analysis records (S20) retain results for all planned discovery pairs, untestable outcomes, sensitivities and exploratory sex contrasts.

Supplementary Figure 5 | Human-brain confirmation, complete participants and sensitivity



a, Participant flow for the 50-Hz healthy-brain comparison.[15] Eight white-matter coverage exclusions leave 66 discovery and 60 confirmation participants; the 17 external-institution participants are nested within confirmation. **b,** All 60 confirmation coefficient pairs, including the one participant without the joint ordering. **c,** Discovery, confirmation, nested external-site and individual-study geometric-mean ratios. **d,** Primary medians and the declared mean, erosion and coverage sensitivities, with joint-order counts. Ratios compare white matter with putamen. Within-person ratios use regional summaries of voxelwise transformed coefficients; people are the independent units. Error bars in c,d are 95% Student t intervals on mean log ratios, exponentiated. The complete five-pair discovery-selected confirmation family is reported in Supplementary Table 14; only white matter versus putamen satisfies every family confirmation criterion. These healthy regional coefficients specify loading-dependent calculated work.

Stored map intensity and the stated stiffness unit have a documented scale discrepancy. A common scale factor cancels in the dimensionless ratios, but absolute work densities require a resolved calibration. Regional medians of G″ and J″ are separate targets; they are not recombined into an invented individual modulus for a finite-source crossover. The observation is a regional comparison in healthy adults, not an injury or disease endpoint.

S7.2 Organoid intervention

The source model describes 18 individual aspiration responses in four groups. Tables 15–17 report individual parameters, group contrasts and an inventory of the underlying sensitivity records; Supplementary Fig. 6 shows individual traces, refits and sensitivity results. The primary treated-mutant versus untreated-mutant comparison uses independent groups of four and five organoids, respectively.[17] The mutant comparison uses a single clone; donor and differentiation-batch replication are not established by the released identifiers.

Supplementary Table 15 | Individual organoid parameters

Organoid	Source row	Source k_0	Source $k\infty$	Source τ (s)	Refit τ (s)
WT_Org1	21	1055.4	869.4	3.241	3.215
WT_Org2	22	1186.7	999.5	2.471	2.468
WT_Org3	23	960.3	842.6	2.596	2.593
WT_Org4	24	1000.8	861.9	2.762	2.761
LIS1_Org1	21	1872.7	1675.3	4.320	4.647
LIS1_Org2	22	1130.7	988.9	2.882	2.891
LIS1_Org3	23	1363.3	1086.6	4.248	4.267
LIS1_Org4	24	1613.9	1454.5	3.955	4.080
LIS1_Org5	25	1308.4	1193.0	1.580	1.793
WT_MMP9_Org1	21	793.6	726.0	2.940	2.938
WT_MMP9_Org2	22	672.2	594.6	2.709	2.712
WT_MMP9_Org3	23	882.3	801.9	2.827	2.752
WT_MMP9_Org4	24	1065.3	913.3	3.269	3.284
WT_MMP9_Org5	25	1140.5	862.2	3.175	3.171
LIS1_MMP9_Org1	21	785.1	626.4	3.455	3.649
LIS1_MMP9_Org2	22	757.5	562.2	2.995	2.996
LIS1_MMP9_Org3	23	858.1	711.9	2.719	2.710
LIS1_MMP9_Org4	24	716.2	546.8	3.076	3.076

The source stiffness normalization is retained and has unresolved absolute calibration. The source workbook is identified by the cited study; the analysis records (S20) retain complete fitted parameters, traces and direct power checks. Source row refers to the Fig. 3b parameter block.

For the maintained five-second stress step, the source-model coefficient ratio is 3.821095 (95% bootstrap interval, 2.429462–5.842594), giving an equal-work amplitude factor of 0.511571 (0.413711–0.641571). The exact two-sided permutation P value is 0.015873; Holm adjustment across the three declared primary stress-step contrasts gives 0.047619. The strain-step ratio is 1.004997 (0.762024–1.296903). Its near-unity estimate does not establish equivalence.

Supplementary Table 16 | Five-second organoid contrasts

Comparison	Step	Coefficient ratio [95% CI]	Amplitude factor	Exact P
LIS1 / WT	Stress	0.550 [0.382, 0.818]	1.348	0.0714
LIS1_MMP9 / LIS1	Stress	3.821 [2.429, 5.843]	0.512	0.0159
LIS1_MMP9 / WT	Stress	2.102 [1.584, 2.723]	0.690	0.0286
LIS1_MMP9 / LIS1	Strain	1.005 [0.762, 1.297]	0.998	0.984

MMP9 denotes treatment. Bootstrap intervals use organoids as sampling units. The primary stress contrast has exact P = 0.015873 and Holm-adjusted P = 0.047619.

Independent refitting gives a stress-step ratio of 3.736528, which supports the direction and scale of the loading divergence while remaining a distinct estimate. Numerical integration of dashpot power agrees with the source-model closed forms. Duration analysis keeps the finite-time protocol explicit, and leave-one-organoid-out comparisons disclose influence. The retained normalization audit records the unresolved common scale discrepancy rather than correcting it by assumption.

Supplementary Table 17 | Organoid sensitivity and normalization records

Underlying analysis records	Rows	Fields per row
Duration sensitivity	48	5
Single-organoid omissions	70	5
Within-workbook duplicate checks	9	5
Source-normalization checks	18	4
Site-level blebbistatin summary	32	8

Table 17 summarizes the underlying sensitivity records. Duration, leave-one-out, duplicate and source-scale outputs retain their original analysis choices. The numerical columns retain source and refitted estimates separately.

Supplementary Fig. 6 connects the source-model coefficients, independent fit checks and equal-work stress factor. The compensation setting compares the treated and untreated mutant groups under a maintained five-second stress step; a biological outcome under that adjusted loading was not measured.

The intervention-associated stiffness ratios are 0.541645 for k_0 and 0.484522 for $k\infty$, corresponding to reductions of 45.84% and 51.55% in geometric-mean fitted stiffness. Using rounded individual parameters, the stress-step coefficient ratio factorizes as 3.728299 for the compliance increment times 1.024837 for the finite-duration factor, giving 3.820900. The amplification is therefore dominated by the compliance contribution. The joint stress-versus-strain treatment-effect contrast is 3.801933, with an exhaustive paired-endpoint bootstrap interval of 2.674184–5.462924. Every treated-mutant stress coefficient exceeds every untreated-mutant coefficient, and all single-organoid omissions retain stress ratios between 3.418411 and 4.491812. Relative to untreated control organoids, the untreated-mutant and treated-mutant stress-coefficient point estimates are 0.550268 and 2.102520, respectively. The control-referenced and treatment-referenced comparisons use different denominators; the 48.8% compensation result uses untreated mutants as its reference. Supplementary Tables 18–19 record the protocol contrast and derived consequences. The joint contrast, stiffness changes and complete omission set are displayed in Supplementary Fig. 6.

Supplementary Table 18 | Organoid loading-protocol contrast

Quantity	Ratio	95% interval	Input and interval
Stress-step treatment ratio	3.821095	2.429462 to 5.842594	Primary parameters; 50,000 resamples
Strain-step treatment ratio	1.004997	0.762024 to 1.296903	Primary parameters; 50,000 resamples
Stress-step calculation (rounded parameters)	3.820900	2.417216 to 5.850713	Rounded parameters; exhaustive resampling
Strain-step calculation (rounded parameters)	1.004989	0.762670 to 1.295866	Rounded parameters; exhaustive resampling
Joint stress/strain treatment-effect contrast	3.801933	2.674184 to 5.462924	Rounded parameters; exhaustive resampling

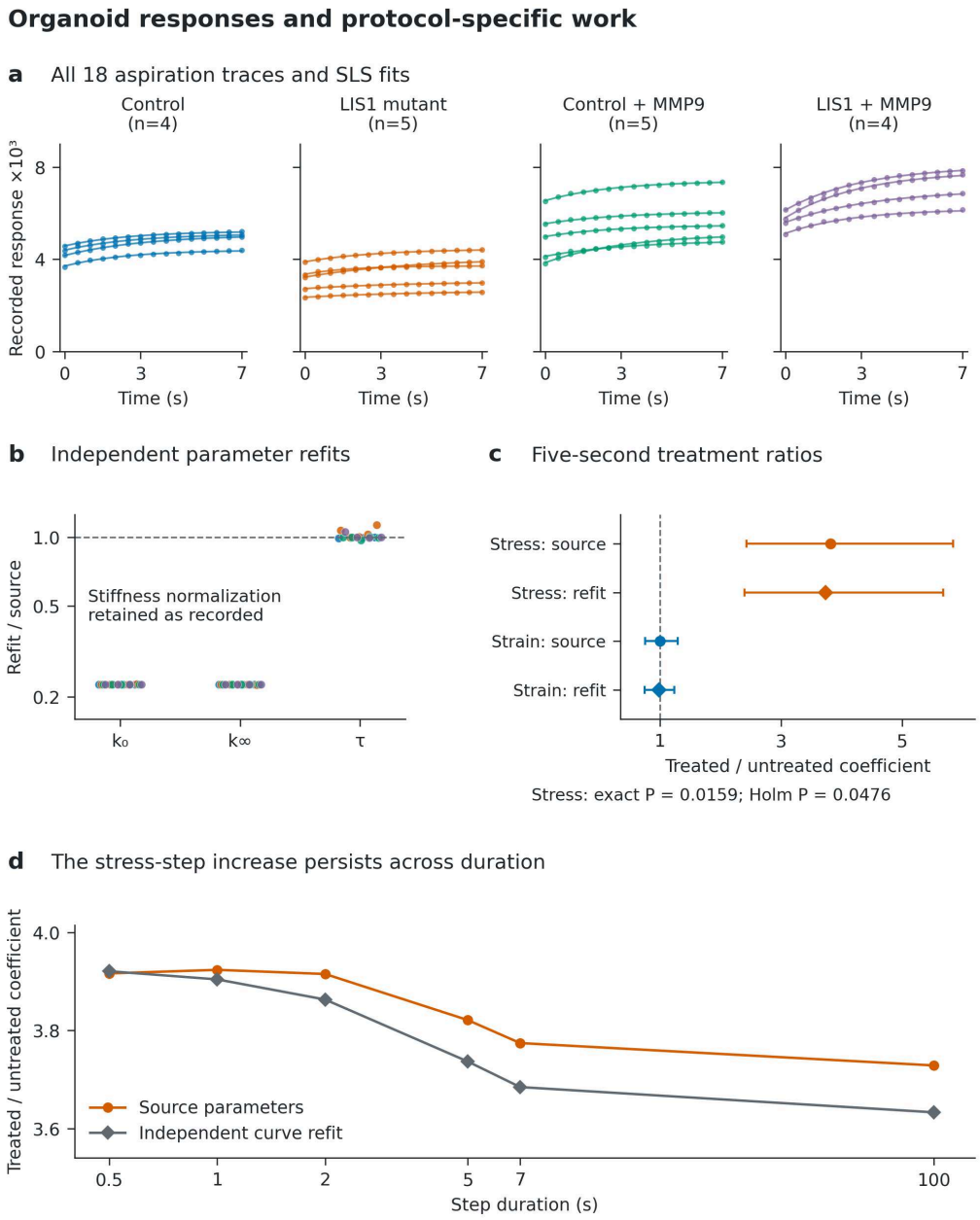
Primary intervals use 50,000 within-group resamples. Supporting intervals enumerate all 800,000 ordered bootstrap pairs from the rounded parameters; the joint contrast retains both endpoints together within each organoid. Treatment compares four MMP9-treated with five untreated LIS1-mutant organoids. The primary exact permutation P is 0.015873 and Holm-adjusted P is 0.047619, within the untreated-LIS1/untreated-control, treated-LIS1/untreated-LIS1 and treated-LIS1/untreated-control family. Full precision and all family rows remain in the numerical record.[17]

Supplementary Table 19 | Organoid mechanical consequences

Quantity	Value	Reference and definition
Instantaneous stiffness ratio	0.541645	Treated / untreated LIS1; Ratio of per-organoid geometric means
Equilibrium stiffness ratio	0.484522	Treated / untreated LIS1; Ratio of per-organoid geometric means
Compliance-increment contribution	3.728299	Treated / untreated LIS1; Ratio of geometric means of ΔJ
Finite-duration contribution	1.024837	Treated / untreated LIS1; Ratio of geometric means of 1-exp(-2T/τ)
Equal-work stress factor	0.511571	Treated / untreated LIS1; 1/sqrt(primary coefficient ratio)
Equal-work stress reduction (%)	48.842883	Treated / untreated LIS1; 100*(1-factor)
Control-referenced factor	0.689652	Treated LIS1 / untreated WT; 1/sqrt(control-referenced ratio)
Lowest leave-one-out stress ratio	3.418411	Treated / untreated LIS1; Minimum across nine omissions
Highest leave-one-out stress ratio	4.491812	Treated / untreated LIS1; Maximum across nine omissions

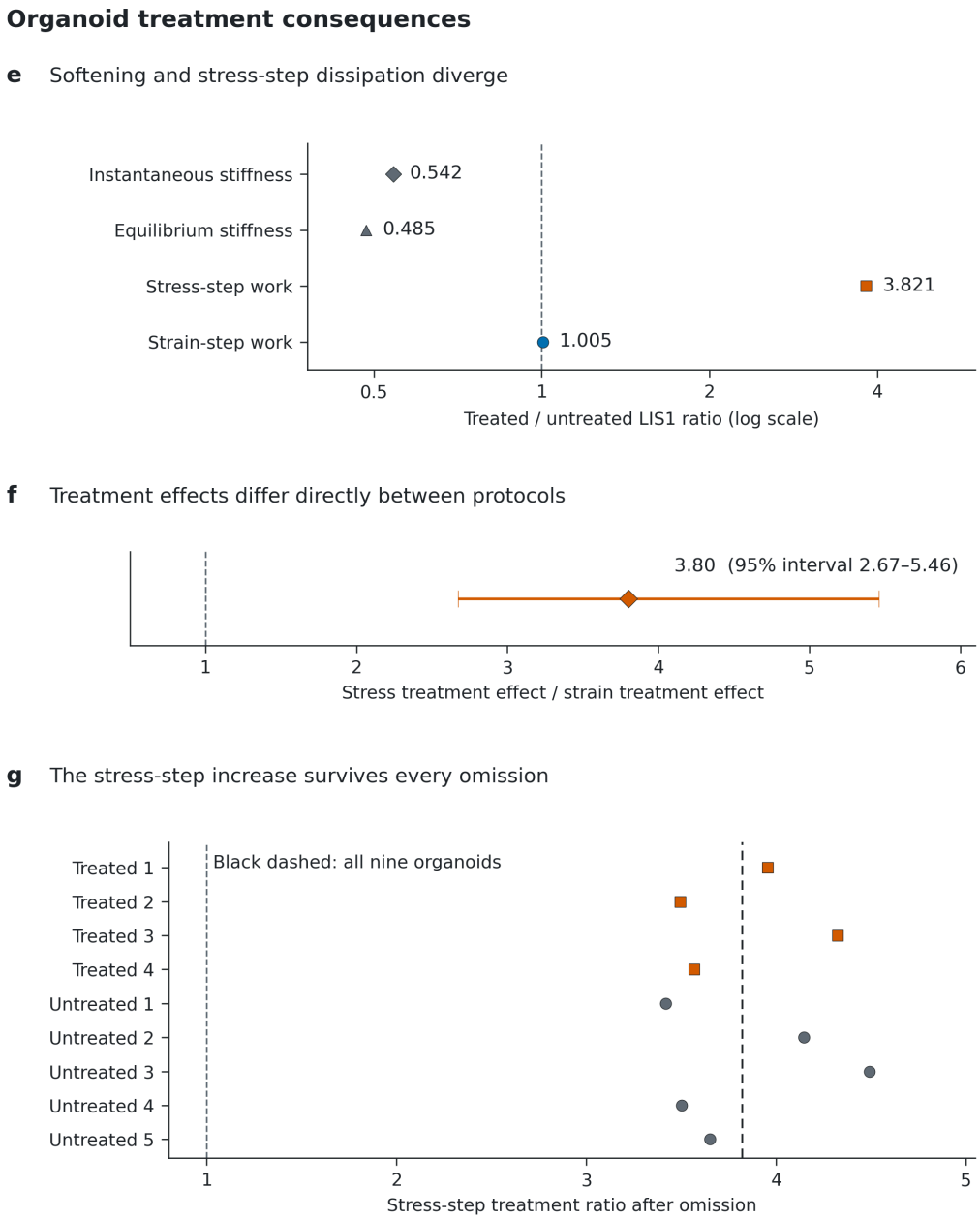
The 48.84% reduction uses untreated mutants as its reference. The control-referenced factor uses untreated controls as its denominator. Stiffness, decomposition, omission and control-referenced estimates use rounded parameters; the treated/untreated-mutant equal-work factor transforms the full-precision primary work ratio.[17]

Supplementary Figure 6 | Protocol-specific energetic consequences of organoid matrix treatment



a, All 18 recorded aspiration traces (points) and standard-linear-solid fits (lines): four control, five LIS1-mutant, five MMP9-treated control and four MMP9-treated mutant organoids [17]. **b,** Independent curve-refit parameters divided by source parameters. The common stiffness-normalization discrepancy is retained without an assumed scale correction. **c,** Five-second treated/untreated mutant coefficient ratios from source parameters and independent refits. Bars are 95% within-group organoid bootstrap intervals (50,000 resamples). The source stress-step ratio is 3.821 (2.429–5.843); its exact two-sided permutation P is 0.0159 and Holm P is 0.0476 across the three primary stress contrasts. The strain-step ratio is 1.005 (0.762–1.297; P = 0.9841). **d,** The complete stored duration grid for both parameter bases. Panels c–d compare four treated with five untreated mutant organoids; the source/refit and duration checks reuse these same units. Coefficients describe normalized protocol-specific dissipation before unloading. Source data and calculation details are in Supplementary Tables 15–17.

Supplementary Figure 6 (continued) | Protocol-specific energetic consequences of organoid matrix treatment



e, Treated/untreated LIS1-mutant geometric-mean ratios for instantaneous and equilibrium stiffness and five-second stress- and strain-step work coefficients [17]. **f,** Direct ratio of the stress-step treatment effect to the strain-step treatment effect, 3.80 (95% interval 2.67–5.46). The joint bootstrap retains both protocol endpoints within each organoid and exhaustively enumerates 800,000 ordered within-group resample pairs. **g,** Every single-organoid omission from the four treated and five untreated mutant organoids; stress-step ratios remain 3.42–4.49. The black dashed line uses all nine organoids. Panels e–g use the preserved rounded-parameter supporting calculation, whose stress-step ratio (3.8209) remains distinct from the retained primary estimate (3.8211) in panel c. The source normalization is preserved. These calculations reuse the same specimens. Source data and resampling definitions are in Supplementary Tables 18–19.

S7.3 Acute injury trajectories

Table 20 retains both impact severities, both regions and all five source time points at 877.5 Hz. Immediately after injury, impact-region strain-coefficient ratios are 0.800000 and 0.739130, while stress-coefficient ratios are 1.386900 and 1.427718. The equal-work stress factors are 0.849136 and 0.836910. All later trajectories and comparison-region responses remain available, rather than presenting the immediate contrasts alone.[16]

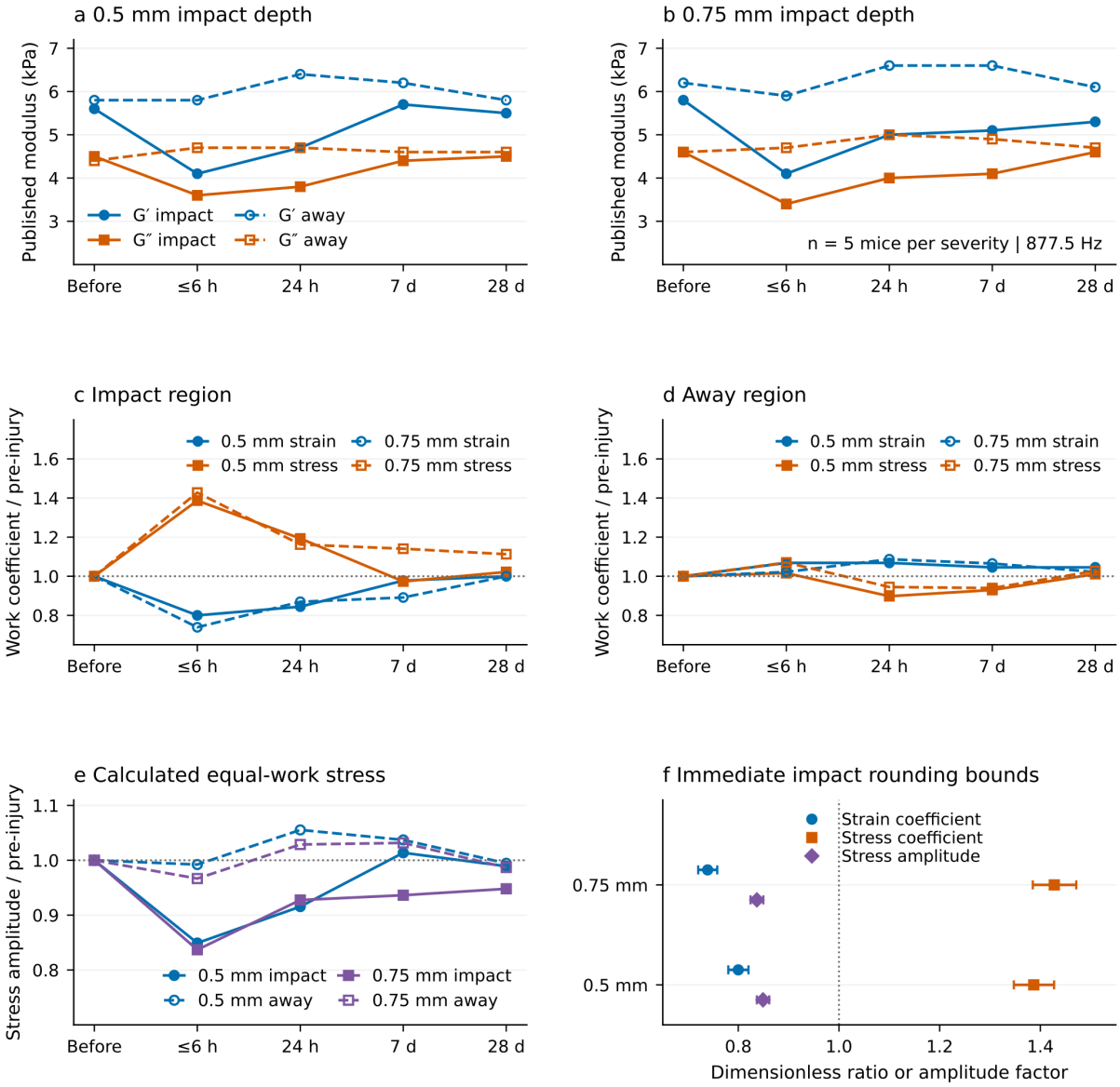
Supplementary Table 20 | Complete injury trajectories

Impact depth	Region	Visit	Strain ratio	Stress ratio	Stress factor
0.5mm	impact	Before	1.000	1.000	1.000
0.5mm	impact	<6 h	0.800	1.387	0.849
0.5mm	impact	24h	0.844	1.193	0.916
0.5mm	impact	7d	0.978	0.973	1.014
0.5mm	impact	28d	1.000	1.022	0.989
0.5mm	away	Before	1.000	1.000	1.000
0.5mm	away	<6 h	1.068	1.016	0.992
0.5mm	away	24h	1.068	0.898	1.055
0.5mm	away	7d	1.045	0.930	1.037
0.5mm	away	28d	1.045	1.011	0.994
0.75mm	impact	Before	1.000	1.000	1.000
0.75mm	impact	<6 h	0.739	1.428	0.837
0.75mm	impact	24h	0.870	1.162	0.928
0.75mm	impact	7d	0.891	1.141	0.936
0.75mm	impact	28d	1.000	1.113	0.948
0.75mm	away	Before	1.000	1.000	1.000
0.75mm	away	<6 h	1.022	1.070	0.967
0.75mm	away	24h	1.087	0.945	1.029
0.75mm	away	7d	1.065	0.940	1.032
0.75mm	away	28d	1.022	1.027	0.987

All rows use 877.5 Hz and n = 5 animals per severity. These are transforms of group means relative to each severity/region baseline. Primary components and reported variability are given in the cited source; the analysis records (S20) retain complete derived values and immediate-impact rounding calculations.

Each coefficient is transformed from the corresponding published group means. The source reports five animals per severity. Rounding sensitivity is retained for the immediate-impact comparisons covered by the archived check; it is not presented as a newly computed confidence band for every time point. Reported source variability, printed-value rounding and uncertainty in a mean nonlinear transform have different meanings. Supplementary Fig. 7 preserves that distinction.

Supplementary Figure 7 | Acute injury trajectories retain the loading distinction



All 20 published group-mean responses are retained. Lines follow the ordered visits; time spacing is categorical.
Panel f shows source-rounding bounds (±0.05 kPa), not sampling confidence intervals; only immediate impact was bounded.

a,b, Published mean storage and loss moduli in impact and away regions for each controlled cortical impact severity.[16] **c,d,** Equal-strain and equal-stress work-coefficient ratios relative to the corresponding pre-injury response, retaining every reported visit. **e,** Calculated equal-work stress-amplitude factors for both severities and regions. **f,** Immediate impact coefficients and stress factors with exact bounds implied by independent rounding of G′ and G″ (±0.05 kPa). The source measured five mice per severity at 877.5 Hz. All 20 published complex responses are retained; visits and regions are not independent groups. J″ is calculated from each published mean complex response. Bounds are source-rounding ranges, not sampling confidence intervals. Lines connect ordered visits with categorical time spacing.

S7.4 Clinical shunt records

The primary shunt table supplies pre/post cohort-mean storage and loss components for 20 patients, comprising 14 with primary and six with secondary normal-pressure hydrocephalus. Their same-frequency transforms give stress-conditioned coefficient ratios above one at all four sampled frequencies. Consequently, the calculated

post/pre stress-amplitude factors needed to preserve harmonic work are below one. Table 21 retains the original components and four targets, together with source-rounding ranges.[18]

Supplementary Table 21 | Four shunt compensation targets

Hz	Pre G* (kPa)	Post G* (kPa)	Stress ratio	Stress factor [rounding]
25	1.29 + 0.51i	1.36 + 0.63i	1.058	0.972 [0.960, 0.984]
37.5	1.64 + 0.63i	1.55 + 0.68i	1.163	0.927 [0.917, 0.937]
50	1.72 + 0.80i	1.64 + 0.80i	1.081	0.962 [0.954, 0.970]
62.5	2.18 + 1.02i	2.01 + 0.96i	1.099	0.954 [0.947, 0.961]

n = 20 patients; published group means. $G^* = G' + iG''$. Ranges propagate independent ±0.005-kPa rounding of the four input components. The calculations use the published cohort-mean mechanics and do not imply patient-level work values.

Finite-source comparisons hold fixed the total shear-strain amplitude across tissue and a common elastic series support, with support compliance c normalized to the tissue geometry (S2).

At 62.5 Hz, the post-shunt loss modulus decreases while loss compliance increases. The arbitrary-response finite-source equation gives c* = 0.271502 kPa^{-1}, with a deterministic rounding range of 0.193545–0.379326 kPa^{-1}. At 50 Hz the printed loss moduli tie at $c = 0$; component rounding permits a nonnegative crossover up to 0.104420 kPa^{-1}, above which post-shunt work is larger throughout the rounding box. The 25- and 37.5-Hz central responses do not show the same opposite limiting order. Table 22 and Supplementary Fig. 8 retain these frequency-specific regimes.

Supplementary Table 22 | Finite-source crossover regimes

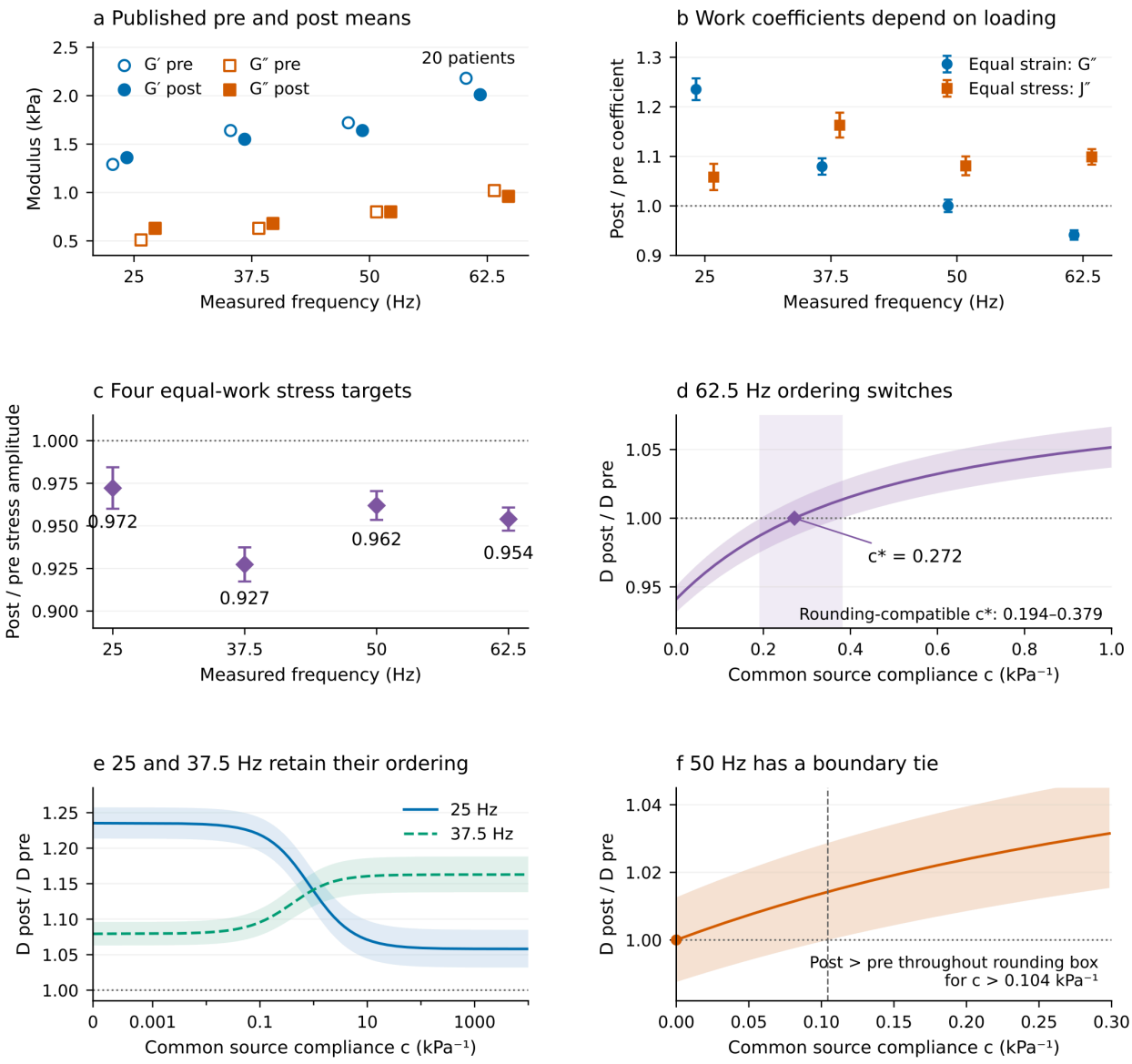
Hz	Central c* (kPa^{-1})	Source rounding range or regime
25	No positive root	No nonnegative root in rounding box
37.5	No positive root	No nonnegative root in rounding box
50	Boundary tie at 0	Possible 0 to 0.104420
62.5	0.271502	0.193545–0.379326

The analysis records (S20) retain complete roots and polynomial coefficients, including inadmissible roots and residuals. Rounding ranges are deterministic. They are not patient-level confidence intervals.

The reconstructed loss-compliance ratios exceed one at all four frequencies, and every equal-work factor remains below one throughout the continuous source-rounding box. At 62.5 Hz the central finite-source equality has exactly one positive root, c = 0.271502 kPa^{-1}, with the source-rounding range 0.193545–0.379326 kPa^{-1}. At 25 and 37.5 Hz the post-shunt coefficient exceeds the pre-shunt coefficient for all nonnegative c across the rounding box. At 50 Hz the printed means tie at c = 0; the rounding box admits a nonnegative crossover up to 0.104420 kPa^{-1}, above which post-shunt work is greater for all admitted inputs. The separate pressure-pulsatility reports establish the clinical response association and reduction after shunting described in the main text. [41,42]

Separate clinical reports establish that intracranial pulsatility is associated with shunt response and decreases after shunting. Among 45 shunted patients, 12-month response occurred in 34 of 37 with elevated overnight mean pulse amplitude (at least 4 mmHg) and one of eight below that threshold. [41] In a separate 13-patient pre/post study, shunting reduced pulse amplitude, with next-day normalization in nine patients; valve-pressure adjustment also modified pulsatility in the two patients examined during adjustment. [42] Together, these findings corroborate the clinical relevance and intervention responsiveness of pulsatile loading. The pressure-pulsatility reports concern cardiac-beat loading. The work factors remain transformations of the frequency-matched MRE cohort means, with four discrete measurement conditions.

Supplementary Figure 8 | Clinical shunt work compensation and coupling-dependent energetic ordering



Bars and shading show printed-mean rounding (±0.005 kPa), not patient sampling confidence. Curves in d–f are model calculations. The four measured frequencies are discrete. $D = G''/|1 + cG^*|^2$ describes fixed remote deformation through a common elastic source.

a, Published pre- and post-shunt mean storage and loss components.[18] **b,** Work-coefficient ratios under prescribed strain and stress. **c,** Calculated equal-work stress-amplitude factors at four discrete measured frequencies. **d,** At 62.5 Hz, the post/pre finite-source coefficient ratio crosses one at c = 0.271502 kPa^{-1}, with a source-rounding range of 0.193545–0.379326 kPa^{-1}. **e,** At 25 and 37.5 Hz, the post-shunt coefficient remains larger for all common real nonnegative compliance. **f,** At 50 Hz, the displayed means tie at c = 0; post > pre is guaranteed throughout the rounding box for c > 0.104420 kPa^{-1}. The finite-source comparisons in d–f fix total shear-strain amplitude across tissue and a common elastic series support; c is the support compliance normalized to tissue geometry. The four-frequency reconstruction from cohort-mean mechanics defines the equal-work loading factors and the finite-source ordering regimes. Bars and envelopes propagate printed-input precision; each frequency retains the same 20-patient cohort.

S7.5 Cross-system evidence

Table 23 retains the complete 20-row synthesis, including canonical comparisons, nested cohorts, historical precision and sensitivity variants. The main comparisons connect incomplete-record discovery, recurrence, individual confirmation and compensation applications. Each row retains loading protocol, frequency or duration, reference/target direction, independent unit and uncertainty class. Harmonic and step coefficients share the quadratic amplitude relation but retain different physical definitions.[14]

Supplementary Table 23 | Complete cross-system coefficient synthesis

Row	System	Strain ratio	Stress ratio	Stress factor
CS-01	Human brain MRE	0.849442	1.532317	0.807841
CS-02	Human brain MRE	0.854913	1.354732	0.859159
CS-03	Human brain MRE	0.849641	1.365891	0.855642
CS-04	Acute mouse TBI	0.800000	1.386900	0.849136
CS-05	Acute mouse TBI	0.739130	1.427718	0.836910
CS-06	LIS1 cortical organoids	1.004997	3.821095	0.511571
CS-07	Hydrocephalus shunt	1.235294	1.058069	0.972172
CS-08	Hydrocephalus shunt	1.079365	1.162854	0.927337
CS-09	Hydrocephalus shunt	1.000000	1.080730	0.961925
CS-10	Hydrocephalus shunt	0.941176	1.098826	0.953972
CS-11	Fan liver	1.022888-1.067805	0.604779-0.627438	1.262451-1.285884
CS-12	Fan liver	1.066251-1.150901	0.692812-0.733261	1.167806-1.201413
CS-13	Kpeglo PDAC	1.912074	0.163945	2.469740
CS-14	Kpeglo PDAC	1.166709-3.271458	0.104998-0.403113	1.575021-3.086103
CS-15	Kpeglo PDAC	1.738849-2.256829	0.107977-0.208170	2.191749-3.043234
CS-16	Joshi pancreas 1 Hz	2.139535	1.999571	0.707183
CS-17	Joshi pancreas 10 Hz historical	1.902778	0.645048	1.245099
CS-18	Joshi pancreas 10 Hz primary	1.901196	0.645349	1.244809
CS-19	Joshi pancreas 10 Hz rounding	1.901194-1.901198	0.645348-0.645350	1.244808-1.244810
CS-20	Dental pulp and hydrogels	30.000000-100.000000	0.003027-0.505000	1.407195-18.174984

The comparison protocols, directions, independent units and uncertainty definitions are given in S5 and S7. Each range keeps its original evidence type. Discovery, nested cohorts, source precision and sensitivity variants are not counted as independent replications. CS-16 is the 1-Hz benchmark; CS-17 retains historical rounded 10-Hz inputs; CS-18 uses refined primary 10-Hz components; CS-19 propagates their printed-value rounding.

Opposite ordering for harmonic responses requires $(R\gamma - 1)(R\sigma - 1) < 0$. A certified interval result additionally requires the direction to hold throughout the declared bounds. Organoid results quantify protocol-dependent work amplification. The 1-Hz native–engineered pancreas stiffness comparison remains separate from its 10-Hz loss-ordering comparison, and the dental literature envelope remains an envelope. The chromosome trajectories retain their ED4/S6 source links. No pooled effect is computed across these protocols.[37,38,39]

Incomplete liver records yield bounded compensation factors without choosing specimen identities. This returns the cross-system synthesis to the original information question: a retained record can identify a directional physical conclusion and a quantitative target even when it does not identify every hidden parameter.

The underlying source-data records provide complete numerical support for every numbered table. The table crosswalk and figure-source index preserve the original source identities and analysis provenance. The indexes are described in S20.

S8 Molecular context for loading-dependent biological responses

S8.1 Condition-level neural-matrix reanalysis

Near-matched initial stiffness concealed large loading-specific differences in the L0–L4 neural-matrix series. [53] L4/L0 initial modulus was 0.963, whereas at 300 s the maintained-strain and maintained-stress work coefficients were 7.24-fold and 23.36-fold higher, with figure-reading sensitivity ranges of 5.31–10.54 and 15.85–36.68 (Supplementary Tables 24–25). The fitted equilibrium modulus fell from approximately 1,710 Pa to 512 Pa. In parallel, GFAP-positive fractions increased approximately threefold in rat and mouse cultures, while Tuj1-positive fractions fell to 0.58 and 0.40 of L0, respectively; an alternative rat figure reading gives 0.62. Relaxation rate, relaxation amplitude, model-derived loss tangent and both work coefficients share the same condition ordering (Supplementary Tables 24–25). The result establishes quantitative concordance between loading-specific material changes and independently measured lineage outcomes. Across these three conditions, the descriptors co-vary and the association is shared among them.

S8.2 Loading protocol and figure-reading sensitivity

Let $E_\infty = p\,E_0$ and $\tau_c = \tau_r E_0 / E_\infty$. Dissipated energy density accumulated during a maintained step is $w_\varepsilon = \varepsilon_0^2 K_\varepsilon(T)$ under strain control and $w_\sigma = \sigma_0^2 K_\sigma(T)$ under stress control, with

$$K_\varepsilon(T) = \frac{E_0 - E_\infty}{2}\left[1 - \exp\left(-\frac{2T}{\tau_r}\right)\right],$$

$$K_\sigma(T) = \frac{1/E_\infty - 1/E_0}{2}\left[1 - \exp\left(-\frac{2T}{\tau_c}\right)\right].$$

The coefficient units are Pa and Pa^{-1}, respectively; multiplying by squared loading amplitude gives energy density in J m^{-3}. The maintained-strain calculation follows the source material-test control, and the maintained-stress calculation supplies its reciprocal-control comparison. Both work windows end before unloading. Direct integration of viscous-branch power verifies the closed forms. The corresponding dynamic response is

$$E^*(\omega) = E_\infty + (E_0 - E_\infty)\frac{i\omega\tau_r}{1 + i\omega\tau_r}, \tan\delta = \frac{\mathrm{Im}\,E^*}{\mathrm{Re}\,E^*}.$$

The loss tangent is evaluated at $\omega = 2\pi / T$ as a co-varying descriptor. Initial modulus is approximately matched, while equilibrium modulus changes with the plateau fraction. Thus the comparison retains both modulus definitions.

The 300-s horizon is motivated by the source study's approximately five-minute RhoA oscillations, rather than an observed cellular strain or stress history.[53] Four horizons and a continuous duration curve are supplied in Supplementary Fig. 9. Independent-uniform input ranges and analysis settings are retained in the analysis records (S20). For 100,000 draws per condition and horizon, the 2.5th and 97.5th percentiles quantify reading sensitivity, not biological sampling confidence. The retained primary and alternative rat L4 Tuj1 readings (26% and 28%) belong to the same source condition. All three-condition rank correlations remain descriptive; the co-varying descriptors cannot be distinguished as predictive explanations from these conditions alone.

Supplementary Table 24 | Neural matrix inputs and lineage endpoints

Neural-matrix inputs and independently measured lineage endpoints. Values were read from the published figures; $E\infty = pE_0$. The primary rat L4 Tuj1 figure reading is approximately 26%, with 28% retained as an alternative figure-reading scenario. Mechanical and lineage entries are condition-level values. [53]

Mechanical inputs

Condition	Initial E_0 (Pa)	Plateau p	Equilibrium E∞ (Pa)	Relaxation τ_r (s)
L0	1900	0.9	1710.0	190
L2	1850	0.73	1350.5	160
L4	1830	0.28	512.4	68

Lineage marker fractions

Condition	Rat Tuj1 (%)	Rat GFAP (%)	Mouse Tuj1 (%)	Mouse GFAP (%)
L0	45	12	15	4
L2	32	27	8	7
L4	26	36	6	12

The alternative rat L4 Tuj1 reading is 28%. All values are rounded readings of published condition-level figures.

Supplementary Table 25 | Neural matrix coefficients and sensitivity

Protocol-defined neural-matrix coefficients and figure-reading sensitivity. Part A lists absolute coefficients at 300 s. Part B reports L4/L0 ratios at four horizons and the 2.5th–97.5th percentile ranges from independent-uniform input draws. The underlying descriptors retain their shared ordering across the three material conditions. The dynamic loss tangent uses the same standard-linear-solid parameters. [53]

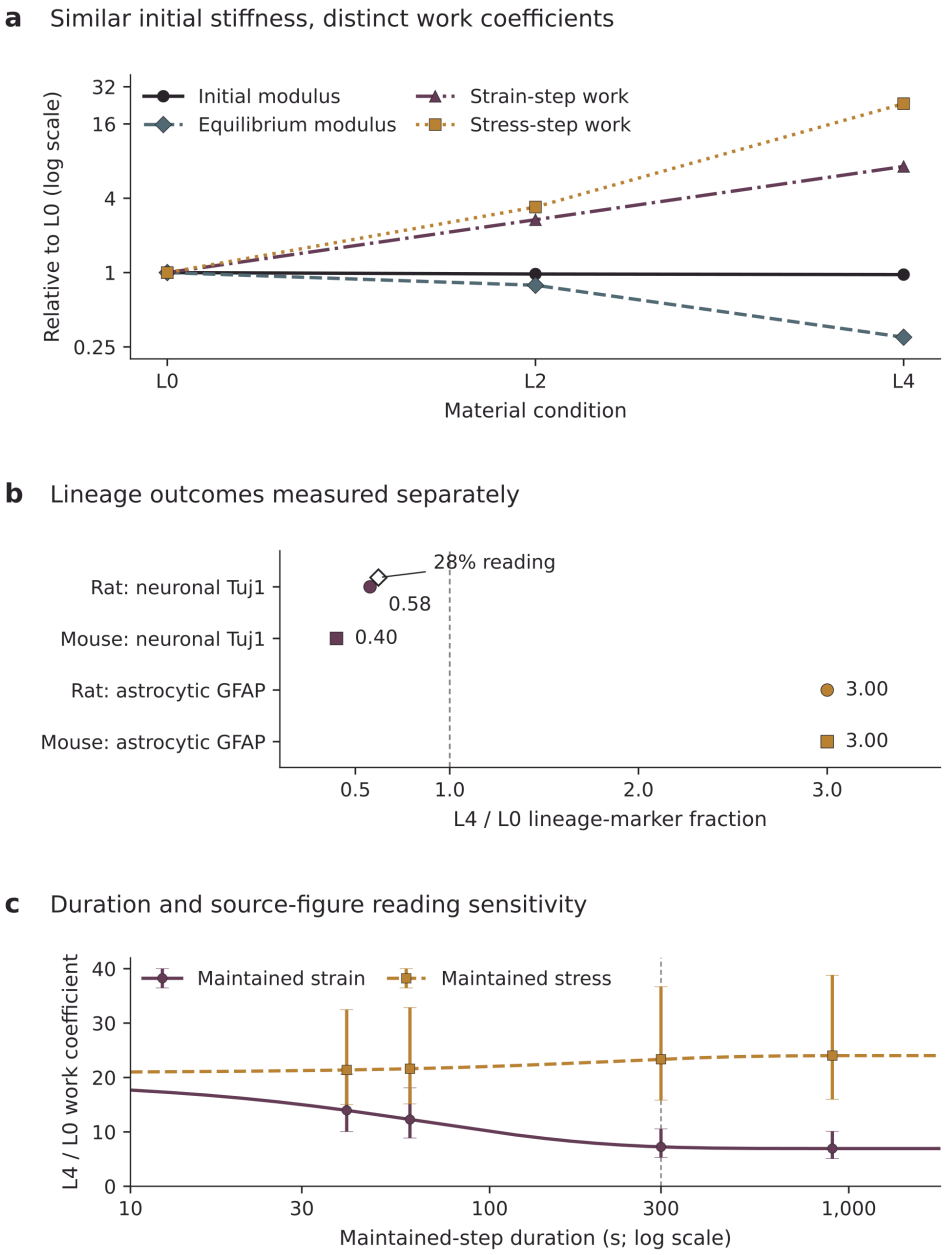
Part A Coefficients at 300 s

Condition	Kε (Pa)	Kσ (Pa^{-1})	Model tan δ
L0	90.961	2.7535e-05	0.023778
L2	243.876	9.34922e-05	0.075654
L4	658.703	0.000643184	0.444227

Part B L4 to L0 ratios and figure reading ranges

Horizon (s)	Strain ratio	Reading range	Stress ratio	Reading range
40	13.957	10.051 to 20.629	21.380	15.040 to 32.483
60	12.274	8.873 to 18.094	21.607	15.152 to 32.852
300	7.242	5.307 to 10.545	23.359	15.847 to 36.685
900	6.935	5.085 to 10.109	24.018	15.980 to 38.806

Supplementary Figure 9 | Neural matrix coefficients and independently measured lineage outcomes



Molecular context and condition-level neural-matrix reanalysis. **a,** L0-normalized initial modulus, fitted equilibrium modulus and maintained-step work coefficients for L0, L2 and L4 at 300 s, calculated from rounded published-figure inputs. The ratio axis is logarithmic. **b,** L4/L0 lineage-marker fractions measured separately from the mechanical calculation in rat and mouse neural-stem-cell cultures. Circles denote rat and squares denote mouse cultures. The primary rat Tuj1 figure reading is approximately 26% (ratio 0.58); an open diamond shows the alternative 28% reading (0.62) of the same source condition. The diamond is offset vertically for visibility. GFAP ratios are approximately 3.0 in each species. **c,** Maintained-strain and maintained-stress coefficient ratios versus duration on a logarithmic time axis. Whiskers at 40, 60, 300 and 900 s show the 2.5th–97.5th percentiles under the specified independent-uniform figure-reading ranges, using 100,000 draws per condition and horizon. These ranges describe sensitivity to source-figure readings. Source: Qiao et al.; Supplementary Tables 24–25 and Supplementary Information S8.[53]

S8.3 Source-specific mechanistic evidence

Qiao et al.'s two-dimensional study combines relaxation-dependent lineage changes with myosin-II and FAK inhibition and pulsed RhoA activation. [53] Their three-dimensional study reverses the neurogenesis trend within a dimensionality-controlled platform and implicates spectrin-dependent transmission of confinement cues and EGR1 expression. [54] Oliva et al. identify Piezo1-dependent sensing of soft-matrix viscoelasticity and a different spreading response in the stiff-matrix regime. [55] Huerta-López et al. link dissipative high-rigidity substrates to reduced mechanosensing and show that myosin perturbation changes the response. [56] These experiments provide mechanistic context for the loading-dependent energetic interpretation: biological responses arise through cellular contractility, adhesion, confinement and sensor activity, with each finding attributed to its experimental system.

These studies supply source-specific mechanisms by which matrix response and cellular loading can affect biological outcomes; the neural-matrix reanalysis quantifies the associated material coefficients.

S9 Reference reconstruction and preservation of a fixed computation

Proposition 3. Three retained reference correspondences recover the original response frame. Let $F(z)=(az+b)/(cz+d)$ have $ad-bc\neq 0$. Suppose a target and three distinct reference responses share this map at the frequency being analysed. Write their original reference values as r_1, r_2, r_3 and use the cross-ratio ordering

$$\chi=\frac{(z-r_2)(r_1-r_3)}{(z-r_3)(r_1-r_2)}.$$

The current observations give the same cross-ratio. With $A=r_1-r_2$ and $B=r_1-r_3$, the original target is

$$D(\chi)=\frac{\chi A r_3-B r_2}{\chi A-B}.$$

Proof. Direct subtraction gives $F(u)-F(v)=(ad-bc)(u-v)/[(cu+d)(cv+d)]$. Substituting the four differences into the cross-ratio cancels each determinant and denominator factor. Rearranging $\chi A(z-r_3)=B(z-r_2)$ then gives the decoder. The argument permits frequency-dependent coefficients when target and references share them at each frequency.

For a homogeneous cross-ratio pair (n,d), the same construction is $D=[nA r_3-dB r_2 : nA-dB]$. The pair $[n:0]$, with $n\neq 0$, represents an infinite affine cross-ratio and decodes to r_3. Three distinct correspondences uniquely determine a fractional-linear frame: conjugating them to $0, 1, \infty$ leaves only the identity. With two correspondences a nontrivial scale freedom remains in that conjugate frame. Conventional three-point fractional-linear calibration supplied with the same correspondences is therefore algebraically equivalent.

Corollary. Fixed-predictor preservation. If f is the original deterministic predictor, its preprocessing and auxiliary inputs *u* are unchanged, and the decoding premises hold, then $f(D(\chi),u)=f(z,u)$. This establishes equality of an existing computation. The recovered coordinate is the retained observed response; its original experimental noise is part of that coordinate.

Algorithm 1. Reference decoding at a measured frequency.

1. Retrieve the three reference identities and their original complex values in the predictor's input convention.
2. Measure the current target and those same reference states under the shared observation conditions.
3. Form the homogeneous cross-ratio numerator and denominator from current observations.
4. Apply the retained-frame decoder above, checking reference separation and the appropriate finite-chart denominator.
5. Restore the original feature ordering, units and saved preprocessing, then evaluate the existing predictor with the same auxiliary inputs.

The calculation does not use the target outcome to select references or fit a replacement model. The measured-data implementations retain their own fixed reference identities and cohort definitions in S17, S15 and S18.

Proposition 4. An affine invariant readout need not preserve the original function. A non-affine fractional-linear decoder has nonzero second derivative on its regular chart. Composing it with a nonconstant linear response function is therefore generally non-affine. A finite sharp witness uses three collinear feature locations $r_0 - h, r_0, r_0 + h$ with desired outputs h_-, h_0, h_+. Every affine approximation has maximum residual at least

$$\frac{\left|h_- - 2h_0 + h_+\right|}{4}.$$

Proof. An affine function has zero second difference. If its three residuals have absolute value at most e, their second difference has absolute value at most $4e$, proving the bound. Residuals $(\delta/4, -\delta/4, \delta/4)$ with $\delta = h_- - 2h_0 + h_+$ attain the bound, since subtracting them leaves zero second difference and hence an affine triple. The result is a statement about the specified readout class; constant or exceptional projections can have zero discrepancy.

Proposition 5. Kernel transport preserves the original learning geometry. Given an original kernel k and retained decoder D, define $k_D(r, r') = k(D(r), D(r'))$. For corresponding training records, k_D has the same Gram matrix as the original kernel. With the same targets, regularization, intercept treatment, preprocessing and selected hyperparameters, training and query-centred kernels are identical, giving identical predictions. The proof is substitution into every Gram-matrix and query-kernel entry. A kernel newly defined directly on invariant coordinates generally describes a different geometry.

Finite-step accuracy. For a fixed map $T(z) = (Az + B)/(Cz + D)$, put $s = Cz + D$ and $\theta = Ch/s$. Exact subtraction gives

$$T(z + h) - T(z) = \frac{T'(z)h}{1 + \theta}.$$

The remainder relative to the tangent displacement is $|\theta|/|1 + \theta|$. When $|\theta| \le \rho < 1$, it is at most $\rho/(1 - \rho)$; a requested tolerance t is therefore ensured by $\rho \le t/(1 + t)$. These relations quantify finite-step error for the fixed map and the role of distance from a pole. Errors in reference values also require propagation through construction of that map. Their inputs must describe the stated perturbation or measurement uncertainty; cancellation at floating-point precision tests the exact algebra separately.

Reference information to retain. A reusable decoding record consists of the original and current reference responses, their identities and shared acquisition conditions, the complex sign and unit conventions, feature order and preprocessing, the chosen model and auxiliary inputs, and the numerical checks used to evaluate the decoder. These entries make the mathematical construction operational without requiring a unique material–apparatus decomposition.

S10 Battery observation design and reference information

S10.1 Physical question and circuit model

The battery analysis asks when a voltage measurement made within a parallel assembly determines a cell impedance in a specified reference frame. It separates three questions: whether the circuit supplies a common observation relation; whether that relation can be calibrated from the available information; and whether its inverse is sufficiently stable for a proposed use. The controlled study embeds measured standalone spectra in prescribed parallel circuits to isolate the observation geometry.

At each frequency, let a parallel assembly contain N independent branches. Cell i has complex impedance z_i, and all series contributions outside its cell-only voltage span are represented by the total external branch impedance r_i. The branches share a bus voltage V_{bus} and injected total small-signal current I. Define

$$Z_{bus} = \frac{V_{bus}}{I} = \left[\sum_{j=1}^{N} \frac{1}{z_j + r_j} \right]^{-1}.$$

The current through cell i is $I_i = V_{bus} / \left(z_i + r_i \right)$. A tap spanning the cell alone records $V_i = I_i z_i$. Normalizing that voltage by the same total current therefore gives

$$y_i = \frac{V_i}{I} = Z_{bus} \frac{z_i}{z_i + r_i}. \left(S10.1 \right)$$

This identity specifies both the voltage nodes and the current normalization. A span across the cell and its entire external branch element instead gives $V_{bus} / I = Z_{bus}$ for every branch. A branch-current-normalized cell voltage would directly give z_i and represents a different measurement set. Shared feed impedances, mutual coupling and voltage spans crossing several current paths define additional circuit contributions whose observation relations must be specified explicitly.

Equal total external branch impedances, $r_i = R$, create the shared observation relation

$$y_i = M\left(z_i \right), M\left(z \right) = Z_{bus} \frac{z}{z + R}.$$

A matrix representing this fractional-linear map is

$$\begin{pmatrix} Z_{bus} & 0 \\ 1 & R \end{pmatrix}, det\ M = Z_{bus} R.$$

The map is nondegenerate when Z_{bus} and R are finite and nonzero, with well-defined denominators on the measured response domain. The bus impedance depends on the entire panel, but is common to all simultaneous responses in that panel. After a cell or state changes, contemporaneous references calibrate the resulting common relation. Sequential measurements require stability of that relation over the calibration sequence.

At $R = 0$, all cell-only taps equal Z_{bus}. Their cell-specific contrast vanishes and the reference cross-ratio inverse is singular. The bus still contains aggregate impedance information; for example, if every other cell impedance is independently known, $z_t^{-1} = Z_{bus}^{-1} - \sum_{j \neq t} z_j^{-1}$. The singular limit therefore identifies the information requirement of the local reference decoder.

S10.2 Calibration information and conventional inverses

Three generic known correspondences determine a nondegenerate fractional-linear map up to a common coefficient scale. Cross-ratio decoding and conventional three-point calibration are algebraically equivalent uses of those correspondences. Three-term calibration is established in impedance metrology, including battery cell measurements using a short and two resistance standards.[45,59] The contribution considered here is the physical arrangement that supplies a common relation to installed cells and the explicit information required to use it.

For consistency with main-text equation 6, let the known reference values be a, b, c and let their current readings be y_a, y_b, y_c. Then

$$\chi = \frac{\left(y - y_b \right)\left(y_a - y_c \right)}{\left(y - y_c \right)\left(y_a - y_b \right)} = \frac{\left(z - b \right)\left(a - c \right)}{\left(z - c \right)\left(a - b \right)}.$$

Writing $\kappa = \chi \left(a - b \right) / \left(a - c \right)$ gives

$$z = \frac{b - \kappa c}{1 - \kappa}. \left(S10.2 \right)$$

Distinct reference values, nonsingular measured differences and a well-conditioned target denominator are required. In the code's ordered triple, the first, second and third entries correspond to b, a, c, respectively. Calibration identifies the composite projective map. The retained references recover this shared map directly while its underlying physical contributions can remain inseparable.

The narrower circuit family in equation S10.1 with equal branches has only two free complex parameters, $B = Z_{bus}$ and R. If its zero-intercept form survives the readout, two generic reference pairs suffice. Since

$$\frac{z}{y} = \alpha z + \beta, \alpha = \frac{1}{B}, \beta = \frac{R}{B},$$

two references give

$$\alpha = \frac{z_1 / y_1 - z_2 / y_2}{z_1 - z_2}, \beta = \frac{z_1}{y_1} - \alpha z_1, z = \frac{\beta y}{1 - \alpha y}. \quad (S10.3)$$

These are sufficient generic conditions; additional known circuit parameters can reduce the required calibration further. An unknown common outer fractional-linear readout generally removes the special known-zero constraint, so three generic correspondences calibrate the resulting general class. A common gain alone preserves the known-zero constraint.

If R and Z_{bus} are independently known in a calibrated frame, the ordinary circuit inverse is

$$z_i = \frac{R y_i}{Z_{bus} - y_i}. \quad (S10.4)$$

For known unequal r_i, replace R by the known branch-specific value. The branch-specific direct inverse therefore recovers a heterogeneous circuit when its required physical calibration is supplied. The reference method uses known current reference values and their current observations in place of separate measurements of these common coefficients. Reference identities must be accompanied by values describing their currently measured states.

Supplementary Table 26 | Sufficient information for the stated inverses.

Observation assumptions	Additional information	Available inference
Calibrated cell-only tap and bus impedance	Known target external branch impedance r_i	Direct circuit inverse, including unequal branches
Known equal-branch zero-intercept circuit form	Two generic current reference pairs	Solve Z_{bus} and R, then invert
Generic shared fractional-linear map	Three generic current reference pairs	Composite map or cross-ratio inverse
Proposed common map requiring a transfer check	Additional known references excluded from calibration	Held-out consistency test beyond the fitted anchors
Cell voltage normalized by its branch current	Calibrated branch-current measurement	Direct cell impedance; a different sensing arrangement

S10.3 Source measurements and panel construction

The standalone input is the public characterization of 250 cylindrical cells by Ank and colleagues.[19,20] The source inventory has one absent cell, Batch1_100, and one cell with empty data, Batch2_090, leaving 248 usable histories. Each supplies three nominal state-of-charge spectra, labelled 80%, 50% and 20%, on 61 common frequencies. The processed archive contains 45,384 finite complex impedance values. Its complex sign has been reconciled with the original export convention, in which the MATLAB field labelled ImZOhm stores minus the imaginary part. Each supplied spectrum is treated as the specified cell response in the computational circuit,

including any original acquisition error. Nominal state-of-charge and source grade labels are retained exactly as supplied.

The principal analysis retains 20 frequencies satisfying $0.1 \le f \le 10$ Hz. For each of the 248 targets at each nominal SOC, ten panels select five different candidate reference cells without replacement from the other 247 cells. Target position is zero; positions one to five are candidates. Panel generation uses NumPy's default random generator with seed 20261026. Thus $248 \times 3 \times 10 = 7,440$ target panels are computational recombinations of measured spectra. The 248 cell histories are the measured source units; panel recombination repeatedly uses their retained spectra. Three candidates calibrate the map; the target and the other two candidates are evaluated as held-out responses, giving 14,880 additional reference checks per geometry.

Reference selection uses only candidate reference spectra. For candidate triple $T \subset \{1,\dots,5\}$, define

$$s(T) = \min_{f} \frac{\min_{j<k;\, j,k \in T} \left| z_j(f) - z_k(f) \right|}{\mathrm{median}_{l \in \{1,\dots,5\}} \left| z_l(f) \right|}.$$

The maximizing triple is selected from all ten possibilities, with the first lexicographically ordered triple retained in a tie. The pair distances and their frequency-dependent normalization use the five reference candidates exclusively. Each selected triple is fixed before evaluating target errors, added noise and full-frequency results.

Candidate-only normalization excludes the target from reference selection. Normalizing instead by the median magnitude of all six spectra includes the target and changes the selected triple in 32 of 7,440 panels. The comparison preserves all panel draws, input spectra and primary contact realizations; the selection records retain both triples for every affected panel. The heterogeneous median error is 5.3332% with six-spectrum normalization and 5.3354% with candidate-only normalization, the latter reported as 5.34%. The circuit identity is independent of this normalization choice.

S10.4 Paired branch-impedance controls

The original controlled contrast used unequal real branch impedances drawn from a lognormal distribution with arithmetic mean 0.1 mΩ and coefficient of variation 0.25, versus equal 10 mΩ branches. These prescribed branch values define paired controls at matched scales and matched realized means. To separate equality from scale, the present paired controls retain identical cell panels and relative heterogeneity at both nominal scales. With seed 20261027, the 0.1 mΩ contacts use log-variance $\log(1 + 0.25^2)$ and log-mean $\log(10^{-4}\,\Omega) - 1/2 \log(1 + 0.25^2)$. Multiplication of each realized branch impedance by 100 gives the 10 mΩ unequal condition. Equal controls use either the nominal value or the arithmetic mean of the six realized unequal impedances in that panel. The latter comparison exactly matches each panel's realized mean.

The scale invariance of the noiseless heterogeneous error has an algebraic explanation. Write $r_i = k\,\rho_i$ and $w_i = z_i / \rho_i$. Then

$$y_i(k) = Z_{bus}(k) \frac{w_i}{w_i + k}.$$

The measurements are a common fractional-linear function of the distorted values w_i. For $c = k'/k$,

$$y_i(k') = \frac{Z_{bus}(k')\, y_i(k)}{c\, Z_{bus}(k) + (1 - c)\, y_i(k)}.$$

Changing the shared scale therefore acts by another common fractional-linear map and leaves observed cross-ratios unchanged. The branch-dependent relation between w_i and the desired z_i persists under this shared rescaling. When the branches are equal, all ρ_i coincide and the required common map of the true cell responses is restored. This identity describes the noiseless linear circuit; the perturbation models below quantify inverse conditioning.

Supplementary Table 27 | Corrected primary and matched-scale computations. Each row uses the same 7,440 target panels and 20 frequencies. Errors are fractions, except the explicitly labelled percentage columns. The maximum column reports the largest target relative RMS error.

Total external branch condition	Median target error (%)	95th percentile (%)	Maximum target relative RMS
Unequal, nominal mean 0.1 mΩ, CV 0.25	5.3354	24.4361	4.8263
Same unequal realizations scaled to mean 10 mΩ	5.3354	24.4361	4.8263
Equal fixed 0.1 mΩ	7.04×10^{-12}	5.39×10^{-11}	1.55×10^{-11}
Equal to each panel's realized mean near 0.1 mΩ	7.16×10^{-12}	5.50×10^{-11}	1.45×10^{-11}
Equal fixed 10 mΩ	8.18×10^{-14}	6.09×10^{-13}	1.84×10^{-13}
Equal to each panel's realized mean near 10 mΩ	8.82×10^{-14}	6.52×10^{-13}	1.85×10^{-13}

At fixed 10 mΩ, the maximum pointwise fractional error over primary targets and held-out references is 4.14×10^{-13}. These numerical residuals quantify closure of the exact common-map identity. Supplementary Fig. 10b places values below 10^{-8}% at that plotting floor, without excluding panels or altering stored values. The two same-scale heterogeneous distributions overlap to floating-point precision. Supplementary Fig. 10 retains further comparator and exactly matched realized-mean controls.

S10.5 Error definitions and comparator implementations

For target spectrum z and reconstruction $\hat{z}$ at F frequencies, the principal error is

$$e_{RMS} = \left[\frac{1}{F} \sum_{f} \left| \frac{\hat{z}(f) - z(f)}{z(f)} \right|^2 \right]^{1/2}.$$

The maximum pointwise fractional error is $max_f \left| [\hat{z}(f) - z(f)] / z(f) \right|$. Each frequency's error is normalized by its own true magnitude before RMS aggregation. Percentiles summarize the finite set of computational panels. All primary and comparator reconstructions are finite.

Independent conventional three-point calibration centers and scales both reference coordinate sets, forms the homogeneous system $[x, 1, -yx, -y]$, and uses its right singular vector to obtain a fractional-linear inverse. With three correspondences this implements the same algebra as equation S10.2.[59] With five correspondences it is a normalized homogeneous least-squares fit under the specified objective. To compare three and five references fairly, 1,500 panel indices are selected by integer conversion of an evenly spaced sequence from 0 to 7,439, inclusive. Both fits use exactly the same target, cell panel and external branch realization. Selection is independent of their errors. The five-reference fit uses all candidates, so only the target remains held out in that comparison.

Supplementary Table 28 | Paired same-information and extra-reference comparisons. Each entry uses the same 1,500 selected panels. Values are target relative RMS errors in percent. The conventional three-point and cross-ratio estimates agree numerically.

Unequal nominal branch scale	Three-reference median (%)	Three-reference p95 (%)	Five-reference median (%)	Five-reference p95 (%)
0.1 mΩ	5.2149	23.6750	4.7789	18.8587
10 mΩ, same scaled realizations	5.2149	23.6750	4.7580	18.9763

The maximum pointwise relative difference between conventional three-point calibration and cross-ratio decoding across the four paired fixed-scale conditions is 1.55×10^{-13}. Five-reference fitting changes an

approximate compromise but retains structural error in this benchmark. Its approximate solution depends on scale because the fitting objective is Euclidean in normalized coordinates. The archived five-reference p95 of 21.18% belongs to a different 2,500-panel/contact realization and is preserved separately as an unpaired historical result.

Direct inversion with calibrated bus impedance and known target branch impedance is numerically valid in both equal and unequal circuits. The computational comparator receives these exact quantities from the generating network; a physical implementation would require independent calibration or measurement of them. The two-reference restricted inverse is evaluated on all 7,440 equal-10-mΩ panels using the first two members of the selected triple; its maximum pointwise fractional error is 4.00×10^{-14}. The two-reference construction uses the additional information supplied by the narrower circuit family.

A common outer-map check further distinguishes the information sets. At each frequency, let s be the median magnitude of the five candidate tap responses and $u_i = y_i / s$. The imposed readout is

$$\tilde{y}_i = s \frac{(1 + 0.1\,i)\,u_i + 0.2}{(0.1 - 0.03\,i)\,u_i + 1}.$$

It is shared within each panel and frequency, and its smallest evaluated denominator magnitude is 1.0915. Three-reference decoding has maximum pointwise fractional error 1.46×10^{-12} across all 7,440 panels. Conventional three-point calibration agrees to 1.93×10^{-15} maximum pointwise relative difference on the paired subset. Applying the special two-reference zero-intercept formula after this unknown outer map violates that formula's assumptions; its residual is retained as an explicit observation-class mismatch control.

S10.6 Noise, reference geometry and inverse stability

The new noise calculation applies independent circular complex multiplicative perturbations to every normalized tap, including the calibration references:

$$\tilde{y}_i(f) = y_i(f)\left[1 + \sigma\,\eta_i(f)\right], \eta_i(f) = \frac{\xi_i(f) + i\,\zeta_i(f)}{\sqrt{2}},$$

where ξ and ζ are independent standard normal variables and $\sigma = 10^{-4}$, or 0.01% complex RMS. The same standardized perturbations are used at fixed equal $R = 0.1$ and 10 mΩ for each of the 7,440 panels. Seed 20269026 fixes the per-panel real-then-imaginary draw order. The imposed perturbation model describes independent relative complex errors in normalized tap responses. Reference truth values remain exact in this calculation.

Equal 0.1 mΩ branches have median target error 6.3458% and p95 17.2277%, whereas equal 10 mΩ branches have median 0.08335% and p95 0.63879%. Map equality makes the inverse exist; its stability is affected by impedance scale and reference geometry. For the calibrated physical inverse with exact R and Z_{bus}, the local sensitivity illustrates the singular limit:

$$\frac{\delta z}{z} \simeq \frac{Z_{bus}}{Z_{bus} - y} \frac{\delta y}{y}.$$

Reference-based inversion introduces further uncertainty from reference separations and reference-value errors. Uncertainty in R, the bus or reference values contributes additional terms when constructing the corresponding measurement-error model.

Extended Data Fig. 8c and Supplementary Table 29 examine a simple score threshold without retuning the reference selector. At each omission fraction, the corresponding empirical quantile of the candidate-only spacing score defines a retained subset. These thresholds describe the observed finite-panel error tails under the imposed tap-noise model. At 10 mΩ the score/error Spearman correlation is −0.3841, and omitting the lowest 10% improves p95 from 0.6388% to 0.4312%. At 0.1 mΩ the correlation is +0.3271 and the same filtering does not

improve the tail. Standalone reference spacing is insufficient to predict inverse stability across both circuit scales.

Supplementary Table 29 | Reference-spacing filtering under 0.01% imposed tap noise. The same reference-only score quantiles are used at both circuit scales. “Maximum” means the largest observed retained-panel RMS error.

Fraction omitted	Retained panels	p95 at 0.1 mΩ (%)	p95 at 10 mΩ (%)	Maximum at 0.1 mΩ (%)	Maximum at 10 mΩ (%)
0	7,440	17.2277	0.6388	140.4401	33.8737
0.10	6,696	17.6335	0.4312	140.4401	10.9074
0.20	5,952	18.0646	0.3541	140.4401	7.8549
0.50	3,720	18.8106	0.2078	135.6888	2.7989

A stability assessment for a physical readout combines propagated measurement uncertainty, current reference values, observed reference geometry and held-out residuals. Three fitted anchors identify the map, and additional known references test its transfer beyond those anchors. The specified observation model and error budget determine how these checks support inference for the target.

S10.7 Full-frequency audit and preserved sensitivity calculations

The full-frequency audit uses the same 1,500 evenly spaced panel indices as the paired comparator, retaining triples chosen in the principal band. It evaluates all 61 archived frequencies, 0.0093132257–10001 Hz, for equal fixed 10 mΩ branches. Maximum target relative RMS error is 8.93×10^{-13} and maximum pointwise fractional error is 5.68×10^{-12}. The full-frequency audit comprises 1,500 target panels. A separate 500-panel zero-R calculation verifies tap collapse to floating-point precision. Any finite quotient returned by raw arithmetic at coincident references is rejected as a singular inverse.

Additional sensitivity grids cover common impedance, noise amplitude, relative mismatch, absolute mismatch, reference drift and shared outer transformations. These grids use the six-spectrum normalization described in S10.3. Table 30 records representative sensitivities with their stated sample sizes and random realizations, separately from the paired controls and all-panel noise comparison.

Supplementary Table 30 | Illustrative sensitivities at nominal 10 mΩ. Values are target relative RMS percentages; these rows use six-spectrum normalization for reference selection. Each row defines a sensitivity under its specified computational perturbation model.

Sensitivity scenario	Panels	Median (%)	p95 (%)
Equal branches; 0.01% complex RMS tap noise	1,000	0.08354	0.73132
0.1% relative branch SD plus 0.01% tap noise	1,000	0.16149	1.42175
0.01 mΩ absolute branch SD plus 0.01% tap noise	1,000	0.17128	1.24154
1% complex RMS reference-value mismatch; no added tap noise	1,200	1.18006	10.88902

The reference-mismatch calculation perturbs the values supplied to the decoder relative to the fixed circuit’s actual reference responses. The archived sweep quantifies sensitivity to incorrect current reference values under the stated perturbation model.

S10.8 Whole-spectrum ambiguity and compatible decisions

The earlier construction of observational twins makes this information boundary explicit. Let six branches have $z_i = k_i z_\star$ and $r_i = k_i R_\star$, and define $p_i = 1/k_i$ and $S = \sum_i p_i$. Then

$$Z_{bus} = \frac{z_\star + R_\star}{S}, \; y_i = \frac{z_\star}{S}, \; \frac{I_i}{I} = \frac{p_i}{S}.$$

The heterogeneous vector $(0.45, 1, 1, 1, 1, 1)$ and the uniform vector $(54/65, \ldots, 54/65)$ both give $S = 65/9$. They therefore have identical terminal and cell-only tap spectra as functions of frequency. With the illustrative criterion $0.8 \le k_i \le 1.2$ for every cell, one satisfies the criterion and the other does not. Extra frequency samples cannot separate functions that are equal at every frequency. Branch-current fractions provide different information: the target-current measurement separates the heterogeneous example, while all six fractions can establish the illustrated uniform case. The continuous admitted family satisfied $0.4 \le k_i \le 1.5$; $R_\star = 3$ mΩ, current-fraction tolerance ± 0.005 and spectral relative tolerance 10^{-8} are the declared parameters of this mathematical construction.

A tight observation-only recovery limit follows for this pair. Choose the first cell as the target and any n retained frequencies at which the common spectrum is nonzero. Its two possible spectra are the common spectrum multiplied by a = 9/20 and b = 54/65, respectively. A deterministic decoder that receives only the identical terminal and cell-tap spectra must return the same estimated spectrum for both networks. Define u_j as that estimate divided by the common spectrum at frequency j, and use the frequency-wise relative RMS metric

$$e_c = \frac{\sqrt{\frac{1}{n}\sum_{j=1}^{n} |u_j - c|^2}}{c}, \qquad c \in \{a, b\}.$$

In the RMS norm on these normalized frequency vectors, the triangle inequality gives

$$b - a \le a e_a + b e_b \le (a + b) \; max(e_a, e_b).$$

Consequently, at least one of the two target spectra has relative RMS error bounded below by

$$max(e_a, e_b) \ge \frac{b - a}{b + a} = \frac{11}{37} \approx 29.73\,\%.$$

The bound is attained for this two-spectrum decision problem by returning the spectrum with the common scale 2ab/(a+b) = 108/185. At every retained frequency, its relative errors against the two targets are equal to 11/37, so their RMS errors are also equal to that value. The same argument holds for any common positive frequency weights normalized to sum to one.

This is a tight lower bound for the constructed observational pair, specified first-cell target and relative RMS metric. It is not a universal error floor for parallel networks. Additional information that separates the two networks, such as the target branch-current fraction, removes the premise that forces the decoder to give both targets the same estimate.

More generally, let Θ be a declared physical model, $H \subseteq \Theta$ an independently justified acceptance family and $C(y)$ the compatible states under a stated error model. Four outcomes distinguish a supported decision from missing information:

Supplementary Table 31 | Decisions defined by the compatible set.

Outcome	Required condition	Interpretation
Outside the acceptance family	$C(y) \neq \varnothing$ and $C(y) \cap H = \varnothing$	Every compatible state violates the criterion
Within the acceptance family	$C(y) \neq \varnothing$ and $C(y) \subseteq H$	Every compatible state meets the criterion
Undecided	Both classes remain possible, or available certificates cannot decide	Abstain from a class conclusion
Model inconsistent	$C(y) = \varnothing$	Observation and admitted model/error budget disagree

If an independently justified uncertainty construction gives $Pr\{\theta_\star \in C(Y)\} \geq 1-\alpha$, an incorrect issued class decision is confined to its coverage failure event. This is a marginal error statement; conditional error among issued decisions is a separate estimand. Reporting abstention and sensitivity characterizes the resulting decision procedure. Exact rational checks of finite optimization certificates verify the algebra for the supplied constraints; the uncertainty construction and acceptance family specify the statistical and physical interpretation. The decision procedure and its fourteen constructed verification cases are documented in the analysis records (S20).

S10.9 Candidate physical realizations and reproducibility

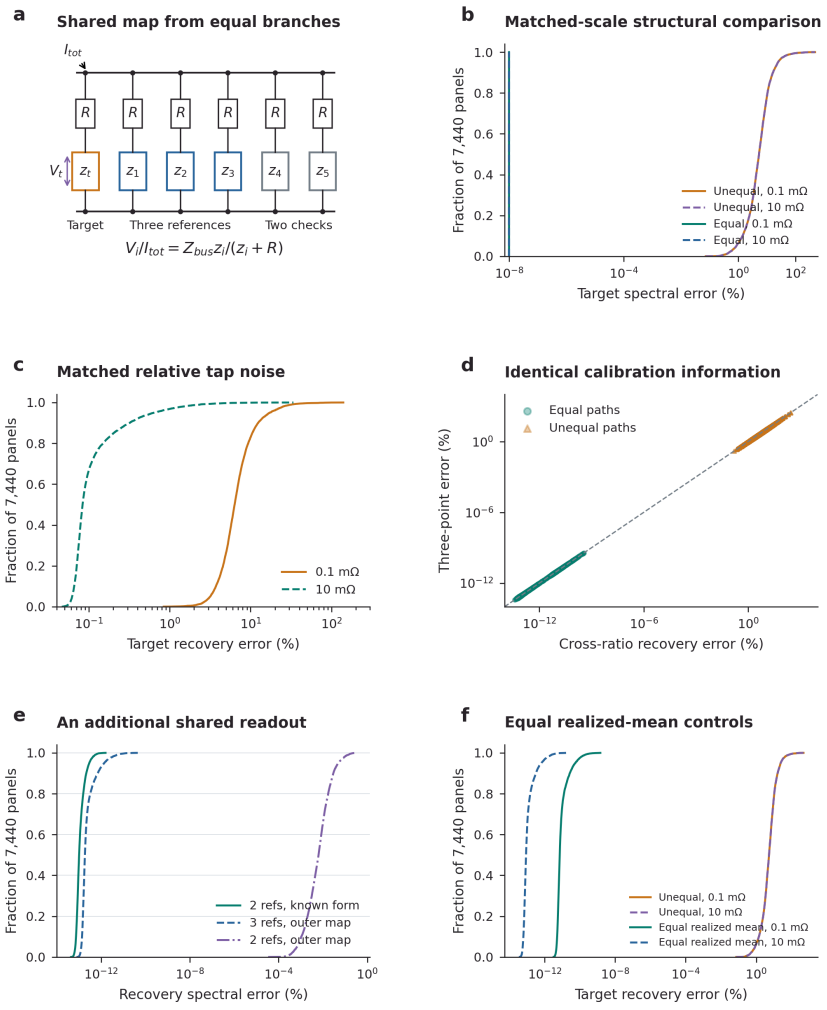
Let the native external path of branch i be $n_i(\omega)$ and its diagnostic compensation be $c_i(\omega)$. The total entering the observation relation is $r_i(\omega) = n_i(\omega) + c_i(\omega)$. Shared-map recovery requires these complete totals to equal the same nonzero $R(\omega)$ over the retained frequency band. Adding the same resistor to every unequal native path preserves the differences; branch-specific compensation instead targets $c_i = R - n_i$. For passive trim, the chosen common target must lie in the realizable range of every branch. Cell spectra remain free to differ.

The matching condition applies during diagnostic acquisition. An end-of-line or service fixture, switchable low-current paths, branch-specific trim or controlled/actively synthesized impedance can supply this relation without requiring identical as-manufactured traction contacts. Controllable interconnection resistance has experimental precedent.[44] The operative specifications are the complete path over frequency, current and sense-node locations, parasitics, temperature and state of charge during acquisition, temporal stability and reference drift. The retained relative, absolute and heterogeneous-path sweeps quantify departure from the specified relation.

Matching is one sufficient observation design. If each unequal r_i and the finite nonzero Z_{bus} are independently calibrated in the same frame, equation (S10.1) instead gives $z_i = r_i y_i / (Z_{bus} - y_i)$. That direct inverse uses the additional branch and bus information identified in Extended Data Fig. 7. The paired perturbation/restoration test evaluates the shared-map decoder under a deliberate violation and restoration of its own design condition; it does not exclude this calibrated unequal-path route.

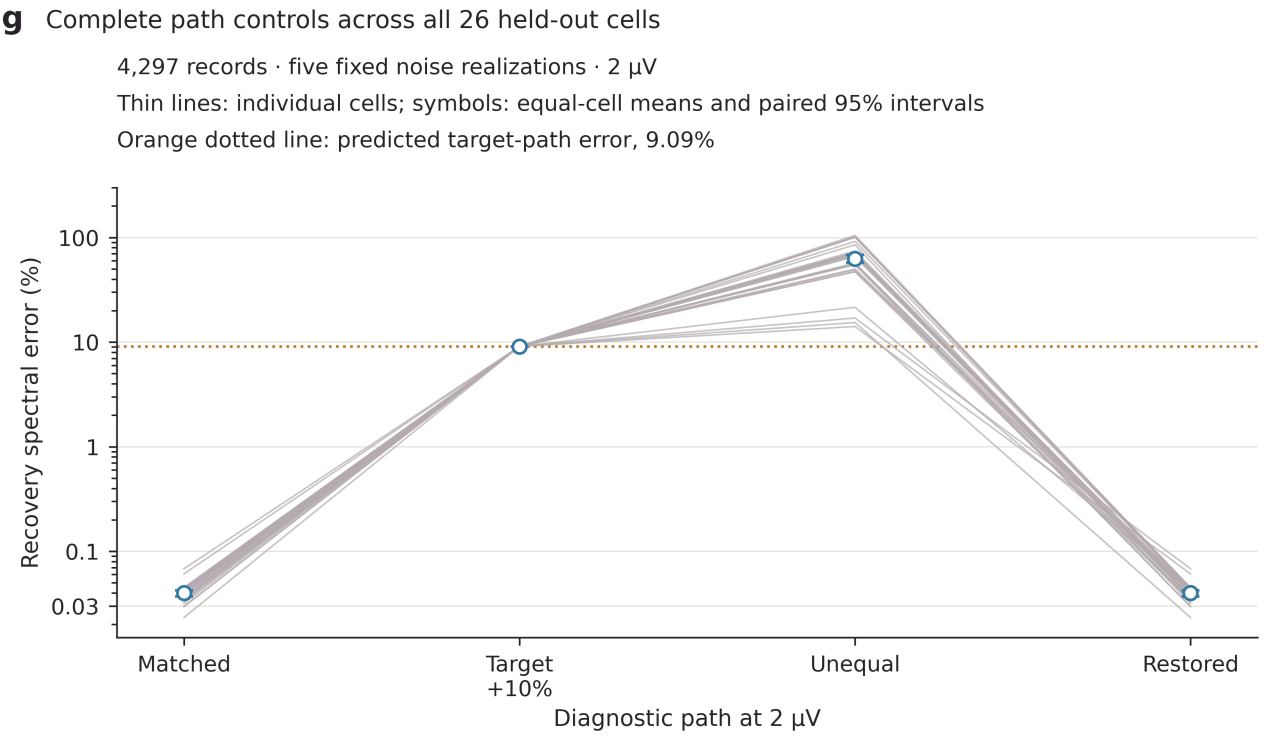
Section S12 carries the observation design through independently assembled component equations, finite sampled acquisition and frozen capacity prediction in the single-cell, NREL–DENSO and four-institution cohorts. Extended Data Figs. 7 and 8 and Supplementary Fig. 10 present the complete retained information, branch-matching and conditioning comparisons.

Supplementary Figure 10 | Physical geometry, calibration equivalence and complete mismatch controls



a, Cell-only voltage taps, normalized by total current, share a fractional-linear map when total external branch impedances are equal and nonzero and bus impedance is finite and nonzero. Three references calibrate the general map, leaving the target and two checks held out. At R = 0, cell-specific tap contrast vanishes. **b,** All 7,440 controlled recombinations of measured standalone spectra from 248 cells at three nominal states of charge. Unequal lognormal branches have arithmetic mean 0.1 mΩ and coefficient of variation 0.25; the same realizations are scaled by 100 at 10 mΩ. Unequal noiseless curves overlap (median 5.34%, 95th percentile 24.44%); equal curves fall below the displayed 10^{-8}% floor. **c,** Equal branches with identical realizations of 0.01% RMS independent circular complex multiplicative tap noise. The 95th-percentile errors are 17.23% at 0.1 mΩ and 0.639% at 10 mΩ. **d,** Cross-ratio decoding and conventional normalized three-point calibration on the same 1,500 targets in each of four equal/unequal branch conditions. The diagonal is equality; the maximum pointwise relative difference is 1.55×10^{-13}. **e,** Two references recover the known zero-intercept circuit; three recover an additional shared fractional-linear readout. Applying the restricted two-reference formula after that transformation gives the complete observation-class mismatch control. **f,** Equal-branch controls match each unequal panel's realized arithmetic mean at both nominal scales. Equal controls retain numerical closure, while unequal curves overlap. Panels e,f contain all 7,440 targets per condition. Panels a–f use twenty frequencies, 0.1–10 Hz.[19,20] There is no added noise in a,b,d–f; no display floor is applied in d–f. Errors equally weight per-frequency fractional deviations. Additional-reference and information-set comparisons are retained in Extended Data Fig. 7.

Supplementary Figure 10 (continued) | Physical geometry, calibration equivalence and complete mismatch controls



g, Complete independent-acquisition path control for all 26 held-out LiBforSecUse cells and 4,297 records at 2-µV voltage-sample RMS noise: matched paths, a target-only +10% path change, unequal paths and restored matching. Thin lines are cell means; symbols and whiskers are equal-cell means and paired 95% whole-cell bootstrap intervals, stratified within institution. Recovery error is RMS fractional spectral deviation from the fitted standalone response, averaged over records and five fixed noise realizations within each cell. The dotted line is the exact noiseless target-path consequence, 100(1−1/1.1)=9.09%. Matched and restored results coincide under paired noise. This panel includes every condition and cell in the four-state path control; S12 gives the independent-acquisition protocol.[22,23]

S11 Parallel-network recovery and masking

For $Z_{pack} = Z_s + \left(1/z + Y_h\right)^{-1}$, knowledge of Z_s gives $\left(Z_{pack} - Z_s\right)^{-1} = 1/z + Y_h$. A difference between states cancels a constant background admittance. A supplied background change can instead be subtracted. If it is only bounded, the result is a bound on the target change rather than a unique reconstruction. The baseline-referenced circuit inverse with the same information is algebraically equivalent to the reference construction.

The NASA network evaluation used 887 prepared impedance sweeps from four cells: 278 each from B0005, B0006 and B0007, and 53 from B0018. Each sweep has 48 complex positions, giving 42,576 values. The first observation in each of eight cell/preceding-operation strata is a baseline, leaving 879 later sweeps. The prepared release lacks a position-specific frequency vector; native positions are not relabelled as a fabricated common frequency grid. [64]

Virtual networks have 1, 4, 16 or 64 branches and baseline background $\left(P - 1\right)/z_0$. The real series baseline is $S_0 = 0.01\,median\left|z_0\right|$. With elapsed days t, parallel drift uses $Y_h(t) = Y_{h,0}\left[1 + 0.1\sin\left(2\pi t/7\right)\right]$ and series drift uses $S(t) = S_0\left[1 + 0.2\sin\left(2\pi t/5\right)\right]$. Stationary, parallel-drift and parallel-plus-series-drift conditions are paired with complex-disk radii 0, 10^{-4} and 10^{-3} times the median clean baseline pack magnitude. Perturbations are independent area-uniform disk draws, including a separate baseline draw, shared among comparison methods.

The evaluation comprises 31,932 vector cases and 223,524 method evaluations across seven methods. Headline errors are medians of four cell medians of postbaseline relative vector error.

Noiseless sixteen-branch recovery is at approximately 3.43×10^{-15} relative error for stationary background and 3.48×10^{-15} with supplied drift. Under both drifts and 0.1% relative complex-disk perturbation, the sixteen-branch median is 4.978565%, rising to 18.934026% at 64 branches (Supplementary Table 34). The result tests recovery from measured cell responses embedded in constructed networks. The branch count controls how strongly the background masks the target: reciprocal network operations magnify terminal uncertainty as the target contribution becomes small.

Complete measured-input coverage and supplied information

Every supplied native impedance sweep is included. Each cell is split by the last preceding non-impedance operation; the first sweep within each cell/operation stratum defines that stratum's baseline. This gives eight baselines and 879 later sweeps (Supplementary Table 32). Each baseline supplies the retained reference state for its cell/operation stratum. Every sweep contains 48 complex positions. The analysis records retain every measured input trajectory and every postbaseline reconstruction error for the stated network conditions (S20).

Supplementary Table 32 | Native NASA spectrum coverage.

Cell	Sweeps after charge	Sweeps after discharge	Baseline spectra	Postbaseline spectra
B0005	136	142	2	276
B0006	136	142	2	276
B0007	136	142	2	276
B0018	24	29	2	51
Total	432	455	8	879

Writing the terminal observation as $W = S + (1/z + H)^{-1}$, with series contribution $S = Z_s$ and parallel admittance $H = Y_h$, the known-change construction uses

$$\widehat{\Delta Y} = \frac{1}{W - S} - \frac{1}{W_0 - S_0} - \Delta H, \hat{z} = \left(z_0^{-1} + \widehat{\Delta Y}\right)^{-1}.$$

The absolute parallel background H_0 is not an input to this expression. The native baseline z_0, the current and baseline series terms, and the parallel-admittance change are supplied. The comparator definitions make these information differences explicit (Supplementary Table 33).

Supplementary Table 33 | Information used by the seven network comparison routes.

Route	Supplied information and reconstruction
Uncorrected	Treat the terminal observation W as the target response
One-point ratio	Supply z_0, S, S_0 and use $z_0(W - S)/(W_0 - S_0)$
Static-background difference	Supply z_0, S, S_0 and set $\Delta H = 0$ in the difference construction
Known-change difference	Supply $z_0, S, S_0, \Delta H$ and use the displayed construction
Circuit-referenced inverse	Supply absolute H, H_0, S, S_0, invert both observations and reference their admittance difference to z_0; algebraically equivalent to the known-change difference
Ninety-percent change	Supply the same quantities as the known-change route, with the declared estimate $0.9\,\Delta H$
Frozen-series difference	Supply $z_0, S_0, \Delta H$, using S_0 in place of the current series contribution

Error metrics and complete scenario accounting

The per-sweep target error uses all 48 complex entries,

$$e_z = \frac{\| \hat{z} - z \|_2}{\| z \|_2}.$$

For each network condition, both preceding-operation strata are retained when taking the median within a cell. The aggregate reported in Supplementary Table 34 is then the median of the four cell medians. It gives equal weight to the four measured cells. The 1, 4, 16 and 64 branches are controlled network constructions from a baseline response.

The complete design contains four branch counts, three background scenarios and three added-error radii for each of the 887 native sweeps: 31,932 vector cases and 223,524 method outputs. For all 10,548 postbaseline known-change cases with zero added error, the maximum relative target-vector discrepancy is 5.03912×10^{-13}. At nonzero radius, the error is a complex random variable sampled uniformly in area from a disk with radius $r = \epsilon \, median \left| W_{0,clean} \right|$. Each baseline has its own draw, and all methods use the same resulting observations. The radii specify the imposed complex-disk perturbation model.

For both prescribed drifts, the median of four cell medians is as follows.

Supplementary Table 34 | Recovery error under finite imposed perturbations.

Constructed parallel branches	Relative target-vector error at 0.01% radius (%)	Relative target-vector error at 0.1% radius (%)
1	0.01846	0.17072
4	0.09489	0.96286
16	0.45759	4.97857
64	2.58072	18.93403

These values quantify the conditioning of target recovery as the target's contribution becomes more strongly masked. The complete machine-readable method table preserves all corresponding records, error bounds and status values, together with the native, terminal and reconstructed vectors.

S12 Independently solved battery acquisition and preservation of frozen predictions

S12.1. Scientific target and evidence units

This experiment tests a constructive consequence of the common-map architecture: a common nonzero external branch impedance gives simultaneously measured cell taps a shared calibratable relation to their standalone impedances. The acquisition is solved from circuit components independently of the three-reference inverse. A capacity predictor trained on measured standalone spectra is then held fixed while its input passes through the designed acquisition and recovery. The resulting prediction displacement measures preservation of that computation.

Three input conditions are retained throughout: original measured standalone impedance, the passive circuit's standalone impedance, and impedance recovered from virtual acquisition of that circuit. The original-to-virtual comparison measures the effect of constructing the specimen. The virtual-to-recovered comparison measures observation recovery. Capacity MAE against the same measured outcome is reported for all three. The original measurements and capacities ground the test; the installed network and its sampled acquisition are controlled virtual experiments.

The 299-record Zhang example supplies one complete held-out cell trajectory. The NREL–DENSO extension holds out seven prespecified cells together. LiBforSecUse supplies 26 whole-cell holdouts, each trained within

its source institution. Table 35 records their separate units. The older 7,440-panel battery geometry construction in S10, the 2,301-record fixed-function calculation and nested capacity analysis in S15, and the 780-record historical predictor-transport analysis retain their original protocols and populations.

Supplementary Table 35 | Cohorts and evaluation units for independent acquisition. Training and test cells are disjoint in every split. LiBforSecUse uses 26 separate models; the other two cohorts each use one. Frequencies are retained in source order within each experiment.

Cohort	Held-out cells	Test spectra	Training cells	Frequencies	Capacity unit
Zhang 299	1	299	6	60	mAh
NREL–DENSO	7	108	24	69	percentage points of relative capacity
LiBforSecUse	26	4297	3–9 per fold	59–60 per fold	mAh

S12.2. Source records, frequencies and capacity definitions

For Zhang et al., the author source matrices contain 1,358 training spectra from six cells and 299 spectra of cell 35C02.[21,52] The columns are sixty real impedance components followed by sixty negative imaginary components. The physical complex spectrum is reconstructed with the corresponding negative imaginary sign. The verified native frequency vector runs from 20,004.453 down to 0.01999 Hz. Held-out capacities range from 27.502 to 40.474 mAh. All 299 source rows enter the retained evaluation in their original order.

For NREL–DENSO, the source repository's example_Denso_models.m specifies cells 7, 10, 13, 17, 24, 30 and 31 as the held-out set.[24,50] The retained CSV has 467 records from 31 cells: 359 training records from the remaining 24 cells and 108 test records from the seven named cells. Its 69-column frequency correspondence is retained. Frequencies are taken from the canonical vector in the original Data_Denso2021.mat file, spanning 31,622.78 down to 0.00501 Hz. This preserves the source column mapping while avoiding use of rounded CSV headings as exact frequencies. Small differences among ancillary source grids are recorded in the provenance audit. The target is relative C/3 discharge capacity at 25 °C, denoted q. Reported capacity errors are $100|\hat{q}-q|$, in percentage points (pp). Recorded EIS temperature and state of charge are covariates and are identical for the measured, virtual and recovered input of a record.

The LiBforSecUse source comprises commercial 18650 cells measured by several institutions during ageing, with capacity and impedance measurements.[22,49] The METAS-processed file used here contains 4,297 spectra, 26 physical cells and four retained institution identifiers.[23] Its published preparation uses natural cubic splines on log frequency, aligns to 61 source frequencies between 0.01 and 10,000 Hz, and represents required extrapolations as missing values. We preserve that preparation. Institution identifiers denote the source groups, without assigning anonymous records to author affiliations. The retained instruments are Modulab/MACCOR, Zahner Zennium/THALES, BioLogic SP200/EC-Lab 11.33 and BioLogic MPG205/EC-Lab 11.31 for institutions 1–4, respectively, as specified in the source documentation. Recorded capacity is in mAh. The 4,297 spectra correspond to 765 distinct cell–cycle capacity-check keys; repeated states of charge share a capacity measurement.

Each LiBforSecUse fold withholds one entire cell and trains on all other cells within the same institution. A frequency is retained only if every training spectrum is finite there. Institutions 1–4 retain 60, 59, 60 and 60 frequencies, respectively, and every test record is complete on its frozen mask. The analysis therefore retains every supplied processed record without test-dependent imputation or frequency deletion. It establishes within-institution preservation across four acquisition sources.

S12.3. Frozen predictors and separation of training from evaluation

The predictor feature order is all real impedance values, all negative imaginary impedance values, and any prespecified covariates. Zhang uses 120 spectral features; NREL–DENSO adds EIS temperature and state of charge; LiBforSecUse adds state of charge. Capacity, state of health, cycle count, cell identity, institution identity and ageing-condition metadata are excluded from predictor features.

Every predictor is a Gaussian process with kernel $a\exp\left[-\left\| x-x'\right\|^2/\left(2l^2\right)\right]$ plus a white-noise term. Input means and population standard deviations, and the capacity mean and population standard deviation, are estimated from training rows only. Constant columns receive unit scale. Initial amplitude, length and noise variance are 1, $\sqrt{d}$ and 0.01, with d the feature count. Their bounds are $\left[10^{-4},10^{4}\right]$, $\left[0.05,10^{3}\right]$ and $\left[10^{-7},1\right]$; diagonal jitter is 10^{-10}. Training likelihood selects parameters by L-BFGS-B without random restarts. The retained Zhang predictor permits 150 iterations on its full training set. Its consistent training transformation and fitted constant mean define a reproducible implementation of the chosen predictor family.

The two extensions preserve that kernel family and parameter bounds. To set hyperparameters, they use at most 64 evenly spaced source-order records per training cell and at most 75 optimizer iterations. With those parameters fixed, they refit to all training records. All 27 new fits converged without recorded warnings. The fixed predictor is applied unchanged to measured, virtual and recovered test inputs. This protocol evaluates a stated prediction function rather than performing a new search over capacity-prediction models.

Training and evaluation are separate executable stages. Each freeze manifest records source rows, physical cell identities, frequencies, model state, reference states, common resistance, excitation, code hashes, protocol hash and time. NREL–DENSO's freeze precedes its test scoring. All 26 LiBforSecUse freezes precede the first LiBforSecUse score. The evaluation verifies those hashes before scoring held-out outcomes. The held-out measured impedance is used only to instantiate its virtual specimen under the already fixed circuit basis and to calculate the original-input comparison. No test outcome selects the model, passive basis, references, branch resistance, excitation, frequency mask or noise condition.

S12.4. Passive virtual specimens and independent component equations

For $s=i2\pi f$, the virtual specimen is

$$Z^{virt}(s)=R_0+sL+\frac{K_C}{s}+\sum_{k=1}^{41}\frac{R_k}{1+s\tau_k},R_0,L,K_C,R_k\geq 0.\quad(S12.1)$$

The 41 relaxation times are fixed logarithmically between 10^{-6} and 10^{3} s. Together with R_0, L and K_C, they give 44 nonnegative coefficients. Stacked real and imaginary nonnegative least squares minimizes $\sum_f\left|Z_f^{virt}-Z_f^{meas}\right|^2/\left|Z_f^{meas}\right|^2$. Each weighted basis column is normalized during solution and restored to physical units afterwards. RC resistances below 10^{-9} of the summed fitted resistive coefficients are pruned. The final residual includes this pruning. Measured capacity never enters the fit. This fixed representation supplies a realizable specimen for acquisition; its discrepancy from measured impedance remains a separately scored endpoint.

The six branches comprise the target and five standard states. A standard state is a fixed virtual circuit instantiated in one branch; the three calibration states originate from three distinct training cells. The two unused check states are additional training states and may share a source cell with another standard. The independent forward solver uses bus voltage V, branch currents i_j, and voltages x_{jk} across the component elements. It assembles

$$\sum_j i_j=I,V-\left(r_j+R_{0j}+sL_j\right)i_j-\sum_k x_{jk}-x_{jC}=0,\quad(S12.2)$$

$$\left(1+s\tau_k\right)x_{jk}=R_{jk}i_j,sx_{jC}=K_{Cj}i_j.\quad(S12.3)$$

Zero-valued absent terms are omitted. The cell-only tap is $v_j = (R_{0j} + s L_j) i_j + \sum_k x_{jk} + x_{jC}$, excluding the external branch resistor r_j. The solver's linear system determines these taps independently at each frequency. The component-network implementation is byte-identical to that used for the 299-record validation. Its forward calculation contains no call to the inverse decoder and does not construct observations by substituting spectra into a fractional-linear tap formula. Independently integrated periodic component trajectories validate selected harmonic solutions in S12.12.

S12.5. Training-only choice of references, resistance and excitation

The 299-record protocol retains its five prespecified training rows, indexed 0, 339, 678, 1017 and 1357. The selected references are rows 0, 339 and 1357, from cells 25C01, 25C02 and 45C01; the remaining two states are checks. Their shared external resistance is the median magnitude across all five candidate spectra and frequencies, 0.9231307038 Ω. Total current peak is fixed at 0.005 A.

For NREL–DENSO and each LiBforSecUse fold, candidate states are up to five evenly spaced source-order records per training cell. At frequency f, candidate magnitude scale m_f is the median magnitude across candidates. A calibration triple from three different physical training cells maximizes $min_f \, min_{a<b} \left| z_{af} - z_{bf} \right| / m_f$, with deterministic row-order resolution of ties. Two further unused states are chosen by the corresponding max–min separation rule. Only training impedances enter these choices. The common external resistance is the median across physical training cells of their within-cell median $\left| Z^{virt} \right|$ over records and retained frequencies.

With those five standards fixed, every training candidate is independently solved as a target at 1 A. If $V_{max}^{(1\,A)}$ is the maximum cell-tap magnitude over these networks and frequencies, the frozen peak current is

$$I_{peak} = min\left(3\,A, \frac{5\,mV}{V_{max}^{(1\,A)}} 1\,A\right). \quad (S\,12.4)$$

The NREL–DENSO reference states are source rows 25, 78 and 420 from cells 2, 6 and 27; unused checks are rows 0 and 328 from cells 1 and 20. The selected resistance is 1.4911063 mΩ and total current peak is 1.5388189 A. Across LiBforSecUse folds, resistance ranges from 18.8465 to 23.1163 mΩ and total current peak from 0.340419 to 0.953605 A. Every held-out target and control uses its fold's unchanged setting. The 5-mV training-candidate envelope is a design target. Maximum physical cell-tap peaks attained across all tested geometries are 5.0822 mV for NREL–DENSO and 7.0251 mV for LiBforSecUse; these values are recorded without post-test amplitude adjustment.

S12.6. Finite sampled acquisition and decoder information

The independently solved harmonic taps generate four sinusoidal cycles with 64 samples per cycle. The common voltage gain is $h(f) = 1.13\, e^{i2^\circ} / (1 + if / 30000)$ and common current feedthrough is $b(f) = 0.03\, R / (1 + if / 5000)$ in Ω, with f in Hz. The sampled voltage is the real part of $\left(h(f) v_j + b(f) I\right) e^{i\omega t}$ plus sample noise. Demodulation uses the complex coefficient $(2/N) \sum_{n=0}^{N-1} v_n e^{-i 2\pi n / 64}$, with $N = 256$. The voltage phasor is divided by the contemporaneous total-current phasor.

Independent Gaussian voltage samples have RMS 0, 2 or 20 μV. Noisy conditions additionally use a shared current-channel sample RMS of 1 μA. The stated values refer to individual time samples; the finite demodulation determines their phasor effects. The common current denominator cancels in the reference cross-ratio, whereas independent voltage-channel perturbations propagate through the inverse. Seeds 202610310–202610314 give five realizations. A record and seed receive the same standardized voltage and current samples across geometry conditions and voltage-noise scales. The main comparison uses 2 μV; 0 and 20 μV are retained controls.

Let y_t, y_1, y_2, y_3 denote current target and reference observations, and z_1, z_2, z_3 the known standalone impedances of the actual virtual reference states. The homogeneous inverse is

$$a=(y_t-y_1)(y_2-y_3)(z_2-z_1),\ b=(y_t-y_3)(y_2-y_1)(z_2-z_3),\ \hat{z}_t=\frac{b\,z_1-a\,z_3}{b-a}. \quad (S12.5)$$

The target spectrum, target capacity, circuit coefficients, predictor, branch resistance and bus impedance are absent from the decoder interface. The same three references separately decode the two unused check states. Distinct current reference correspondences and a nondegenerate inverse are the operating conditions of the calibration. Conventional normalized three-point fractional-linear calibration uses the same information and matches the homogeneous inverse at numerical precision. The affirmative result is construction of an acquisition to which that calibration applies.

S12.7. Mechanistic controls and restoration

The matched condition uses $r_j = R > 0$ for all six branches. The target-only mismatch changes r_t to $1.1\,R$, leaving calibration and check paths unchanged. In the noiseless circuit, the unchanged inverse then returns $Z_t^{virt}/1.1$, predicting a 9.090909% relative spectral error without fitting a control parameter. The heterogeneous condition imposes fixed factors $(0.6, 0.8, 1, 1.2, 1.4, 1)$ on the six paths. Restoration returns all factors to one while reusing the identical sampled noise. The restored and matched results coincide for every record and seed.

The zero-path control sets all external resistances to zero. All cell-only taps then equal the bus voltage, removing cell-specific contrast from this observation channel. The audit checks the collapse and does not invert a degenerate set of references. A separate calibration-mismatch control supplies original measured reference spectra while acquiring their fitted virtual circuits. It quantifies the effect of reference values that do not exactly describe the states actually measured. An uncorrected comparator submits the observed matched target tap divided by total current directly to the frozen predictor, with the same common gain and feedthrough. All controls retain the same predictor, record covariates and measured capacity outcomes.

S12.8. Endpoints, aggregation and bootstrap

The per-record recovery spectral error and prediction displacement are

$$e_i=\left[\frac{1}{F}\sum_f \frac{\left|Z_{if}^{rec}-Z_{if}^{virt}\right|^2}{\left|Z_{if}^{virt}\right|^2}\right]^{1/2},\ d_i=\left|g\left(Z_i^{rec},u_i\right)-g\left(Z_i^{virt},u_i\right)\right|. \quad (S12.6)$$

Here u_i contains unchanged covariates. Measured-to-virtual spectral error replaces the two spectra in e_i with virtual and measured spectra. Its prediction displacement similarly compares $g\left(Z_i^{virt},u_i\right)$ with $g\left(Z_i^{meas},u_i\right)$. Original, virtual and recovered MAEs compare each prediction against the same observed capacity. Consequently, a smaller capacity MAE under a distorted observation is distinguishable from preservation of the original prediction. Recordwise, the absolute change in capacity absolute error is bounded by d_i for the virtual-to-recovered comparison; the output audit verifies this inequality.

For NREL–DENSO and LiBforSecUse, we average each error over the five fixed seeds, average over records within each physical cell, then weight cells equally. We average absolute errors rather than averaging predictions before scoring. The LiBforSecUse primary aggregate therefore weights its 26 cells equally; institution-specific aggregates and a secondary equal-institution summary remain in the machine-readable outputs. Each worst-cell result maximizes the relevant within-cell mean independently.

The paired bootstrap uses 10,000 whole-cell resamples and seed 202610319. NREL–DENSO resamples its seven held-out cells. LiBforSecUse resamples within each institution, preserving the observed counts of 10, 6, 6 and 4 cells. The same sampled cells generate each endpoint, baseline and paired difference. Intervals are percentile 95% intervals conditional on the fitted models and five noise realizations. Folds can share training cells; models are held fixed during this descriptive resampling. Noise seeds, individual frequencies and repeated

state-of-charge spectra are not independent experimental units. The Zhang example retains its single-cell record summaries, including the mean of the five per-seed median spectral errors.

S12.9. Preservation results and the three input baselines

In the 299-record example, original measured-input, virtual-input and recovered-input MAEs are 2.201167, 2.238834 and 2.234174 mAh, respectively, at 2-μV sample RMS. Mean absolute prediction displacement from virtual standalone is 0.086067 mAh. The mean of the five per-seed median recovery spectral errors is 0.131009%; the passive fit's test-record median spectral error is separately 0.185344%. Noiseless acquisition changes the virtual standalone prediction by a mean of 2.89×10^{-13} mAh. This complete trajectory illustrates preservation within one held-out physical cell.

Table 36 gives the two whole-cell extensions with paired uncertainty. Across 26 LiBforSecUse cells, recovered spectra differ from virtual standalone by a cell-balanced 0.03987%, and predictions move by 2.858 mAh. Measured-input, virtual-input and recovered-input MAEs are 86.058, 99.114 and 99.207 mAh. Thus the additional acquisition stage changes virtual-input MAE by 0.093 mAh, with a 95% interval of 0.030–0.159 mAh, while the measured-to-virtual input change has its own larger prediction displacement. Table 37 reports each institution separately (Extended Data Fig. 9).

For the seven prespecified NREL–DENSO cells, recovery spectral error is 0.17787% and prediction displacement is 0.203 pp. The measured-input, virtual-input and recovered-input MAEs are 2.235, 9.142 and 9.140 pp. The acquisition preserves the virtual input and its prediction closely; the larger accuracy change occurs when measured spectra are represented by the fixed passive basis (Extended Data Fig. 10). An existing post hoc diagnostic of the frozen inputs localizes 95.18% of the pooled squared fractional spectral change, and 99.77% of the pooled squared standardized feature change, to frequencies at or above 1 kHz. The basis in equation (S12.1) has $\mathrm{Re}\, Z = R_0 + \sum_k R_k / \left[1 + \left(\omega \tau_k\right)^2\right]$, so its real part cannot increase with frequency. Such an increase between 1 kHz and 31.6 kHz occurs in 343 of 359 training records and 107 of 108 test records. These checks describe the representation change already present before acquisition. These diagnostics did not alter the prespecified analysis. The separately labelled follow-up in S16 tests a broader passive representation after completion of the primary analysis.

Supplementary Table 36 | Primary whole-cell estimates at 2-μV voltage sample RMS. Entries are cell-balanced estimates with paired whole-cell 95% bootstrap intervals in parentheses. Capacity and prediction quantities are in pp for NREL–DENSO and mAh for LiBforSecUse; spectral quantities are percentages. "Virtual" means the standalone fitted passive circuit. The measured-to-virtual endpoints describe specimen construction; recovery endpoints compare recovered input with virtual standalone.

Endpoint	NREL–DENSO (capacity: pp)	LiBforSecUse (capacity: mAh)
Measured-input capacity MAE	2.235 (1.707–2.775)	86.058 (62.840–112.788)
Passive virtual-input capacity MAE	9.142 (7.715–10.353)	99.114 (74.719–126.660)
Recovered-input capacity MAE	9.140 (7.726–10.341)	99.207 (74.809–126.731)
Recovery spectral RMS error (%)	0.1779 (0.1704–0.1879)	0.0399 (0.0370–0.0424)
Recovery prediction displacement	0.203 (0.187–0.219)	2.858 (2.384–3.342)
Recovered minus virtual MAE	-0.002 (-0.026–0.025)	0.093 (0.030–0.159)
Recovered minus measured MAE	6.905 (5.546–8.276)	13.149 (5.880–20.685)
Measured-to-virtual spectral RMS error (%)	3.245 (3.012–3.515)	0.411 (0.393–0.431)
Measured-to-virtual prediction displacement	7.654 (6.891–8.509)	31.817 (25.906–37.924)

Supplementary Table 37 | LiBforSecUse preservation within each institution. All capacity MAEs and prediction displacements are in mAh. Recovery errors are percentages. Each row weights that institution's physical cells equally; parenthetical counts give cells and spectra. Full intervals are retained in the source summary tables.

Institution (cells; spectra)	Measured MAE	Virtual MAE	Recovered MAE	Recovery error (%)	Displacement
1 (10; 2297)	107.425	119.972	119.967	0.0392	1.769
2 (6; 1217)	51.826	75.745	76.053	0.0321	5.367
3 (6; 607)	87.747	107.443	107.518	0.0427	3.516
4 (4; 176)	81.453	69.527	69.572	0.0492	0.829

S12.10. Controlled mismatch, noise and recovery

Table 38 separates spectral recovery, prediction displacement and capacity error under the fixed perturbations. The 10% target-path change produces the predicted 9.090909% noiseless spectral error in both new cohorts. Its NREL–DENSO capacity MAE is lower than the matched virtual-input MAE even though the recovered spectrum is wrong by the predicted factor. This is compensation of predictor error, which is visible because the spectral and displacement endpoints are scored independently. At 2 μV, heterogeneous paths produce cell-balanced spectral errors of 243.761% for NREL–DENSO and 62.689% for LiBforSecUse. Returning to equal paths restores the primary results exactly under paired samples. These perturbation–restoration controls identify the common-branch condition that enables the calibration.

Supplementary Table 38 | Acquisition controls with the same frozen predictors. NREL capacity and displacement are in pp; LiB quantities are in mAh. All spectral errors compare the input supplied to the predictor with the virtual standalone spectrum. The last row for each cohort is the uncorrected observed tap, rather than a decoded input. Reference-calibration mismatch is evaluated without added noise. Restored values coincide with matched values record by record and seed by seed.

Cohort	Condition	Recovery error (%)	Displacement	Input capacity MAE
NREL	Matched, no added noise	2.83e-13	2.56e-11	9.142
NREL	Matched, 2 μV	0.1779	0.203	9.140
NREL	Matched, 20 μV	1.7822	2.026	9.395
NREL	Target path +10%, no added noise	9.0909	2.846	7.372
NREL	Target path +10%, 2 μV	9.0910	2.862	7.370
NREL	Heterogeneous paths, 2 μV	243.7612	10.826	17.029
NREL	Restored matched paths, 2 μV	0.1779	0.203	9.140
NREL	Measured reference values, no added noise	2.7322	6.582	3.806
NREL	Uncorrected matched tap, no added noise	78.2965	46.926	37.969
LiB	Matched, no added noise	2.48e-13	4.19e-09	99.114
LiB	Matched, 2 μV	0.0399	2.858	99.207
LiB	Matched, 20 μV	0.4002	29.303	107.734
LiB	Target path +10%, no added noise	9.0909	111.373	137.535
LiB	Target path +10%, 2 μV	9.0909	111.437	137.675

Cohort	Condition	Recovery error (%)	Displacement	Input capacity MAE
LiB	Heterogeneous paths, 2 µV	62.6890	442.441	447.395
LiB	Restored matched paths, 2 µV	0.0399	2.858	99.207
LiB	Measured reference values, no added noise	0.4617	32.035	88.421
LiB	Uncorrected matched tap, no added noise	76.0641	499.862	528.848

S12.11. Individual cells and worst-cell results

Tables 39–40 retain every held-out physical cell at the primary noise level. The analysis records (S20) preserve unrounded values, baseline construction errors, completeness counts and the number of seed–record evaluations. The maximum is calculated separately for spectral error, prediction displacement, recovered capacity MAE and capacity-MAE change. These endpoint-specific maxima identify different cells.

Supplementary Table 39 | All seven prespecified NREL–DENSO cells. Capacity MAEs and displacement are in pp; recovery error is a percentage. Each row averages errors over the five fixed noise seeds and that cell's source records.

Cell	Spectra	Measured MAE	Virtual MAE	Recovered MAE	Recovery error (%)	Displacement
7	14	2.405	10.769	10.770	0.1770	0.170
10	14	2.227	11.175	11.146	0.2051	0.232
13	26	1.589	5.546	5.579	0.1658	0.235
17	16	3.452	8.514	8.466	0.1736	0.197
24	12	1.194	10.502	10.494	0.1686	0.199
30	14	1.857	8.380	8.355	0.1726	0.186
31	12	2.919	9.110	9.170	0.1823	0.204

Supplementary Table 40 | All 26 LiBforSecUse whole-cell holdouts. Capacity MAEs and displacement are in mAh; recovery error is a percentage. Cell identifiers retain their institution prefix. Every prediction is from a model trained on other cells within that same institution.

Cell	Spectra	Measured MAE	Virtual MAE	Recovered MAE	Recovery error (%)	Displacement
Inst1-04	130	16.069	43.018	43.045	0.0356	1.497
Inst1-05	238	81.949	95.935	95.879	0.0414	1.461
Inst1-06	232	58.287	90.971	91.018	0.0445	2.515
Inst1-09	156	24.421	16.273	16.327	0.0362	1.583
Inst1-10	394	129.217	140.784	140.820	0.0417	1.797
Inst1-11	396	218.566	223.792	223.948	0.0407	2.117
Inst1-13	276	59.654	51.764	51.796	0.0374	1.452
Inst1-14	79	304.732	313.384	313.194	0.0386	1.616
Inst1-17	198	107.664	158.079	157.887	0.0392	2.332
Inst1-19	198	73.690	65.725	65.756	0.0364	1.320
Inst2-06	202	23.781	66.399	66.613	0.0330	3.223

Cell	Spectra	Measured MAE	Virtual MAE	Recovered MAE	Recovery error (%)	Displacement
Inst2-07	203	23.455	35.369	35.714	0.0342	3.008
Inst2-10	203	152.636	176.784	176.766	0.0318	4.654
Inst2-11	203	17.065	83.471	83.878	0.0298	8.149
Inst2-12	202	45.581	40.708	41.341	0.0342	6.202
Inst2-13	204	48.436	51.741	52.008	0.0295	6.964
Inst3-01	121	48.466	82.441	82.158	0.0402	2.980
Inst3-02	96	89.647	76.937	76.964	0.0417	1.546
Inst3-03	102	19.481	57.007	56.999	0.0430	4.610
Inst3-04	96	146.205	171.008	171.156	0.0425	4.547
Inst3-07	96	49.453	53.120	53.141	0.0451	1.359
Inst3-08	96	173.231	204.143	204.691	0.0435	6.052
Inst4-03	59	143.134	145.149	145.206	0.0444	0.675
Inst4-04	59	64.574	35.290	35.310	0.0681	1.068
Inst4-07	29	87.535	64.874	64.950	0.0608	0.945
Inst4-08	29	30.570	32.796	32.820	0.0233	0.630

The largest primary recovery errors are 0.2051% for NREL cell 10 and 0.06813% for LiBforSecUse Inst4-04. Maximum prediction displacement occurs for NREL cell 13 (0.235 pp) and Inst2-11 (8.149 mAh), whereas maximum recovered capacity MAE occurs for cell 10 (11.146 pp) and Inst1-14 (313.194 mAh). The largest signed recovered-minus-standalone MAE increases are 0.060 pp for cell 31 and 0.633 mAh for Inst2-12.

S12.12. Numerical independence and complete output audit

The independently solved acquisition evaluates 46 record–conditions per source record: four geometries with one noiseless and ten noisy evaluations each, plus measured-reference calibration and uncorrected-input controls. This produces 4,968 NREL–DENSO and 197,662 LiBforSecUse prediction records, all finite. Aggregation reduces them to fourteen condition families after seed averaging. The independent audit verifies expected rows and conditions, source/model/protocol/code hashes, disjoint physical training and test cells, freeze order, prediction arithmetic, complete coverage, paired restoration and worst-cell selection. Independently recomputed summary estimates and bootstrap endpoints agree within 3.41×10^{-13} in their reported units. The saved original, virtual and selected noisy predictions also agree with independent inference from the frozen states at numerical precision.

Component-current balance, standalone port closure and the exact target-mismatch scaling are checked throughout acquisition. Table 41 reports their maxima. The actual time-integration check uses the first source record of each held-out cell at the middle retained frequency, initialized at the independently solved periodic state and integrated through the component differential equations before demodulation. All 33 probes have positive fitted inductances and pass. The seven NREL probes share a common fresh-input signature, so they are seven cell-associated checks of the same target circuit state. The earlier Zhang validation separately integrated fifteen cases: three prespecified target rows at five prespecified frequencies, with maximum relative cell-phasor error 5.62×10^{-9}.

Supplementary Table 41 | Numerical verification of the independent acquisition. Relative quantities are fractions, without multiplication by 100. Tap peaks include all tested geometries. Harmonic acquisition and finite sampled demodulation generate the primary data; the stated integration probes independently verify selected component trajectories.

Verification quantity	NREL–DENSO	LiBforSecUse
Maximum Kirchhoff current residual (A)	4.45e-16	3.33e-16
Maximum relative component-to-port residual	1.27e-14	1.01e-14
Maximum record relative recovery RMS, no noise	1.03e-14	8.58e-14
Maximum relative error from Z/1.1, target mismatch	4.09e-14	2.16e-13
Maximum relative restored-versus-matched difference	0.000000	0.000000
Maximum relative tap spread at zero external path	2.27e-15	3.31e-15
Maximum relative difference from same-information three-point calibration	1.94e-15	2.15e-15
Maximum physical cell-tap peak over all tested geometries (V)	0.005082	0.007025
Periodic time-integration probes	7	26
Maximum relative time-integration phasor error	9.67e-11	2.67e-10

S12.13. Source-input identity check

The native NREL author CSV contains two full predictor-input signatures shared by training and test cells: fresh relative capacity $q = 1$, state of charge 0.5, and temperature −10 or 25 °C. They affect fourteen test rows, two per held-out cell, and 45 training rows. Their equality is present in the source file; it does not establish whether the source values arose from separate acquisitions, common preprocessing or averaging. The primary analysis retains all 108 prespecified rows. An explicitly post hoc diagnostic removes the fourteen shared-signature test rows and summarizes the existing predictions for the remaining 94 records, without refitting or changing any acquisition choice. It retains all seven physical test cells and the same five seeds. The measured-input, virtual-input and recovered-input MAEs become 2.556, 9.312 and 9.301 pp; recovery error is 0.17256% and displacement is 0.191 pp. The scientific separation of representation change and acquisition recovery is unchanged. Table 42 gives the paired comparison; full intervals and exact source-row flags are retained.

The LiBforSecUse source contains one exact cross-cell predictor-input signature affecting two records, Inst3-07_2900_20 and Inst3-08_1700_20. These records remain in their prespecified primary folds. This input-identity audit complements the disjoint physical-cell split and does not alter its frozen models or primary population.

Supplementary Table 42 | NREL source-overlap diagnostic using saved predictions. Capacity MAEs and displacement are in pp; recovery error is a percentage. Both rows use seven cells and the same five noise realizations. The 94-record row is post hoc and excludes shared input signatures from evaluation only.

Analysis	Measured MAE	Virtual MAE	Recovered MAE	Recovery error (%)	Displacement
Prespecified 108 records	2.235	9.142	9.140	0.1779	0.203
Post hoc 94 records	2.556	9.312	9.301	0.1726	0.191

S12.14. Reproduction and display provenance

Figure 6 presents the independent-acquisition prediction comparisons. Extended Data Fig. 9 gives all LiBforSecUse whole-cell results and Extended Data Fig. 10 gives the prespecified NREL–DENSO replication.

Figure 3, Extended Data Figs. 7 and 8, S10 and Supplementary Fig. 10 retain the controlled geometry and information comparisons.

Tables 35–42 report cohort definitions, the three input baselines, acquisition controls, individual-cell results and numerical checks. The underlying protocols, frozen predictors, reference identities, frequency vectors, record-level outputs, per-cell metrics, bootstrap summaries and source-overlap diagnostics are retained in the analysis records (S20). Verification of saved outputs is distinguished from re-running circuit fitting, predictor training, acquisition simulation and resampling.

S13 Superconducting precursor selection and incomplete trajectory records

S13.1 Source-defined protocols and comparison targets

Pressure release reverses the ranking of two BST precursor states at a common nominal quench temperature of 77 K. The 20.3-GPa precursor has the higher source onset, 8.3 versus 6.2 K, but the lower recovered onset, 4.9 versus 10.2 K. All four values use the source study's onset criterion. The 10.2-K value identifies the higher transition component in the recovered mixed sample.[25] The scientific target is the ordering of the recovered transitions and the difference between their source-to-release changes.

Let $T_{S,j}$ and $T_{R,j}$ denote the source and recovered onsets for protocol j. Define $A_j = T_{R,j} - T_{S,j}$ and the source-to-recovered ratio $Q_j = T_{R,j} / T_{S,j}$. The approximately neutral 8.0-GPa protocol and the near-matched 32.3-GPa, 4.2-K protocol complete the within-study comparison (Supplementary Table 43). Each row retains its own source pressure and quench temperature.

Supplementary Table 43 | Source and recovered onsets in the BST protocol record.

Source pressure (GPa)	Quench (K)	Source onset (K)	Recovered onset (K)	Amplification (K)
8.0	77	4.8	approximately 4.8	approximately 0
20.3	77	8.3	4.9	−3.4
33.3	77	6.2	10.2, high component	+4.0
32.3	4.2	at least 6.2 by branch ordering	5.9	at most −0.3

Source: Deng et al.[25] The 8.0-GPa recovered value is an approximate source-figure reading and supplies the neutral comparison. The two 77-K loss/amplification rows use text-reported values. The cold-source entry is an ordering constraint; its precise source onset is left as a free compatible value.

S13.2 Rank reversal excludes order-preserving release laws

Proposition S13a. Let a common candidate release law map source onset to recovered onset through a nondecreasing scalar function f. For source onsets $T_{S,1} > T_{S,2}$, the law requires $f(T_{S,1}) \geq f(T_{S,2})$. If the recovered ordering is $T_{R,1} < T_{R,2}$, no such law represents both records.

Proof. Monotonicity imposes the first ordering directly, in contradiction to the recovered ordering. The contradiction holds for every nondecreasing f, including every common additive shift and every common nonnegative multiplicative factor. Thus a higher source onset is not an order-preserving precursor-selection rule for these records.

Define the source gap $g_S = T_{S,1} - T_{S,2}$ and reversed recovered gap $g_R = T_{R,2} - T_{R,1}$. The release-response contrast is

$$D = A_2 - A_1 = g_S + g_R. \quad (S13a)$$

For the 20.3- and 33.3-GPa protocols, $g_S = 2.1$ K, $g_R = 5.3$ K and $D = 7.4$ K. This identity separates the initial disadvantage of the successful precursor from its final recovered advantage. It supplies a protocol-specific selection result directly from the four retained onsets.

S13.3 Complete deterministic sensitivity bounds

Let every reported source and recovered onset vary independently within its nominal value plus or minus ϵ. Since the relevant gaps are affine in those inputs, the exact extrema occur at endpoints:

$$g_S \in [2.1 - 2\epsilon, 2.1 + 2\epsilon], g_R \in [5.3 - 2\epsilon, 5.3 + 2\epsilon],$$
$$D \in [7.4 - 4\epsilon, 7.4 + 4\epsilon]. \quad (S13b)$$

At $\epsilon = 0.2$ K, both reversed orderings remain strict and $D \geq 6.6$ K (Supplementary Table 44). Independent enumeration of all sixteen four-input corners gives the same endpoints. The 0.2-K convention is a displayed-value stress test, not a confidence interval. The affine bounds also give exact failure radii: the precursor rank reversal remains strict for every $\epsilon < 1.05$ K; the opposite loss and amplification signs remain strict for every $\epsilon < 1.70$ K; D remains positive for $\epsilon < 1.85$ K; the warm-cold advantage remains positive for $\epsilon < 2.15$ K; and compression-envelope escape remains positive for $\epsilon < 0.60$ K. Supplementary Fig. 11b displays the full functions through 2.2 K.

For positive source onsets, ratio monotonicity gives

$$Q_j \in \left[\frac{T_{R,j} - \epsilon}{T_{S,j} + \epsilon}, \frac{T_{R,j} + \epsilon}{T_{S,j} - \epsilon}\right]. \quad (S13c)$$

The two 77-K intervals, 0.5529–0.6296 and 1.5625–1.7333, remain separated on opposite sides of unity. A common source-to-recovered retention factor therefore fails throughout the entire sensitivity set. Supplementary Fig. 11a shows the complete transfer-ratio intervals; all numerical endpoints are retained in the machine-readable data.

Supplementary Table 44 | Nominal contrasts and exact sensitivity endpoints at ε = 0.2 K.

Quantity	Nominal	Lower endpoint	Upper endpoint	Symmetric failure radius (K)
Source ordering gap (K)	2.1	1.7	2.5	1.05
Recovered reverse-ordering gap (K)	5.3	4.9	5.7	2.65
Amplification, 20.3 GPa (K)	−3.4	−3.8	−3.0	1.70
Amplification, 33.3 GPa (K)	+4.0	+3.6	+4.4	2.00
Release-response contrast D (K)	7.4	6.6	8.2	1.85
Ratio Q, 20.3 GPa	0.5904	0.5529	0.6296	1.70
Ratio Q, 33.3 GPa	1.6452	1.5625	1.7333	2.00
Compression-envelope excess E (K)	1.2	0.8	1.6	0.60

S13.4 Trajectory advantage survives a missing source onset

The 4.2-K protocol begins at 32.3 GPa and yields a recovered onset of 5.9 K. The source reports a decreasing compression branch between the near-matched starting pressures of 32.3 and 33.3 GPa, so

$$\Delta_S = T_S(32.3) - T_S(33.3) \geq 0.$$

Consequently,

$$A_{77} - A_{4.2} = 10.2 - 5.9 + \Delta_S = 4.3 + \Delta_S \geq 4.3\,K. \quad (S13d)$$

This applies to every cold-source value compatible with the reported ordering. Shifting the warm recovered onset down by 0.2 K and the cold recovered onset up by 0.2 K gives the lower sensitivity bound $3.9 + \Delta_S \geq 3.9$ K. The source-ordering constraint is retained while the two recovered values are perturbed. Figure 4c expresses the same result as interval geometry: the warm trajectory has $A_{77} = +4.0$ K, whereas the cold trajectory obeys $A_{4.2} \leq -0.3$ K. Their separation is therefore at least 4.3 K. The unreported source value is not assigned a fitted or interpolated point. Updated diffraction places both 32.3- and 33.3-GPa source conditions in the same cubic high-pressure structural family, so the warm-cold bound is not generated by crossing a known average structural phase boundary.[51]

S13.5 Escape from the measured compression set

Let $\Gamma_{\uparrow}$ be the source-defined measured compression set and $T_{comp,max}$ its largest reported onset. Every state in that measured set has onset at most $T_{comp,max}$. A recovered onset above it therefore excludes identification with any measured compression state. Under the non-interacting component model, a mixture whose component onsets are all bounded by $T_{comp,max}$ also cannot initiate superconductivity above that maximum.

The BST record gives $T_{comp,max} \simeq 9.0$ K and $T_R = 10.2$ K, hence $E = T_R - T_{comp,max} = 1.2$ K. The adverse 0.2-K endpoint shifts leave $E \geq 0.8$ K. The high recovered component is therefore outside the measured compression-onset range throughout the sensitivity set. This is the scalar observed-set exclusion corresponding to the answer-set construction in S1.

S13.6 Calculated branch gain and ambient stabilization

The source's harmonic calculations distinguish amplification along a modeled basin from that basin's reachability at ambient pressure.[25] Calculated Im-3m transition temperatures rise from 1.7 K at 40 GPa on compression to 6.0 K at 20 GPa and 7.2 K at 15 GPa on decompression. The tabulated 5.5-K gain is compatible with favorable same-basin evolution. At 0 GPa, the modeled Im-3m and C2/m structures are not harmonic local minima (Supplementary Table 45).

Thus the ambient recovered component requires stabilization or transformation beyond passive harmonic continuation of those modeled structures. Compatible routes include anharmonic stabilization, a transformed basin, defects, microstructure, atomic ordering and interacting phase coexistence. The endpoint restriction follows from the stated harmonic model; the source and recovered onsets determine the experimental ranking separately.

Updated diffraction resolves the sequence R-3m, C2/m, C2/c and a cubic high-pressure family near 11, 16 and 25 GPa.[51] The 20.3-GPa experimental precursor belongs to the updated C2/c regime, while the older adverse-branch calculation used C2/m. Those phase labels retain their respective source definitions. The 32.3- and 33.3-GPa precursors share the high-pressure family. Its cubic charge-density symmetry coexists with an atomic-order coordinate, providing structural context for history-dependent recovery.

Supplementary Table 45 | Source-calculated transition temperatures and harmonic endpoints.

Modeled phase	Source path	Pressure (GPa)	Calculated Tc (K)	Harmonic local minimum
R-3m	compression	9	1.3	yes
C2/m	compression	10	1.7	yes
C2/m	compression	14	2.3	yes
C2/m	compression	20	2.6	yes
C2/m	decompression	1	1.2	yes
C2/m	ambient endpoint	0	not assigned	no
Im-3m	compression	40	1.7	yes

Modeled phase	Source path	Pressure (GPa)	Calculated Tc (K)	Harmonic local minimum
Im-3m	decompression	20	6.0	yes
Im-3m	decompression	15	7.2	yes
Im-3m	ambient endpoint	0	not assigned	no

Source: the calculations retained from Deng et al.[25] “Not assigned” denotes an unstable modeled endpoint rather than a calculated zero transition temperature. Calculated values and measured transition onsets remain separately identified.

S13.7 Component response and retained source information

Current-dependent transport supports the superconducting origin of the high recovered component: its onset shifts from 10.2 to 9.8 K as the current increases from 10 to 100 mA. A separate 31.6-GPa, 77-K record shows the high component beginning to degrade during thermal excursions near 77 K. These observations place the recovered component within a preparation-and-retention history (Supplementary Table 46). The target used for precursor selection is the onset of that component under the source-defined recovery conditions.

Supplementary Table 46 | Source observations accompanying the recovered component.

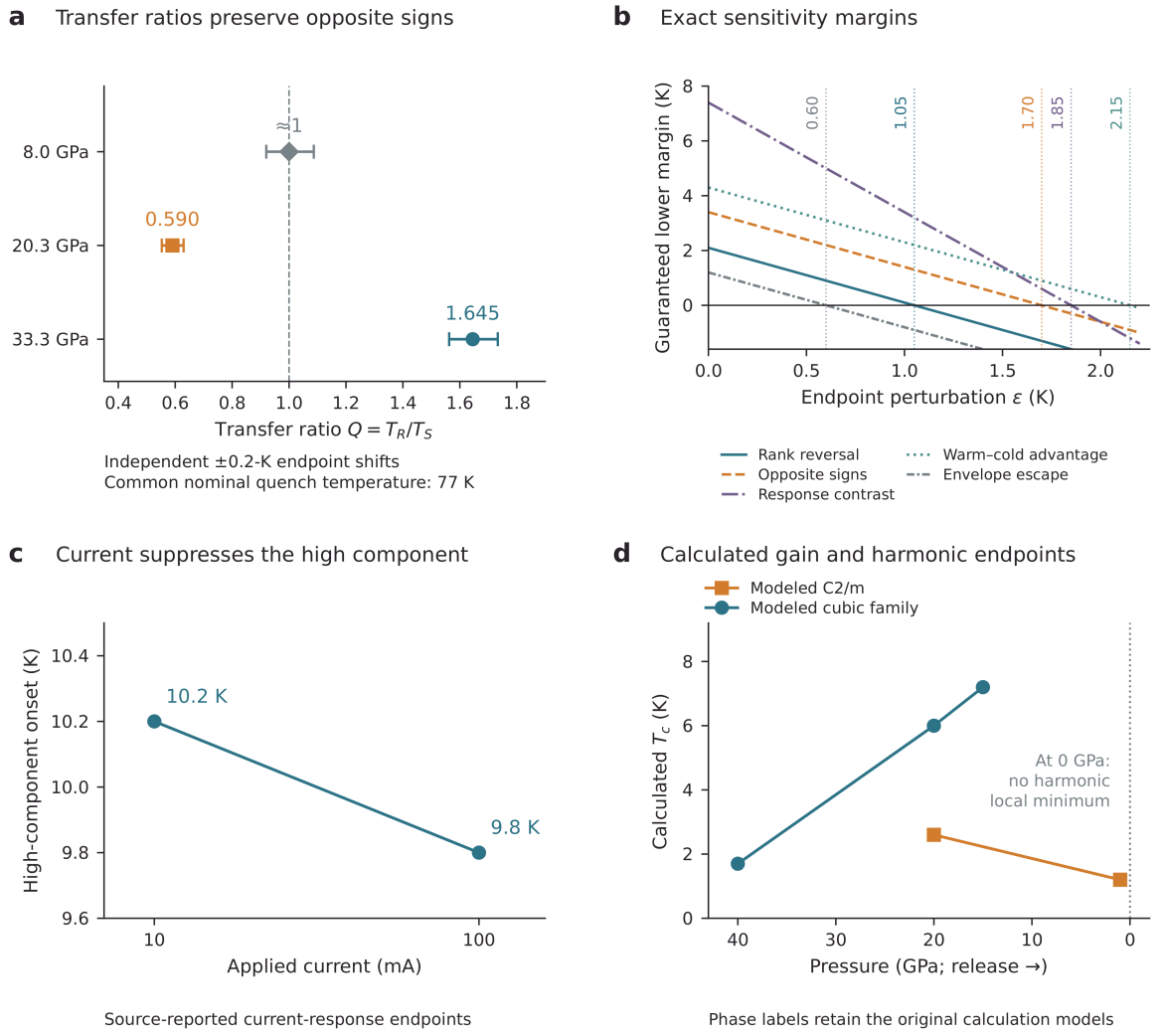
Source observation	Retained result	Use in this analysis
Current increase, 10 to 100 mA	High onset shifts from 10.2 to 9.8 K	Superconducting transport context
Thermal excursions, 31.6-GPa / 77-K source	High component begins to degrade	Recovery-history context
Repeated low-temperature measurements	High component changes over the recorded five-day sequence	Time-history context
Magnetic response after sample handling	Approximately 46% diamagnetic shift below approximately 4 K	Characterization of the surviving lower branch

Source: Deng et al.[25] The transition component, observation modality and history are retained separately in each row.

S13.8 Reproduction and figure sources

Tables 43–46 give the protocol values, onset definitions, source-branch ordering, harmonic calculations and structural assignments used in Figure 4 and Supplementary Fig. 11. Gaps, amplification changes, transfer-ratio intervals, deterministic bounds and failure radii are calculated from the stated decimal inputs and checked independently at all sixteen perturbation corners. The analysis records (S20) include the underlying calculations and figure-generation code. The four protocol histories remain the source units; perturbation corners are alternative numerical inputs to the same records.

Supplementary Figure 11 | Superconducting release ratios, sensitivity and component response



a, Source-to-recovered ratios for the three 77-K protocols. Whiskers give exact extrema under independent ±0.2-K endpoint shifts. **b,** Guaranteed lower margins under endpoint perturbation ϵ. Vertical labels mark the exact first zero of compression-envelope escape (0.60 K), precursor rank reversal (1.05 K), opposite response signs (1.70 K), positive response contrast (1.85 K) and the warm–cold trajectory advantage (2.15 K). The warm–cold calculation retains the source-ordering constraint and perturbs the two recovered onsets. **c,** Source-reported high-component onsets at 10 and 100 mA. **d,** Tabulated transition temperatures in the original C2/m and cubic-family harmonic calculations; connecting lines are guides. Neither modeled structure is a harmonic local minimum at 0 GPa. The updated structural assignment places the 20.3-GPa experimental source in C2/c, while the older calculation retains its original C2/m model identity. Sources: Deng et al. and Halbert et al.[25,51]

S14 Surfactant measurements and energetic comparisons

S14.1 Measured formulation and frequency coverage

The CAPB–SLES measurements are reported here for the first time. Sixty formulations span pH 4.5 and 5.5, total active-surfactant concentrations of 8, 10 and 12 wt%, CAPB:SLES active-mass ratios of 1:0, 2:1, 1:1, 1:2 and 0:1, and 0 or 8 wt% added NaCl. Concentrations refer to the final formulation mass after salt addition. Steady-shear and oscillatory tests were repeated three times per formulation. The analysis uses arithmetic mean viscosity, storage modulus and loss modulus at the corresponding shear rates or frequencies. Each formulation

has 21 paired mean moduli from 0.01 to 100 Hz, giving 1,260 paired responses; the steady-shear dataset contains 941 mean viscosity values. Loss compliance is calculated from each paired mean response. Methods gives the preparation, 0.5% strain amplitude, linear-response verification, instrument, geometry and acquisition protocol. The formulation is the experimental unit; the ranges below quantify deterministic preprocessing sensitivity.

Nominal salt pairs match pH, CAPB weight percentage, SLES weight percentage and recorded frequency. There are fifteen pairs per pH, thirty pairs overall and 630 pair–frequency comparisons. Matching is exact at the recorded frequencies and requires no frequency interpolation. The source-row crosswalk retains the correspondence between the original components, processed components and comparison rows. Frequency observations remain nested within their formulations.

S14.2 Transformation from modulus components to energetic contrasts

For each measured storage–loss pair, write $G^* = x + iy$ with $x = G'$ and $y = G''$. The positive loss compliance is

$$J''(x, y) = \frac{y}{x^2 + y^2}.$$

The raw value is calculated from the unsmoothed paired mean moduli. The processed value is calculated separately from the corresponding processed components. Processing uses the archived nine-point, second-order Savitzky–Golay operation in log-response coordinates. The retained positive component ranges retain the residual-based processing variation used in the original analysis. Supplementary Fig. 12 shows all original component spectra and all raw/processed compliance and contrast pairs.

At equal small stress amplitude τ_0, the linear-response work density is $w = \pi \tau_0^2 J''$. Therefore the normalized difference for a matched pair is

$$\frac{\Delta w}{\pi \tau_0^2} = \Delta J'' = J''_{0\%\,NaCl} - J''_{8\%\,NaCl}.$$

A positive difference means greater inferred energy loss in the lower-salt formulation under that loading comparison. The support-cancellation argument in S2 supplies the physical interpretation when the unresolved series contribution is purely elastic.

S14.3 Exact extrema over the specified component rectangles

Let the positive storage and loss ranges be $x \in [x_L, x_U]$ and $y \in [y_L, y_U]$. For $f(x, y) = y/(x^2 + y^2)$, the derivative with respect to x is negative. At fixed x, the derivative with respect to y changes sign at $y = x$. Consequently the exact extrema over this rectangle are

$$J''_L = min\left\{\frac{y_L}{x_U^2 + y_L^2}, \frac{y_U}{x_U^2 + y_U^2}\right\},$$

$$J''_U = \frac{y_*}{x_L^2 + y_*^2}, \; y_* = min\{y_U, max\{y_L, x_L\}\}.$$

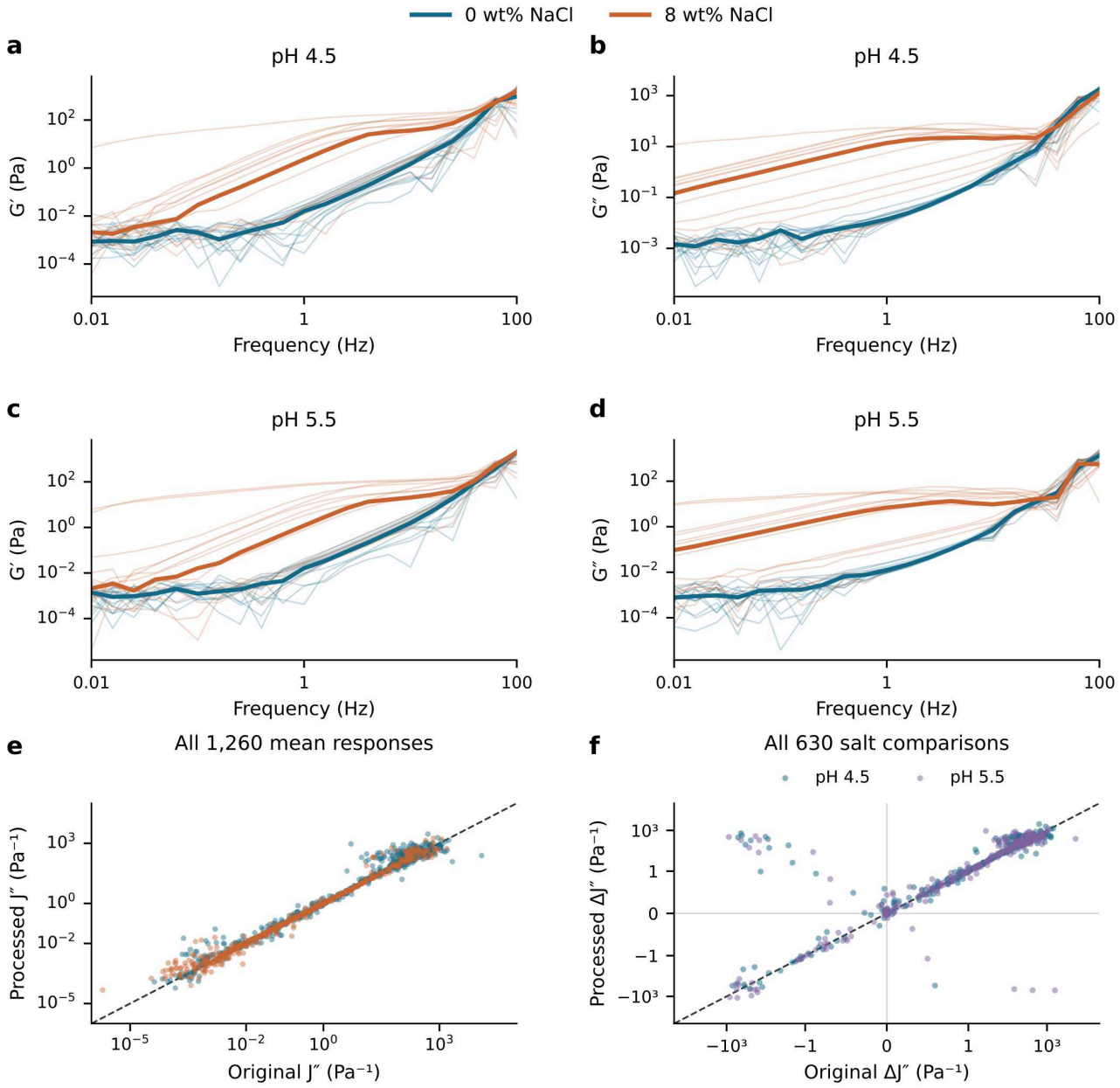
These expressions include an interior maximum in the loss coordinate when the rectangle contains $y = x_L$. Using only the four corners would miss that maximum. For the two salt states, the contrast range is

$$[\Delta J''_L, \Delta J''_U] = [J''_{L,0\%} - J''_{U,8\%}, J''_{U,0\%} - J''_{L,8\%}].$$

The three classifications in Figure 5b are positive throughout when $\Delta J''_L > 0$, negative throughout when $\Delta J''_U < 0$, and zero-containing otherwise. The component rectangles define the deterministic processing envelope. Raw and processed contrasts are retained separately.

S14.4 Complete comparisons and display conventions

Supplementary Figure 12 | Measured components and processing of the CAPB–SLES responses



a–d, Original averaged storage and loss moduli at pH 4.5 and 5.5 for all sixty formulations. Each thin line is one formulation; thick lines are pointwise medians of fifteen formulations within each pH/salt group. Blue and orange indicate 0 and 8 wt% NaCl. **e,** All 1,260 averaged-input/processed loss-compliance pairs, calculated separately from their corresponding modulus components. Colours retain the salt grouping. **f,** All 630 averaged-input/processed lower-salt-minus-higher-salt contrasts, coloured by pH. Dashed diagonals in e,f mark equality. Both axes in f are symmetric-logarithmic and linear between - 0.01 and 0.01 Pa^{-1}. Each formulation response is the arithmetic mean of three runs at matching frequencies; paired mean moduli are converted to loss compliance. Every recorded formulation, frequency and nominal salt pair is included. The processing construction uses the recorded nine-point, second-order Savitzky–Golay operation in log-response coordinates; its component ranges support the sensitivity classification in Figure 5. Spectral medians summarize different formulations. Component ranges are deterministic processing envelopes defined in section S14. Supplementary Information S14 specifies the calculation.

All 630 pair–frequency comparisons are retained: 420 ranges are positive, 200 contain zero and ten are negative. At the observed 1 Hz coordinate, 24 of the thirty ranges are positive and six contain zero. Figure 5c preserves the complete 1 Hz set, and Figure 5b displays every frequency comparison in the same composition order. The complete map makes the frequency support of each energetic ordering explicit.

The spectral summaries in Figure 5a and Supplementary Fig. 12 use pointwise medians across the fifteen different compositions at each pH/salt condition. All individual spectra remain visible. These medians are descriptive formulation summaries; the paired energetic result uses each formulation's own components. Figure 5c uses a symmetric-log scale with a linear interval from -1 to 1 Pa^{-1}, while Supplementary Fig. 12 uses a linear interval from -0.01 to 0.01 Pa^{-1}. Display transformations do not alter the recorded values or range classifications.

S15 Reference decoding and battery predictions

Three different cohorts answer three different questions. The frozen-function study evaluates all 2,301 development records from eighteen cells against an existing raw-coordinate predictor. The nested utility study produces 1,921 outer predictions from fifteen evaluated cells, with the three reference-source cells always available for training. The historical transport study uses 780 records from six previously outcome-exposed cells. The evaluations respectively measure preservation of a fixed function, prediction of measured capacity and retention of an established predictor under imposed maps.

Supplementary Table 47 | Fixed nested capacity comparison.

Representation and readout	Mean-cell MAE (mAh)	Mean-cell RMSE (mAh)	Maximum absolute error (mAh)
Actions, linear	4.81279	5.74700	18.2257
Actions, Gaussian kernel	4.66121	5.55837	17.5854
Raw impedance, linear	2.67937	3.34681	14.9136
Raw impedance, Gaussian kernel	2.14385	2.60456	9.89448
Finite cross-ratio, linear	3.80123	4.88735	32.7453
Finite cross-ratio, Gaussian kernel	3.30247	4.28366	25.0563
Bounded projective, linear	3.48492	4.35223	18.3207
Bounded projective, Gaussian kernel	3.41068	4.21623	26.9917

Every route in Table 47 predicts all 1,921 outer records. Cell means are weighted equally. Training-only feature centring, scaling, block normalization and selection prevent held-cell outcomes entering preprocessing. The free-intercept kernel-ridge solution is $\alpha = (CKC + n\lambda I)^{-1}(y - \bar{y})$, with query kernels centred against training means. Inner selection uses mean-cell MAE; ties prefer stronger regularization and then a larger Gaussian length scale. All representations receive the same recorded ensuing-cycle currents. The estimand is source-defined discharge capacity conditional on these recorded current variables.

In the fixed-function study, the best affine projection has RMS discrepancy 3.620354 mAh despite full design rank and a numerically verified least-squares optimum. Exact decoding recovers coordinates to 1.34424×10^{-14} Ω and function outputs to $3.0482283364 \times 10^{-12}$ mAh. These discrepancies measure preservation of the same fixed computation. Extended Data Fig. 3 keeps this distinction visible beside the nested evaluation.

Under shared maps I1–I6, decoded mean-cell MAE stays at 1.698417 mAh, while direct raw application spans 9.46969–122.094 mAh. Current references and target inputs change together; stored original references, model parameters, currents and outcomes remain fixed. The N1 nonshared control raises decoded MAE to 119.997 mAh. The quadratic N2 control remains outside the admitted shared fractional-linear class, including for

endpoint predictors with small observed changes. Supplementary Fig. 13 retains both controls and every map. In the complete source export, all 133,380 predictions for nineteen routes, nine conditions and 780 records are finite; 13,356 negative values are retained without clipping.

Cohort definitions and retained reference information

The three evaluations use distinct targets and should be read separately (Supplementary Table 48). For any collection of C cells, the reported mean-cell capacity MAE is

$$MAE_{cell} = \frac{1}{C}\sum_{c=1}^{C}\frac{1}{n_c}\sum_{i\in c}\left|\hat{Q}_i - Q_i\right|.$$

In contrast, frozen-function discrepancies compare two outputs for the same input record, and transformation discrepancies compare the same predictor before and after a change of measurement frame. These quantities need not equal capacity error.

Supplementary Table 48 | Battery evaluation populations and targets.

Evaluation	Records	Cells	Target of comparison	Reference handling
Frozen-function construction	2,301	18 development cells	Output of the original fixed linear function	Three retained reference spectra define the original coordinate frame
Nested capacity utility	1,921 per route	15 held cells	Measured capacity conditional on recorded actions	The three reference-source cells remain available for training
Historical prediction transport	780 per route and condition	6 historical cells	Retention of an existing output, with capacity error also reported	Current target and references change together; original references and predictor remain fixed

The reference spectra are PJ097_002_01_GEIS_CA1, PJ098_002_01_GEIS_CA2 and PJ099_002_01_GEIS_CA3. Each comprises 57 complex responses. Their full original values, frequency coordinates and decoder-pole quantities are retained in the analysis records (S20), so reference decoding does not require recovery of a constitutive battery model. The frozen linear function contains 114 real impedance components and three recorded action variables. Its stored feature scaling is absorbed into original-unit coefficients, giving intercept 102.940339084211 mAh and a fixed function of the form

$$f(z,u) = b + \Re\sum_{j=1}^{57}\beta_j z_j + w_u^T u,\ \beta_j = w_{\Re,j} - i\,w_{\Im,j}.$$

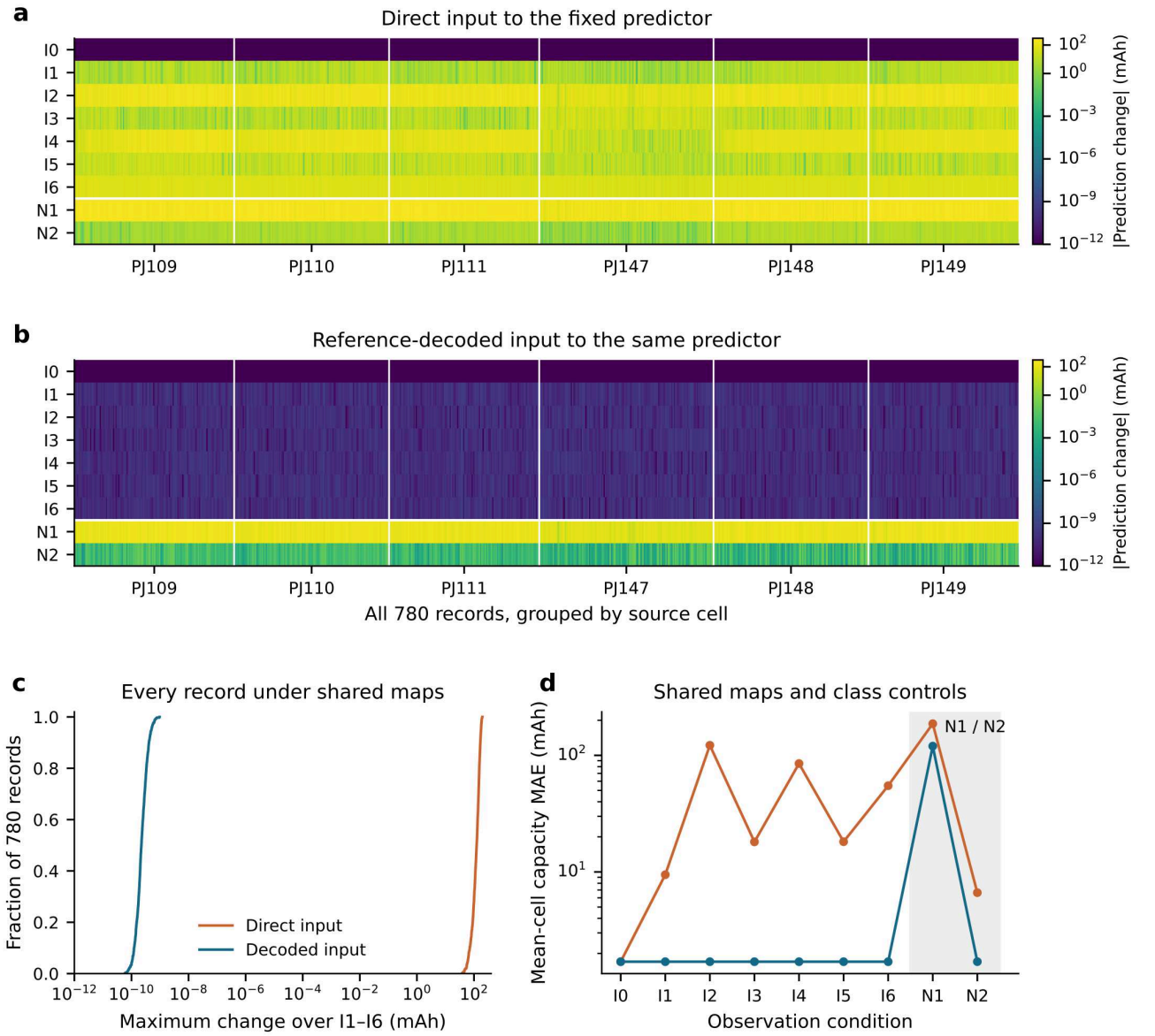
The stored complex weights are therefore an algebraic conversion of the original model. Both the original-unit real coefficients and equivalent complex coefficients are retained. Extended Data Fig. 3 displays every record and every development cell when comparing the best affine invariant readout with exact decoding of this same function.

Complete imposed-map preservation

For the development-selected Gaussian-kernel raw/decoded pair, the complete record-by-condition matrices appear in Supplementary Fig. 13. The six cell MAEs remain unchanged to the displayed precision throughout I0–I6 (Supplementary Fig. 13 and underlying source data). Two numerically different residual conventions are retained explicitly: comparison of decoded outputs with the original raw I0 output gives a maximum of 8.60912×10^{-10} mAh over I0–I6; comparison with the decoded route's own I0 output gives 9.69344×10^{-10} mAh. Both verify the same preservation result at the numerical precision of the recorded computations.

The underlying source data for Supplementary Fig. 13 contain the complete table of 133,380 predictions, rather than a subset of successful maps or records. All six shared transformations and both observation-class controls are retained.

Supplementary Figure 13 | Complete shared-map battery predictions and observation-class controls



a,b, Absolute change from each route's native I0 output for direct input to the fixed raw-coordinate predictor (a) and reference-decoded input to the same predictor (b). Each matrix contains all 780 records in all nine conditions, with columns grouped by the six source cells. Vertical white lines separate cells and the horizontal line separates I0–I6 from the N1 nonshared and N2 quadratic controls. A common logarithmic colour scale is used; values below 10^{-12} mAh, including exact zeros, are displayed at that floor. **c,** Empirical cumulative distributions of the maximum absolute change across the six shared transformations for every record. The largest change for the decoded route relative to its own I0 output is 9.69344×10^{-10} mAh. **d,** Mean-cell MAE against measured capacity for every condition, with N1/N2 shaded. The controls specify the shared fractional-linear observation class within which exact preservation follows. The complete source table retains all nineteen evaluated routes, nine conditions and 780 records (133,380 prediction rows); the two routes displayed here account for 14,040 rows.

S16 Passive representation and acquisition follow-up

A broader passive representation restores fidelity to the measured NREL–DENSO spectra while the same observation design preserves the resulting standalone computation. The original fixed RC-plus-series-RLC basis has a real part that cannot increase with frequency, whereas this increase occurs in 343 of 359 training records and 107 of 108 test records. The post hoc component follow-up adds parallel RL elements and retains the original data, frozen predictor, acquisition settings and complete primary results. Capacity outcomes do not enter specimen fitting or reference selection.[24,50]

For $s = i\omega$, the expanded passive specimen is

$$Z_{RC/RL}(s) = R_0 + sL + \frac{C^{-1}}{s} + \sum_{k=1}^{41} \frac{a_k}{1 + s\tau_k} + \sum_{k=1}^{41} \frac{b_k s\tau_k}{1 + s\tau_k}, R_0, L, C^{-1}, a_k, b_k \geq 0. \quad (S\,16.1)$$

The original 41 logarithmically spaced time constants, 10^{-6}–10^{3} s, were reused for both sums. Each additional term is a physical parallel RL element with resistance b_k and inductance $b_k\tau_k$. Its real part, $b_k(\omega\tau_k)^2/\left[1+(\omega\tau_k)^2\right]$, can rise with frequency while the element remains passive. The expanded basis therefore retains a physical component realization while removing the original basis's monotone-real-part restriction. It identifies a representation sufficient for the acquisition experiment; it does not assign a microscopic origin to the source's high-frequency rise.

All 467 source spectra were fitted using the original fractional complex-residual weighting, stacked real–imaginary least squares, unit-norm basis-column scaling and nonnegative least-squares solver with a 20,000-iteration cap. The original relative pruning threshold, 10^{-9} of the summed fitted resistive coefficients, was applied to both RC and RL terms. This produces 85 nonnegative coefficients per spectrum. The original predictor, input standardization, recorded temperature and state of charge, frequency grid, training/test labels and all 108 test rows were preserved. No alternate frequency subset, relaxation grid, regularization setting or capacity predictor was selected.

The expanded specimens were then passed through an independently assembled component network. In a parallel RL element, the inductor-current state j_k obeys

$$\tau_k \dot{j}_k + j_k = I_i, v_k = b_k(I_i - j_k). \quad (S\,16.2)$$

These component laws were added to the branch Kirchhoff voltage equations and bus current balance. The forward solver accepts component coefficients and never accepts target impedance or evaluates the fractional-linear impedance-to-tap formula. The original source-row identities of the five standards (25, 78, 420, 0 and 328), common external resistance (1.4911063 mΩ), total-current peak (1.5388189 A), common readout gain/feedthrough and five noise seeds were retained. The independently known reference values describe the corresponding expanded virtual standards. The same original finite-sample acquisition and reference-decoding code was used at zero noise and 2-μV voltage-sample RMS, with the original 1-μA current-sample noise. All four original geometries (matched, target-only +10%, heterogeneous and restored) were retained, together with measured-reference calibration and uncorrected-input controls. No acquisition setting was retuned after changing the representation.

The equal-cell measured-to-virtual spectral RMS fell from 3.2451% with the original RC basis to 0.3378% with the expanded basis; every test cell improved. The corresponding displacement of the unchanged predictor from its measured-input output fell from 7.6537 to 0.5575 percentage points (pp). Measured-input, expanded-standalone and expanded-recovered capacity MAEs were 2.2347, 2.3910 and 2.4082 pp, respectively. Recovery error itself remained 0.1772% and recovery-stage prediction displacement was 0.1970 pp. The two stages are therefore resolved separately: the expanded component representation restores fidelity to the measured input, and the unchanged observation design preserves the resulting standalone computation (Supplementary Table 49). All means first average the five fixed noise seeds within a record, then records within each of the seven physical cells, then cells equally; no new p-value or population-level confirmatory claim is assigned.

Supplementary Table 49 | Passive representation sensitivity with an unchanged acquisition and predictor. All entries use the same seven NREL–DENSO test cells and 108 source rows. Original RC results are retained from the primary experiment; RC/RL results are the separately labelled post hoc follow-up. Spectral endpoints are percentages and capacity/prediction endpoints are percentage points of relative capacity. Recovery is evaluated at 2-μV voltage-sample RMS.

Endpoint	Original RC basis	Expanded RC/RL basis
Measured-input capacity MAE	2.2347	2.2347
Measured-to-virtual spectral RMS	3.2451%	0.3378%
Measured-to-virtual prediction displacement	7.6537	0.5575
Virtual-standalone capacity MAE	9.1423	2.3910
Recovered capacity MAE	9.140	2.4082
Virtual-to-recovered spectral RMS	0.1779%	0.1772%
Virtual-to-recovered prediction displacement	0.203	0.1970

The follow-up retains 2,808 finite record–condition predictions. Component-to-port closure has maximum relative error 3.05×10^{-14}; noiseless target recovery has maximum recordwise fractional RMS 7.47×10^{-15}. The exact +10% target-path consequence is reproduced with maximum relative discrepancy 4.46×10^{-14}, and restoration reproduces every matched response under identical samples. The maximum attained cell-tap peak across the evaluated geometries is 4.8094 mV. Seven actual time-domain integrations, using the median source-order test record from each cell at the middle retained frequency, agree with the harmonic cell phasors to 1.69×10^{-11} maximum relative error. The analysis records (S20) retain scripts, coefficient arrays, reference identities, recovered spectra, individual-cell summaries and sample waveforms.

S17 Reference relations in measured electrical responses

The battery descriptor panel has 120 spectra from twelve cells at 57 native frequencies, grouped into thirty fixed quartets. The tissue panel has sixteen acquisitions from two pigs at ten frequency means, grouped into four quartets that preserve source acquisition conditions. Native frequency order and complex signs are retained. Incomplete tissue support is excluded from complete-quartet arithmetic rather than imputed. The retained phase-branch flags remain in the source accounting.

The seven admitted normalized maps and two controls are defined below. For each quartet and frequency, both numerator and denominator of the cross-ratio are calculated before forming the chordal discrepancy. This avoids treating an infinite finite-chart ratio as missing. There are 1,710 battery and forty tissue relations per map. Their maximum shared-map discrepancies are 7.465342×10^{-14} and 1.89902×10^{-15} (Extended Data Fig. 2). The nonshared N1 and quadratic N2 controls change all tested relations under the numerical decision rule recorded in the source summaries.

For these descriptor tests, write $\zeta = Z / s$. The normalization scales are $s = 0.9271544211513835\ \Omega$ for the battery set and $s = 3323.3252971709107\ \Omega$ for the tissue set. The transformations are applied in normalized coordinates and then returned to the original impedance scale. These descriptor scales are specific to this calculation; the predictor analysis retains its own stored normalization.

Map	Normalized transformation
I0	ζ
I1	1.2ζ
I2	$\zeta + 0.1i$

Map	Normalized transformation
I3	$\zeta/(1+0.1i\zeta)$
I4	$(0.99\zeta+0.1i)/(0.1i\zeta+1)$
I5	$\zeta+0.1$
I6	$(0.6+0.8i)\zeta$
N1	Apply I4 to all quartet members, then add $0.1i$ only to the fourth member
N2	$\zeta+0.05\zeta^2$

These computational perturbations test the shared-map relation on measured spectra, with N1 and N2 checking responses outside that class. The coefficients may vary with frequency but must be shared by the four states at each frequency. The chordal discrepancies measure numerical closure of the projective identity. Acquisition precision is represented separately through the measurement-error model.

S18 Retaining a physical readout across measured instrument changes

Published measurements and the inference target

We used the public sliding-transmission-line measurements of Hatab and colleagues, who measured a common microwave network with three uncalibrated vector network analysers: Rohde & Schwarz ZNA, Keysight ENA and Anritsu VectorStar. [26,27] Their experiment provides ten nominal slider settings on each instrument, stored in thirty Touchstone files. The source study determines propagation properties using the complete two-port response. Here, the scalar S11 component is used to ask whether three retained references allow one fixed position readout to operate after the instrument changes.

ZNA defines the retained original frame. The reference settings are 0, 93 and 192 mm for every instrument; the seven other settings, 21, 66, 81, 84, 117, 123 and 171 mm, are held out from construction of the reference maps and physical readout. Errors are reported against these nominal source settings. Each file supplies frequency in GHz and the real and imaginary parts of the four scattering parameters with a 50-ohm reference impedance. The analysis uses the 111 exactly shared native frequencies from 3 to 14 GHz in 0.1-GHz increments, without interpolation.

Reference transport and the fixed physical readout

At each frequency, the three measured reference values on the current instrument and their retained ZNA values define the decoder in section S9. The seven current target responses are decoded into the original frame before applying the same readout. For the physical coordinate we use the stated lossless-air phase law

$$q(x,f)=\exp(-4\pi ifx/c_0),\ c_0=299\,792\,458\ m\,s^{-1}.$$

The readout uses the three ZNA reference responses and the corresponding phase coordinates $q_j(f)$ at the known reference positions. For a scalar input $r(f)$ and original reference values a_1,a_2,a_3, define

$$N=(a_1-a_3)(a_2-r),\ D=(a_1-r)(a_2-a_3),\ k_q=\frac{q_1-q_3}{q_2-q_3},$$

$$q_N=N\,q_1-k_q D\,q_2,\ q_D=N-k_q D.$$

The pair (q_N, q_D) is retained in homogeneous form. A frequency is used for physical readout when the minimum pairwise separation of the three reference phase coordinates exceeds 0.2. This reference-geometry rule retains 89 frequencies and excludes 22; the complete frequency list and mask are retained in the analysis records (S20). Values must also satisfy $|q_N|^2 + |q_D|^2 > 10^{-24}$. The inferred position minimizes

$$J(x) = \frac{1}{|F|} \sum_{f \in F} \frac{|q_N(f) - q(x,f) q_D(f)|^2}{2\{|q_N(f)|^2 + |q_D(f)|^2\}}.$$

A global scan of the reference interval 0–192 mm on a 0.1-mm grid is followed by bounded local refinement around the best grid position. No held-out nominal position enters this calculation. The propagation speed, reference set, frequency-selection rule and readout are unchanged across instruments and correction routes. These are explicitly specified choices for a secondary analysis of the published measurements.

Comparisons using the same reference information

Four routes are compared: direct application of the fixed readout, complex-affine least-squares alignment using the same three reference pairs, reference decoding, and a conventional fractional-linear calibration obtained independently by a homogeneous coefficient solve. The final two routes encode the same three-point coordinate transformation. The independent solve checks implementation agreement: their decoded complex S11 values differ by at most 5.42×10^{-13}.

Supplementary Table 50 | Position-readout errors for all instruments and routes.

Instrument	Direct readout MAE (mm)	Complex-affine alignment MAE (mm)	Reference decoding MAE (mm)	Conventional three-point calibration MAE (mm)
ZNA, retained original frame	0.152624	0.152624	0.152624	0.152624
ENA	0.358231	0.150578	0.152954	0.152954
VectorStar	90.616653	0.160223	0.152202	0.152202

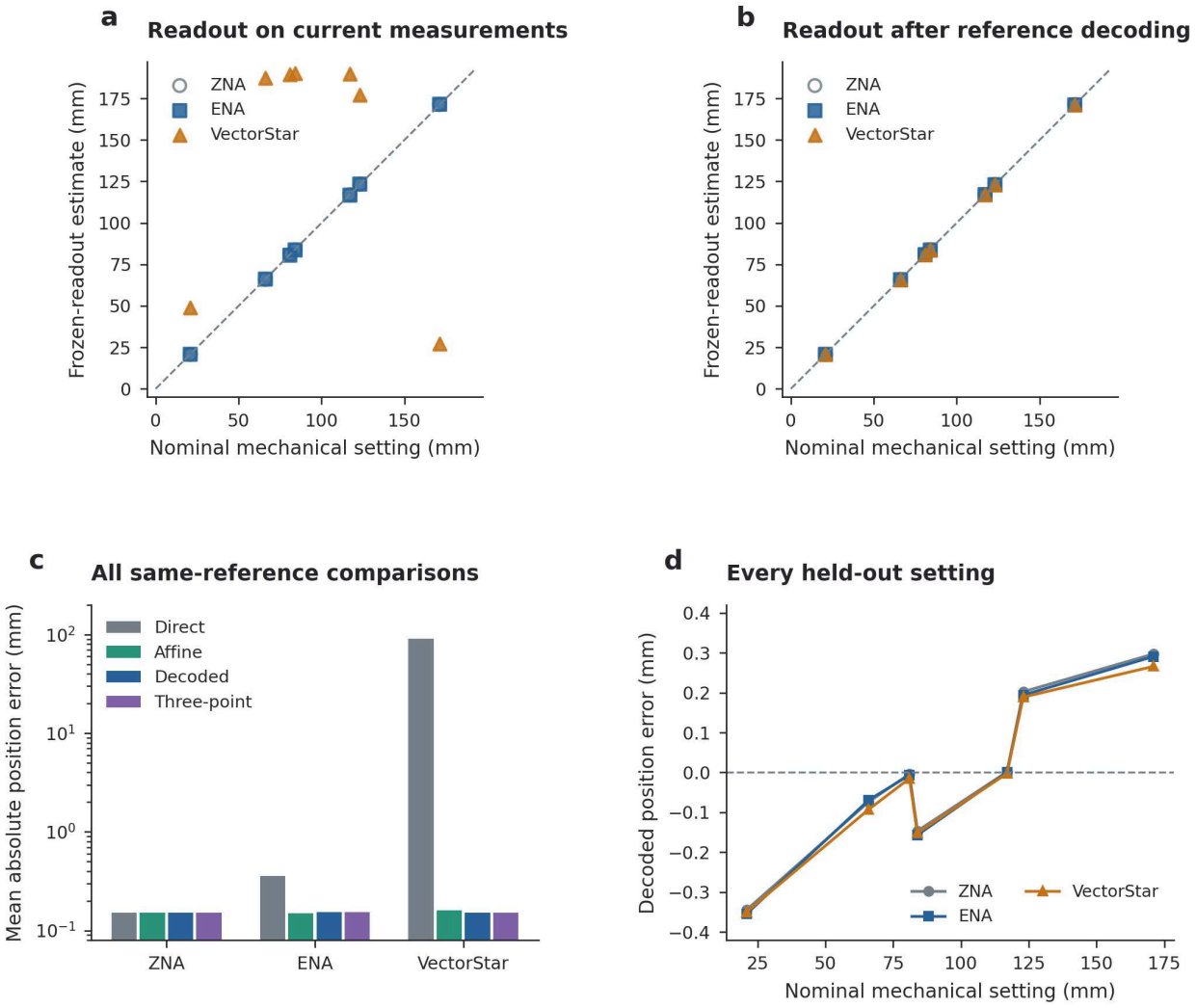
Every value averages the same seven held-out nominal settings. Supplementary Fig. 14 displays all settings and all comparison routes. The source files retain all 84 instrument/route/setting predictions and all 2,331 instrument/target/frequency frame comparisons, including frequencies excluded from the physical readout. The thirty native measurement files are also retained with their source hashes. Frequencies form one input spectrum for each nominal setting.

Interpretation for physical inference

Reference decoding returns the ENA and VectorStar position-readout MAEs to approximately 0.153 and 0.152 mm, respectively, close to the 0.153-mm value obtained in the original ZNA frame. Complex-affine correction also performs well for this readout, and conventional three-point calibration agrees numerically with decoding. Thus this comparison supplies a measured example of transferring an existing physical readout using retained references.

The scalar frame relation is approximate for this two-port network. Across the complete target spectra, decoded S11 retains relative vector discrepancies of 19.62% for ENA and 19.74% for VectorStar against ZNA, while the position readout remains useful. Reference decoding restores the fixed position readout across instruments while leaving measurable full-spectrum discrepancies. This target-specific transfer illustrates preservation of the information needed by a chosen physical computation. The position errors measure agreement with nominal settings under the stated lossless-air model.

Supplementary Figure 14 | A fixed physical readout transfers across three measured microwave instruments



Reanalysis of the public sliding-transmission-line measurements of Hatab and colleagues uses measured S11 responses from three uncalibrated vector network analysers, with ZNA as the original frame. [26,27] Three reference settings (0, 93 and 192 mm) are used for every instrument; seven other nominal settings are held out from construction of the map and readout. **a,b,** The same frozen physical position readout applied directly to current measurements (a) and after reference decoding into the ZNA frame (b). Dashed lines denote equality with the nominal source settings. **c,** Mean absolute error across the seven held-out settings for direct input, complex-affine alignment, reference decoding and an independently solved conventional three-point fractional-linear calibration, all using the same reference pairs. **d,** Every signed position error after decoding. Input spectra share 111 native frequencies from 3 to 14 GHz; a geometry-based reference-separation rule retains 89 frequencies for the physical readout. Reference decoding transfers the specified readout across the measured instrument changes, with errors near the original-frame baseline. Errors measure agreement with nominal mechanical settings. Section S18 gives the phase model, selection rule, search procedure and complete results.

S19 Passive transport families and known temperature

A physical question can concern a response family rather than a particular coefficient. Electrical temperature dependence combines intrinsic transport with stationary contact or network effects. To distinguish linear from quadratic intrinsic responses, we pass both laws through the same admitted readout class before comparing their

predictions with the data. The test uses twelve source-designated strange-metal curves from one moiré WSe_2 device.[58] Each family receives the same three nuisance coefficients for a passive readout network. Temperature is known, and the network remains fixed within each sweep under the observation model (Methods).

Across 0.1–10 K, all twelve curves favour the linear family under contiguous temperature-block holdout: quadratic-to-linear RMS error ratios range from 2.90 to 10.46, and all sixty withheld blocks favour the same family (Supplementary Fig. 15). A source-designated Fermi-liquid comparator over 0.1–4 K instead favours the quadratic family. Restricting the targets to 0.1–2 K leaves eight of twelve favouring linear, showing why the sampled control range matters. The full-window preference survives a broader monotone fractional-linear readout, although near-unity fitted exponents depend on the passive subclass (Extended Data Fig. 6). The supported conclusion is a distinction between physical response families through a stationary passive readout, conditional on that observation class, even while its intrinsic decomposition remains unresolved.

The Xia workbook contributes twelve 66-point target curves, six from panel i and six from panel j, and two 62-point controls. There are 916 selected points from one device. Target measurements are at 0.3 T and controls at zero field. Native temperature and resistance units are retained. Three windows are analyzed without resampling: 0.1–2, 0.1–4 and 0.1–10 K. [58]

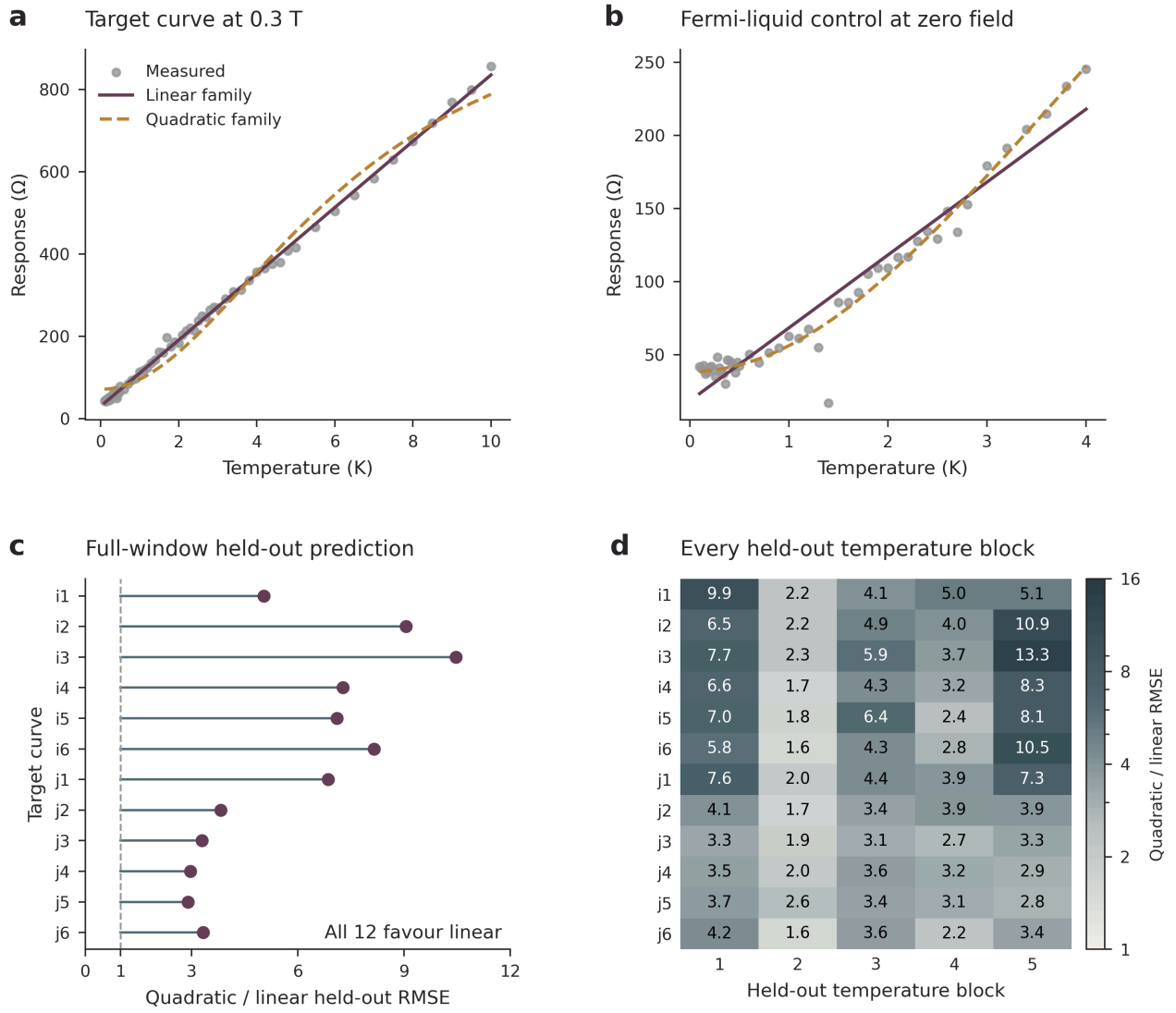
For $u=\left(T/T_{ref}\right)^{\beta}$, write the intrinsic family as $r=r_0+Au$ and the stationary passive readout as $m=R_s+gr/\left(1+Gr\right)$, with $r_0,R_s,G\geq 0$ and $A,g>0$. Collecting terms gives $m=a+ku/\left(1+cu\right)$, where $a=R_s+g\,r_0/\left(1+G\,r_0\right)$, $k=gA/\left(1+G\,r_0\right)^2$ and $c=GA/\left(1+G\,r_0\right)$. Thus $a\geq 0$, $k>0$ and $c\geq 0$. Conversely every such reduced triple has a passive realization by choosing $r_0=0$, $R_s=a$ and suitable A,g,G. The fitted nuisance parameters do not identify a unique contact or material decomposition.

The fixed alternatives set $\beta=1$ or 2 and have the same three nuisance coefficients. Their objective is the unweighted sum of squared residuals in source ohms. At fixed c, the coefficients are solved linearly with the stated constraints. The solver scans 81 values in $\log\left(1+c\right)$, refines local minima and includes the boundaries. Passive fits constrain $0\leq c\leq 100$. Free-exponent fits profile $0.1\leq\beta\leq 5$. The reference temperature is the maximum known temperature in the full chosen window, including held-out covariates, never held-out responses.

Five contiguous temperature blocks are withheld in turn, with each nuisance fit using the remaining responses only. Held-out RMSE aggregates squared errors over all withheld points before taking the square root. Because withheld blocks include extremes, some folds test extrapolation as well as interpolation. The comparison statistic is the ratio of held-out quadratic and linear RMSEs on the same response scale.

All twelve targets favour the passive linear family in both the 0.1–10 and 0.1–4 K windows. Full-window ratios range from 2.897629 to 10.463741; free exponents range from 0.907676 to 1.021711. In the 0.1–2 K window, eight of twelve favour the linear family. The panel-h control at filling 0.78 and zero field favours the quadratic family across 0.1–4 K: its ratio is 0.748935 and free exponent 2.219047. Across 0.1–10 K that control has free exponent 1.553839, illustrating the importance of the window. Supplementary Fig. 15 and Extended Data Fig. 6 show these curve-specific and window-specific comparisons.

Supplementary Figure 15 | Temperature dependence remains distinguishable under a stationary passive readout



Twelve target curves from one device. Upper panels show full-curve fits; lower panels evaluate withheld observations.

a,b, Measured responses and full-curve fits of the linear ($\beta = 1$) and quadratic ($\beta = 2$) passive families, $m = a + ku/(1 + cu)$ with $u = (T/T_{ref})^{\beta}$, $a \geq 0$, $k > 0$ and $c \geq 0$. Panel a shows target i1 at filling $\nu = 0.874$ and 0.3 T over 0.1–10 K. Panel b shows the zero-field control at $\nu = 0.78$ over 0.1–4 K. **c,** Quadratic/linear held-out root-mean-square error (RMSE) ratios for all twelve target curves over 0.1–10 K. Each point in c pools squared prediction errors across five contiguous withheld temperature blocks. **d,** The corresponding twelve-by-five matrix of individual block ratios. All sixty exceed one, spanning 1.598–13.348. The five withheld blocks contain 14, 13, 13, 13 and 13 points, respectively; training uses the remaining responses. The twelve target curves contain 66 temperatures each and originate from one source device; five contiguous temperature blocks assess prediction outside the fitted regions. Panels a,b show full-curve fits, whereas panels c,d evaluate held-out predictions. Labels i1–i6 and j1–j6 retain the original source-panel order, with fillings listed in section S19; the source data retain every target curve and full-fit residual. [58]

The broader monotone sensitivity allows a signed offset and $-0.999 \leq c \leq 100$. Target full-window free exponents range from 0.672254 to 0.914063 even while the fixed-family comparison favours linear. This variation shows that exponent interpretation depends on the admitted observation class. Two broader-class held-out control fits

reach the negative-c boundary when the highest-temperature block is withheld; they remain in the audit. No full-fit exponent or upper-c boundary is reached. The passive class supplies the principal physical comparator.

The analysis comprises 84 curve/window/class records, 252 full fits and 840 held-out training fits. Aggregate held-out errors are calculated from fold sums of squares and counts. The principal result uses the stationary passive model; temperature-dependent observation parameters define a different class. Curves and folds retain their common origin in one device. The comparison addresses response-family preference, with microscopic interpretation supplied by the source system's additional physical evidence.

Complete target and held-out block evidence

Supplementary Fig. 16 shows every selected target curve and its full-fit residuals. The twelve targets contribute 792 native observations, all retained in the 0.1–10 K comparison. Supplementary Figure 15d reports every individual blockwise prediction comparison. All sixty quadratic/linear held-out RMSE ratios exceed one, ranging from 1.598123 to 13.347715. Each target therefore favours the linear passive family in every withheld block as well as in its aggregate score. [58]

Supplementary Table 51 | Contiguous temperature blocks for the 66-point targets.

Withheld block	Observed temperature range (K)	Withheld points	Training points
1	0.10–0.36	14	52
2	0.38–1.10	13	53
3	1.20–2.40	13	53
4	2.50–4.40	13	53
5	4.60–10.00	13	53

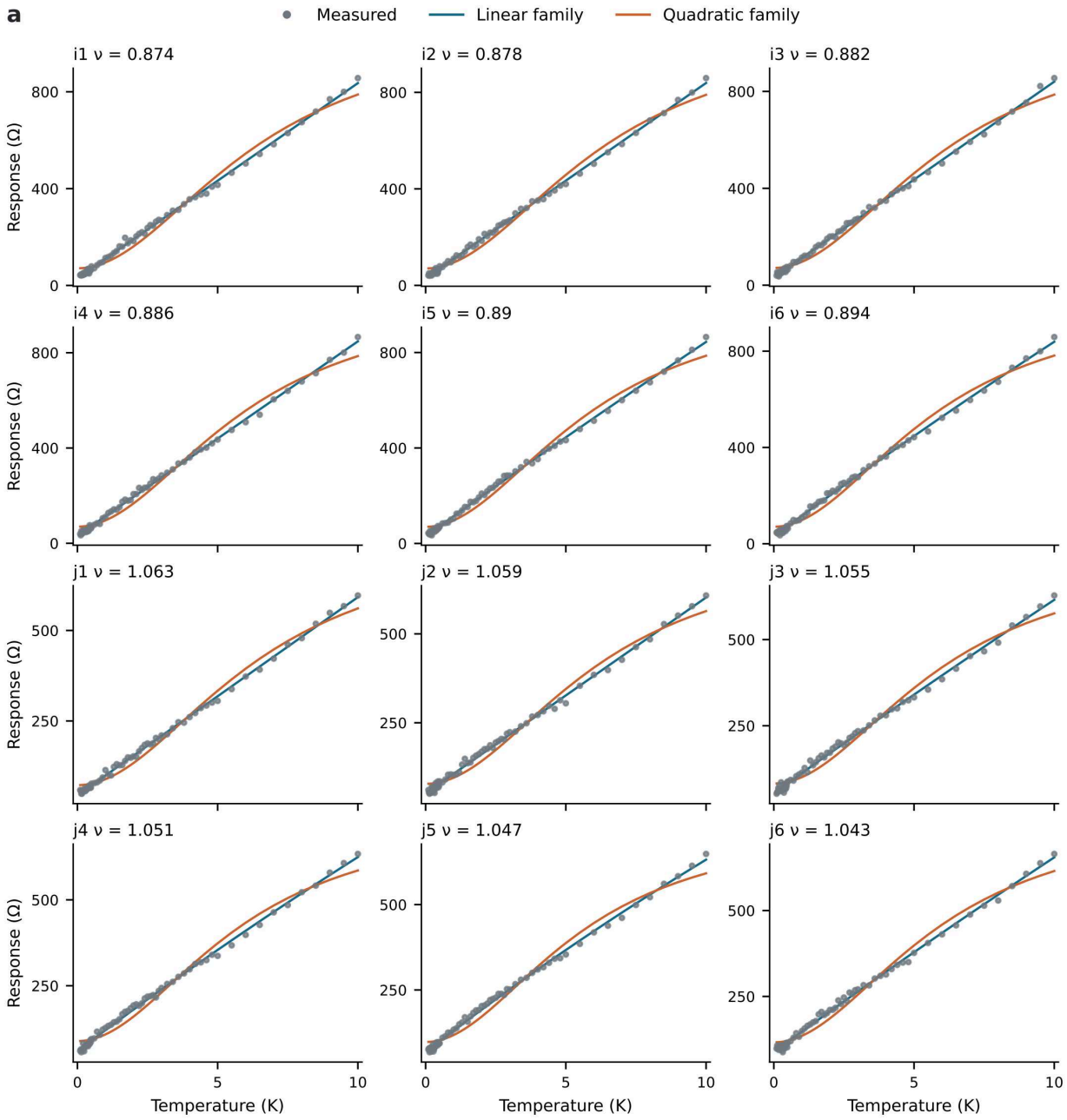
The common grid gives the same block membership in all twelve targets. For a fixed family, the aggregate held-out error is $\left[\sum_b SSE_b / \sum_b n_b\right]^{1/2}$, not the arithmetic mean of block RMSEs. Reconstruction from the fold sums of squares and counts reproduces every reported aggregate ratio to numerical precision (maximum absolute difference 1.8×10^{-15}).

Supplementary Table 52 | Full-window passive-model comparisons.

Target	Filling ν	Aggregate held-out RMSE ratio	Minimum block ratio	Maximum block ratio
i1	0.874	5.045970	2.209393	9.928374
i2	0.878	9.051301	2.185176	10.890027
i3	0.882	10.463741	2.304492	13.347715
i4	0.886	7.278899	1.709383	8.349902
i5	0.89	7.107534	1.760823	8.119627
i6	0.894	8.153832	1.601835	10.471515
j1	1.063	6.853905	2.038501	7.597308
j2	1.059	3.824757	1.699581	4.082852
j3	1.055	3.297572	1.941301	3.340574
j4	1.051	2.975106	2.041085	3.586903
j5	1.047	2.897629	2.560103	3.691553
j6	1.043	3.328297	1.598123	4.214891

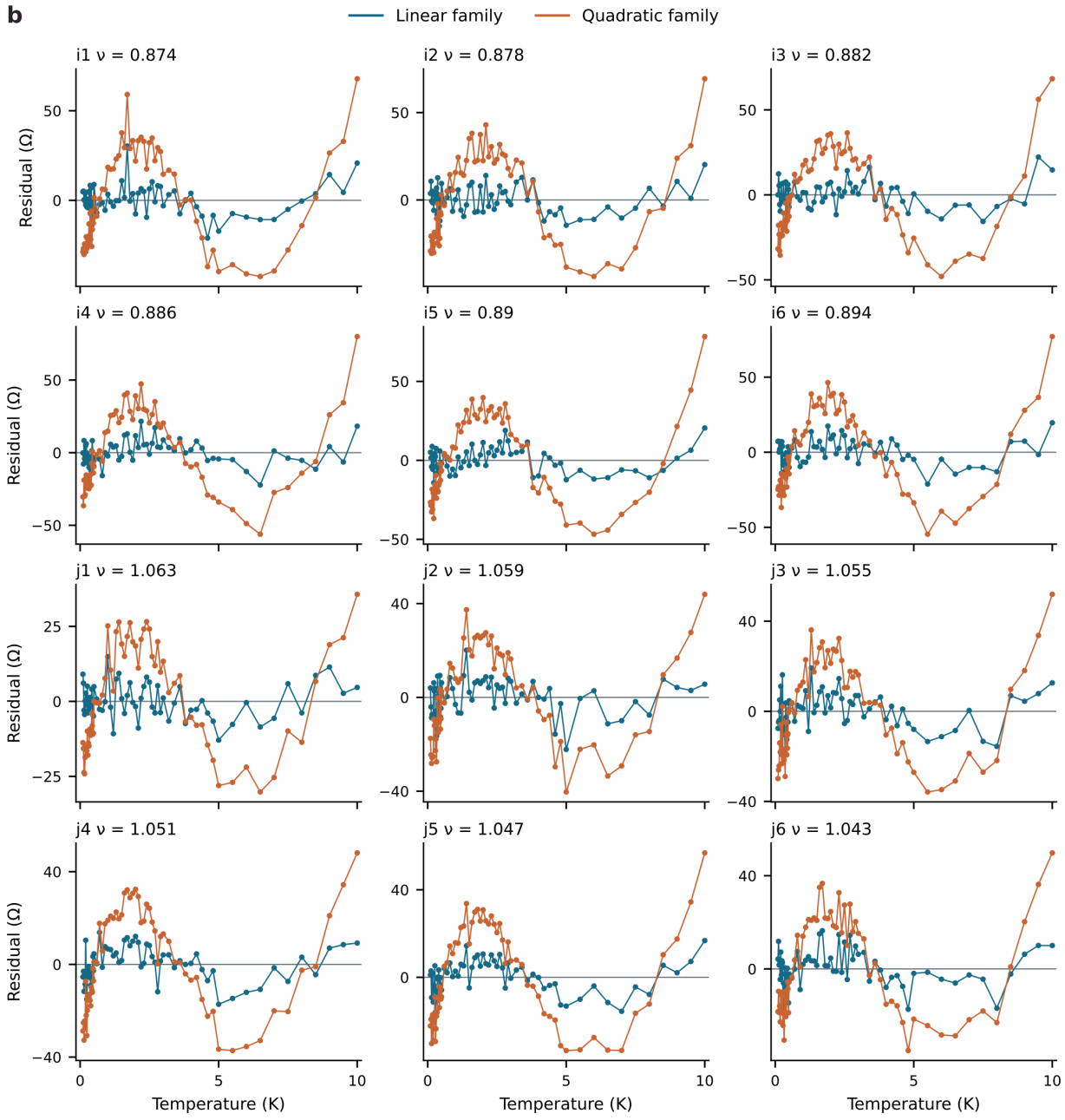
Every ratio uses quadratic-family error divided by linear-family error. Labels i1–i6 follow fillings 0.874–0.894 in increasing order, and j1–j6 follow fillings 1.063–1.043 in decreasing order, retaining the original source-panel order used in Extended Data Fig. 6. The figure gallery uses complete-curve fits; the tabulated comparisons use predictions from separately withheld blocks. Both retain the stated stationary passive model and the common origin of the curves in one device.

Supplementary Figure 16 | Complete transport fits and residuals



a, The twelve panels show all 792 selected target observations: 66 temperatures from 0.1 to 10 K for each of six source-panel-i curves and six source-panel-j curves at 0.3 T. Filling ν is given above each panel. Grey points are native workbook measurements; blue and orange curves are the fitted $\beta = 1$ and $\beta = 2$ families under the same stationary passive observation model and three nuisance coefficients. Each curve is fitted using all observations in its panel. The separate held-out evaluation within these curves is given in Supplementary Fig. 15c,d and the block table in Supplementary Information section S19. The source labels, response units and full temperature grid are retained. [58]

Supplementary Figure 16 (continued) | Complete transport fits and residuals



b, Signed residuals, measured response minus the fitted response, for every observation and both fixed-exponent families in Supplementary Fig. 16a. Blue denotes the linear family and orange the quadratic family. The horizontal line marks zero; connected points follow increasing temperature. Each panel contains 66 observed responses and corresponds to the same source curve and filling as Supplementary Fig. 16a. These are residuals of the complete-curve fits over 0.1–10 K. Predictive comparisons use the separately withheld temperature blocks reported in Supplementary Fig. 15c,d and Supplementary Information section S19. [58]

S20 Data and analysis records

Internal figure-source and data-code indexes link each retained display and numbered table to its numerical inputs, generating code and execution scope. The records distinguish original measurements, reused public data, published summary inputs, derived records, controlled simulations and model outputs.

The retained records include the original CAPB–SLES mean-component table and processing outputs; imposed-map battery predictions and controls; frozen-function and reference records; complete gel and liver matching summaries; native chromosome estimates; transport fits and held-out errors; NASA network-scenario results; microwave measurement files and readout predictions; individual biological records; intervention calculations; whole-cell battery results; and the passive-representation follow-up. Numerical checks compare exact bounds with complete enumeration, source summaries with recomputed values, held-out scores with their component sums and prediction-preservation statements with the complete recorded outputs.

Original CAPB–SLES measurements, derived numerical records, figure inputs, data indexes, frozen model states and custom analysis code, including figure-generation scripts and numerical verification routines, are stored in a private repository for editorial and peer review. These materials will be released publicly upon acceptance. Public third-party data and software remain available through the cited repositories and publications.

References

13. Fan, W. et al. Matrix viscoelasticity promotes liver cancer progression in the pre-cirrhotic liver. Nature 626, 635–642 (2024). doi:10.1038/s41586-023-06991-9

14. Kpeglo, D. et al. Modeling the mechanical stiffness of pancreatic ductal adenocarcinoma. Matrix Biol. Plus 14, 100109 (2022). doi:10.1016/j.mbplus.2022.100109

15. Hiscox, L. V. et al. Standard-space atlas of the viscoelastic properties of the human brain. Human Brain Mapping 41, 5282–5300 (2020). doi:10.1002/hbm.25192

16. Boulet, T., Kelso, M. L. & Othman, S. F. Long-Term In Vivo Imaging of Viscoelastic Properties of the Mouse Brain after Controlled Cortical Impact. Journal of Neurotrauma 30, 1512–1520 (2013). doi:10.1089/neu.2012.2788

17. Karlinski Zur, M. et al. Altered extracellular matrix structure and elevated stiffness in a brain organoid model for disease. Nature Communications 16, 4094 (2025). doi:10.1038/s41467-025-59252-w

18. Freimann, F. B. et al. Alteration of brain viscoelasticity after shunt treatment in normal pressure hydrocephalus. Neuroradiology 54, 189–196 (2012). doi:10.1007/s00234-011-0871-1

19. Ank, M., Kröger, T., Schreiber, M. & Lienkamp, M. Experimental analysis of lithium-ion cell procurement: Quality differences, correlations, and importance of cell characterization. J. Energy Storage 66, 107430 (2023). doi:10.1016/j.est.2023.107430

20. Ank, M., Kröger, T., Schreiber, M. & Lienkamp, M. Characterization data of 250 cylindrical lithium-ion cells. Technical University of Munich (2023). doi:10.14459/2023mp1699705

21. Zhang, Y., Tang, Q., Zhang, Y., Wang, J., Stimming, U. & Lee, A. A. Identifying degradation patterns of lithium ion batteries from impedance spectroscopy using machine learning. Nat. Commun. 11, 1706 (2020). doi:10.1038/s41467-020-15235-7

22. Chan, H. S. et al. Comparison of methodologies to estimate state-of-health of commercial Li-ion cells from electrochemical frequency response data. J. Power Sources 542, 231814 (2022). doi:10.1016/j.jpowsour.2022.231814

23. Guignard, F. & Hoffmann, J. LiBforSecUse processed data for machine learning modelling and uncertainty propagation. Version v1. Zenodo (2025). doi:10.5281/zenodo.17792537

24. Gasper, P., Schiek, A., Smith, K., Shimonishi, Y. & Yoshida, S. Predicting battery capacity from impedance at varying temperature and state of charge using machine learning. Cell Rep. Phys. Sci. 3, 101184 (2022). doi:10.1016/j.xcrp.2022.101184

25. Deng, L. et al. Creation, stabilization, and investigation at ambient pressure of pressure-induced superconductivity in Bi0.5Sb1.5Te3. Proc. Natl Acad. Sci. USA 122, e2423102122 (2025). doi:10.1073/pnas.2423102122

26. Hatab, Z., Abdi, A., Steinbauer, G., Gadringer, M. E. & Bösch, W. Propagation constant measurement based on a single transmission line standard using a two-port VNA. Sensors 23, 4548 (2023). doi:10.3390/s23094548

27. Hatab, Z. Propagation Constant Measurement Based on a Single Transmission Line Standard Using a Two-port VNA: Dataset and Code. Graz University of Technology (2023). doi:10.3217/6bd26-5cp67

36. Kpeglo, D. Modeling the Mechanical Stiffness of Pancreatic Ductal Adenocarcinoma: dataset. University of Leeds (2022). doi:10.5518/952

37. Joshi, K. et al. Quantifying the viscoelastic properties of pancreatic tissue: a comparative study of human, porcine and engineered hydrogel. Ann. Biomed. Eng. (2026). doi:10.1007/s10439-026-04235-1

38. Erisken, C., Kalyon, D. M., Zhou, J., Kim, S. G. & Mao, J. J. Viscoelastic properties of dental pulp tissue and ramifications on biomaterial development for pulp regeneration. J. Endod. 41, 1711–1717 (2015). doi:10.1016/j.joen.2015.07.005

39. Witt, H. et al. Ion-mediated condensation controls the mechanics of mitotic chromosomes. Nat. Mater. 23, 1556–1562 (2024). doi:10.1038/s41563-024-01975-0

40. Witt, H. Data for the manuscript Ion-mediated condensation controls the mechanics of mitotic chromosomes. Zenodo, version 1 (2023). doi:10.5281/zenodo.7801755

41. Eide, P. K. & Brean, A. Cerebrospinal fluid pulse pressure amplitude during lumbar infusion in idiopathic normal pressure hydrocephalus can predict response to shunting. Cerebrospinal Fluid Research 7, 5 (2010). doi:10.1186/1743-8454-7-5

42. Eide, P. K. & Sorteberg, W. Changes in intracranial pulse pressure amplitudes after shunt implantation and adjustment of shunt valve opening pressure in normal pressure hydrocephalus. Acta Neurochirurgica 150, 1141–1147 (2008). doi:10.1007/s00701-008-0138-8

44. Jocher, P., Steinhardt, M., Ludwig, S., Schindler, M., Martin, J. & Jossen, A. A novel measurement technique for parallel-connected lithium-ion cells with controllable interconnection resistance. J. Power Sources 503, 230030 (2021). doi:10.1016/j.jpowsour.2021.230030

45. Moradpour, A., Kasper, M. & Kienberger, F. Quantitative cell classification based on calibrated impedance spectroscopy and metrological uncertainty. Batteries Supercaps 6, e202200524 (2023). doi:10.1002/batt.202200524

49. Chan, H. S. et al. LiBforSecUse Data Release – Impedance spectra of life cycle tests of commercial 18650 cells. Version V2. Zenodo (2022). doi:10.5281/zenodo.6418665

50. Gasper, P. et al. battery_capacity_from_eis: author code and data. GitHub https://github.com/NatLabRockies/battery_capacity_from_eis (accessed 31 October 2026).

51. Halbert, C. et al. High-pressure structures of Bi0.5Sb1.5Te3 at room temperature and in its superconducting states. Phys. Rev. Mater. 10, 094804 (2026). doi:10.1103/ks5f-s1hm

52. Zhang, Y. et al. Identifying degradation patterns of lithium ion batteries from impedance spectroscopy using machine learning. Zenodo (2020). doi:10.5281/zenodo.3633835

53. Qiao, E., Fulmore, C. A., Schaffer, D. V. & Kumar, S. Substrate stress relaxation regulates neural stem cell fate commitment. Proceedings of the National Academy of Sciences 121, e2317711121 (2024). doi:10.1073/pnas.2317711121

54. Qiao, E. et al. Spectrin mediates 3D-specific matrix stress-relaxation response in neural stem cell lineage commitment. Science Advances 10, eadk8232 (2024). doi:10.1126/sciadv.adk8232

55. Oliva, M. A. G. et al. Piezo1 regulates the mechanotransduction of soft matrix viscoelasticity. Nature Communications 16, 9155 (2025). doi:10.1038/s41467-025-64185-5

56. Huerta-López, C. et al. Cell response to extracellular matrix viscous energy dissipation outweighs high-rigidity sensing. Science Advances 10, eadf9758 (2024). doi:10.1126/sciadv.adf9758

57. Fan, W. et al. Author Correction: Matrix viscoelasticity promotes liver cancer progression in the pre-cirrhotic liver. Nature 648, E9 (2025). doi:10.1038/s41586-025-09947-3

58. Xia, Y. et al. Bandwidth-tuned Mott transition and superconductivity in moiré WSe2. Nature 650, 585–591 (2026). doi:10.1038/s41586-025-10049-3

59. scikit-rf developers. OnePort one-port calibration documentation. Accessed 27 October 2026. https://scikit-rf.readthedocs.io/en/latest/api/calibration/generated/skrf.calibration.calibration.OnePort.html

64. Saha, B. & Goebel, K. Battery Data Set. NASA Prognostics Data Repository, NASA Ames Research Center (2007). https://www.nasa.gov/intelligent-systems-division/discovery-and-systems-health/pcoe/pcoe-data-set-repository/